

# **Introduction to Contact Mechanics**

*Anthony C. Fischer-Cripps*

**Springer**

# Mechanical Engineering Series

---

Frederick F. Ling  
*Series Editor*

**Springer**

*New York*

*Berlin*

*Heidelberg*

*Barcelona*

*Hong Kong*

*London*

*Milan*

*Paris*

*Singapore*

*Tokyo*

This page intentionally left blank

Anthony C. Fischer-Cripps

# Introduction to Contact Mechanics

With 93 Figures



Springer

Anthony C. Fischer-Cripps  
CSIRO  
Bradfield Road, West Lindfield  
Lindfield NSW 2070, Australia

*Series Editor*

Frederick F. Ling  
Ernest F. Gloyna Regents Chair  
in Engineering  
Department of Mechanical Engineering  
The University of Texas at Austin  
Austin, TX 78712-1063, USA  
and  
William Howard Hart Professor Emeritus  
Department of Mechanical Engineering,  
Aeronautical Engineering and Mechanics  
Rensselaer Polytechnic Institute  
Troy, NY 12180-3590, USA

*Consulting Editor*

Iain Finnie  
Department of Mechanical Engineering  
University of California  
Berkeley, CA 94720, USA

Library of Congress Cataloging-in-Publication Data  
Fischer-Cripps, Anthony C.

Introduction to contact mechanics / Anthony C. Fischer-Cripps.

p. cm. — (Mechanical engineering series)

Includes bibliographical references and index.

ISBN 0-387-98914-5 (hc. : alk. paper)

I. Contact mechanics. I. Title. II. Series: Mechanical  
engineering series (Berlin, Germany)

TA353.F57 2000

620.1—dc21

99-42671

Printed on acid-free paper.

© 2000 Springer-Verlag New York, Inc.

All rights reserved. This work may not be translated or copied in whole or in part without the written permission of the publisher (Springer-Verlag New York, Inc., 175 Fifth Avenue, New York, NY 10010, USA), except for brief excerpts in connection with reviews or scholarly analysis. Use in connection with any form of information storage and retrieval, electronic adaptation, computer software, or by similar or dissimilar methodology now known or hereafter developed is forbidden.

The use of general descriptive names, trade names, trademarks, etc., in this publication, even if the former are not especially identified, is not to be taken as a sign that such names, as understood by the Trade Marks and Merchandise Marks Act, may accordingly be used freely by anyone.

Production coordinated by Robert Wexler and managed by Francine McNeill; manufacturing supervised by Jeffrey Taub.

Photocomposed copy prepared from the author's Microsoft Word files.

Printed and bound by Edwards Brothers, Inc., Ann Arbor, MI.

Printed in the United States of America.

9 8 7 6 5 4 3 2 1

ISBN 0-387-98914-5 Springer-Verlag New York Berlin Heidelberg SPIN 10742874

*To Dianne, Raymond and Henry*

This page intentionally left blank

# Series Preface

Mechanical engineering, an engineering discipline forged and shaped by the needs of the industrial revolution, is once again asked to do its substantial share in the call for industrial renewal. The general call is urgent as we face profound issues of productivity and competitiveness that require engineering solutions. The Mechanical Engineering Series features graduate texts and research monographs intended to address the need for information in contemporary areas of mechanical engineering.

The series is conceived as a comprehensive one that covers a broad range of concentrations important to mechanical engineering graduate education and research. We are fortunate to have a distinguished roster of consulting editors on the advisory board, each an expert in one of the areas of concentration. The names of the consulting editors are listed on the facing page of this volume. The areas of concentration are applied mechanics, biomechanics, computational mechanics, dynamic systems and control, energetics, mechanics of materials, processing, production systems, thermal science, and tribology.

Professor Finnie, the consulting editor for mechanics of materials, and I are pleased to present *Introduction to Contact Mechanics* by Anthony C. Fischer-Cripps.

Austin, Texas

Frederick F. Ling

This page intentionally left blank

# Preface

There has been considerable interest in the last decade in the mechanical characterisation of thin film systems and small volumes of material using depth-sensing indentation tests utilising either spherical or pyramidal indenters. Usually, the principal goal of such testing is to obtain values for elastic modulus and hardness of the specimen material from experimental readings of indenter load and depth of penetration. The forces involved are usually in the millinewton range and are measured with a resolution of a few nanonewtons. The depths of penetration are in the order of nanometres, hence the term “nanoindentation.”

In a book such as this, it is not possible to present a summary of the work of every group or worker in the field and the omission of anyone’s particular area of expertise should definitely not imply that that work is in any way unworthy of a report. The many published proceedings of international conferences provide a rich source of information about the many applications of nanoindentation. This book presents the most popular methods of test for nanoindentation, the underlying theory behind the extraction of elastic modulus and hardness from the load-displacement data, the various corrections involved, a description of the methods of operation of the present commercially available instruments, and some examples of application of the technique. The book is intended for those who are entering the field for the first time and to act as a reference for those already conversant with the technique.

In preparing this book, I was encouraged and assisted by many friends and colleagues. Particular thanks to Trevor Bell, Avi Bendavid, Alec Bendeli, Robert Bolster, Yang-Tse Cheng, John Field, Asa Jamting, Brian Lawn, Darien Northcote, Paul Rusconi, Jim Smith, Eric Thwaite, and Yvonne Wilson for their advice and assistance. I acknowledge the support of the CSIRO Division of Telecommunications and Industrial Physics and, in particular, Ken Hews-Taylor who supported the UMIS instrument for many years in his management portfolio, the staff of the library, and the Chief of the Division for his permission to use the many figures that appear in this book. I also thank the many authors and colleagues who publish in this field from whose work I have drawn and without which this book would not be possible. Finally, I thank Dr. Thomas von Foerster, the editorial and production team at Springer-Verlag New York, Inc., for their very professional and helpful approach to the whole publication process.

This page intentionally left blank

# Contents

Series Preface.....	vii
Preface.....	ix
List of Symbols.....	xv
Introduction.....	xix
1. Contact Mechanics .....	1
1.1 Introduction.....	1
1.2 Elastic Contact .....	1
1.3 Geometrical Similarity .....	6
1.4 Elastic–Plastic Contact.....	8
1.4.1 <i>The constraint factor</i> .....	8
1.4.2 <i>Indentation response of materials</i> .....	9
1.4.3 <i>Elastic–plastic stress distribution</i> .....	10
1.4.4 <i>Hardness theories</i> .....	11
1.5 Indentations at the Nanometre Scale.....	14
References .....	16
2. Nanoindentation Testing .....	20
2.1 Nanoindentation Test Data.....	20
2.2 Indenter Types .....	20
2.3 Indentation Hardness and Modulus .....	23
2.3.1 <i>Spherical indenter</i> .....	24
2.3.2 <i>Vickers indenter</i> .....	25
2.3.3 <i>Berkovich indenter</i> .....	25
2.3.4 <i>Cube corner</i> .....	26
2.3.5 <i>Knoop hardness</i> .....	26
2.4 Load-Depth Compliance Curves.....	27
2.5 Experimental Techniques.....	30
2.5.1 <i>Basic instrument construction and installation</i> .....	30
2.5.2 <i>Indenters</i> .....	31
2.5.3 <i>Specimen mounting</i> .....	32
2.5.4 <i>Working distance and initial penetration</i> .....	33
2.5.5 <i>Test cycles</i> .....	34
References .....	35

- 3. Analysis of Nanoindentation Test Data..... 36
  - 3.1 Analysis of Indentation Test Data..... 36
  - 3.2 Analysis Methods ..... 36
    - 3.2.1 *Cylindrical punch indenter*..... 36
    - 3.2.2 *Conical indenter — cylindrical punch method*..... 38
    - 3.2.3 *Spherical indenter*..... 40
      - 3.2.3.1 *Multiple-point unload method*..... 42
      - 3.2.3.2 *Single-point unload method* ..... 43
    - 3.2.4 *Berkovich indenter*..... 44
      - 3.2.4.1 *Multiple-point unload method*..... 46
      - 3.2.4.2 *Single-point unload method* ..... 47
    - 3.2.5 *Knoop indenter* ..... 48
    - 3.2.6 *Hardness as a function of depth*..... 51
    - 3.2.7 *Energy methods* ..... 53
    - 3.2.8 *Dynamic methods* ..... 55
    - 3.2.9 *Other methods of analysis* ..... 56
  - References ..... 58
- 4. Factors Affecting Nanoindentation Test data..... 61
  - 4.1 Introduction..... 61
  - 4.2 Thermal Drift ..... 61
  - 4.3 Initial Penetration Depth ..... 62
  - 4.4 Instrument Compliance ..... 65
  - 4.5 Indenter Geometry ..... 67
  - 4.6 Piling-Up and Sinking-In ..... 71
  - 4.7 Indentation Size Effect ..... 74
  - 4.8 Surface Roughness ..... 76
  - 4.9 Tip Rounding ..... 77
  - 4.10 Residual Stresses ..... 79
  - 4.11 Specimen Preparation ..... 80
  - References ..... 81
- 5. Simulation of Nanoindentation Test Data ..... 83
  - 5.1 Introduction..... 83
  - 5.2 Spherical Indenter..... 83
  - 5.3 Berkovich Indenter ..... 85
  - 5.4 Other Indenters ..... 86
  - 5.5 Comparison with Experimental Data..... 87
  - References ..... 89
- 6. Scaling Relationships in Nanoindentation..... 90
  - 6.1 Scaling Relationships in Nanoindentation..... 90
  - References ..... 94

7. Methods of Nanoindentation.....	96
7.1 Introduction.....	96
7.2 Dynamic Indentation Testing.....	96
7.3 Thin Films.....	100
7.3.1 Elastic modulus.....	101
7.3.2 Hardness.....	103
7.3.3 Film adhesion.....	104
7.4 Scratch Testing.....	105
7.5 Acoustic Emission Testing.....	108
7.6 Constant Strain Rate Testing.....	110
7.7 Creep.....	111
7.8 Fracture Toughness.....	113
7.9 High-Temperature Nanoindentation Testing.....	116
7.10 Strain-hardening exponent.....	119
7.11 Impact.....	120
References.....	122
8. Nanoindentation Test Standards.....	126
8.1 Nanoindentation Test Standards.....	126
8.2 ISO 14577.....	126
8.2.1 ISO 14577 Part 1: Test method.....	128
8.2.1.1 Test method and requirements.....	128
8.2.1.2 Analysis procedures.....	129
8.2.1.3 Load and Depth Control.....	135
8.2.1.4 Diamond Indenters.....	135
8.2.1.5 Specimen Roughness.....	135
8.2.1.6 Instrument Compliance and Indenter Area Function.....	136
8.2.1.7 Correlation of $H_{IT}$ with Other Scales.....	137
8.2.2 ISO 12577 Part 2: Verification and calibration of machines.....	137
8.2.2.1 Indenters.....	137
8.2.2.2 Calibration of force and depth.....	139
8.2.2.3 Verification of compliance and area function.....	139
8.2.2.4 Verification of the instrument.....	139
8.2.2.5 Annexes to Part 2.....	140
8.2.3 ISO 12577 Part 3: Calibration of reference blocks.....	140
References.....	141
9. Nanoindentation Test Instruments.....	142
9.1 Specifications of Nanoindentation Test Instruments.....	142
9.2 “Nano Indenter <sup>®</sup> ,” MTS Systems Corporation.....	146
9.3 “NanoTest <sup>®</sup> ,” Micro Materials Ltd.....	147
9.4 “TriboIndenter <sup>®</sup> ,” Hysitron Inc.....	150
9.5 “Nano-Hardness Tester <sup>®</sup> ,” CSEM Instruments.....	153

9.6 “UMIS <sup>®</sup> ,” CSIRO .....	155
References .....	158
10. Examples of Nanoindentation Testing .....	159
10.1 Introduction .....	159
10.2 Fused Silica .....	160
10.3 Titanium Dioxide Thin Film .....	161
10.4 Superhard Thin Film .....	162
10.5 Diamond-like Carbon (DLC) Thin Film .....	163
10.6 Creep in Polymer Film .....	164
10.7 Fracture and Delamination of Silicon Oxide Film .....	166
10.8 High-Temperature Testing on Fused Silica .....	167
10.9 Adhesion Measurement .....	168
10.10 Dynamic Hardness .....	169
10.11 Repeatability Testing .....	170
10.12 Assessment of Thin Film Adhesion by Scratch Testing .....	171
10.13 Other Applications .....	172
References .....	173
Appendix 1 Elastic Indentation Test Fields .....	174
A1.1 Contact Pressure Distributions .....	174
A1.2 Indentation Stress Fields .....	175
A1.2.1 Spherical indenter .....	175
A1.2.2 Conical indenter .....	177
Appendix 2 Surface Forces, Adhesion and Friction .....	179
A2.1 Adhesion Forces in Nanoindentation .....	179
A2.2 Forces in Nature .....	179
A2.3 Interaction Potentials .....	180
A2.4 Van der Waals Forces .....	181
A2.5 Surface Interactions .....	182
A2.6 Adhesion .....	184
A2.7 Friction .....	188
Appendix 3 Common Indenter Geometries .....	191
A3.1 Berkovich Indenter .....	191
A3.2 Vickers Indenter .....	192
A3.3 Knoop Indenter .....	193
A3.4 Sphero-Conical Indenter .....	194
Index	195

# List of Symbols

$\alpha$	cone semi-angle, geometry correction factor for Knoop indenter analysis, surface roughness parameter, thin film hardness parameter, buckling parameter
$\beta$	indenter cone inclination angle, indenter geometry shape factor
$\phi$	phase angle between force and depth in oscillatory indentation tests
$\delta$	distance of mutual approach between indenter and specimen
$\varepsilon$	strain
$\gamma$	half of the total energy required to separate two surfaces
$\Gamma$	work of indentation
$\eta$	coefficient of viscosity
$\theta$	half angle
$\rho$	number density of molecules
$\sigma$	normal stress
$\sigma_I$	indentation stress
$\sigma_r$	residual stress
$\sigma_s$	maximum asperity height
$\sigma_z$	normal pressure underneath the indenter
$\tau$	shear stress
$\mu$	coefficient of friction
$\nu$	Poisson's ratio
$\omega$	frequency
$a$	radius of circle of contact, constant for linear fit
$A$	contact area, constant for P vs h relationship
$a_c$	radius of circle of contact at transition from elastic to plastic deformation with spherical indenter
$A_f$	portion of contact area carried by film
$A_i$	area of contact that would be obtained for an ideal indenter at a particular penetration depth
$a_o$	contact radius obtained for smooth surfaces
$A_p$	projected contact area
$A_s$	portion of contact area carried by substrate
$b$	length of the short diagonal of the residual impression made by a Knoop indenter, Burgers vector, constant for linear fit
$C$	constraint factor, coefficients for area function expansion
$C_0$	size of plastic zone
$C_f$	load frame compliance

$d$	length of diagonal of residual impression, diameter of residual impression, length of long side of impression from a Knoop indenter
$D$	diameter of spherical indenter, damping factor
$E$	elastic modulus
$E^*$	combined or reduced elastic modulus
$E_{\text{eff}}$	effective modulus of film and substrate combination
$E_f$	film modulus
$E_s$	substrate modulus
$F$	force
$F_L$	lateral force (normal to scratch)
$F_N$	normal force
$F_T$	tangential force (parallel to scratch)
$G$	shear modulus
$h$	indentation depth
$H$	hardness
$h^*$	characteristic length for depth dependence on Hardness
$h_a$	depth of circle of contact measured from specimen free surface
$h_e$	elastic depth of penetration for unloading
$H_{\text{eff}}$	effective hardness of film–substrate combination
$H_f$	film hardness
$h_i$	initial penetration depth
$h_o$	amplitude of oscillatory depth reading
$H_o$	hardness measured without presence of dislocations
$h_p$	depth of circle of contact measured from maximum depth $h_t$ (the plastic depth)
$h_r$	depth of residual impression
$h_{\text{rp}}$	plastic depth of penetration for an equivalent punch
$h_s$	penetration depth at unloading force $P_s$ , depth at which spherical indenter tip meets conical support measured from indenter tip
$H_s$	substrate hardness
$h_t$	total indentation depth measured from specimen free surface
$I_o$	weighting function for thin film analysis
$K$	constant for determining initial penetration depth, Boltzmann's constant, bulk modulus, intercept correction factor, coefficient for stress–strain response in uniaxial plastic regime
$K_c$	fracture toughness
$K_s$	stiffness of indenter support springs
$L, l$	length or distance
$M$	mass of oscillating components, power law exponent that describes the form of the loading and unloading curves
$n$	Meyer's index, depth index for $P$ vs $h$ relationship, slope of logarithmic method of determining $h_t$
$P$	indenter load (force), hydrostatic pressure
$P_c$	critical load at onset of plastic deformation with spherical indenter, pull-off load due to adhesive forces

$P_I$	indenter load at initial penetration
$p_m$	mean contact pressure
$p_o$	amplitude of oscillatory force
$P_s$	indenter load at partial unload
$R$	spherical indenter radius
$r$	radial distance measured from axis of symmetry
$R^+$	equivalent rigid indenter radius for contact involving a deformable indenter of radius $R$
$R_i$	radius of indenter
$R_o$	initial radius of curvature
$R_r$	radius of curvature of residual impression
$S$	contact stiffness $dP/dh$
$S_L$	slope of loading curve
$S_U$	slope of unloading curve
$T$	temperature, interfacial shear strength
$T$	time, film thickness
$t_f$	film thickness
$t_s$	substrate thickness
$U$	energy
$u_z$	displacement
$V$	volume
$w$	interaction potential
$W$	work
$x$	strain-hardening exponent
$Y$	yield stress
$Y_f$	yield stress of film
$Y_s$	yield stress of substrate
$z_o$	equilibrium spacing in the Lennard-Jones potential

This page intentionally left blank

# Introduction

Indentation testing is a simple method that consists essentially of touching the material of interest whose mechanical properties such as elastic modulus and hardness are unknown with another material whose properties are known. The technique has its origins in Moh's hardness scale of 1822 in which materials that are able to leave a permanent scratch in another were ranked harder material with diamond assigned the maximum value of 10 on the scale. The establishment of the Brinell, Knoop, Vickers, and Rockwell tests all follow from a refinement of the method of indenting one material with another. Nanoindentation is simply an indentation test in which the length scale of the penetration is measured in nanometres ( $10^{-9}$  m) rather than microns ( $10^{-6}$  m) or millimetres ( $10^{-3}$  m), the latter being common in conventional hardness tests. Apart from the displacement scale involved, the distinguishing feature of most nanoindentation testing is the indirect measurement of the contact area — that is, the area of contact between the indenter and the specimen. In conventional indentation tests, the area of contact is calculated from direct measurements of the dimensions of the residual impression left in the specimen surface upon the removal of load. In nanoindentation tests, the size of the residual impression is of the order of microns and too small to be conveniently measured directly. Thus, it is customary to determine the area of contact by measuring the depth of penetration of the indenter into the specimen surface. This, together with the known geometry of the indenter, provides an indirect measurement of contact area at full load. For this reason, nanoindentation testing is sometimes referred to as depth-sensing indentation (DSI).

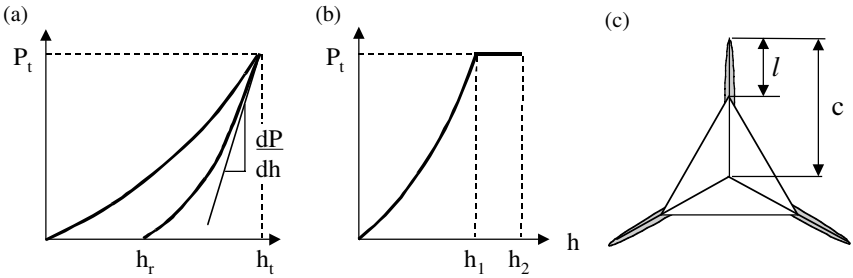


**Fig. 1.** Load-displacement curves for (a) an elastic plastic solid and (b) a viscoelastic solid for a spherical indenter and (c) cracks emanating from the corners of the residual impression in a brittle material.

It is not only hardness that is of interest to materials scientists. Indentation techniques can also be used to calculate elastic modulus, strain-hardening exponent, fracture toughness (for brittle materials), and viscoelastic properties. How can such a wide variety of properties be extracted from such a simple test, which, in many respects, can be considered a “non-destructive” test method? Consider the load-displacement response shown in Fig. 1. This type of data is obtained when an indenter, shaped as a sphere, is placed into contact with the flat surface of the specimen with a steadily increasing load. Both load and depth of penetration are recorded at each load increment (ultimately providing a measure of modulus and hardness as a function of depth beneath the surface). Following the attainment of the maximum load, in the material shown in Fig. 1 (a), the load is steadily removed and the penetration depth recorded. The loading part of the indentation cycle may consist of an initial elastic contact, followed by plastic flow, or yield, within the specimen at higher loads. Upon unloading, if yield has occurred, the load-displacement data follow a different path until at zero applied load, a residual impression is left in the specimen surface. The maximum depth of penetration for a particular load, together with the slope of the unloading curve measured at the tangent to the data point at maximum load, lead to a measure of both hardness and elastic modulus of the specimen material. In some cases, it is possible to measure elastic modulus from not only the unloading portion, but also the loading portion of the curve. For a viscoelastic material, the relationship between load and depth of penetration is not so straightforward. That is, for a given load, the resulting depth of penetration may depend upon the rate of application of load as well as the magnitude of the load itself. For such materials, the indentation test will be accompanied by “creep,” and this manifests itself as a change in depth for a constant applied load as shown in Fig. 1 (b). An analysis of the creep portion of the load-displacement response yields quantitative information about the elastic “solid-like” properties of the specimen, and also the “liquid-like” or “out-of-phase” components of the specimen properties. In brittle materials, cracking of the specimen may occur, especially when using a pyramidal indenter such as the three-sided Berkovich or the four-sided Vickers indenter. As shown in Fig. 1 (c), the length of the crack, which often begins at the corners of the indentation impression, can be used to calculate the fracture toughness of the specimen material.

More advanced methods can be employed to study residual stresses in thin films, the properties of materials at high temperatures, scratch resistance and film adhesion, and, in some cases, van der Waals type surface forces. In this book, all these issues are examined and reported beginning with a description of the method of test and the basis upon which the analysis is founded. Later chapters deal with the various corrections required to account for a number of instrumental and materials related effects that are a source of error in the measurement, theoretical aspects behind the constitutive laws that relate the mechanical properties to the measurement quantities, recent attempts at formulating an international standard for nanoindentation, examples of applications, and a brief description of commercially available instruments.

# Chapter 1

## Contact Mechanics

### 1.1 Introduction

There has been considerable recent interest in the mechanical characterisation of thin film systems and small volumes of material using depth-sensing indentation tests with either spherical or pyramidal indenters. Usually, the principal goal of such testing is to extract elastic modulus and hardness of the specimen material from experimental readings of indenter load and depth of penetration. These readings give an indirect measure of the area of contact at full load, from which the mean contact pressure, and thus hardness, may be estimated. The test procedure, for both spheres and pyramidal indenters, usually involves an elastic–plastic loading sequence followed by an unloading. The validity of the results for hardness and modulus depends largely upon the analysis procedure used to process the raw data. Such procedures are concerned not only with the extraction of modulus and hardness, but also with correcting the raw data for various systematic errors that have been identified for this type of testing. The forces involved are usually in the millinewton ( $10^{-3}$  N) range and are measured with a resolution of a few nanonewtons ( $10^{-9}$  N). The depths of penetration are on the order of microns with a resolution of less than a nanometre ( $10^{-9}$  m). In this chapter, we consider the general principles of elastic and elastic–plastic contact and how these relate to indentations at the nanometre scale.

### 1.2 Elastic Contact

The stresses and deflections arising from the contact between two elastic solids are of particular interest to those undertaking indentation testing. The most well-known scenario is the contact between a rigid sphere and a flat surface as shown in Fig. 1.1.

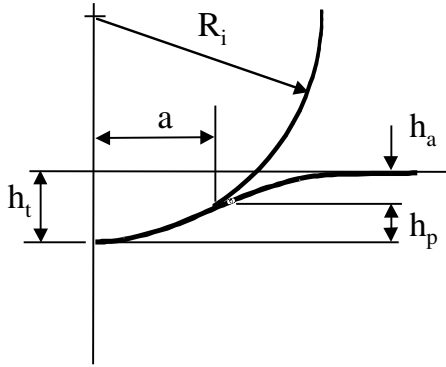


**Fig. 1.1** Schematic of contact between a rigid indenter and a flat specimen with modulus  $E$ . The radius of the circle of contact is  $a$ , and the total depth of penetration is  $h_t$ .  $h_a$  is the depth of the circle of contact from the specimen free surface, and  $h_p$  is the distance from the bottom of the contact to the contact circle.

Hertz<sup>1,2</sup> found that the radius of the circle of contact  $a$  is related to the indenter load  $P$ , the indenter radius  $R$ , and the elastic properties of the contacting materials by:

$$a^3 = \frac{3 PR}{4 E^*} \quad (1.2a)$$

The quantity  $E^*$  combines the modulus of the indenter and the specimen and is given by:

$$\frac{1}{E^*} = \frac{(1 - \nu^2)}{E} + \frac{(1 - \nu'^2)}{E'} \quad (1.2b)$$

where the primed terms apply to the indenter properties.  $E^*$  is often referred to as the “reduced modulus” or “combined modulus” of the system. If both contacting bodies have a curvature, then  $R$  in the above equations is their relative radii given by:

$$\frac{1}{R} = \frac{1}{R_1} + \frac{1}{R_2} \quad (1.2c)$$

In Eq. 1.2c we set the radius of the indenter to be positive always, and the radius of the specimen to be positive if its center of curvature is on the opposite side of the lines of contact between the two bodies.

It is important to realize that the deformations at the contact are localized and the Hertz equations are concerned with these and not the bulk deformations and stresses associated with the method of support of the contacting bodies. The

deflection  $h$  of the original free surface in the vicinity of the indenter is given by:

$$h = \frac{1}{E^*} \frac{3}{2} \frac{P}{4a} \left( 2 - \frac{r^2}{a^2} \right) \quad r \leq a \quad (1.2d)$$

It can be easily shown from Eq. 1.2d that the depth of the circle of contact beneath the specimen free surface is half of the total elastic displacement. That is, the distance from the specimen free surface to the depth of the radius of the circle of contact at full load is  $h_a = h_p = h_t/2$ :

The distance of mutual approach of distant points in the indenter and specimen is calculated from

$$\delta^3 = \left( \frac{3}{4E^*} \right)^2 \frac{P^2}{R} \quad (1.2e)$$

Substituting Eq. 1.2d into 1.2a, we can express the distance of mutual approach as:

$$\delta = \frac{a^2}{R} \quad (1.2f)$$

For the case of a non-rigid indenter, if the specimen is assigned a modulus of  $E^*$ , then the contact can be viewed as taking place between a rigid indenter of radius  $R$ .  $\delta$  in Eq. 1.2e becomes the total depth of penetration  $h_t$  beneath the specimen free surface. Rearranging Eq. 1.2e slightly, we obtain:

$$P = \frac{4}{3} E^* R^{1/2} h_t^{3/2} \quad (1.2g)$$

Although the substitution of  $E^*$  for the specimen modulus and the associated assumption of a rigid indenter of radius  $R$  might satisfy the contact mechanics of the situation by Eqs. 1.2a to 1.2g, it should be realized that for the case of a non-rigid indenter, the actual deformation experienced by the specimen is that obtained with a contact with a rigid indenter of a larger radius  $R^+$  as shown in Fig. 1.2. This larger radius may be computed using Eq. 1.2a with  $E'$  in Eq. 1.2b set as for a rigid indenter. In terms of the radius of the contact circle  $a$ , the equivalent rigid indenter radius is given by<sup>3</sup>:

$$R^+ = \frac{4a^3 E}{3(1 - \nu^2) P} \quad (1.2h)$$

The mean contact pressure,  $p_m$ , is given by the indenter load divided by the contact area and is a useful normalizing parameter, which has the additional virtue of having actual physical significance.

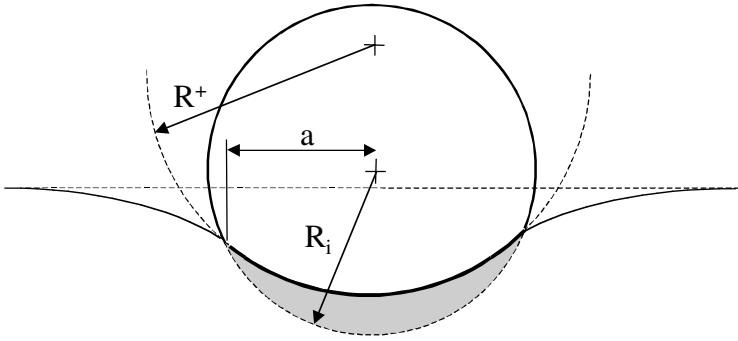


**Fig. 1.2** Contact between a non-rigid indenter and the flat surface of a specimen with modulus  $E$  is equivalent to that, in terms of distance of mutual approach, radius of circle of contact, and indenter load, as occurring between a rigid indenter of radius  $R_i$  and a specimen with modulus  $E^*$  in accordance with Eq. 1.2a. However, physically, the shaded volume of material is not displaced by the indenter and so the contact could also be viewed as occurring between a rigid indenter of radius  $R^+$  and a specimen of modulus  $E$  (Courtesy CSIRO).

$$p_m = \frac{P}{\pi a^2} \quad (1.2i)$$

Combining Eqs. 1.2a and Eq. 1.2i, we obtain:

$$p_m = \left( \frac{4E^*}{3\pi} \right) \frac{a}{R} \quad (1.2j)$$

We may refer to the mean contact pressure as the “indentation stress” and the quantity  $a/R$  as the “indentation strain.” This functional relationship between  $p_m$  and  $a/R$  foreshadows the existence of a stress–strain response similar in nature to that more commonly obtained from conventional uniaxial tension and compression tests. In both cases, a fully elastic condition yields a linear response. However, owing to the localized nature of the stress field, an *indentation* stress–strain relationship yields valuable information about the elastic–plastic properties of the test material that is not generally available from uniaxial tension and compression tests, especially for brittle materials.

For a conical indenter, similar equations apply where the radius of circle of contact is related to the indenter load by<sup>4</sup>:

$$P = \frac{\pi a}{2} E^* a \cot \alpha \quad (1.2k)$$

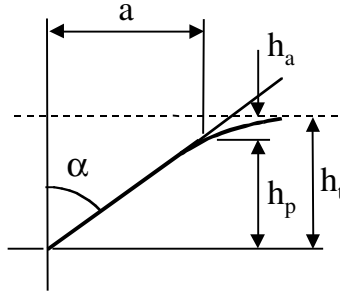


**Fig. 1.3** Geometry of contact with conical indenter.

The depth profile of the deformed surface within the area of contact is:

$$h = \left( \frac{\pi}{2} - \frac{r}{a} \right) a \cot \alpha \quad r \leq a \quad (1.21)$$

where  $\alpha$  is the cone semi-angle as shown in Fig. 1.3. The quantity  $a \cot \alpha$  is the depth of penetration  $h_p$  measured at the circle of contact. Substituting Eq. 1.2k into 1.2l with  $r = 0$ , we obtain:

$$P = \frac{2E \tan \alpha}{\pi} h_t^2 \quad (1.2m)$$

where  $h_t$  is the depth of penetration of the apex of the indenter beneath the original specimen free surface.

In indentation testing, the most common types of indenters are spherical indenters, where the Hertz equations apply directly, or pyramidal indenters. The most common types of pyramidal indenters are the four-sided Vickers indenter and the three-sided Berkovich indenter. Of particular interest in indentation testing is the area of the contact found from the dimensions of the contact perimeter. For a spherical indenter, the radius of the circle of contact is given by:

$$a = \sqrt{2R_i h_p - h_p^2} \quad (1.2n)$$

$$\approx \sqrt{2R_i h_p}$$

where  $h_p$  is the depth of the circle of contact as shown in Fig. 1.1. The approximation of Eq. 1.2n is precisely that which underlies the Hertz equations (Eqs. 1.2a and 1.2d) and thus these equations apply to cases where the deformation is small, that is, when the depth  $h_p$  is small in comparison to the radius  $R_i$ .

For a conical indenter, the radius of the circle of contact is simply:

$$a = h_p \tan \alpha \quad (1.2o)$$

**Table 1.1** Projected areas, intercept corrections, and geometry correction factors for various types of indenters. The semi-angles given for pyramidal indenters are the face angles with the central axis of the indenter.

Indenter type	Projected area	Semi-angle $\theta$ (deg)	Effective cone angle $\alpha$ (deg)	Intercept factor	Geometry correction factor $\beta$
Sphere	$A \approx \pi 2Rh_p$	N/A	N/A	0.75	1
Berkovich	$A = 3\sqrt{3}h_p^2 \tan^2 \theta$	$65.3^\circ$	$70.2996^\circ$	0.75	1.034
Vickers	$A = 4h_p^2 \tan^2 \theta$	$68^\circ$	$70.32^\circ$	0.75	1.012
Knoop	$A = 2h_p^2 \tan \theta_1 \tan \theta_2$	$\theta_1 = 86.25^\circ$ , $\theta_2 = 65^\circ$	$77.64^\circ$	0.75	1.012
Cube Corner	$A = 3\sqrt{3}h_p^2 \tan^2 \theta$	$35.26^\circ$	$42.28^\circ$	0.75	1.034
Cone	$A = \pi h_p^2 \tan^2 \alpha$	$\alpha$	$\alpha$	0.72	1

In indentation testing, pyramidal indenters are generally treated as conical indenters with a cone angle that provides the same area to depth relationship as the actual indenter in question. This allows the use of convenient axial-symmetric elastic equations, Eqs. 1.2k to 1.2m, to be applied to contacts involving non-axial-symmetric indenters. Despite the availability of contact solutions for pyramidal punch problems,<sup>5,6</sup> the conversion to an equivalent axial-symmetric has found a wide acceptance.

The areas of contact as a function of the depth of the circle of contact for some common indenter geometries are given in Table 1.1 along with other information to be used in the analysis methods shown in Chapter 3.

### 1.3 Geometrical Similarity

With a pyramidal or conical indenter, the ratio of the length of the diagonal or radius of circle of contact to the depth of the indentation,  $d/\delta$ , remains constant for increasing indenter load, as shown in Fig. 1.4. Indentations of this type have the property of “geometrical similarity.” For geometrically similar indentations, it is not possible to set the scale of an indentation without some external reference. The significance of this is that the strain within the material is a constant, independent of the load applied to the indenter.

\* In this section only,  $\delta$  is the indentation depth measured from the contact circle, not below the original free surface.

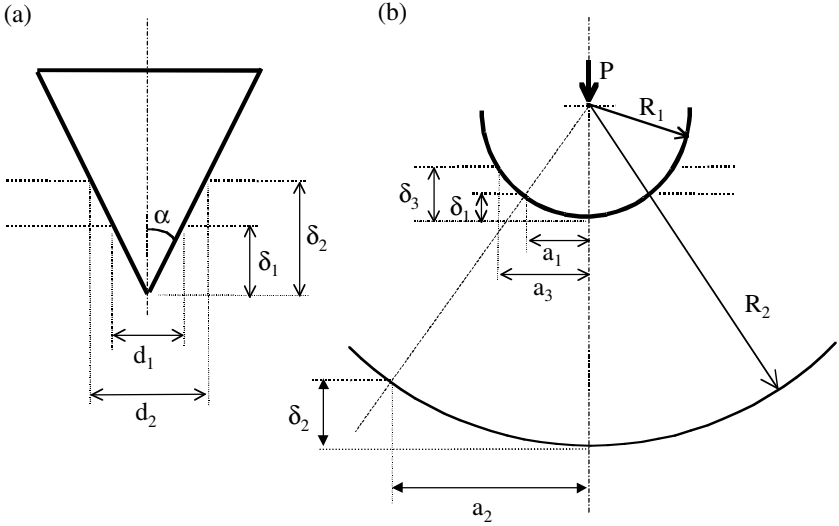


**Fig. 1.4** Geometrical similarity for (a) diamond pyramid or conical indenter; (b) spherical indenter (after reference 7).

Unlike a conical indenter, the radius of the circle of contact for a spherical indenter increases faster than the depth of the indentation as the load increases. The ratio  $a/\delta$  increases with increasing load. In this respect, indentations with a spherical indenter are not geometrically similar. Increasing the load on a spherical indenter is equivalent to decreasing the tip semi-angle of a conical indenter.

However, geometrically similar indentations may be obtained with spherical indenters of different radii. If the indentation strain,  $a/R$ , is maintained constant, then so is the mean contact pressure, and the indentations are geometrically similar. The principle of geometrical similarity is widely used in hardness measurements. For example, owing to geometrical similarity, hardness measurements made using a diamond pyramid indenter are expected to yield a value for hardness that is independent of the load. For spherical indenters, the same value of mean contact pressure may be obtained with different sized indenters and different loads as long as the ratio of the radius of the circle of contact to the indenter radius,  $a/R$ , is the same in each case.

The quantity  $a/R$  for a spherical indentation is equivalent to  $\cot \alpha$  for a conical indenter. Tabor<sup>8</sup> showed that the representative strain in a Brinell hardness test is equal to about  $0.2a/R$  and hence the representative strain in a typical indentation test performed with a Vickers indenter is approximately 8% (setting  $\alpha = 68^\circ$ ). This is precisely the indentation strain at which a fully developed plastic zone is observed to occur in the Brinell hardness test.

## 1.4 Elastic–Plastic Contact

Indentation tests on many materials result in both elastic and plastic deformation of the specimen material. In brittle materials, plastic deformation most commonly occurs with pointed indenters such as the Vickers diamond pyramid. In ductile materials, plasticity may be readily induced with a “blunt” indenter such as a sphere or cylindrical punch. Indentation tests are used routinely in the measurement of hardness of materials, but Vickers, Berkovich, and Knoop diamond indenters may be used to investigate other mechanical properties of solids such as specimen strength, fracture toughness, and internal residual stresses. The meaning of hardness has been the subject of considerable attention by scientists and engineers since the early 1700s. It was appreciated very early on that hardness indicated a resistance to penetration or permanent deformation. Early methods of measuring hardness, such as the scratch method, although convenient and simple, were found to involve too many variables to provide the means for a scientific definition of hardness. Static indentation tests involving spherical or conical indenters were first used as the basis for theories of hardness. Compared to “dynamic” tests, static tests enabled various criteria of hardness to be established since the number of test variables was reduced to a manageable level. The most well-known criterion is that of Hertz, who postulated that an absolute value for hardness was the least value of pressure beneath a spherical indenter necessary to produce a permanent set at the center of the area of contact. Later treatments by Auerbach,<sup>9</sup> Meyer,<sup>10</sup> and Hoyt<sup>11</sup> were all directed to removing some of the practical difficulties in Hertz’s original proposal.

### 1.4.1 The constraint factor

Static indentation hardness tests usually involve the application of load to a spherical or pyramidal indenter. The pressure distribution beneath the indenter is of particular interest. The value of the mean contact pressure  $p_m$  at which there is no increase with increasing indenter load is shown by experiment to be related to the hardness number  $H$ . For hardness methods that employ the projected contact area, the hardness number  $H$  is given directly by the mean pressure  $p_m$  at this limiting condition. Experiments show that the mean pressure between the indenter and the specimen is directly proportional to the material’s yield, or flow stress in compression, and can be expressed as:

$$H \approx CY \quad (1.4.1a)$$

where  $Y$  is the yield, or flow stress, of the material. The mean contact pressure in an indentation test is higher than that required to initiate yield in a uniaxial compression test because it is the shear component of stress that is responsible for plastic flow. The maximum shear stress is equal to half the difference between the maximum and minimum principal stresses, and in an indentation stress field, where the stress material is constrained by the surrounding matrix,

there is a considerable hydrostatic component. Thus, the mean contact pressure is greater than that required to initiate yield when compared to a uniaxial compressive stress. It is for this reason that  $C$  in Eq. 1.4.1a is called the “constraint factor,” the value of which depends upon the type of specimen, the type of indenter, and other experimental parameters. For the indentation methods mentioned here, both experiments and theory predict  $C \approx 3$  for materials with a large value of the ratio  $E/Y$  (e.g., metals). For low values of  $E/Y$  (e.g., glasses<sup>12,13</sup>),  $C \approx 1.5$ . The flow, or yield stress  $Y$ , in this context is the stress at which plastic yielding first occurs.

### 1.4.2 Indentation response of materials

A material’s hardness value is intimately related to the mean contact pressure  $p_m$  beneath the indenter at a limiting condition of compression. Valuable information about the elastic and plastic properties of a material can be obtained with spherical indenters when the mean contact pressure, or “indentation stress,” is plotted against the indentation strain  $a/R$ . The indentation stress–strain response of an elastic–plastic solid can generally be divided into three regimes, which depend on the uniaxial compressive yield stress  $Y$  of the material<sup>8</sup>:

1.  $p_m < 1.1Y$  — full elastic response, no permanent or residual impression left in the test specimen after removal of load.
2.  $1.1Y < p_m < CY$  — plastic deformation exists beneath the surface but is constrained by the surrounding elastic material, where  $C$  is a constant whose value depends on the material and the indenter geometry.
3.  $p_m = CY$  — plastic region extends to the surface of the specimen and continues to grow in size such that the indentation contact area increases at a rate that gives little or no increase in the mean contact pressure for further increases in indenter load.

In Region 1, during the initial application of load, the response is elastic and can be predicted from Eq. 1.2j. Equation 1.2j assumes linear elasticity and makes no allowance for yield within the specimen material. For a fully elastic response, the principal shear stress for indentation with a spherical indenter is a maximum at  $\approx 0.47p_m$  at a depth of  $\approx 0.5a$  beneath the specimen surface directly beneath the indenter.<sup>14</sup> Following Tabor,<sup>8</sup> we may employ either the Tresca or von Mises shear stress criteria, where plastic flow occurs at  $\tau \approx 0.5Y$ , to show that plastic deformation in the specimen beneath a spherical indenter can be first expected to occur when  $p_m \approx 1.1Y$ . Theoretical treatment of events within Region 2 is difficult because of the uncertainty regarding the size and shape of the evolving plastic zone. At high values of indentation strain (Region 3), the mode of deformation appears to depend on the type of indenter and the specimen material. The presence of the free surface has an appreciable effect, and the plastic deformation within the specimen is such that, assuming no work hardening, little or no increase in  $p_m$  occurs with increasing indenter load.

### 1.4.3 Elastic–plastic stress distribution

The equations for elastic contact given above form the basis of analysis methods for nanoindentation tests, even if these tests involve plastic deformation in the specimen. Hertz's original analysis was concerned with the form of the pressure distribution between contacting spheres that took the form:

$$\frac{\sigma_z}{P_m} = -\frac{3}{2} \left( 1 - \frac{r^2}{a^2} \right)^{1/2} \quad (1.4.3a)$$

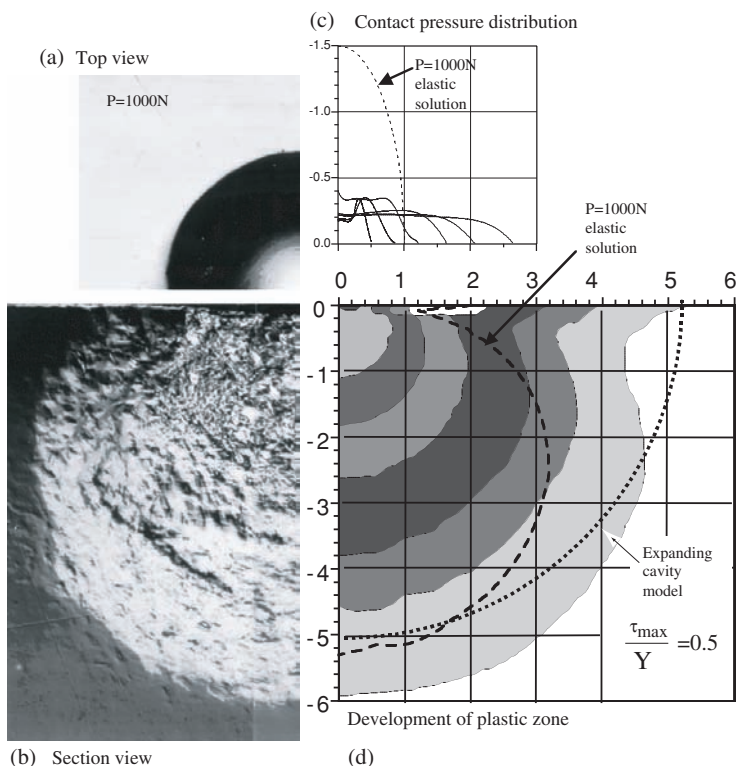


**Fig. 1.5** Elastic–plastic indentation response for mild steel material,  $E/Y = 550$ . (a) Test results for an indenter load of  $P = 1000$  N and indenter of radius 3.18 mm showing residual impression in the surface. (b) Section view with subsurface accumulated damage beneath the indentation site. (c) Finite element results for contact pressure distribution. (d) Finite element results showing development of the plastic zone in terms of contours of maximum shear stress at  $\tau_{\max}/Y = 0.5$ . In (c) and (d), results are shown for indentation strains of  $a/R = 0.04, 0.06, 0.08, 0.11, 0.14, 0.18$ . Distances are expressed in terms of the contact radius  $a = 0.218$  mm for the elastic case of  $P = 1000$  N (after reference 15).

The pressure distribution  $\sigma_z$  in Eq. 1.4.3a is normalized to the mean contact pressure  $p_m$ , and it can be seen that the pressure is a maximum equal to 1.5 times the mean contact pressure at the center of the contact as shown in Fig. 1.5 (c).<sup>15</sup>

When plastic deformation occurs, the pressure distribution is modified and becomes more uniform. Finite element results for an elastic–plastic contact are shown in Fig. 1.5 (c). There is no currently available analytical theory that generally describes the stress distribution beneath the indenter for an elastic–plastic contact. The finite element method, however, has been used with some success in this regard and Fig. 1.5 (d) shows the evolution of the plastic zone (within which the shear stress is a constant) compared with an experiment on a specimen of mild steel, Fig. 1.5 (b). Mesarovich and Fleck<sup>16</sup> have calculated the full elastic plastic contact for a spherical indenter that includes elasticity, strain-hardening, and interfacial friction.

#### 1.4.4 Hardness theories

Theoretical approaches to hardness can generally be categorized according to the characteristics of the indenter and the response of the specimen material. Various semiempirical models that describe experimentally observed phenomena at values of indentation strain at or near a condition of full plasticity have been given considerable attention in the literature.<sup>8,13,17–29</sup> These models variously describe the response of the specimen material in terms of slip lines, elastic displacements, and radial compressions. For sharp wedge or conical indenters, substantial upward flow is usually observed, and because elastic strains are thus negligible compared to plastic strains, the specimen can be regarded as being rigid plastic. A cutting mechanism is involved, and new surfaces are formed beneath the indenter as the volume displaced by the indenter is accommodated by the upward flow of plastically deformed material. The constraint factor  $C$  in this case arises due to flow and velocity considerations.<sup>17</sup> For blunt indenters, the specimen responds in an elastic–plastic manner, and plastic flow is usually described in terms of the elastic constraint offered by the surrounding material. With blunt indenters, Samuels and Mulhearn<sup>20</sup> noted that the mode of plastic deformation at a condition of full plasticity appears to be a result of compression rather than cutting, and the displaced volume is assumed to be taken up entirely by elastic strains within the specimen material. This idea was given further attention by Marsh,<sup>19</sup> who compared the plastic deformation in the vicinity of the indenter to that which occurs during the radial expansion of a spherical cavity subjected to internal pressure, an analysis of which was given previously by Hill.<sup>18</sup> The most widely accepted treatment is that of Johnson,<sup>22,29</sup> who replaced the expansion of the cavity with that of an incompressible hemispherical core of material subjected to an internal pressure. Here, the core pressure is directly related to the mean contact pressure. This is the so-called “expanding cavity” model.

In the expanding cavity model, the contacting surface of the indenter is encased by a hydrostatic “core” of radius  $a_c$ , which is in turn surrounded by a hemispherical plastic zone of radius  $c$  as shown in Fig. 1.6. An increment of penetration  $dh$  of the indenter results in an expansion of the core  $da$  and the volume displaced by the indenter is accommodated by radial movement of particles  $du(r)$  at the core boundary. This in turn causes the plastic zone to increase in radius by an amount  $dc$ .

For geometrically similar indentations, such as with a conical indenter, the radius of the plastic zone increases at the same rate as that of the core, hence,  $da/dc = a/c$ .

Using this result Johnson shows that the pressure in the core can be calculated from:

$$\frac{p}{Y} = \frac{2}{3} \left[ 1 + \ln \left( \frac{(E/Y)\tan\beta + 4(1-2\nu)}{6(1-\nu^2)} \right) \right] \tag{1.4.4a}$$

where  $p$  is the pressure within the core and  $\beta$  is the angle of inclination of the indenter with the specimen surface.

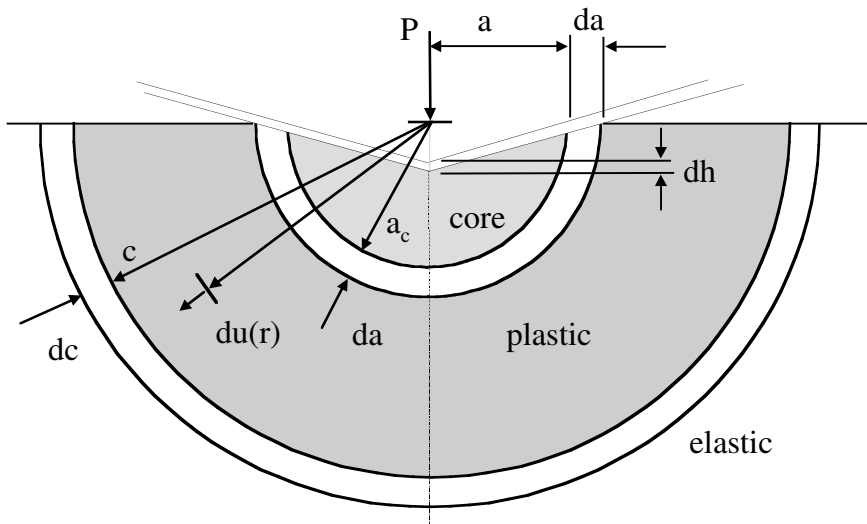


**Fig. 1.6** Expanding cavity model schematic. The contacting surface of the indenter is encased by a hydrostatic “core” of radius  $a_c$  that is in turn surrounded by a hemispherical plastic zone of radius  $c$ . An increment of penetration  $dh$  of the indenter, results in an expansion of the core  $da$  and the volume displaced by the indenter is accommodated by radial movement of particles  $du(r)$  at the core boundary. This in turn causes the plastic zone to increase in radius by an amount  $dc$  (after reference 15).

The mean contact pressure is found from:

$$p_m = p + \frac{2}{3}Y \quad (1.4.4b)$$

and this leads to an value for the constraint factor  $C$ . When the free surface of the specimen begins to influence appreciably the shape of the plastic zone, and the plastic material is no longer elastically constrained, the volume of material displaced by the indenter is accommodated by upward flow around the indenter. The specimen then takes on the characteristics of a rigid-plastic solid, because any elastic strains present are very much smaller than the plastic flow of unconstrained material. Plastic yield within such a material depends upon a critical shear stress, which may be calculated using either of the von Mises or Tresca failure criteria. In the slip-line field solution, developed originally in two dimensions by Hill, Lee, and Tupper,<sup>17</sup> the volume of material displaced by the indenter is accounted for by upward flow, as shown in Fig. 1.7.

The material in the region ABCDE flows upward and outward as the indenter moves downward under load. Because frictionless contact is assumed, the direction of stress along the line AB is normal to the face of the indenter. The lines within the region ABDEC are oriented at  $45^\circ$  to AB and are called “slip lines” (lines of maximum shear stress). This type of indentation involves a “cutting” of the specimen material along the line OA and the creation of new surfaces that travel upward along the contact surface. The contact pressure across the face of the indenter is given by:

$$p_m = 2\tau_{\max}(1 + \alpha) = H \quad (1.4.4c)$$

where  $\tau_{\max}$  is the maximum value of shear stress in the specimen material and  $\alpha$  is the cone semi-angle (in radians).

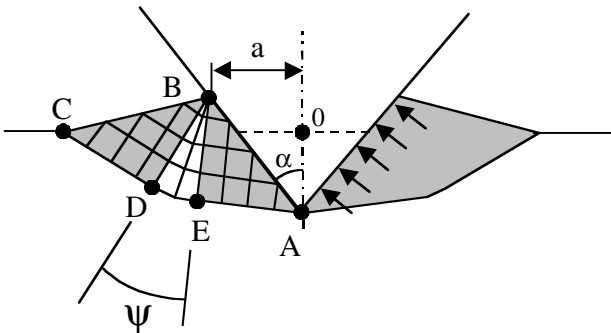


**Fig. 1.7** Slip-line theory. The material in the region ABCDE flows upward and outward as the indenter moves downward under load (after reference 7).

Invoking the Tresca shear stress criterion, where plastic flow occurs at  $\tau_{\max} = 0.5Y$ , and substituting into Eq. 1.4.4c, gives:

$$\begin{aligned} H &= Y(1 + \alpha) \\ \therefore & \\ C &= (1 + \alpha) \end{aligned} \tag{1.4.4d}$$

The constraint factor determined by this method is referred to as  $C_{\text{flow}}$ . For values of  $\alpha$  between  $70^\circ$  and  $90^\circ$ , Eq. 1.4.4b gives only a small variation in  $C_{\text{flow}}$  of 2.22 to 2.6. Friction between the indenter and the specimen increases the value of  $C_{\text{flow}}$ . A slightly larger value for  $C_{\text{flow}}$  is found when the von Mises stress criterion is used (where  $\tau_{\max} \approx 0.58Y$ ). For example, at  $\alpha = 90^\circ$ , Eq. 1.3.4b with the von Mises criterion gives  $C = 3$ .

## 1.5 Indentations at the Nanometre Scale

The present field of nanoindentation grew from a desire to measure the mechanical properties of hard thin films and other near surface treatments in the early 1980s. Microhardness testing instruments available at the time could not apply low enough forces to give penetration depths less than the required 10% or so of the film thickness so as to avoid influence on the hardness measurement from the presence of the substrate. Even if they could, the resulting size of the residual impression cannot be determined with sufficient accuracy to be useful. For example, the uncertainty in a measurement of a  $5 \mu\text{m}$  diagonal of a residual impression made by a Vickers indenter is on the order of 20% when using an optical method and increases with decreasing size of indentation and can be as high as 100% for a  $1 \mu\text{m}$  impression.

Since the spatial dimensions of the contact area are not conveniently measured, modern nanoindentation techniques typically use the measured depth of penetration of the indenter and the known geometry of the indenter to determine the contact area. Such a procedure is sometimes called “depth-sensing indentation testing.” For such a measurement to be made, the depth measurement system needs to be referenced to the specimen surface, and this is usually done by bringing the indenter into contact with the surface with a very small “initial contact force,” which, in turn, results in an inevitable initial penetration of the surface by the indenter that must be accounted for in the analysis. Additional corrections are required to account for irregularities in the shape of the indenter, deflection of the loading frame, and piling-up of material around the indenter (see Fig. 1.8). These effects contribute to errors in the recorded depths and, subsequently, the hardness and modulus determinations. Furthermore, the scale of deformation in a nanoindentation test becomes comparable to the size of material defects such as dislocations and grain sizes, and the continuum approximation used in the analysis can become less valid.

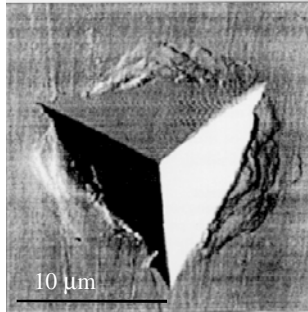


**Fig. 1.8.** Atomic force micrograph of a residual impression in steel made with a triangular pyramid Berkovich indenter. Note the presence of piling up at the periphery of the contact impression (Courtesy CSIRO).

The nanoindentation test results provide information on the elastic modulus, hardness, strain-hardening, cracking, phase transformations, creep, and energy absorption. The sample size is very small and the test can in many cases be considered non-destructive. Specimen preparation is straightforward. Because the scale of deformation is very small, the technique is applicable to thin surface films and surface modified layers. In many cases, the microstructural features of a thin film or coating differs markedly from that of the bulk material owing to the presence of residual stresses, preferred orientations of crystallographic planes, and the morphology of the microstructure. The applications of the technique therefore cover technologies such as cathodic arc deposition, physical vapor deposition (PVD), and chemical vapor deposition (CVD) as well as ion-implantation and functionally graded materials. Nanoindentation instruments are typically easy to use, operate under computer control, and require no vacuum chambers or other expensive laboratory infrastructure.

The technique relies on a continuous measurement of depth of penetration with increasing load and appears to have first demonstrated by Pethica<sup>30</sup> in 1981 and was applied to the measurement of the mechanical properties of ion-implanted metal surfaces, a popular application of the technique for many years.<sup>31</sup> The notion of making use of the elastic recovery of hardness impressions to determine mechanical properties is not a new one, being reported in 1961 by Stillwell and Tabor,<sup>32</sup> by Armstrong and Robinson<sup>33</sup> in 1974, and also by Lawn and Howes<sup>34</sup> in 1981. The present modern treatments probably begin with Bulychev, Alekhin, Shorshorov, and Ternovskii<sup>35</sup>, who in 1975 showed how the area of contact could be measured using the unloading portion of the load-displacement curve. Loubet, Georges, Marchesini, and Meille<sup>36</sup> used this method for relatively high load testing (in the order of 1 Newton) and Doerner and Nix<sup>37</sup> extended the measurements into the millinewton range in 1986. The most commonly used method of analysis is a refinement of the Doerner and Nix

approach by Oliver and Pharr<sup>38</sup> in 1992. A complementary approach directed to indentations with spherical indenters was proposed by Field and Swain and co-workers<sup>39,40</sup> in 1993 and was subsequently shown to be equivalent to the Oliver and Pharr method.<sup>41</sup> Review articles<sup>42–44</sup> on micro, and nanoindentation show a clear evolution of the field from traditional macroscopic measurements of hardness. The field now supports specialized symposia on an annual basis attracting papers covering topics from fundamental theory to applications of the technique.

The first “ultramicro” hardness tests were done with apparatus designed for use inside the vacuum chamber of a scanning electron microscope (SEM), where load was applied to a sharply pointed tungsten wire via the movement of a galvanometer that was controlled externally by electric current. Depth of penetration was determined by measuring the motion of the indenter support using an interferometric method. The later use of strain gauges to measure the applied load and finely machined parallel springs operated by an electromagnetic coil brought the measurement outside the vacuum chamber into the laboratory, but, although the required forces could now be applied in a controlled manner, optical measurements of displacement or sizes of residual impressions remained a limiting factor. Developments in electronics lead to the production of displacement measuring sensors with resolutions greater than those offered by optical methods and, in the last ten years, some six or seven instruments have evolved into commercial products, often resulting in the creation of private companies growing out of research organizations to sell and support them.

There is no doubt that as the scale of mechanisms becomes smaller, interest in mechanical properties on a nanometre scale and smaller, and the nature of surface forces and adhesion, will continue to increase. Indeed, at least one recent publication refers to the combination of a nanoindenter and an atomic force microscope as a “picoindenter”<sup>45</sup> suitable for the study of pre-contact mechanics, the process of making contact, and actual contact mechanics. The present maturity of the field of nanoindentation makes it a suitable technique for the evaluation of new materials technologies by both academic and private industry research laboratories and is increasingly finding application as a quality control tool.

## References

1. H. Hertz, “On the contact of elastic solids,” *J. Reine Angew. Math.* 92, 1881, pp. 156–171. Translated and reprinted in English in *Hertz’s Miscellaneous Papers*, Macmillan & Co., London, 1896, Ch. 5.
2. H. Hertz, “On hardness,” *Verh. Ver. Beförderung Gewerbe Fleisses* 61, 1882, p. 410. Translated and reprinted in English in *Hertz’s Miscellaneous Papers*, Macmillan & Co., London, 1896, Ch. 6.

3. A.C. Fischer-Cripps, "The use of combined elastic modulus in the analysis of depth sensing indentation data," *J. Mater. Res.*, 16 11, 2001, pp. 3050–3052.
4. I.N. Sneddon, "Boussinesq's problem for a rigid cone," *Proc. Cambridge Philos. Soc.* 44, 1948, pp. 492–507.
5. J.R. Barber and D.A. Billings, "An approximate solution for the contact area and elastic compliance of a smooth punch of arbitrary shape," *Int. J. Mech. Sci.* 32 12, 1990, pp. 991–997.
6. G.G. Bilodeau, "Regular pyramid punch problem," *J. App. Mech.* 59, 1992, pp. 519–523.
7. A.C. Fischer-Cripps, *Introduction to Contact Mechanics*, Springer-Verlag, New York, 2000.
8. D. Tabor, *The Hardness of Metals*, Clarendon Press, Oxford, 1951.
9. F. Auerbach, "Absolute hardness," *Ann. Phys. Chem. (Leipzig)* 43, 1891, pp.61–100. Translated by C. Barus, Annual Report of the Board of Regents of the Smithsonian Institution, July 1, 1890 – June 30 1891, reproduced in "Miscellaneous documents of the House of Representatives for the First Session of the Fifty-Second Congress," Government Printing Office, Washington, D.C., 43, 1891–1892, pp.207–236.
10. E. Meyer, "Untersuchungen über Harteproofung und Harte," *Phys. Z.* 9, 1908, pp. 66–74.
11. S.L. Hoyt, "The ball indentation hardness test," *Trans. Am. Soc. Steel Treat.* 6, 1924, pp. 396–420.
12. M.C. Shaw, "The fundamental basis of the hardness test," in *The Science of Hardness Testing and its Research Applications*, J.H. Westbrook and H. Conrad, Eds. American Society for Metals, Cleveland, OH, 1973, pp. 1–15.
13. M.V. Swain and J.T. Hagan, "Indentation plasticity and the ensuing fracture of glass," *J. Phys. D: Appl. Phys.* 9, 1976, pp. 2201–2214.
14. M.T. Huber, "Contact of solid elastic bodies," *Ann. D. Physik*, 14 1, 1904, pp. 153–163.
15. A.C. Fischer-Cripps, "Elastic–plastic response of materials loaded with a spherical indenter," *J. Mater. Sci.* 32 3, 1997, pp. 727–736.
16. S.Dj. Mesarovic and N. A. Fleck, "Spherical indentation of elastic–plastic solids," *Proc. R. Soc. Lond.* A455, 1999, pp. 2707–2728.
17. R. Hill, E.H. Lee and S.J. Tupper, "Theory of wedge-indentation of ductile metals," *Proc. R. Soc. London*, A188, 1947, pp. 273–289.
18. R. Hill, *The Mathematical Theory of Plasticity*, Clarendon Press, Oxford, 1950.
19. D.M. Marsh, "Plastic flow in glass," *Proc. R. Soc. London*, A279, 1964, pp. 420–435.
20. L.E. Samuels and T.O. Mulhearn, "An experimental investigation of the deformed zone associated with indentation hardness impressions," *J. Mech. Phys. Solids*, 5, 1957, pp. 125–134.
21. T.O. Mulhearn, "The deformation of metals by Vickers-type pyramidal indenters," *J. Mech. Phys. Solids*, 7, 1959, pp. 85–96.
22. K.L. Johnson, "The correlation of indentation experiments," *J. Mech. Phys. Sol.* 18, 1970, pp. 115–126.

23. M.C. Shaw and D.J. DeSalvo, "A new approach to plasticity and its application to blunt two dimension indenters," *J. Eng. Ind. Trans. ASME*, 92, 1970, pp. 469–479.
24. M.C. Shaw and D.J. DeSalvo, "On the plastic flow beneath a blunt axisymmetric indenter," *J. Eng. Ind. Trans. ASME* 92, 1970, pp. 480–494.
25. C. Hardy, C.N. Baronet, and G.V. Tordion, "The elastic–plastic indentation of a half-space by a rigid sphere," *Int. J. Numer. Methods Eng.* 3, 1971, pp. 451–462.
26. C.M. Perrott, "Elastic–plastic indentation: Hardness and fracture," *Wear* 45, 1977, pp. 293–309.
27. S.S. Chiang, D.B. Marshall, and A.G. Evans, "The response of solids to elastic/plastic indentation. 1. Stresses and residual stresses," *J. Appl. Phys.* 53 1, 1982, pp. 298–311.
28. S.S. Chiang, D.B. Marshall, and A.G. Evans, "The response of solids to elastic/plastic indentation. 2. Fracture initiation," *J. Appl. Phys.* 53 1, 1982, pp. 312–317.
29. K.L. Johnson, *Contact Mechanics*, Cambridge University Press, Cambridge, 1985.
30. J.B. Pethica, "Microhardness tests with penetration depths less than ion implanted layer thickness in ion implantation into metals," Third International Conference on Modification of Surface Properties of Metals by Ion-Implantation, Manchester, England, 23-26, 1981, V. Ashworth et al. eds., Pergamon Press, Oxford, 1982, pp. 147–157.
31. J.S. Field, "Understanding the penetration resistance of modified surface layers," *Surface and Coatings Technology*, 36, 1988, pp. 817–827.
32. N.A. Stillwell and D. Tabor, "Elastic recovery of conical indentations," *Phys. Proc. Soc.* 78 2, 1961, pp. 169–179.
33. R.W. Armstrong and W.H. Robinson, "Combined elastic and plastic deformation behaviour from a continuous indentation hardness test," *New Zealand Journal of Science*, 17, 1974, pp. 429–433.
34. B.R. Lawn and V.R. Howes, "Elastic recovery at hardness indentations," *J. Mat. Sci.* 16, 1981, pp. 2745–2752.
35. S.I. Bulychev, V.P. Alekhin, M. Kh. Shorshorov, and A.P. Ternorskii, "Determining Young's modulus from the indenter penetration diagram," *Zavod. Lab.* 41 9, 1975, pp. 11137–11140.
36. J.L. Loubet, J.M. Georges, O. Marchesini, and G. Meille, "Vicker's indentation of magnesium oxide," *J. Tribol.* 106, 1984, pp. 43–48.
37. M.F. Doerner and W.D. Nix, "A method for interpreting the data from depth-sensing indentation instruments," *J. Mater. Res.* 1 4, 1986, pp. 601–609.
38. W.C. Oliver and G.M. Pharr, "An improved technique for determining hardness and elastic modulus using load and displacement sensing indentation experiments," *J. Mater. Res.* 7 4, 1992, pp. 1564–1583.
39. T.J. Bell, A. Bendeli, J.S. Field, M.V. Swain, and E.G. Thwaite, "The determination of surface plastic and elastic properties by ultra-micro indentation," *Metrologia*, 28, 1991, pp. 463–469.
40. J.S. Field and M.V. Swain, "A simple predictive model for spherical indentation," *J. Mater. Res.* 8 2, 1993, pp. 297–306.
41. A.C. Fischer-Cripps, "Study of analysis methods for depth-sensing indentation test data for spherical indenters," *J. Mater. Res.* 16 6, 2001, pp. 1579–1584.

42. A.G. Atkins, "Topics in indentation hardness," *Metal Science*, 16, 1982, pp. 127–137.
43. H.M. Pollock, "Nanoindentation", *ASM Handbook, Friction, Lubrication, and Wear Technology*, 18, 1992, pp. 419–429.
44. J.L. Hay and G.M. Pharr, "Instrumented indentation testing," *ASM Handbook, Materials Testing and Evaluation*, 8, 2000, pp. 232–243.
45. S.A. Syed, K.J. Wahl, and R.J. Colton, "Quantitative study of nanoscale contact and pre-contact mechanics using force modulation," *Mat. Res. Soc. Symp. Proc.* 594, 2000, pp. 471–476.

# Chapter 2

## Nanoindentation Testing

### 2.1 Nanoindentation Test Data

The goal of the majority of nanoindentation tests is to extract elastic modulus and hardness of the specimen material from load-displacement measurements. Conventional indentation hardness tests involve the measurement of the size of a residual plastic impression in the specimen as a function of the indenter load. This provides a measure of the area of contact for a given indenter load. In a nanoindentation test, the size of the residual impression is often only a few microns and this makes it very difficult to obtain a direct measure using optical techniques. In nanoindentation testing, the depth of penetration beneath the specimen surface is measured as the load is applied to the indenter. The known geometry of the indenter then allows the size of the area of contact to be determined. The procedure also allows for the modulus of the specimen material to be obtained from a measurement of the “stiffness” of the contact, that is, the rate of change of load and depth. In this chapter, we review the mechanics of the actual indentation test and, in particular, the nature of the indenters used in this type of testing.

### 2.2 Indenter Types

Nanoindentation hardness tests are generally made with either spherical or pyramidal indenters. Consider a Vickers indenter with opposing faces at a semi-angle of  $\theta = 68^\circ$  and therefore making an angle  $\beta = 22^\circ$  with the flat specimen surface. For a particular contact radius  $a$ , the radius  $R$  of a spherical indenter whose edges are at a tangent to the point of contact with the specimen is given by  $\sin \beta = a/R$ , which for  $\beta = 22^\circ$  gives  $a/R = 0.375$ . It is interesting to note that this is precisely the indentation strain<sup>†</sup> at which Brinell hardness tests, using a spherical indenter, are generally performed, and the angle  $\theta = 68^\circ$  for the Vickers indenter was chosen for this reason.

<sup>†</sup> Recall that the term “indentation strain” refers to the ratio  $a/R$ .

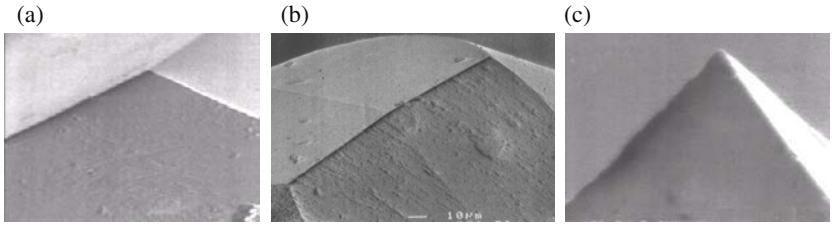


**Fig. 2.1** SEM images of the tips of (a) Berkovich, (b) Knoop, and (c) cube-corner indenters used for nanoindentation testing. The tip radius of a typical diamond pyramidal indenter is in the order of 100 nm (Courtesy CSIRO).

The Berkovich indenter,<sup>1</sup> (a) in Fig. 2.1, is generally used in small-scale indentation studies and has the advantage that the edges of the pyramid are more easily constructed to meet at a single point, rather than the inevitable line that occurs in the four-sided Vickers pyramid. The face angle of the Berkovich indenter normally used for nanoindentation testing is  $65.3^\circ$ , which gives the same projected area-to-depth ratio as the Vickers indenter. The original Berkovich indenter is constructed with a face angle of  $65.03^\circ$ , and this gives the same *actual* surface area to depth ratio as a Vickers indenter in accordance with the definition of the Vickers hardness value. The tip radius for a typical Berkovich indenter is on the order of 50–100nm. The Knoop indenter, (b) in Fig. 2.1, is a four-sided pyramidal indenter with two different semi-angles. Measurement of the unequal lengths of the diagonals of the residual impression is very useful for investigating anisotropy of the surface of the specimen. The indenter was originally developed to allow the testing of very hard materials where a longer diagonal line could be more easily measured for shallower depths of residual impression. The cube corner indenter, (c) in Fig. 2.1, is finding increasing popularity in nanoindentation testing. It is similar to the Berkovich indenter but has a semi-angle at the faces of  $35.26^\circ$ .

Conical indenters have the advantage of possessing axial symmetry, and, with reference to Fig. 2.1, equivalent projected areas of contact between conical and pyramidal indenters are obtained when:

$$A = \pi h_p^2 \tan^2 \alpha \quad (2.2a)$$

where  $h_p$  is depth of penetration measured from the edge of the circle or area of contact. For a Vickers or Berkovich indenter, the projected area of contact is  $A = 24.5h^2$  and thus the semi-angle for an equivalent conical indenter is  $70.3^\circ$ . It is convenient when analyzing nanoindentation test data taken with pyramidal indenters to treat the indentation as involving an axial-symmetric conical indenter with an apex semi-angle that can be determined from Eq. 2.2a. Table 1.1 gives expressions for the contact area for different types of pyramidal indenters in terms of the penetration depth  $h_p$  for the geometries shown in Fig. 2.2.

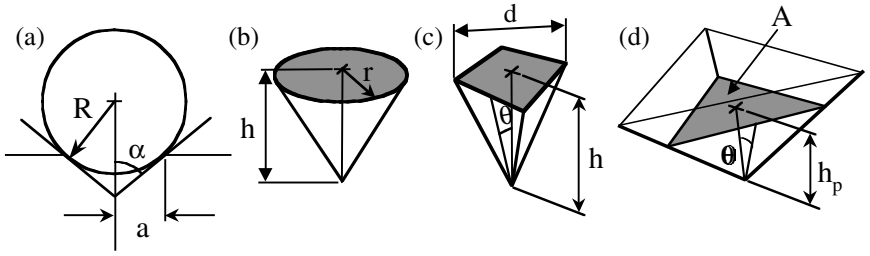


**Fig. 2.2** Indentation parameters for (a) spherical, (b) conical, (c) Vickers, and (d) Berkovich indenters (not to scale).

Spherical indenters are finding increasing popularity, as this type of indenter provides a smooth transition from elastic to elastic-plastic contact. It is particularly suitable for measuring soft materials and for replicating contact damage in in-service conditions. As shown in Fig. 2.3, the indenter is typically made as a sphero-cone for ease of mounting. Only the very tip of the indenter is used to penetrate the specimen surface in indentation testing. Diamond spherical indenters with a radius of less than 1 micron can be routinely fashioned.

Indenters can generally be classified into two categories — sharp or blunt. The criteria upon which a particular indenter is classified, however, are the subject of opinion.

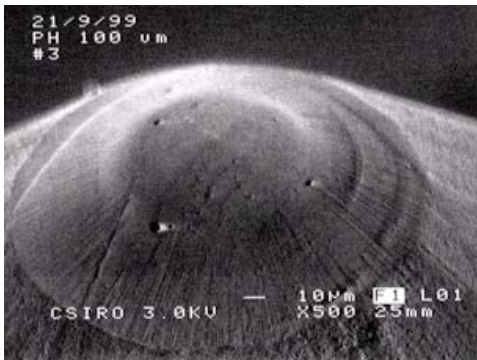


**Fig. 2.3** Tip of a sphero-conical indenter used for nanoindentation and scratch testing. Nominal tip radius is 100  $\mu\text{m}$  in this example. Tip radii of  $<1 \mu\text{m}$  are available (Courtesy CSIRO).

For example, some authors<sup>2</sup> classify sharp indenters as those resulting in permanent deformation in the specimen upon the removal of load. A Vickers diamond pyramid is such an example in this scheme. However, others prefer to classify a conical or pyramidal indenter with a cone semi-angle  $\alpha > 70^\circ$  as being blunt. Thus, a Vickers diamond pyramid with  $\theta = 68^\circ$  would in this case be considered blunt. A spherical indenter may be classified as sharp or blunt depending on the applied load according to the angle of the tangent at the point of contact. The latter classification is based upon the response of the specimen material in which it is observed that plastic flow according to the slip-line theory occurs for sharp indenters and the specimen behaves as a rigid-plastic solid. For blunt indenters, the response of the specimen material follows that predicted by the expanding cavity model or the elastic constraint model, depending on the type of specimen material and magnitude of the load. Generally speaking, spherical indenters are termed blunt, and cones and pyramids are sharp.

## 2.3 Indentation Hardness and Modulus

A particularly meaningful quantity in indentation hardness is the mean contact pressure of the contact, and is found by dividing the indenter load by the projected area of the contact. The mean contact pressure, when determined under conditions of a fully developed plastic zone, is taken to be the indentation hardness,  $H$ , of the specimen material. Similarly, the elastic modulus determined from the slope of the unloading of the load-depth response in an indentation test is formally called the “Indentation Modulus” of the specimen material.

There is an important distinction to be made between conventional definitions of hardness and the hardness obtained by nanoindentation using depth-sensing measurements. In conventional hardness tests, such as the Brinell test (see Section 2.3.1 below), the size of the residual impression in the surface is used to determine the area of contact and hence the hardness value. In depth-sensing indentation tests, such as that used in nanoindentation, the size of the contact area under full load is determined from the depth of penetration of the indenter and the shape of the elastic recovery during the removal of load. The latter method provides an estimate of the area of the contact under full load. Usually, the area given by the shape of the residual impression and that given by the depth-sensing technique are almost identical, but this is not always the case. For example, a highly elastic material may give a very small residual impression (say when testing a block of rubber) while giving an appreciable contact area under load. In the former case, the hardness would be very high, while in the latter, the hardness could be quite low.<sup>‡</sup>

<sup>‡</sup> The hardness of rubber is conventionally defined in terms of the penetration depth of a specially shaped indenter is measured under a specified load using a specially designed instrument called a “durometer” – this method is similar to the well-known Rockwell hardness test.

### 2.3.1 Spherical indenter

The mean contact pressure, and, hence, indentation hardness, for an impression made with a spherical indenter is given by:

$$p_m = H = \frac{4P}{\pi d^2} \quad (2.3.1a)$$

where  $d$  is the diameter of the contact circle at full load (assumed to be equal to the diameter of the residual impression in the surface). The mean contact pressure determined in this way is often called the “Meyer” hardness in contrast to the Brinell hardness number (BHN), which uses the actual area of the curved surface of the impression and is given by:

$$\text{BHN} = \frac{2P}{\pi D \left( D - \sqrt{D^2 - d^2} \right)} \quad (2.3.1b)$$

where  $D$  is the diameter of the indenter. The Brinell hardness is usually performed at a value for  $a/R$  (the indentation strain) of 0.4, a value found to be consistent with a fully developed plastic zone. The angle of a Vickers indenter (see Section 2.3.2 below) was chosen originally so as to result in this same level of indentation strain.

The use of the area of the actual curved surface of the residual impression in the Brinell test was originally thought to compensate for strain hardening of the specimen material during the test itself. However, it is now more generally recognized that the Meyer hardness is a more physically meaningful concept.

Meyer found that there was an empirical size relationship between the diameter of the residual impression and the applied load, and this is known as Meyer’s law:

$$P = kd^n \quad (2.3.1c)$$

In Eq. 2.3.1c,  $k$  and  $n$  are constants for the specimen material. It was found that the value of  $n$  was insensitive to the radius of the indenter and is related to the strain-hardening exponent  $x$  of the specimen material according to

$$n = x + 2 \quad (2.3.1d)$$

Values of  $n$  were found to be between 2 and 2.5, the higher the value applying to annealed materials, while the lower value applying to work-hardened materials (low value of  $x$  in Eq. 2.3.1d). It is important to note that Meyer detected a lower limit to the validity of Eq. 2.3.1c. Meyer fixed the lower limit of validity to an indentation strain of  $a/R = 0.1$ . Below this, the value of  $n$  increased — a result of particular relevance to nanoindentation testing.

### 2.3.2 Vickers indenter

For a Vickers diamond pyramid indenter (a square pyramid with opposite faces at an angle of  $136^\circ$  and edges at  $148^\circ$ ), the Vickers diamond hardness, VDH, is calculated using the indenter load and the actual surface area of the impression. The VDH is lower than the mean contact pressure by  $\approx 7\%$ . The Vickers diamond hardness is found from:

$$\text{VDH} = \frac{2P}{d^2} \sin \frac{136^\circ}{2} = 1.86 \frac{P}{d^2} \quad (2.3.2a)$$

with  $d$  equal to the length of the diagonal measured from corner to corner on the residual impression in the specimen surface. The mean contact pressure is found using the projected area of contact, in which case we have:

$$p_m = 2 \frac{P}{d^2} \quad (2.3.2b)$$

### 2.3.3 Berkovich indenter

The Berkovich indenter is used routinely for nanoindentation testing because it is more readily fashioned to a sharper point than the four-sided Vickers geometry, thus ensuring a more precise control over the indentation process. The mean contact pressure is usually determined from a measure of the “plastic” depth of penetration,  $h_p$  in (see Fig. 2.5), such that the area of the contact is given by:

$$A = 3\sqrt{3}h_p^2 \tan^2\theta \quad (2.3.3a)$$

which for  $\theta = 65.3^\circ$ , evaluates to:

$$A = 24.5h_p^2 \quad (2.3.3b)$$

and hence the mean contact pressure is:

$$H = \frac{P}{24.5h_p^2} \quad (2.3.3c)$$

For both the Vickers and the Berkovich indenters, the representative strain within the specimen material is approximately 8% (see Section 1.3).

### 2.3.4 Cube corner

The Berkovich and Vickers indenters have a relatively large semi-angle, which ensures that deformation is more likely to be described by the expanding cavity model rather than slip-line theory, which is equivalent to saying that the stresses beneath the indenter are very strongly compressive. In some instances, it is desirable to indent a specimen with more of a cutting action, especially when intentional radial and median cracks are required to measure fracture toughness. A cube corner indenter offers a relatively acute semi-angle that can be beneficial in these circumstances. Despite the acuteness of the indenter, it is still possible to perform indentation testing in the normal manner and area of contact is the same as that for a Berkovich indenter where in this case  $\theta = 35.26^\circ$ :

$$A = 3\sqrt{3}h_p^2 \tan^2\theta \quad (2.3.4a)$$

### 2.3.5 Knoop hardness

The Knoop indenter is similar to the Vickers indenter except that the diamond pyramid has unequal length edges, resulting in an impression that has one diagonal with a length approximately seven times the shorter diagonal.<sup>3</sup> The angles for the opposite faces of a Knoop indenter are  $172^\circ 30'$  and  $130^\circ$ . The Knoop indenter is particularly useful for the study of very hard materials because the length of the long diagonal of the residual impression is more easily measured compared to the dimensions of the impression made by Vickers or spherical indenters.

As shown in Fig. 2.4, the length  $d$  of the longer diagonal is used to determine the projected area of the impression. The Knoop hardness number is based upon the projected area of contact and is calculated from:

$$\text{KHN} = \frac{2P}{a^2 \left[ \cot \frac{172.5}{2} \tan \frac{130}{2} \right]} \quad (2.3.5a)$$

For indentations in highly elastic materials, there is observed a substantial difference in the length of the short axis diagonal for a condition of full load compared to full unload. Marshall, Noma, and Evans<sup>4</sup> likened the elastic recovery along the short axis direction to that of a cone with major and minor axes and applied elasticity theory to arrive at an expression for the recovered indentation size in terms of the geometry of the indenter and the ratio  $H/E$ :

$$\frac{b'}{a'} = \frac{b}{a} - \alpha \frac{H}{E} \quad (2.3.5b)$$

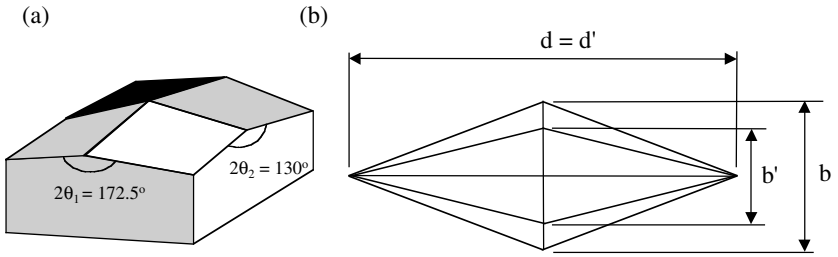


**Fig. 2.4** (a) Geometry of a Knoop indenter. (b) The length of the long diagonal of the residual impression remains approximately the same from full load to full unload. The size of the short diagonal reduces from  $b$  to  $b'$  due to elastic recovery during unloading.

In Eq. 2.3.5b,  $\alpha$  is a geometry factor found from experiments on a wide range of materials to be equal to 0.45. The ratio of the dimension of the short diagonal  $b$  to the long diagonal  $a$  at full load is given by the indenter geometry and for a Knoop indenter,  $b/a = 1/7.11$ . The primed values of  $a$  and  $b$  are the lengths of the long and short diagonals after removal of load. Since there is observed to be negligible recovery along the long diagonal, we can say that  $a' \approx a$ . When  $H$  is small and  $E$  is large (e.g. metals), then  $b' \approx b$  indicating negligible elastic recovery along the short diagonal. When  $H$  is large and  $E$  is small (e.g. glasses and ceramics), there we would expect  $b' \ll b$ . Using measurements of the axes of the recovered indentations, it is possible to estimate the ratio  $E/H$  for a specimen material using Eq. 2.3.5b.

## 2.4 Load-Depth Compliance Curves

The principal goal of nanoindentation testing is to extract elastic modulus and hardness of the specimen material from experimental readings of indenter load and depth of penetration. In a typical test, load and depth of penetration are recorded as load is applied from zero to some maximum and then from maximum load back to zero. If plastic deformation occurs, then there is a residual impression left in the surface of the specimen. Unlike conventional indentation hardness tests, the size (and hence the projected contact area) of the residual impression for nanoindentation testing is too small to measure accurately with optical techniques. The depth of penetration together with the known geometry of the indenter provides an indirect measure of the area of contact at full load, from which the mean contact pressure, and thus hardness, may be estimated. When load is removed from the indenter, the material attempts to regain its original shape, but it is prevented from doing so because of plastic deformation. However, there is some degree of recovery due to the relaxation of elastic strains within

the material. An analysis of the initial portion of this elastic unloading response gives an estimate of the elastic modulus of the indented material.

The form of the compliance curves for the most common types of indenter are very similar and is shown in Fig. 2.5. For a spherical indenter, it will be shown in Chapter 5 that the relationship between load and penetration depth for the loading portion for an elastic-plastic contact is given by:

$$h = \frac{1}{2} \left( \frac{P}{\pi R_i H} + \frac{3}{4} \frac{\sqrt{P\pi H}}{\beta E^*} \right) \tag{2.4a}$$

For the elastic unloading, we have from Eq. 1.2g:

$$h = \left[ \frac{3}{4E^* R^{1/2}} \right]^{2/3} P^{2/3} \tag{2.4b}$$

For a Berkovich indenter, it will be shown in Chapter 5 that the expected relationship between load and depth for an elastic-plastic contact is given by:

$$h = \sqrt{P} \left[ \left( 3\sqrt{3} H \tan^2 \theta \right)^{-1/2} + \left[ \frac{2(\pi - 2)}{p} \right] \frac{\sqrt{H\pi}}{2\beta E^*} \right] \tag{2.4c}$$

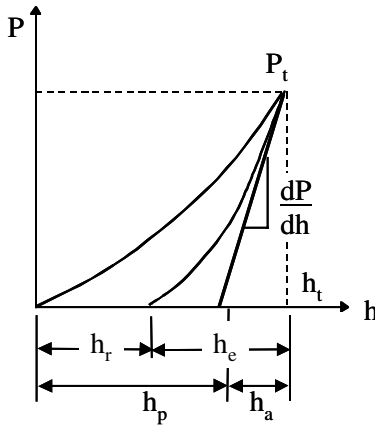


**Fig. 2.5** Compliance curves, loading and unloading, from a nanoindentation experiment with maximum load  $P_t$  and depth beneath the specimen free surface  $h_t$ . The depth of the contact circle  $h_p$  and slope of the elastic unloading  $dP/dh$  allow specimen modulus and hardness to be calculated.  $h_r$  is the depth of the residual impression, and  $h_e$  is the displacement associated with the elastic recovery during unloading.

Upon elastic unloading we have from Eq. 1.2m:

$$h = \left( \frac{P\pi}{2E^*} \right)^{\frac{1}{2}} \left( \frac{\pi}{3\sqrt{3}} \right)^{\frac{1}{4}} \frac{1}{\tan\theta'} \quad (2.4d)$$

where in Eqs. 2.4b and 2.4d the quantities  $R'$  and  $\theta'$  are the combined radii and angle of the indenter and the shape of the residual impression in the specimen surface. The dependence of depth on the square root of the applied load in Eqs. 2.4a to 2.4d is of particular relevance. This relationship is often used in various methods of analysis to be described in Chapter 3.

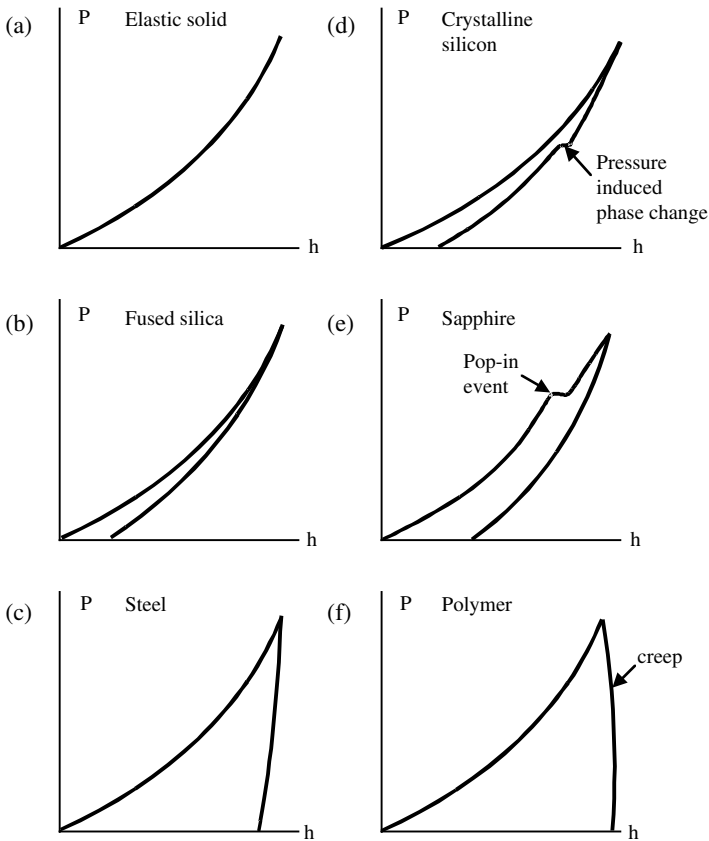


**Fig. 2.6** Schematic examples of load-displacement curves for different material responses and properties. (a) Elastic solid, (b) brittle solid, (c) ductile solid, (d) crystalline solid, (e) brittle solid with cracking during loading, and (f) polymer exhibiting creep.

In subsequent chapters, the methods by which elastic modulus and hardness values are obtained from experimental values of load and depth are described along with methods of applying necessary corrections to the data. All of the methods of analysis rely on the assumption of an elastic-plastic loading followed by an elastic unloading — with no plastic deformation (or “reverse” plasticity) occurring during the unloading sequence. Variations on the basic load-unload cycle include partial unloading during each loading increment, superimposing an oscillatory motion on the loading, and holding the load steady at a maximum load and recording changes in depth. These types of tests allow the measurement of viscoelastic properties of the specimen material.

In practice, nanoindentation testing is performed on a wide variety of substances, from soft polymers to diamond-like carbon thin films. The shape of the load-displacement curve is often found to be a rich source of information, not only for providing a means to calculate modulus and hardness of the specimen material, but also for the identification of non-linear events such as phase transformations, cracking, and delamination of films. Fig. 2.6 shows a schematic of some of the more commonly observed phenomena. It should be noted that in many cases the permanent deformation or residual impression is not the result of plastic flow but may involve cracking or phase or structural changes within the specimen.

## 2.5 Experimental Techniques

Despite the mature evolution of nanoindentation test instruments, the process of undertaking such a test requires considerable experimental skill and resources. Such tests are extremely sensitive to thermal drifts and mechanical vibration. It is necessary to ensure that the instrument is in thermal equilibrium with its environment, and that the specimen and indenter are also thermally stabilized with the instrument. Handling the specimen or the indenter requires at least a one hour delay in beginning such a test to ensure that no temperature gradients exist that might introduce errors into the displacement measurement. Should there be any long-term thermal drifts, then these should be quantified and the appropriate correction made (see Chapter 4). In this section, specified matters requiring attention in practical indentation tests are summarized and commented upon.

### 2.5.1 Basic instrument construction and installation

The nanoindentation instrument should be insulated against temperature variation, vibration, and acoustic noise in normal laboratory conditions. A specially designed enclosure designed to reduce thermal and electrical interference to a minimum is usually supplied by the manufacturer as part of the installation.

The loading column and base of a nanoindentation instrument should be of heavy construction so as to act as a seismic mass, to reduce mechanical vibra-

tion, and to have a very high compliance, so as to minimize the effect of reaction forces on the readings. The indenter is typically mounted on a shaft that is made from stiff, yet light weight material.

Specimens are typically mounted on a metal base with wax or mounting adhesive. The specimen holder is in turn placed on a stage. Stage movement is usually controlled by motorized axes that have a resolution, or step size, of less than  $0.5\ \mu\text{m}$ . Such fine positioning is usually needed to allow indentations to be made on very small features such as grains in a ceramic or conductive pads in an integrated circuit. Stage movement is usually servo controlled with proportional, integral, and derivative gains that can be set to allow for the most precise positioning. Optical rotary or linear track encoders are usually employed. The encoder is usually mounted on the lead screw of the axis drive and a high-quality ball nut drives converts rotary motion to linear motion of the stage. Backlash in this nut is negligible. The operating software allows automatic positioning of the specimen beneath the indenter.

Load is typically applied to the indenter shaft by an electromagnetic coil or the expansion of a piezoelectric element. Displacements are usually measured using either a changing capacitance or inductance signal. Most nanoindentation instruments are load controlled, that is, a commanded force is applied and the resulting displacement is read. Particular features of some commercially available indentation instruments are described in Chapter 10.

### 2.5.2 Indenters

Diamond indenters are very hard, but also very brittle and can easily be chipped or broken. Figure 2.7 shows a failed indenter where cleavage along crystallographic planes is evident. The mechanical properties of diamond differ according to the orientation of the measurement due to the crystalline nature of the diamond structure. Literature values for modulus range from about 800 GPa to 1200 GPa. A value of 1000 GPa is usually used in the analysis of nanoindentation test data with a Poisson's ratio of 0.07.

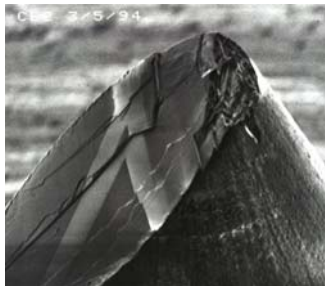


**Fig. 2.7** Brittle failure of a  $2\ \mu\text{m}$  radius sphero-conical indenter. Cleavage planes are evident along the fracture face (Courtesy CSIRO).

The indenter must be absolutely clean and free from any contaminants. Diamond indenters are most effectively cleaned by pressing them into a block of dense polystyrene. The chemicals in the polystyrene act as a solvent for any contaminants and the polystyrene itself offers a mechanical cleaning action that is not likely to fracture the indenter. The indenter itself should be attached to the indenter shaft firmly and in such a manner so as to minimize its compliance — this is often a matter for the manufacturer of the instrument.

The choice of indenter is important and depends upon the information one wishes to obtain from the indentation test. The representative strain in the specimen material, for geometrically similar indentations such as that made by Vickers and Berkovich indenters, depends solely on the effective cone angle of the indenter. The sharper the angle, the greater the strain. According to Tabor, the representative strain for a conical indenter is given by:

$$\epsilon = 0.2 \cot \alpha \quad (2.5.2a)$$

which for a Berkovich and Vickers indenter, evaluates to about 8%. If larger strains are required, say, for example, to induce cracking or other phenomena, then a sharper tip may be required. The representative strain for a cube corner indenter evaluates to about 22%. Indentations made with sharp indenters induce plasticity from the moment of contact (neglecting any tip-rounding effects). This may be desirable when testing very thin films in which the hardness of the film, independent of the substrate is required.

Spherical indenters offer a gradual transition from elastic to elastic–plastic response. The representative strain varies as the load is applied according to:

$$\epsilon = 0.2 \frac{a}{R} \quad (2.5.2b)$$

It is important that when measuring hardness using a spherical indenter, a fully developed plastic zone is obtained. In metals, this usually corresponds to a value for  $a/R$  of greater than 0.4. The changing strain throughout an indentation test with a spherical indenter enables the elastic and elastic–plastic properties of the specimen to be examined along with any strain-hardening characteristics.

### 2.5.3 Specimen mounting

Test specimens are usually prepared as coupons about 10 mm x 10 mm, hot mounted on a hardened base using heat-softening wax. Other specimen shapes and other holding devices such as vacuum chucks or spring clamps may also be used. The specimen holder is required to be firmly clamped, either mechanically or magnetically to the stage.



**Fig. 2.8** Example of a fused silica specimen mounted on a cylindrical hardened steel magnetic specimen mount and placed into position on a servo-motor-driven X-Y positioning stage. In this instrument, there is provision for four specimen mounts on the stage with powerful magnets mounted beneath each position to firmly clamp the specimen holder to the stage (Courtesy CSIRO).

As the indentations made by a nanoindentation instrument are very small, specimens must have a smoothly finished surface and, because the working range (see Section 2.5.4) is small, the surfaces must be parallel; however, a departure from parallelism of  $25\ \mu\text{m}$  over the length of a traverse may be tolerated. Specimens often comprise surface layers added to a substrate. Any well-prepared material may be used as the substrate, such as a glass microscope slide or silicon wafer.

If a polishing technique is employed to prepare a surface, the properties of the surface material may be altered (see Section 4.11). Indentations placed on scratches, inclusions, or voids will give unpredictable results.

### 2.5.4 Working distance and initial penetration

A typical nanoindentation instrument has a limited range of displacement over which the indentation depth may be measured. It is therefore necessary to ensure that the full range of the depth measurement system is available for measuring penetration depth into the specimen and not used for bringing the indenter into contact with the surface from its initial parked position. Usually, the measurement head of the instrument is allowed to translate vertically in coarse steps until the indenter is within  $20\ \mu\text{m}$  or so of the specimen surface. This is called the “working distance” and ensures that most of the available high resolution displacement occurs during the final approach to the surface and the subsequent penetration into the sample.

Once the measurement head has been set so that the indenter is at the working distance, it is then necessary to bring the indenter down to touch the surface with the minimum possible contact force. This becomes the reference position for any subsequent displacement readings. The minimum contact force is a very important measurement of performance for a nanoindentation instrument. No matter how small the minimum contact force is, it will result in some penetration into the specimen surface that has to be corrected for in the final analysis. Of course, if the initial penetration is too large, then it is possible that the indenter will penetrate past the surface layer or film desired to be measured. In many respects, the specification of the minimum contact force is the parameter that distinguishes a nanoindentation instrument from a microindentation instrument.

Some nanoindentation instruments apply the initial contact force by bringing the indenter down at a very small velocity until a preset initial contact force is measured by a separate force sensor. Others monitor the “stiffness” of the contact by oscillating the indenter shaft and noting when the oscillations undergo a sudden reduction in amplitude. The process can be automated so that it becomes independent of the operator. The initial contact force is typically in the range of 5  $\mu\text{N}$  or less.

### 2.5.5 Test cycles

A typical nanoindentation test cycle consists of an application of load followed by an unloading sequence — but there are many variations. Load may be applied continuously until the maximum load is reached, or as a series of small increments. At each increment, a partial unloading may be programmed that provides information about the stiffness of the contact ( $dP/dh$ ), which is important for measuring changes in modulus or hardness with penetration depth. Contact stiffness may also be found by superimposing a small oscillatory motion onto the load signal.

The indentation instrument may be set into either load or depth control. In load control, the user specifies the maximum test force (usually in mN) and the number of load increments or steps to use. The progression of load increments may be typically set to be a square root or linear progression. A square root progression attempts to provide equally spaced displacement readings. In depth control, the user specifies a maximum depth of penetration. However, it should be noted that most nanoindentation instruments are inherently load controlled devices and when operating under a depth control mode, they typically apply small increments of force until the required depth has been reached.

It is customary for a nanoindentation instrument to allow for a dwell or hold period at each load increment and at maximum load. The dwell settings at each load increment allow the instrument and specimen to stabilize before depth and load readings are taken.

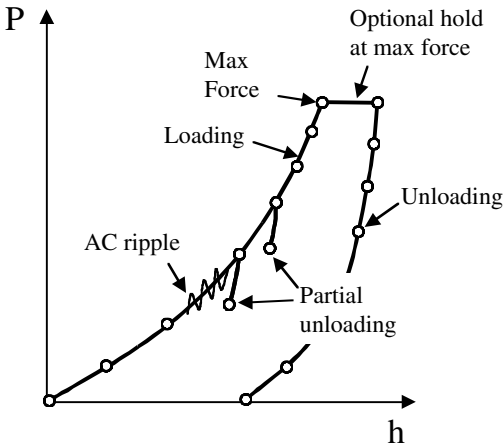


**Fig. 2.9** Various components of a nanoindentation test cycle.

Hold period data at maximum load can be used to measure creep within the specimen or thermal drift of the apparatus during a test. Hold measurements for the purposes of thermal drift are probably best carried out at the end of the indentation test, at a low load, so as to minimize any effects from creep within the specimen. Figure 2.9 summarizes the loading, hold and unloading periods in a typical test cycle.

## References

1. E.S. Berkovich, "Three-faceted diamond pyramid for micro-hardness testing," *Ind. Diamond Rev.* 11 127, 1951, pp. 129–133.
2. B.R. Lawn, *Fracture of Brittle Solids*, 2<sup>nd</sup> Ed., Cambridge University Press, Cambridge, 1993.
3. F. Knoop, C.G. Peters, and W.B. Emerson, "A sensitive pyramidal-diamond tool for indentation measurements," Research Paper 1220, *Journal of Research, National Bureau of Standards*, 23 1, 1939.
4. D.B. Marshall, T. Noma, and A.G. Evans, "A simple method for determining elastic-modulus-to-hardness ratios using Knoop indentation measurements," *J. Am. Ceram. Soc.* 65, 1980, pp. C175–C176.

# Chapter 3

## Analysis of Nanoindentation Test Data

### 3.1 Analysis of Indentation Test Data

As described in Chapter 2, estimations of both elastic modulus and hardness of the specimen material in a nanoindentation test are obtained from load versus penetration measurements. Rather than a direct measurement of the size of residual impressions, contact areas are instead calculated from depth measurements together with a knowledge of the actual shape of the indenter. For this reason, nanoindentation testing is sometimes referred to as depth-sensing indentation testing. In this chapter, methods of the analysis of load-displacement data that are used to compute hardness and modulus of test specimens are presented in detail. It is an appropriate introduction to first consider the case of a cylindrical punch indenter — even though this type of indenter is rarely used for this type of testing, its response illustrates and introduces the theory for the more complicated cases of spherical and pyramidal indenters.

### 3.2 Analysis Methods

#### 3.2.1 Cylindrical punch indenter

Consider the case of a cylindrical flat punch indenter that has an elastic–plastic load displacement response as shown in Fig. 3.1. Figure 3.1 (a) shows the displacements for the elastic–plastic contact at full load  $P_1$  and the displacements at full unload. The unloading response is assumed to be fully elastic. Elastic displacements can be calculated using Eq. 3.2.1a:

$$P = 2aE^* h \quad (3.2.1a)$$

With  $h$  equal to the displacement  $u_z$  at  $r = 0$  and by taking the derivative  $dP/dh$ , we can arrive at an expression for the slope of the unloading curve:

$$\frac{dP}{dh} = 2aE^* \quad (3.2.1b)$$

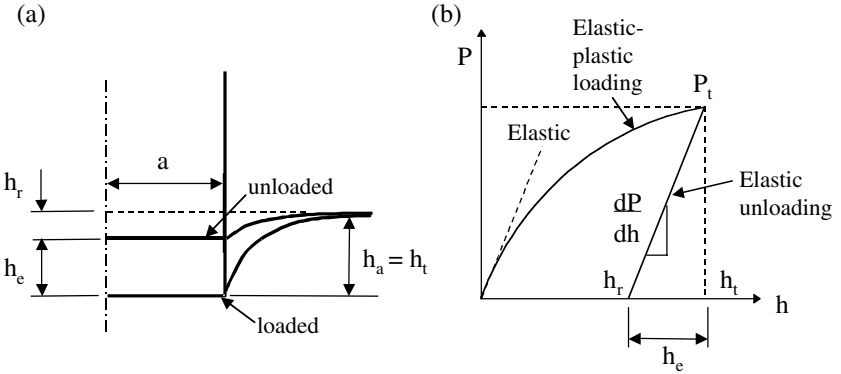


**Fig. 3.1** (a) Schematic of indenter and specimen surface geometry at full load and full unload for cylindrical punch indenter. (b) Load versus displacement for elastic-plastic loading followed by elastic unloading.  $h_r$  is the depth of the residual impression,  $h_t$  is the depth from the original specimen surface at maximum load  $P_t$ ,  $h_e$  is the elastic displacement during unloading, and  $h_a$  is the distance from the edge of the contact to the specimen surface, here equal to  $h_t$  for cylindrical indenter (after reference 1).

In Eqs. 3.2.1a and 3.2.1b,  $a$  is the contact radius, which, for the case of a cylindrical punch, is equal to the radius of the indenter. Expressing this in terms of the contact area:

$$\frac{dP}{dh} = 2E^* \frac{\sqrt{A}}{\sqrt{p}} \quad (3.2.1c)$$

Pharr, Oliver, and Brotzen<sup>2</sup> show that Eq. 3.2.1c applies to all axial-symmetric indenters. Equation 3.2.1c shows that the slope of the unloading curve is proportional to the elastic modulus and may be calculated from the known radius of the punch. As shown in Fig. 3.1,  $h_e$  is the displacement for the elastic unloading. Thus, the slope of the unloading curve is also given by:

$$\frac{dP}{dh} = \frac{P_t}{h_e} \quad (3.2.1d)$$

Now, for a cylindrical indenter, there is no need for an estimation of the size of the contact area from depth measurements because it is equal to the radius of the indenter. However, the situation becomes quite complicated when this is not the case, such as for the Berkovich indenter.

### 3.2.2 Conical indenter — cylindrical punch method

As can be seen from Fig. 3.1, the slope of the elastic unloading curve for a cylindrical punch indenter is linear. Doerner and Nix<sup>3</sup> observed that for tests with a Berkovich indenter, the *initial* unloading curve appeared to be linear for a wide range of test materials. These workers then applied cylindrical punch equations to the initial part of an unloading curve to determine the size of the contact from depth measurements. Their analysis considered the case of a conical indenter and assumed that the actual pyramidal geometry had only a small effect on the final result.<sup>2</sup>

Consider the elastic-plastic loading and elastic unloading of a specimen with a conical indenter. The shape of the surface for the sequence is shown in Fig. 3.2 (a). As the indenter is unloaded from full load, the contact radius remains fairly constant (due to a fortuitous combination of the geometry of the deformation and the shape of the indenter) until the surface of the specimen no longer conforms to the shape of the indenter. Thus, for the initial part of the unloading, if the contact radius is assumed to be constant, the unloading curve is linear. Unloading from the fully loaded impression for a cone is therefore similar to that seen for the elastic unloading of a cylindrical punch.

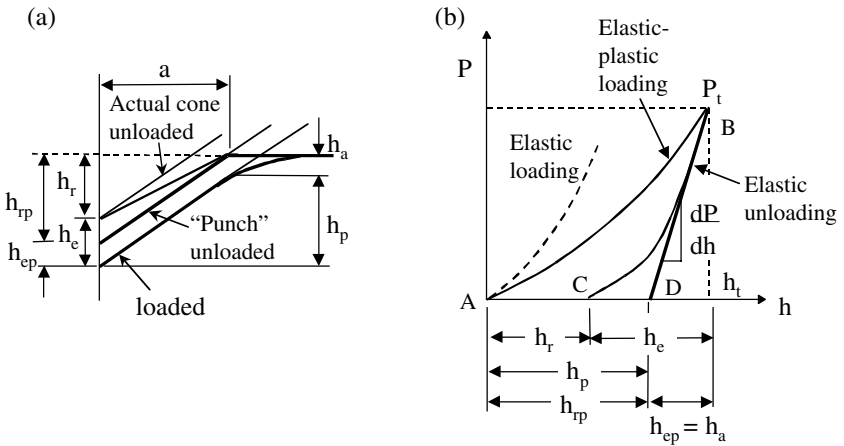


**Fig. 3.2** (a) Schematic of indenter and specimen surface geometry at full load and full unload for conical indenter. (b) Load versus displacement for elastic-plastic loading followed by elastic unloading.  $h_r$  is the depth of the residual impression,  $h_{rp}$  is the depth of the residual impression for an equivalent punch,  $h_t$  is the depth from the original specimen surface at maximum load  $P_t$ ,  $h_e$  is the elastic displacement during unloading of the actual cone,  $h_{ep}$  is the elastic displacement for an equivalent punch, and  $h_a$  is the distance from the edge of the contact to the specimen surface at full load (after reference 1).

Doerner and Nix<sup>3</sup> thus use Eq. 3.2.1c, with  $A$  being the contact area of the punch, to obtain the depth of the edge of the circle of contact  $h_a$ , and hence  $h_p$ . The radius of the circle of contact at full load is obtained from the slope of the initial unloading.

With reference to Fig. 3.2 (b), for the initial unloading, the cone acts like a punch in terms of its “constant” area of contact, since the initial unloading appears to be linear. If the area of contact remained constant during the entire unloading, then the unloading curve would be linear: from  $P_t$  to  $P = 0$ . The unloading curve associated with a punch that has the slope  $dP/dh$  at  $P_t$  would be that which is extrapolated to zero load, that is, the path  $BD$  in Fig. 3.2 (b). If unloading were to take place along this line, then the elastic displacement of this imaginary punch would be the distance  $h_{ep}$  (the subscript “p” denoting “punch”). The cone actually travels the path  $BC$  during unloading, which is a distance  $h_e$ , leaving a residual impression of depth  $h_r$ . Now, with reference to Fig. 3.2 (a), it is easy to see that for a cone that acts like a punch (by having a constant radius of circle of contact during unloading) and unloads through a distance  $h_{ep}$ , the distance  $h_{ep}$  is equal to the distance  $h_a$  that exists at full load, which is where we require an estimate of  $h_a$  for the actual cone. As a consequence, the distance  $h_{rp}$ , which is the intercept of the unloading curve for the punch, is equal to  $h_p$ . Thus:

$$\begin{aligned} h_t - h_{rp} &= h_s \\ h_{rp} &= h_t - h_s \\ &= h_p \end{aligned} \quad (3.2.2a)$$

Equation 3.2.2a indicates that the depth  $h_{rp}$ , and hence  $h_p$ , can be obtained from the intercept of the linear unloading curve with the displacement axis. Once  $h_p$  is known, then the area of the contact can be calculated and the hardness and elastic modulus determined from the geometry of the indenter. For example, for a Vickers or Berkovich indenter, the relationship between the projected area  $A_p$  of the indentation and the distance  $h_p$  is:

$$A_p = 24.5h_p^2 \quad (3.2.2b)$$

Thus:

$$\frac{dP}{dh} = 2h_p E^* \sqrt{\frac{24.5}{\pi}} \quad (3.2.2c)$$

The displacement  $h_p$  is found from the intercept of the linear unloading curve with the displacement axis. The procedure assumes that the initial unloading is linear. The actual cone and the imaginary punch meet at  $P_t$ . We assume that the initial unloading can be extrapolated to zero load, which gives us a measure of  $h_{ep}$ , and then we say that due to the geometrical similarity of this punch-like cone  $h_{ep} = h_a$  and thus we find  $h_p$  for the actual cone. Values of  $H$  and  $E$  can be

calculated from the maximum load  $P_t$  divided by the projected area (Eq. 3.2.2b)  $A_p$  and from Eq 3.2.2c, respectively.

### 3.2.3 Spherical indenter

Historically, the cylindrical punch equations were applied to data obtained with a Berkovich indenter. Oliver and Pharr<sup>4</sup> later noted that the unloading response for many materials tested with a Berkovich indenter was curved rather than linear. This led these workers to use the expected non-linear elastic response of a cone rather than a cylindrical punch to the unloading data. Oliver and Pharr considered the case of a Berkovich indenter and this will be reviewed shortly. Field and Swain<sup>5</sup> also considered an alternative method of analysis based upon a single unload point and applied it to the case of a spherical indenter. Either method may be used for both types of indenter, and we will begin with the case of a spherical indenter.

Consider the loading of an initially flat specimen with a spherical indenter. Upon loading, there may be an initial elastic response at low loads followed by elastic and plastic deformations within the specimen material at higher loads.

With reference to Fig. 3.3, the depth of penetration of a rigid spherical indenter beneath the original specimen free surface is  $h_t$  at full load  $P_t$ . When the load is removed, assuming no reverse plasticity, the unloading is elastic and at complete unload, there is a residual impression of depth  $h_r$ .

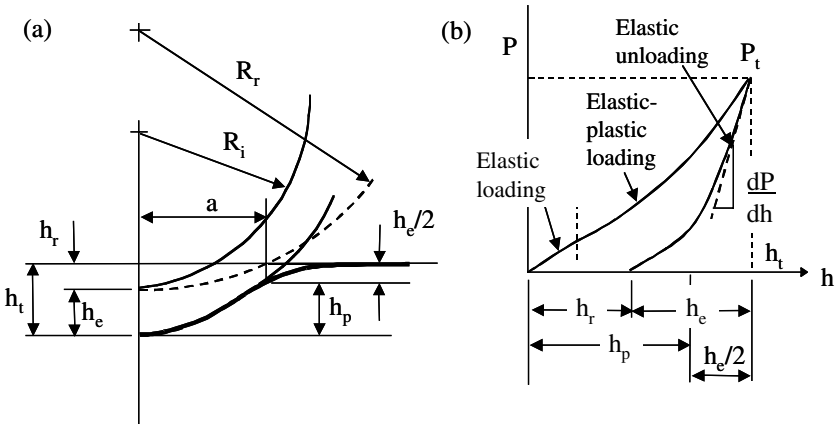


**Fig. 3.3** (a) Geometry of loading a preformed impression of radius  $R_r$  with a rigid indenter radius  $R_i$ . (b) Compliance curve (load vs displacement) for an elastic-plastic specimen loaded with a spherical indenter showing both loading and unloading response. Upon loading, there is an initial elastic response followed by elastic-plastic deformation. Upon complete unload, there is a residual impression of depth  $h_r$  (after reference 1).

If the load  $P_t$  is reapplied, then the reloading is elastic through a distance  $h_e = h_t - h_r$  according to the “Hertz” equation<sup>6</sup>:

$$P = \frac{4}{3} E^* R^{1/2} h_e^{3/2} \quad (3.2.3a)$$

It should be borne in mind that the quantity  $h_e$  in Eq. 3.2.3a is, strictly speaking, the load-point displacement, which is only equal to the displacement of the specimen surface along the axis of symmetry ( $r = 0$ ) for the special case of a perfectly rigid indenter. However, if we assign  $E^*$  to the specimen, then it is possible to consider the indentation to be occurring with a perfectly rigid indenter and to extract the actual specimen modulus  $E$  at the end of the analysis using the known values of mechanical properties  $E'$  and  $\nu'$  for the indenter. Furthermore, it should be noted that since the elastic unloading/reloading involves the deformation of the preformed residual impression,  $R$  in Eq. 3.2.3a is the relative radius of curvature of the residual impression  $R_r$  and the indenter  $R_i$  and is given by:

$$\frac{1}{R} = \frac{1}{R_i} - \frac{1}{R_r} \quad (3.2.3b)$$

Note that the center of curvature for the residual impression is on the same side of the surface as the indenter, hence the presence of the negative sign in Eq. 3.2.3b. The radius of the residual impression serves to increase the effective radius of the indenter. We shall see that it is not necessary to measure the radius of the residual impression  $R_r$  to perform the analysis.

There are two important matters to consider at this point. First, the chordal diameter of the residual impression may be assumed to be identical to that of the circle of contact at full load (owing to a fortuitous combination of the geometry of the deformation and the shape of the indenter). That is, during an imagined elastic reloading of the residual impression, the radius of the circle of contact between the indenter and the specimen moves outward (and downward) until it meets the edge of the residual impression, by which time the load has reached  $P_t$ . Second, since the loading/unloading from  $h_r$  to  $h_t$  is elastic, the Hertz equations show that depth of the circle of contact beneath the specimen free surface is half of the elastic displacement  $h_e$ . That is, the distance from the specimen free surface (at full unload) to the depth of the radius of the circle of contact at full load is  $h_a = h_e/2$ . With reference to Fig. 3.3:

$$\begin{aligned} h_t &= h_p + h_a \\ h_p &= h_t - \frac{h_e}{2} \end{aligned} \quad (3.2.3c)$$

The multiple-point and the single-point unload methods are concerned with the determination of the quantity  $h_p$ , often referred to as the “plastic depth,” and is the distance from the circle of contact to the maximum penetration depth.

Once  $h_p$  is known, the resulting radius of circle of contact is then determined by simple geometry from which the area of the contact is calculated and used to determine the mean contact pressure or hardness value  $H$ :

$$H = \frac{P}{A} \tag{3.2.3d}$$

where  $A$  is the area of contact given by  $\pi a^2$  with the term “ $a$ ” being the radius of the circle of contact at  $P = P_t$ . Elastic modulus is determined from the slope of the unloading curve or by the Hertz equations directly.

### 3.2.3.1 Multiple-point unload method

The multiple-point unload method<sup>§</sup> uses the slope of the initial portion of the unloading curve to determine the depth of the circle of contact  $h_a$  and hence  $h_p$ . The slope of the elastic unloading, for the case of a spherical indenter, is given by the derivative of Eq. 3.2.3a with respect to  $h$ :

$$\frac{dP}{dh} = 2E^* R^{1/2} h_e^{1/2} \tag{3.2.3.1a}$$

The quantity  $dP/dh$  is sometimes referred to as the contact stiffness and given the symbol  $S$ . Substituting Eq. 3.2.3.1a into Eq. 3.2.3a, we have:

$$P = \frac{2}{3} \frac{dP}{dh} h_e \tag{3.2.3.1b}$$

Thus,

$$h_e = \frac{3}{2} P \frac{dh}{dP} \tag{3.2.3.1c}$$

With reference to Fig. 3.3, the unloading from  $h_t$  to  $h_r$  is assumed to be elastic, and for a spherical indenter, the Hertz equations show that the depth of the circle of contact  $h_a$  beneath the specimen free surface is half of the elastic displacement  $h_e$ , that is:

$$h_a = \frac{h_e}{2} \tag{3.2.3.1d}$$

Thus:

$$h_a = \left[ \frac{3}{4} \right] \frac{P_t}{dP/dh} \tag{3.2.3.1e}$$

Once we have  $h_a$ , the plastic depth  $h_p$  can be found from Eq. 3.2.3c. The radius of the circle of contact can then be found from geometry:

<sup>§</sup> This is the “Oliver and Pharr” method applied to a spherical indenter

$$\begin{aligned}
 a &= \sqrt{2R_i h_p - h_p^2} \\
 &\approx \sqrt{2R_i h_p}
 \end{aligned}
 \tag{3.2.3.1f}$$

and the hardness computed from the load divided by the area of contact. The approximation in Eq. 3.2.3.1f is precisely the same as that underlying the Hertz equations and is equivalent to the restriction that the indentations are to be small — i.e.  $h_p \ll a$ . For a rigid spherical indenter, Hertz showed that the elastic displacement is given by:

$$h_e = \frac{a^2}{R} \tag{3.2.3.1g}$$

Equation 3.2.3.1a becomes:

$$\begin{aligned}
 \frac{dP}{dh} &= 2E^* R^{1/2} \frac{a}{R^{1/2}} \\
 &= 2E^* a
 \end{aligned}
 \tag{3.2.3.1h}$$

Note that the relative radius of the indenter and specimen  $R$  has been cancelled out in Eq. 3.2.3.1h. The combined modulus of the system can thus be determined from the slope of the initial unloading:

$$\begin{aligned}
 E^* &= \frac{dP}{dh} \frac{1}{2a} \\
 &= \frac{dP}{dh} \frac{\sqrt{\pi}}{\sqrt{A}} \frac{1}{2}
 \end{aligned}
 \tag{3.2.3.1i}$$

where  $A = \pi a^2$ , the area of contact. Equation 3.2.3.1i should be compared with Eq. 3.2.1c and is a general relationship that applies to all axial-symmetric indenters with a smooth profile.<sup>7</sup> The multiple-point unload method is most well known when it is applied to indentations performed with a three-sided Berkovich indenter, although, as shown above, it is equally applicable to the case of spherical indenters.

### 3.2.3.2 Single-point unload method

In contrast to the multiple-point unload method, the single-point unload method<sup>\*\*</sup> uses a single unload point together with the Hertz equations directly (rather than the derivative) as the basis for estimating the plastic depth and unloading characteristics, and hence hardness and modulus.

In terms of the radius of the circle of contact, the Hertz equation, Eq. 3.2.3a, can be expressed:

<sup>\*\*</sup>The “Field and Swain” method.

$$P = \frac{4}{3} E^* a h_e \quad (3.2.3.2a)$$

Since the unloading from  $h_t$  to  $h_r$  is elastic, the depth of the circle of contact beneath the specimen free surface is half of the elastic displacement  $h_e$ :

$$\begin{aligned} h_p &= h_t - \frac{h_e}{2} \\ &= h_t - \frac{h_t - h_r}{2} \\ &= \frac{h_t + h_r}{2} \end{aligned} \quad (3.2.3.2b)$$

The depth  $h_t$  is given directly by the instrument. The depth of the residual impression  $h_r$  can be found by a measurement of load and displacement at a reduced or a partial unload  $P_s$  from a higher load  $P_t$  and forming the ratio of the elastic displacements thus:

$$\begin{aligned} h_e &= h_t - h_r = \left[ \left( \frac{3}{4E^*} \right)^{\frac{2}{3}} \frac{1}{R^{\frac{1}{3}}} \right] P_t^{2/3} \\ h_s - h_r &= \left[ \left( \frac{3}{4E^*} \right)^{\frac{2}{3}} \frac{1}{R^{\frac{1}{3}}} \right] P_s^{2/3} \\ \frac{h_t - h_r}{h_s - h_r} &= \left( \frac{P_t}{P_s} \right)^{\frac{2}{3}} \\ h_r &= \frac{h_s (P_t/P_s)^{2/3} - h_t}{(P_t/P_s)^{2/3} - 1} \end{aligned} \quad (3.2.3.2c)$$

The plastic depth  $h_p$  and also the elastic displacement  $h_e$  can now be calculated from Eq. 3.2.3.2b. From geometry, the radius of the circle of contact at full load (at depth  $h_p$ ) is given by Eq. 3.2.3.1f. The hardness  $H$  is thus computed from Eq. 3.2.3d. The modulus can be calculated using Eq. 3.2.3.2a using a calculated from Eq. 3.2.3.1f at  $P = P_t$ .

### 3.2.4 Berkovich indenter

The Berkovich indenter has a face angle of  $\theta = 65.3^\circ$ , which gives the same projected area-to-depth ratio as the Vickers indenter. It should be noted that the original Berkovich indenter<sup>8</sup> had a slightly different angle, that of  $65.03^\circ$ . This latter angle gives the same *actual* area to depth ratio as a Vickers indenter.



Upon unloading, the contact is elastic and the relationship between the load and the depth of penetration for a cone is given by<sup>9</sup>:

$$P = \frac{2}{\pi} E^* h_e^2 \tan \alpha' \quad (3.2.4c)$$

where  $\alpha'$  is now the combined angle of the indenter and the residual impression. The normal displacement  $h$  of points on the surface beneath the indenter is a function of the radial distance  $r$  from the axis of symmetry and is given by:

$$h = \left( \frac{\pi}{2} - \frac{r}{a} \right) a \cot \alpha' \quad r \leq a \quad (3.2.4d)$$

As shown in Fig. 3.4, as the indenter is unloaded, the tip of the indenter ( $r = 0$ ) moves through a distance  $h_e$  and the edge of the circle of contact with the specimen surface ( $r = a$ ) moves through a distance  $h_a$ . Making use of Eq. 3.2.4d, at load  $P_t$  the displacements  $h_e$  and  $h_a$  are thus:

$$\begin{aligned} h_e &= \frac{\pi}{2} a \cot \alpha' \\ h_a &= \left( \frac{\pi}{2} - 1 \right) a \cot \alpha' \end{aligned} \quad (3.2.4e)$$

and hence:

$$h_a = \left( \frac{\pi - 2}{\pi} \right) h_e \quad (3.2.4f)$$

and also

$$h_t = h_p + h_a \quad (3.2.4g)$$

We are now in a position to examine the single- and multiple-point methods of analysis for the Berkovich indenter.

### 3.2.4.1 Multiple-point unload method

The multiple-point unload method uses the slope of the tangent to the initial unloading to determine the quantities of interest. From Eq. 3.2.4c, the slope of the elastic unloading is given by:

$$\frac{dP}{dh} = 2 \frac{2E^* \tan \alpha'}{\pi} h_e \quad (3.2.4.1a)$$

Substituting back into Eq. 3.2.4c, we have:

$$P = \frac{1}{2} \frac{dP}{dh} h_e \quad (3.2.4.1b)$$

Substituting Eq 3.2.4.1b into 3.2.4f, we have:

$$h_a = \left[ \frac{2(\pi-2)}{\pi} \right] \frac{P_t}{dP/dh} \quad (3.2.4.1c)$$

from which  $h_p$  can be found from Eq. 3.2.4g and the projected area of contact  $A$  from Eq. 3.2.4a and the combined modulus  $E^*$  from Eq. 3.2.3.1i. The square-bracketed term in Eq. 3.2.4.1c is significant and may be called the “intercept correction” term and here it is equal to 0.72. For a spherical indenter, it evaluates to 0.75 (see Eq. 3.2.3.1e). Oliver and Pharr,<sup>4</sup> however, found that the intercept correction for a Berkovich indenter should be increased to 0.75 to account for the inevitable rounded tip of a real indenter.

So far, we have not accounted for the non-symmetrical pyramidal shape of a real Berkovich indenter. Finite element calculations for indentations formed with flat-ended punches of triangular cross sections<sup>10</sup> yield a correction factor  $\beta$  equal to 1.034 for a Berkovich indenter and this is applied to the unloading stiffness  $dP/dh$ . Elastic modulus is thus found from:

$$E^* = \frac{dP}{dh} \frac{1}{2h_p} \frac{1}{\beta} \sqrt{\frac{\pi}{24.5}} \quad (3.2.4.1d)$$

which is equivalent to Eqs. 3.2.3.1h and 3.2.3.1i. The multiple-point unload method is widely used for tests performed with Berkovich indenters. It relies on a least squares fit to the initial portion of the unloading curve, which is assumed to be elastic. In practice, the method is reasonably robust, although, along with the methods described for the spherical analysis, the results are greatly influenced by instrumental errors that must be accounted for and methods for doing this are presented later in this document.

### 3.2.4.2 Single-point unload method

The single-point unload method uses a single unload point rather than a determination of the slope of a fitted line to several unload points. Now, from Eq. 3.2.4g, we have:

$$\begin{aligned} h_t &= h_p + h_a \\ &= h_p + \frac{\pi-2}{\pi} h_e \end{aligned} \quad (3.2.4.2a)$$

Since  $h_e = h_t - h_r$ , then

$$h_t = h_p + \frac{\pi-2}{\pi} (h_t - h_r) \quad (3.2.4.2b)$$

leading to:

$$h_p = h_t - \left[ \frac{\pi - 2}{\pi} \right] h_t + \left[ \frac{\pi - 2}{\pi} \right] h_r \quad (3.2.4.2c)$$

Now, in a similar manner to the case of a spherical indenter, the depth  $h_r$  is found by forming the ratio of elastic displacements for a partial unload  $P_s$ :

$$h_r = \frac{h_s (P_t/P_s)^{1/2} - h_t}{(P_t/P_s)^{1/2} - 1} \quad (3.2.4.2d)$$

Equation 3.2.4.2d, substituted into Eq. 3.2.4.2c allows  $h_p$  to be determined and hence  $A$  from Eq. 3.2.4a and thus hardness  $H$ . Elastic modulus can be computed using Eq. 3.2.3.1i.

It is convenient to retain the square-bracketed terms in Eq. 3.2.4.2c as separate entities since this, multiplied by a factor of 2, represents the intercept correction factor in Eq. 3.2.4.1c. The significance of this is that Oliver and Pharr<sup>4</sup> found that to obtain the best correspondence with independently measured mechanical properties, the intercept correction term in Eq. 3.2.4.1c for a Berkovich indenter should be in fact increased from 0.72 to 0.75 — the same as that for a spherical indenter (see Eq. 3.2.3.1e). By retaining the form of Eq. 3.2.4.2c, a similar adjustment may be made within the single-point unload method if desired.

### 3.2.5 Knoop indenter

The analysis methods described above for the Berkovich indenter rely on the conversion of the actual indenter geometry to an equivalent cone. That is, the elastic theory applied to the unloading is for a conical indenter of semi-angle  $\alpha$ . We have described the various adjustments that may be made to account for the real indenter geometry. Similar analyses may be applied to the case of Vickers, cube corner, and other indenters (see Table 1.1). However, an interesting issue arises for the case of a Knoop indenter. A Knoop indenter is a four-sided pyramidal indenter with unequal angles such as shown in Fig. 2.4 and where the projected area of contact is given by:

$$A = \frac{d^2}{2} [\cot \theta_1 \tan \theta_2] \quad (3.2.5a)$$

where  $\theta_1 = 86.25^\circ$  and  $\theta_2 = 65^\circ$  and where  $d$  is the length of the long diagonal. Expressed in terms of the plastic depth  $h_p$ , Eq. 3.2.5a becomes:

$$A = 2h_p^2 \tan \theta_1 \tan \theta_2 \quad (3.2.5b)$$

Analysis of experimental data obtained with a Knoop indenter on fused silica, using the methods above for an equivalent cone angle of  $77.64^\circ$  show that both the hardness and the modulus are over estimated by about 10% and 50%,

respectively. The reason is that there is substantial elastic recovery of the short diagonal of the residual impression compared with negligible elastic recovery of the long axis direction. The long axis of the impression made by a Knoop indenter is approximately seven times larger than the short axis at full load. Upon removal of load, elastic strains stored within the material are relaxed as the specimen material attempts to regain its original shape. Now, since the long axis of the impression made by a Knoop indenter is much greater than the short axis, the restoring forces perpendicular to the long axis (i.e., those resulting from the relaxation of elastic strains on the short axis) have a much longer “moment arm” than those perpendicular to the short axis. In other words, the sides “collapse” inwards as the indenter is withdrawn. (A similar effect is demonstrated when breaking an egg by pressing along the long axis as compared with along the short axis).<sup>11</sup> This means that observed elastic recovery in the short axis direction can be substantial compared to that in the long axis direction, especially for materials with a low value of  $E/Y$  (or  $E/H$ ), where elastic recovery is more pronounced (see Fig. 3.5). Other indenters (such as Vickers or Berkovich), while not axial-symmetric, have equal lengths of axes and there is an equal balance of restoring forces on the specimen material during unloading.

Marshall, Noma, and Evans<sup>12</sup> likened the elastic recovery for a Knoop indenter to that of a cone with major and minor axes.

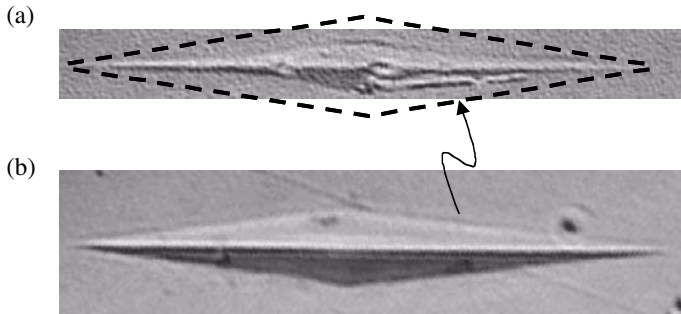


**Fig. 3.5.** Optical micrographs of residual impression in specimen surface for Knoop indenter at 500 mN load for (a) fused silica and (b) hardened steel. The outline of the impression in (b) is overlaid on the photograph for the fused silica specimen in (a). The measured lengths of the long diagonals are (a) 33  $\mu\text{m}$  and (b) 31  $\mu\text{m}$  and these provide a scale for the figure. The degree of elastic recovery in the fused silica sample ( $E/H \approx 10$ ) is much greater than that for the hardened steel sample ( $E/H \approx 28$ ) (Courtesy CSIRO and after reference 13).

They applied elasticity theory to arrive at an expression for the recovered indentation size in terms of the geometry of the indenter and the ratio  $H/E$ :

$$\frac{b'}{d'} = \frac{b}{d} - \alpha \frac{H}{E} \quad (3.2.5c)$$

In Eq. 3.2.5c,  $\alpha$  is a geometry factor found from experiments on a wide range of materials to be equal to 0.45. The ratio of the dimension of the short diagonal  $b$  to the long diagonal  $d$  at full load is given by the indenter geometry and for a Knoop indenter,  $b/a = 1/7.3$ . The primed values of  $d$  and  $b$  are the lengths of the long and short diagonals after removal of load. Since there is observed to be negligible recovery along the long diagonal, we can say that  $d' \approx d$ . When  $H$  is small and  $E$  is large (e.g., metals), then  $b' \approx b$  indicating negligible elastic recovery along the short diagonal. When  $H$  is large and  $E$  is small (e.g., glasses and ceramics), there we would expect  $b' \ll b$ .

The elastic analyses described in previous sections rely on Sneddon's solution for a conical indenter in which the depth as a function of load is given by Eq. 3.2.4c. For materials with a low value of  $E/Y$  (e.g., metals), we would expect these analysis methods to give acceptable results even for a Knoop indenter, since the amount of elastic recovery is small. For glass and ceramics, the experimental readings of load and displacement for a Knoop indenter will be affected by the elastic recovery along the short axis dimension and this will not be accommodated by Eq. 3.2.4c. Upon loading, to reach a particular depth of penetration, we would need to apply a higher value of load compared with an equivalent conical indenter to overcome the elastic recovery forces arising from the elastic recovery along the short axis direction. Thus, in an experiment involving a Knoop indenter on say, glass, the depth of penetration at any particular load would be less than for an equivalent conical indenter.

Figure 3.6 shows the region of interest about the short axis of a Knoop indenter. For a load/unload cycle with a Knoop indenter, elastic recovery forces act in addition to those experienced by an equivalent cone owing to the required compression, and subsequent expansion, of the "elastic recovery volume" ABC in Fig. 3.6. This volume goes to zero as the dimension  $b'$  approaches  $b$ . It is possible to account for this in the analysis methods given here by increasing the effective angle  $\theta_2$  so that compression and relaxation of the elastic recovery volume is accommodated. How much should the angle  $\theta_2$  be adjusted? Evidently, the adjustment should be a function of  $E/H$  and incorporate the results of Eq. 3.2.5c. Rearranging Eq. 3.2.5c and assuming that there is no recovery along the long axis such that  $d' = d$ , then:

$$\frac{b'}{b} = 1 - \alpha \frac{d}{b} \frac{H}{E} \quad (3.2.5d)$$

where  $d/b = 7.11$  and  $\alpha = 0.45$ .<sup>12</sup>

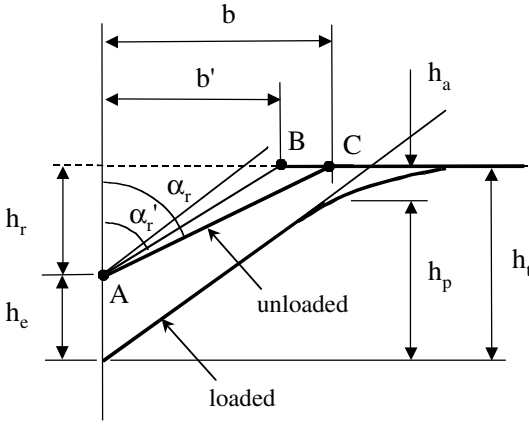


**Fig. 3.6.** Schematic of the geometry of contact near the recovered impression made by Knoop indenter. When there is elastic recovery along the short axis of the diagonal, the dimension of the short diagonal changes from  $b$  to  $b'$  and the corresponding change in the angle of the residual impression is from  $\alpha_r$  to  $\alpha_r'$  (Courtesy CSIRO and after reference 13).

With reference to Fig. 3.6, it can be seen that the angle of the residual impression changes from  $\alpha_r$  to  $\alpha_r'$  according to:

$$\frac{\tan \alpha_r'}{\tan \alpha_r} = \frac{b'}{b} \quad (3.2.5e)$$

Let us assume that the same fractional change of angle may be attributed to the proposed increase in angle  $\theta_2$  of the indenter. The corrected angle  $\theta_2'$  for the Knoop indenter that accounts for elastic recovery forces is thus:

$$\tan \theta_2' = \left( \frac{b'}{b} \tan \theta_2 \right) \quad (3.2.5f)$$

where  $b/b'$  is given by Eq. 3.2.5d. For the purposes of analyses, we can immediately see that an initial guess at the ratio of  $E/H$  is required for insertion into Eq. 3.2.5d.  $E$  and  $H$  can then be calculated by the methods described earlier and the ratio  $E/H$  adjusted for convergence.

### 3.2.6 Hardness as a function of depth

For tests with a Berkovich indenter, the hardness  $H$  and the modulus  $E^*$  are determined from the slope  $dP/dh$  and the plastic depth  $h_p$  at maximum load. Once the slope at maximum load is known, then, assuming that the modulus  $E^*$  is con-

stant (i.e., independent of depth), the hardness may be computed at any point along the loading curve. At any points P and  $h_t$  along the loading curve:

$$h_p = h_t - h_s$$

$$h_s = P\varepsilon \frac{dh}{dP} \quad (3.2.6a)$$

$$h_p = h_t - P\varepsilon \frac{dh}{dP}$$

The constant  $\varepsilon$  is the intercept correction term and equals 1 for a hypothetical cylindrical punch unloading, and 0.75 for a paraboloid of revolution. Now,  $h_t$  and  $P_t$  are both provided (after certain corrections) by the indentation testing machine. The question is: "What is the value of  $dP/dh$  at any point P?" The only value of  $dP/dh$  available thus far is that measured at maximum load  $P_t$ . However, if  $E^*$  does not depend on indentation depth, then Eq. 3.2.6a applies for *any* load P. Thus:

$$\frac{dP}{dh} \frac{1}{2h_p} \sqrt{\frac{\pi}{24.5}} = \frac{dP}{dh_t} \frac{1}{2h_{P_t}} \sqrt{\frac{\pi}{24.5}} \quad (3.2.6b)$$

$$\frac{dh}{dP} = \frac{dh}{dP_t} \frac{h_{P_t}}{h_p}$$

Equation 3.2.6b shows that  $dh/dP$  at load P is a function of  $h_p$  at that point. Note also that we have ignored the differences in area function correction that would apply at the different loads P and  $P_t$ . Inserting Eq. 3.2.5b into Eq. 3.2.6a, we obtain:

$$h_p = h_t - P\varepsilon \frac{dh}{dP_t} \frac{h_{P_t}}{h_p} \quad (3.2.6c)$$

which is a quadratic equation in  $h_p$ . The hardness H at load P can then be found from:

$$H = \frac{P}{24.5h_p^2} \quad (3.2.6d)$$

If the variation of hardness H with depth is expected to be small, then a rough estimate of the quantity  $dP/dh$  at load P may be found from:

$$\frac{dP}{dh} \frac{\pi}{2} \frac{\sqrt{H}}{\sqrt{P}} = \frac{dP}{dh_t} \frac{\pi}{2} \frac{\sqrt{H}}{\sqrt{P_t}} \quad (3.2.6e)$$

$$\frac{dP}{dh} = \frac{dP}{dh_t} \frac{\sqrt{P}}{\sqrt{P_t}}$$

Equation 3.2.6e has the advantage of not requiring a solution to a quadratic equation but only applies when the  $H$  is not a strong function of depth of penetration and that, along with Eq. 3.2.6c,  $E^*$  is a constant with depth.

A value of hardness may be more accurately determined at intermediate depths by a partial unload during the loading sequence. In this way, direct measurements of  $dP/dh$  are available from which  $h_p$ , and hence  $H$ , is obtained from Eqs. 3.2.6a and 3.2.6d.

### 3.2.7 Energy methods

Another increasingly popular method of determining hardness from nanoindentation measurements is a consideration of the energies involved in the loading and unloading processes. In general, the indentation process consists of an elastic-plastic loading followed by an elastic unloading in which the load  $P$  and depth of penetration  $h$  are related by the general expression:

$$P = Ah^n \quad (3.2.7a)$$

where  $A = A_p$  for the elastic-plastic loading and  $A = A_e$  for the elastic unloading and  $n$  depends upon the shape of the indenter (e.g.,  $n = 1$  for a cylindrical punch,  $n = 2$  for a conical indenter). In Chapter 5, we show that  $A_p$ , for a conical indenter of half-angle  $\alpha$ , can be expressed by:

$$A_p = E^* \left[ \frac{1}{\sqrt{\pi \tan^2 \alpha}} \sqrt{\frac{E^*}{H}} + \left[ \frac{2(\pi - 2)}{\pi} \right] \sqrt{\frac{\pi}{4}} \sqrt{\frac{H}{E^*}} \right]^{-2} \quad (3.2.7b)$$

and from Eq. 1.2m, we have:

$$A_e = \frac{2}{\pi} E^* \tan \alpha \quad (3.2.7c)$$

Application of the load to the indenter and the resulting displacement represents work done on the system and is manifested as both plastic and elastic strains within the specimen. The contribution to the elastic recoverable energy to the total energy depends only weakly on the geometry of the indenter and is characteristic of the hardness of the material<sup>14</sup> (see also Section 8.2.1.2.7).

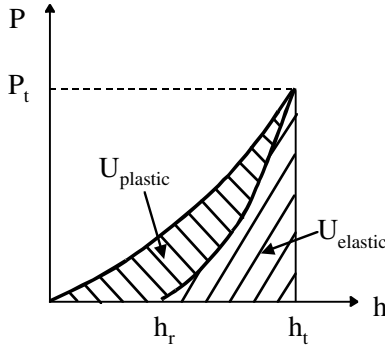


**Fig. 3.7.** The net area  $U_{\text{plastic}}$  enclosed by the load-displacement curve represents the energy lost due to plastic deformation and elastic strains for residual stresses in the specimen material.

During unloading, work is done by the system as the material elastically recovers. As shown in Fig. 3.7, the net area enclosed by the load-displacement response represents the energy lost in plastic deformation (and stored elastic energy from residual stresses) within the specimen material.

At the condition of maximum load,  $P = P_t$ , we have:

$$P = A_p h_t^2 = A_e (h_t - h_r)^2 \tag{3.2.7d}$$

The net area enclosed by the loading and unloading curves can be calculated by integrating  $P$  with respect to  $h$ :

$$U = \int_0^{h_t} A_p h^2 dh - \int_{h_r}^{h_t} A_e (h - h_r)^2 dh \tag{3.2.7e}$$

The volume of the indenter measured below the contact circle is given by:

$$V = \frac{1}{3} 2a^3 \cot \alpha \tag{3.2.7f}$$

where  $a$  is the radius of the circle of contact. The energy required to create a unit volume of indentation is called the “work of indentation” and is given by:

$$\Gamma = \frac{U}{V} \tag{3.2.7g}$$

The work of indentation is physically equivalent to the hardness  $H$  for an ideal plastic material (small values of  $H/E$ ). The work of indentation for a completely elastic contact is zero.<sup>15</sup>

Substituting the expressions for  $A_p$  and  $A_c$  into Eq. 3.2.7e and integrating, and making use of Eq. 3.2.7a, yields:

$$U = \left( \frac{1}{3} \sqrt{\frac{1}{\pi \tan^2 \alpha}} \right) \frac{1}{\sqrt{H}} P^{3/2} \quad (3.2.7h)$$

The slope of the line of best fit of experimentally derived values of  $U$  plotted against  $P^{3/2}$  provide a measure of the hardness  $H$ .

### 3.2.8 Dynamic methods

Measurement of elastic modulus and hardness involves the measurement of the contact stiffness,  $dP/dh$ , at the loading point (see Eq. 3.2.3.1i). In a typical indentation test involving an oscillatory motion, a small AC modulated force  $p$  is applied with a frequency  $\omega$  and amplitude  $p_o$ <sup>16</sup>:

$$p = p_o e^{i\omega t} \quad (3.2.8a)$$

The resulting displacement  $h$  will have the same frequency of oscillation but may have a phase difference  $\phi$  leading to:

$$h = h_o e^{i(\omega t + \phi)} \quad (3.2.8b)$$

The resulting displacements will be affected by the dynamics of the instrument as well as the indenter-sample interaction. The magnitude of the stiffness of the contact is found by summing the stiffness and damping terms shown in Fig. 3.8.

$$\left| \frac{p_o}{h_o} \right| = \sqrt{(S + K_s - m\omega^2)^2 + \omega^2 D^2} \quad (3.2.8c)$$

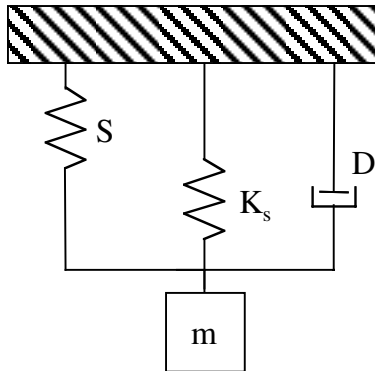


**Fig. 3.8** Dynamic mechanical model of a nanoindentation instrument.

The phase difference  $\phi$  between the load and depth terms is given by:

$$\tan \phi = \frac{\omega D}{S + K_s - m\omega^2} \quad (3.2.8d)$$

In Eqs. 3.2.8c and 3.2.8d,  $K_s$  is the stiffness of the indenter shaft support springs,  $p_o$  is the magnitude of the oscillatory load,  $D$  is a damping coefficient,  $h_o$  and  $p_o$  are the magnitudes of the displacement and force oscillations,  $\omega$  is the frequency of the oscillation,  $m$  is the mass of the components, and  $S$  is the contact stiffness  $dP/dh$ . The measured stiffness  $S$  together with Eq. 3.2.3.1i can be used to determine the area  $A$  of the contact continuously during the loading cycle of an indentation test:

$$A = \left[ \frac{dP}{dh} \right]^2 \frac{\pi}{4} \frac{1}{E^*} \quad (3.2.8e)$$

The area given by Eq. 3.2.8e thus provides a hardness value by Eq. 3.2.3d. Note that this method presumes that the combined elastic modulus  $E^*$  of the specimen and indenter is already known. The geometry correction factor  $\beta$  may also need to be included (see Eq. 3.2.4.1d). Further developments of this mode of analysis are given in Chapter 7.

Using a similar approach, Lorenz, Fränzel, Einax, Grau, and Berg<sup>17</sup> have demonstrated a method of determining the modulus of elastic materials (low values of  $E/H$ ) using a nanoindentation technique whereby the contact force is modulated by an oscillatory motion of the specimen. The contact stiffness is obtained from the resonant response of the system.

### 3.2.9 Other methods of analysis

The analysis methods given in the previous sections are not the only means of determining material properties from indentation test data, but are presented as being the most common, and all utilize the elastic unloading response as the basis of the measurement. Joslin and Oliver<sup>18</sup> proposed that a new parameter that characterizes the resistance to plastic penetration,  $H/E^2$ , could be obtained from measurements of the contact stiffness ( $dP/dh$ ). The method has the advantage of not requiring the precise shape of the indenter to be determined and is less affected by surface roughness.

Hainsworth, Chandler, and Page,<sup>19</sup> showed that the loading curve of a specimen could be described using a linear relationship between the load  $P$  and the square of the displacement:

$$P = Ah^2 \quad (3.2.9a)$$

Superimposing the displacements arising from both elastic and plastic deformation, the constant of proportionality  $A$  was found to be:

$$A = E \left( \phi_m \sqrt{\frac{E}{H}} + \varphi_m \sqrt{\frac{H}{E}} \right)^{-2} \quad (3.2.9b)$$

where  $\phi_m$  and  $\varphi_m$  are constants that evaluate to 0.194 and 0.930 for a Berkovich indenter, respectively. Equations 3.2.9a and 3.2.9b have been shown to provide a good fit to experimental data for specimens with a wide range of modulus and hardness values. It should be also noted that Eqs. 3.2.9a and 3.2.9b, with a little rearrangement, are consistent with Eq. 2.4c.

It is possible to determine mechanical properties of interest in a “forward” direction rather than the “reverse” direction as shown above. For example, using material property parameters as inputs, the expected load-displacement response can be predicted and compared with that obtained experimentally. Alternately, the expected  $P$  vs  $h^2$  relationship for an ideally sharp indenter may be used to determine  $E$  and  $H$  by fitting this function to the experimental loading curve. Venkatesh, Van Vliet, Giannakopolous, and Suresh<sup>20</sup> computed the load-displacement curves for a wide variety of material properties and varied these by  $\pm 5\%$  to determine the sensitivity of the method to small variations in the inputs. They found that the least sensitive quantity was the plastic to elastic work ratio. In the reverse analysis, using the load-displacement curve as an input to determine mechanical properties, it was found that small variations in the unloading slope  $dP/dh$  and curvature of the loading response had little effect on the final results, but a strong sensitivity was observed for small changes in the elastic to plastic work ratio.

Gerberich, Yu, Kramer, Strojny, Bahr, Lilleodden, and Nelson<sup>21</sup> summarize the various methods of analysis and propose another scheme based upon the elastic and plastic deformations associated with contact using a spherical indenter. In an elastic contact with a spherical indenter, the depth of the circle of contact is exactly half that of the total depth of penetration (see Eq. 3.2.3c). These authors assumed (with justification) that when plastic deformation occurs, the depth of the circle of contact measured from the specimen free surface ( $h_a$ ) decreases in proportion to the elastic displacement  $h_e$  and, at the same time, decreases in proportion to the elastic displacement at large indentation depths according to:

$$h_a = \frac{h_e}{2} \left( \frac{h_{e\max}}{h_{t\max}} \right) \quad (3.2.9c)$$

The terms with the max subscript are evaluated at some large indentation load and Eq. 3.2.9c is then applied to indentations made at smaller loads as desired. For a completely elastic contact,  $h_{e\max} = h_{t\max}$  and Eq. 3.2.9a reverts to the Hertzian contact condition of  $h_a = h_e/2$ . Once  $h_a$  is known, then the plastic depth  $h_p$  and hence the area of the contact can be determined from which follows  $E^*$  and  $H$  for the specimen material.

More recently, Page, Pharr, Hay, Oliver, Lucas, Herbert, and Riester<sup>22</sup> have demonstrated that the parameter given by the load divided by the contact stiffness (dP/dh) squared provides material property information from load-displacement curves:

$$\frac{P}{S^2} = \frac{\pi H}{4E^{*2}} \quad (3.2.9d)$$

One major advantage of using this technique is that it does not require a detailed knowledge of the indenter geometry (i.e., the tip shape). An interesting consequence of this is that the technique is not so sensitive to changes in hardness but is sensitive to changes in modulus  $E^*$  while the converse appears to be the case for estimations of properties based upon  $P$  vs  $h^2$  relationships.

Equation 3.2.9d bears a close relationship to an earlier theoretical treatment by Stone,<sup>23</sup> and Yoder, Stone, Hoffman, and Lin<sup>24</sup> who propose a theoretical model which proposes that the parameter:

$$\frac{\sqrt{P}}{S} = \frac{\sqrt{H}}{E^*} + C_f P \quad (3.2.9e)$$

can be used to obtain a modulus and hardness for thin film specimens where  $C_f$  is the compliance of the load frame. These authors concluded that for layered specimens, the conventional methods of analysis are unreliable due to the influence of the substrate, and the values obtained from Eq. 3.2.9e are also somewhat unreliable, but the two techniques, used in conjunction with each other, permit some measure of verification and estimation of the confidence in the values obtained. The appropriateness of Eqs. 3.2.9d and 3.2.9e are related to the theoretical relationships given by Eqs. 3.2.8e and 3.2.3.1i.

## References

1. A.C. Fischer-Cripps, *Introduction to Contact Mechanics*, Springer-Verlag, New York, 2000.
2. G.M. Pharr, W.C. Oliver, and F.R. Brotzen, "On the generality of the relationship among contact stiffness, contact area, and the elastic modulus during indentation," *J. Mater. Res.* 7 3, 1992, pp. 613–617.
3. M.F. Doerner and W.D. Nix, "A method for interpreting the data from depth-sensing indentation instruments," *J. Mater. Res.* 1 4, 1986, pp. 601–609.
4. W.C. Oliver and G.M. Pharr, "An improved technique for determining hardness and elastic modulus using load and displacement sensing indentation experiments," *J. Mater. Res.* 7 4, 1992, pp. 1564–1583.
5. J.S. Field and M.V. Swain, "A simple predictive model for spherical indentation," *J. Mater. Res.* 8 2, 1993, pp. 297–306.

6. H. Hertz, "On the contact of elastic solids," *J. Reine Angew. Math.* 92, 1881, pp. 156–171. Translated and reprinted in English in *Hertz's Miscellaneous Papers*, Macmillan & Co., London, 1896, Ch. 5.
7. G.M. Pharr, W.C. Oliver, and F.R. Brotzen, "On the generality of the relationship among contact stiffness, contact area, and the elastic modulus during indentation," *J. Mater. Res.* 7 3, 1992, pp. 613–617.
8. E.S. Berkovich, "Three-faced diamond pyramid for micro-hardness testing," *Ind. Diamond Rev.* 11 127, 1951, pp. 129–133.
9. I.N. Sneddon, "Boussinesq's problem for a rigid cone," *Proc. Cambridge Philos. Soc.* 44, 1948, pp. 492–507.
10. R.B. King, "Elastic analysis of some punch problems for a layered medium," *Int. J. Solids Structures*, 23 12, 1987, pp. 1657–1664.
11. D.B. Marshall and B.R. Lawn, "Indentation of Brittle Materials," *Microindentation Techniques in Materials Science and Engineering*, ASTM STP 889, P.J. Blau and B.R. Lawn, eds. American Society for Testing and Materials, Philadelphia, 1986, pp. 26–46.
12. D.B. Marshall, T. Noma, and A.G. Evans, "A simple method for determining elastic-modulus-to-hardness ratios using Knoop indentation measurements," *J. Am. Ceram. Soc.* 65, 1980, pp. C175–C176.
13. L. Riester, T.J. Bell, and A.C. Fischer-Cripps, "Analysis of depth-sensing indentation tests with a Knoop indenter," *J. Mater. Res.* 16 6, 2001, pp. 1660–1667.
14. M.Kh. Shorshorov, S.I. Bulychev, and V.O. Alekhin, "Work of plastic and elastic deformation during indenter indentation," *Sov. Phys. Dokl.* 26 8, 1981, pp. 769–771.
15. M. Sakai, "Energy principle of the indentation-induced inelastic surface deformation and hardness of brittle materials," *Acta. Metal. Mater.* 41 6, 1993, pp. 1751–1758.
16. B.N. Lucas, W.C. Oliver, and J.E. Swindeman, "The dynamics of frequency specific, depth sensing indentation testing," *Mat. Res. Soc. Symp. Proc.* 522, 1998, pp. 3–14.
17. D. Lorenz, W. Fränzel, M. Einax, P. Grau, and G. Berg, "Determination of the elastic properties of glasses and polymers exploiting the resonant characteristic of depth-sensing indentation tests," *J. Mater. Res.* 16 6, 2001, pp. 1776–1783.
18. D.L. Joslin and W.C. Oliver, "A new method for analyzing data from continuous depth-sensing microindentation tests," *J. Mater. Res.* 5 1, 1990, pp. 123–126.
19. S.V. Hainsworth, H.W. Chandler, and T.F. Page, "Analysis of nanoindentation load-displacement loading curves," *J. Mater. Res.* 11 8, 1996, pp. 1987–1995.
20. T.A. Venkatesh, K.J. Van Vliet, A.E. Giannakopoulos, and S. Suresh, "Determination of elasto-plastic properties by instrumented sharp indentation: Guidelines for property extraction," *Scripta Mater.* 42, 2000, pp. 833–839.
21. W.W. Gerberich, W. Yu, D. Kramer, A. Strojny, D. Bahr, E. Lilleodden, and J. Nelson, "Elastic loading and elastoplastic unloading from nanometer level indentations for modulus determinations," *J. Mater. Res.* 13 2, 1998, pp. 421–439.
22. T.F. Page, G.M. Pharr, J.C. Hay, W.C. Oliver, B.N. Lucas, E. Herbert, and L. Riester, "Nanoindentation characterization of coated systems: P:S2 – a new approach using the continuous stiffness technique," *Mat. Res. Symp. Proc.* 522, 1998, pp. 53–64.

23. D.S. Stone, "Elastic rebound between an indenter and a layered specimen: Part I. Model," *J. Mater. Res.* 13 11, 1998, pp. 3207–3213.
24. K.B. Yoder, D.S. Stone, R.A. Hoffman, and J.C. Lin, "Elastic rebound between an indenter and a layered specimen: Part II. Using contact stiffness to help ensure reliability of nanoindentation measurements," *J. Mater. Res.* 13 11, 1998, pp. 3214–3220.

# Chapter 4

## Factors Affecting Nanoindentation Test Data

### 4.1 Introduction

In conventional indentation tests, the area of contact between the indenter and the specimen at maximum load is usually calculated from the diameter or size of the residual impression after the load has been removed. The size of the residual impression is usually considered to be identical to the contact area at full load, although the depth of penetration may of course be significantly reduced by elastic recovery. Direct imaging of residual impressions made in the submicron regime are usually only possible using inconvenient means and, for this reason, it is usual to measure the load and depth of penetration directly during loading and unloading of the indenter. These measurements are then used to determine the projected area of contact for the purpose of calculating hardness and elastic modulus. In practice, various errors are associated with this procedure. The most serious of these errors manifests themselves as offsets to the depth measurements. Others arise from environmental changes during the test and the non-ideal shape of the indenter. In addition to the above, there are a number of materials related issues that also affect the validity of the results. The most serious of these are an indentation size effect and the phenomenon of piling-up and sinking-in. The sensitivity of nanoindentation tests to these phenomena and others is a subject of continuing research.<sup>1</sup> In this chapter, we review some of the most commonly encountered sources of error and methods of accounting for them.

### 4.2 Thermal Drift

There are two types of “drift” behavior that might be observed in nanoindentation testing. The first is creep within the specimen material as a result of plastic flow. Creep may manifest itself most clearly when the load is held constant, and the depth readings increase as the indenter “sinks” into the specimen. Another reason for an observed change in depth with constant load that is virtually indistinguishable from specimen creep is a change in dimensions of the instrument

due to thermal expansion or contraction of the apparatus. This change in depth imposes a “thermal drift” error onto the real depth of penetration readings. If the rate of change of depth reading with time is measured for a constant value of load at some point during an indentation test, then the thermal drift rate can be computed and the depth readings taken throughout the test adjusted accordingly.

To correct for thermal drift, some nanoindentation instruments allow for a “hold” series of data points to be accumulated at either maximum load or at the end of the unloading from maximum load. For the purposes of calculating thermal drift, the hold period data at “unload” should be used, since this is done at a low value of load where creep within the material is less likely to occur, especially for the case of a spherical indenter. When creep properties of the specimen material are of interest, then hold at maximum load is more appropriate. A linear regression to the load-depth response within the hold period can be used to obtain a thermal drift rate. The thermal drift rate is then applied to all the depth readings according to the time at which they were logged during the actual test. A good test of the effectiveness of the correction is that the thermal drift rate, when applied to the thermal drift data, should collapse that data into a single point, or very close thereto.

### 4.3 Initial Penetration Depth

Indentation tests are usually performed by bringing the indenter into contact with the surface of the specimen with a controlled load and then measuring the resulting depth of penetration. The penetration depth is ideally measured from the level of the specimen free surface. However, in practice, the indenter must first make contact with the specimen surface before the depth measurements can be taken. That is, in practice, it is necessary to make actual contact with the specimen surface to establish a datum for the test depth measurements. This initial contact depth is usually made to be as small as possible, and is often set using the smallest obtainable force of the instrument. An initial contact force on the order of 1  $\mu\text{N}$  is usually achievable. However, no matter how small the initial contact force is made, there is a corresponding penetration of the indenter beneath the undisturbed specimen free surface as shown schematically in Fig. 4.1. Thus, all subsequent depth measurements taken from this datum will be in error by this small initial penetration depth. The initial penetration depth,  $h_i$ , has to be added to all depth measurements,  $h$ , to correct for this initial displacement.

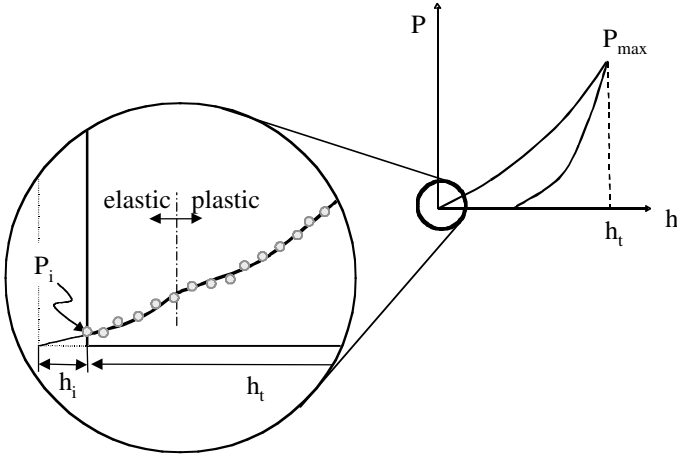


**Fig. 4.1.** Schematic of the effect of initial penetration depth on load-depth data for a depth-sensing indentation test. The initial contact load  $P_i$  results in an initial penetration depth  $h_i$ . Depth readings must be corrected for  $h_i$ .

For contact with a spherical indenter, it may be assumed that the first few loading points result in a purely elastic deformation of the specimen. It is then possible to model these initial data points using the Hertz equations. The Hertz equations predict that the relationship between load and penetration for an elastic response is of the form:

$$h \propto P^n \quad (4.3a)$$

where  $n = 2/3$  for a spherical indenter,  $n = 1$  for a cylindrical flat punch indenter, and  $n = 1/2$  for a conical indenter. At the initial contact load  $P_i$ , there is an initial depth  $h_i$ . During this initial loading, where the response is elastic, the instrument measures  $P$  and  $h_t$  where the total penetration  $h_t' = h_t + h_i$ . Thus,

$$h_t + h_i \propto P^n \quad (4.3b)$$

and therefore

$$\begin{aligned} h_t &\propto P^n - h_i \\ &= k(P^n - P_i^n) \end{aligned} \quad (4.3c)$$

where  $k$  is a constant whose value depends upon the shape of the indenter. For an initial elastic response, say for the first five or so data points in a typical test, we have a series of values for  $h_t$  and  $P$ , and also a value for  $P_i$ . The terms  $n$  and  $k$  are the unknowns. Once values for  $n$  and  $k$  are found, the initial penetration  $h_i$  can be found from:

$$h_i = kP_i^n \quad (4.3d)$$

From Eq. 4.3c, a plot of  $h_t$  vs  $(P^n - P_i^n)$  should be linear with a slope  $k$ . The easiest way to adjust the variables  $n$  and  $k$  for a linear response is to plot the logarithm of both sides to obtain a slope equal to unity. Thus:

$$\log h_t = \log k + m \log(P^n - P_i^n) \quad (4.3e)$$

where  $m = 1$ . A plot of  $\log h_t$  vs  $\log(P^n - P_i^n)$  should have a slope = 1 if  $n$  and  $k$  are chosen correctly. Note that the first data point of the experimental data with  $h_t = 0$  and  $P = P_i$  is not included in the fitting procedure owing to the impossibility of taking the log of zero.

As mentioned previously, the initial contact with the specimen surface is usually made using the smallest possible indenter load of the instrument. Under these conditions, the measuring instrument is typically operating at the limit of its resolution. Thus, the actual load applied to the indenter may be substantially different from the user-specified value. The difference between the actual and specified loads decreases with increasing load as the instrument moves into a more stable operating regime. To minimize the instrumentation errors at the minimum load  $P_i$ , the slope  $m$  of a plot of  $\log h_t$  vs  $\log(P^n - P_i^n)$  is optimized by first adjusting  $P_i$  with  $n$  set to  $n = 2/3$  until  $m$  is as close to unity as possible. Although the value of  $h_i$  has not yet been estimated, this initial fitting reduces the effect of any errors in the recorded value of  $P_i$ .

The adjusted initial contact force  $P_i$  and measured values of  $P$  and  $h_t$  are then plotted according to Eq. 4.3e and the value of  $n$  varied until the slope  $m$  is as close to unity as possible. The resulting intercept provides a value for  $k$ . A value for  $h_i$  can then be determined from Eq. 4.3d. The corrected depth  $h_t'$  is thus:

$$h_t' = h_t + h_i \quad (4.3f)$$

Care must be taken with the choice of the number of initial data points to be used in the analysis. It is assumed that the material response is elastic and thus one must remain within the elastic regime otherwise the fitting will be influenced by data which reflect plastic deformation, in which case Eq. 4.3a does not apply.

For a Berkovich indenter, we may make use of the square root relationship between indenter load and penetration depth (Eq. 2.4c) for a completely plastic contact and simply fit a second-order polynomial to the data. Some care should be taken in the event that the bluntness of the tip leads to an initial elastic response, in which case the first method presented here may be used.

## 4.4 Instrument Compliance

The depth measuring system of a typical indentation instrument registers the depth of penetration of the indenter into the specimen and also any displacements of the instrument arising from reaction forces during loading. These displacements are directly proportional to the load and the general scenario is shown in Fig. 4.2.

The compliance  $C_f$  of the loading instrument is defined as the deflection of the instrument divided by the load. The measured unloading stiffness  $dP/dh$  during an indentation test has contributions from both the responses of the specimen and the instrument. The contribution from the instrument,  $C_f$ , includes the compliance of the loading frame, the indenter shaft, and the specimen mount. The compliance of the indenter material,  $1/S$ , is included in the composite modulus  $E^*$  where the stiffness of the contact  $S$  is given a rearrangement of Eq. 3.2.3.1i. The specimen/indenter combination and the load frame can be considered as springs in series, in which case, the compliance of each can be added directly to give the total compliance  $dh/dP$  measured by the instrument:

$$\frac{dh}{dP} = \frac{1}{S} + C_f \quad (4.4a)$$

For the case of a Berkovich indenter, where  $A = 24.5h_p^2$ , we obtain from Eq. 3.2.3.1i:

$$\frac{dh}{dP} = \sqrt{\frac{\pi}{24.5}} \frac{1}{2E^*} \frac{1}{h_p} + C_f \quad (4.4b)$$

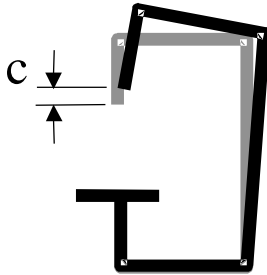


**Fig. 4.2.** Schematic of the effect of load frame deflection arising from reaction forces during an indentation test. The displacement of the load frame  $c$  is measured by the depth measurement system and interpreted as penetration into the specimen material. The magnitude of the deflection is proportional to the load and must be subtracted from the depth readings to obtain the true depth of penetration of the indenter into the sample.

For the case of a spherical indenter, with  $A = 2\pi R_i h_p$ , we have:

$$\frac{dh}{dP} = \left[ \frac{1}{2E^* R_i^{1/2}} \right] \frac{1}{h_p^{1/2}} + C_f \tag{4.4c}$$

The most common method of obtaining a value for  $C_f$ , for the case of a spherical indenter, is to plot  $dh/dP$  vs  $1/h_p$  (or  $1/h_p$  for a Berkovich indenter) obtained for an elastic unloading into an elastic-plastic material for a range of maximum indentation depths. This plot should be linear with a slope proportional to  $1/E^*$  and an intercept which gives the compliance of the instrument  $C_f$  directly. A typical plot is shown in Fig. 4.3.

Experience shows that errors in the data at low values of  $h_p$  significantly affect the slope of the fitted line and thus introduce large errors in the estimate of the compliance. It is usual practice to discard a few of the initial data points in the series to obtain the best possible linear fit to the remaining data.

Since the compliance estimate obtained in this way is dependent upon the area function of the indenter, an iterative procedure is necessary to arrive at a converged value. In routine data analysis of indentation tests, the compliance of the instrument  $C_f$  may be subtracted from experimental values of  $dh/dP$  before calculating  $E^*$ . Alternately, since the displacements arising from instrument compliance are proportional to the load, a correction may be made to the indentation depths  $h_t'$  (already corrected for initial contact) to give a further corrected depth  $h_t''$  according to:

$$h_t'' = h_t' - C_f P \tag{4.4d}$$

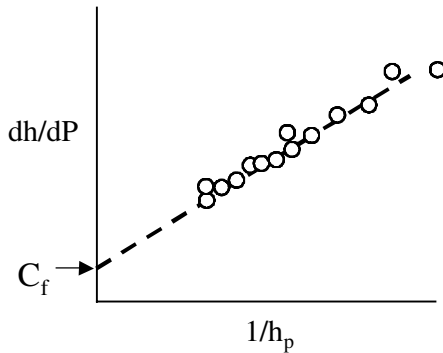


**Fig. 4.3.** Schematic of  $dh/dP$  vs  $1/h_p$  (for Berkovich) or  $1/h_p^{1/2}$  (for spherical indenter) showing the spread of typical test data and the determination of the compliance  $C_f$  from the intercept. Data obtained at low forces, where the uncertainty errors are high, greatly influence the determination of  $C_f$  owing to a leverage effect.

An alternative method of establishing instrument compliance involves the testing of a range of specimen materials with a relatively large radius spherical indenter using repeated loading at a single location. The repeated loading minimizes surface effects such as roughness and other irregularities. A relatively large indenter ( $R \approx 200 \mu\text{m}$ ) is used at reasonably high loads where compliance effects are more readily observed and where indenter tip effects (such as non-ideal geometry) are minimized. Since the displacement of the loading column is proportional to the load, we can express the total elastic displacement between two fixed points, remote from the indentation, under a load  $P$  as:

$$\delta = \left[ \frac{3}{4E^*} \right]^{2/3} P^{2/3} R^{1/3} + C_f P \quad (4.4e)$$

The displacement  $\delta$  and load  $P$  are measured by the indentation instrument. For any two loads  $P_1$  and  $P_2$  resulting in deflections  $\delta_1$  and  $\delta_2$ , we may form the ratios of Eq. 4.4e and obtain:

$$C_f = \frac{\left[ \delta_1 - \left( \frac{P_1}{P_2} \right)^{2/3} \delta_2 \right]}{\left[ P_1 - \left( \frac{P_1}{P_2} \right)^{2/3} P_2 \right]} \quad (4.4f)$$

Note that a knowledge of the modulus or hardness of the specimen material is not required in this procedure.

## 4.5 Indenter Geometry

In nanoindentation testing, the area of contact at penetration depth  $h_p$  is found from geometry. The areas  $A$  given in Table 1.1 assume that the geometry of the indenter is ideal, a circumstance impossible to achieve in practice. Crystal anisotropy of diamond indenters can also affect the expected shape of the indenter. Figure 4.4 shows the profile of a nominally  $1 \mu\text{m}$  spherical indenter along with an AFM surface profile of a nominal  $10 \mu\text{m}$  indenter from which the non-ideal character of some indenters are evident.

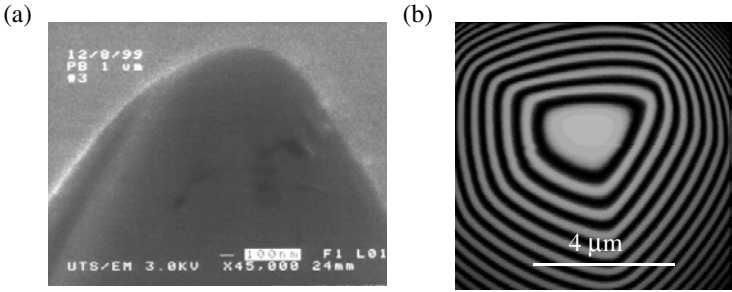


**Fig. 4.4.** (a) SEM micrograph of the tip of a nominally 1  $\mu\text{m}$  radius diamond spheroconical indenter used for depth-sensing indentation tests. (b) AFM image showing surface profile of a nominal 10  $\mu\text{m}$  diamond spherical indenter (Courtesy CSIRO).

To account for non-ideal geometry of the indenter used in any practical test, it is necessary to apply a correction factor to the equations shown in Table 1.1 so as to determine the real area of contact at a depth  $h_p$ . The actual area of contact is given the symbol  $A$  and the ideal area of contact for a given value of  $h_p$  (that computed from Table 1.1) as  $A_i$ . The correction factor to be applied is the ratio  $A/A_i$  and is illustrated in Fig. 4.5.

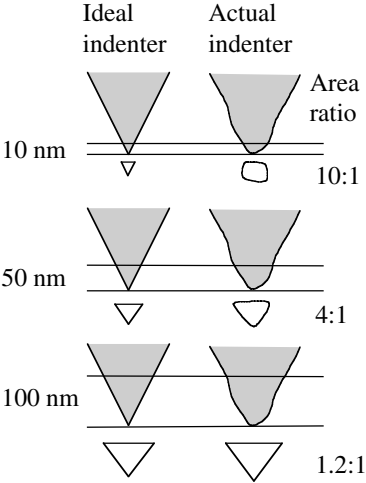


**Fig. 4.5.** Schematic of comparison of areas of contact with an ideal conical indenter and a real indenter with a non-ideal shape. For the same depth of penetration, the actual area of contact is often larger than that computed with the nominal dimensions of the indenter.

The correction factor can be found from independent measurements of indenter geometry using either an AFM or SEM.<sup>2,3</sup> The measured area  $A$  is then plotted against the plastic depth  $h_p$  determined from the measured depths (corrected for compliance and initial contact). Regression analysis of the appropriate order may then provide an analytical function that gives the actual projected area for a given value of  $h_p$ . This function is commonly called the “area function” for the particular indenter being characterized.

The disadvantage of the direct measurement approach is that it is inconvenient. It is now regular practice to use an indirect method for determining area functions where the procedure is to perform a series of indentations at varying maximum loads on standard test specimens whose elastic modulus and Poisson’s ratio are known. If  $E^*$  is known (embodying the elastic properties of both indenter and specimen), then the actual area of contact at each load is found from Eq. 3.2.1c thus:

$$A = \pi \left[ \frac{dP}{dh} \frac{1}{2\beta E^*} \right]^2 \quad (4.5a)$$

Values of  $A$  and  $h_p$  for each test on the reference material provide the data for an area function lookup or calibration table. It is often convenient to express the area function as a ratio of the actual area  $A$  to the ideal area of indentation  $A_i$ . The response for a typical Berkovich indenter is shown in Fig. 4.6. The large value of  $A/A_i$  at low values of depth is a consequence of the inevitable bluntness of the indenter tip.

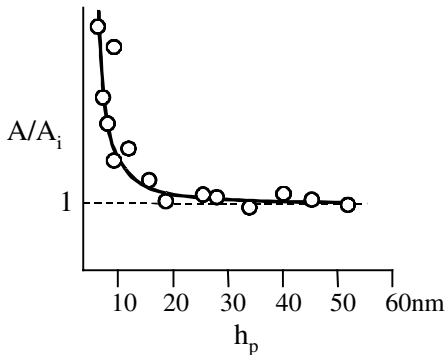


**Fig. 4.6.** Area correction function for a typical Berkovich indenter. The plot shows the ratio  $A/A_i$  as a function of penetration depth  $h_p$ . The high value of  $A/A_i$  is a consequence of the bluntness of the very tip of the indenter.  $A/A_i$  approaches unity as the penetration depth increases.

The corrected hardness is obtained from:

$$H = \frac{P}{A} \left[ \frac{A_i}{A} \right] \quad (4.5b)$$

and the corrected modulus is given by:

$$E^* = \frac{dP}{dh} \frac{\sqrt{\pi}}{2\beta\sqrt{A}} \sqrt{\frac{A_i}{A}} \quad (4.5c)$$

where the geometry correction factor  $\beta$  has been included (see Eq. 3.2.4.1d). It should be noted that for a spherical indenter, the contact area is proportional to  $R$ . Hence, if the nominal indenter radius is say  $5 \mu\text{m}$ , and the area correction at a particular value of  $h_p$  is 0.8, then the effective radius of the indenter at that value of  $h_p$  is  $4 \mu\text{m}$ . A value of  $A/A_i$  greater than one indicates an indenter with a larger radius than its nominal value. For a given load, this results in a higher value of hardness using uncorrected data in the calculations. A value of  $A/A_i$  less than one indicates that the actual area of contact is less than the ideal value, which means that the indenter has a smaller radius than its nominal value. This results in a smaller value of hardness if no correction is applied.

When applying the area correction, a graphical approach can be used (such as that shown in Fig. 4.6) or a look-up table. Some practitioners prefer to express the area of contact as a mathematical function of the depth  $h_p$  in the form:

$$A = C_1 h_p^2 + C_2 h_p + C_3 h_p^{1/2} + C_4 h_p^{1/4} + \dots \quad (4.5d)$$

where the first term represents the ideal area function of the indenter.

In an alternative approach,<sup>4</sup> for a Berkovich indenter, data from an indentation test on a known specimen can be used to predict the indenter shape function rather more conveniently by plotting the square root of the indenter load  $P^{1/2}$  against the plastic depth  $h_p$  to obtain a slope and an intercept term. By Eq. 2.3.3c, the relationship should be linear with the intercept representing the rounding of the tip. Also, by Eq. 3.2.8e, a plot of  $dP/dh$  against  $P^{1/2}$  should also be linear. These two plots lead to functions of the form:

$$\sqrt{P} = \frac{h_p - b}{a} \quad (4.5e)$$

$$\frac{dP}{dh} = a\sqrt{P} + b \quad (4.5f)$$

where  $a$  and  $b$  are the slope and intercept terms for each plot, respectively. Any number of values of the square root of the indenter load can be calculated for the desired range and spacing of plastic depth terms  $h_p$  from Eq. 4.5e and inserted into Eq. 4.5f to give the associated values of  $dP/dh$ . Now, rearranging Eq. 4.5c, we obtain, for a Berkovich indenter:

$$\frac{A}{A_i} = \left( \frac{dP}{dh} \frac{\sqrt{\pi}}{2\beta E^*} \frac{1}{24.5h_p^2} \right)^2 \quad (4.5g)$$

Using the known value of  $E^*$  and values of  $dP/dh$  from Eq. 4.5f, the desired value of  $A/A_i$  for any value of  $h_p$  can be calculated using Eq. 4.5g.

## 4.6 Piling-Up and Sinking-In

In an indentation into an elastic material, the surface of the specimen is typically drawn inwards and downwards underneath the indenter and sinking-in occurs. When the contact involves plastic deformation, the material may either sink in, or pile up around the indenter. In the fully plastic regime (see Chapter 1), the behavior is seen to be dependent on the ratio  $E/Y$  and the strain-hardening properties of the material. The mechanical nature of a typical specimen can be described by a conventional stress-strain relationship that includes a strain-hardening exponent.

$$\begin{aligned} \sigma &= E\varepsilon & \varepsilon &\leq Y/E \\ \sigma &= K\varepsilon^x & \varepsilon &\geq Y/E \end{aligned} \quad (4.6a)$$

where  $K$  is equal to:

$$K = Y[E/Y]^x \quad (4.6b)$$

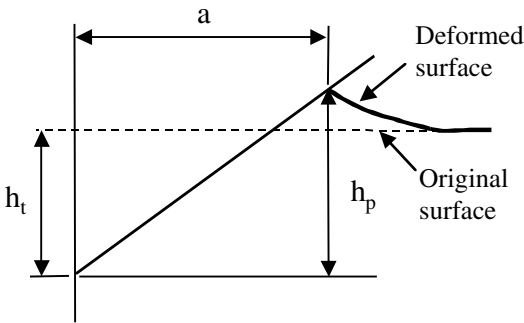


**Fig. 4.7** The pile-up parameter is given by  $h_p/h_t$  and can be less than or greater than 1.

The degree of pile-up or sink-in depends upon the ratio  $E/Y$  of the specimen material and the strain-hardening exponent  $x$ . Piling-up or sinking-in can be quantified by a pile-up parameter given by the ratio of the plastic depth  $h_p$  over the contact depth  $h_t$  as shown schematically in Fig. 4.7.

For non-strain-hardening materials with a large value of  $E/Y$  (e.g., a strain-hardened metal), the plastic zone is observed to have a hemispherical shape meeting the surface well outside the radius of the circle of contact. Piling up in these materials is to be expected, since most of the plastic deformation occurs in the near the indenter. For materials with a low value of  $E/Y$  (e.g., some glasses and ceramics), the plastic zone is typically contained within the boundary of the circle of contact and the elastic deformations that accommodate the volume of the indentation are spread at a greater distance from the indenter. Sinking-in is more likely to occur.

For materials that do exhibit strain-hardening (e.g., a well-annealed metal with  $n > 0$ ), the yield strength effectively increases as its strain increases. Thus, during an indentation test, the material within the plastic zone becomes “harder” as the amount of deformation increases. This means that the outermost material in the plastic zone, which is now “softer,” is more susceptible to plastic deformation as the indentation proceeds — the effect is that the plastic zone is driven deeper into the specimen material. Since the material farther away from the indentation is being deformed, the material near the indenter is observed to sink-in as the indenter proceeds downward into the specimen.<sup>5</sup> It is seen therefore that piling-up is most pronounced for non-strain-hardening materials with a high value of  $E/Y$ . Sinking-in is more pronounced for strain-hardening or non-strain-hardening materials with a low value of  $E/Y$ .

Finite element analysis of contact in which piling-up occurs has demonstrated that the true contact area can be significantly greater than that calculated using the methods of analysis given in previous sections (i.e., from the measured depth of penetration and the assumed elastic unloading response). The effect of piling-up and sinking-in on the contact area is shown schematically in Fig. 4.8. Errors in contact area of up to 60% can be obtained.<sup>5</sup> The existence of piling-up and sinking-in can have a detrimental effect on the determination of the area function of the indenter if the specimen used for determination of the area function behaves differently to that of the eventual sample to be tested.

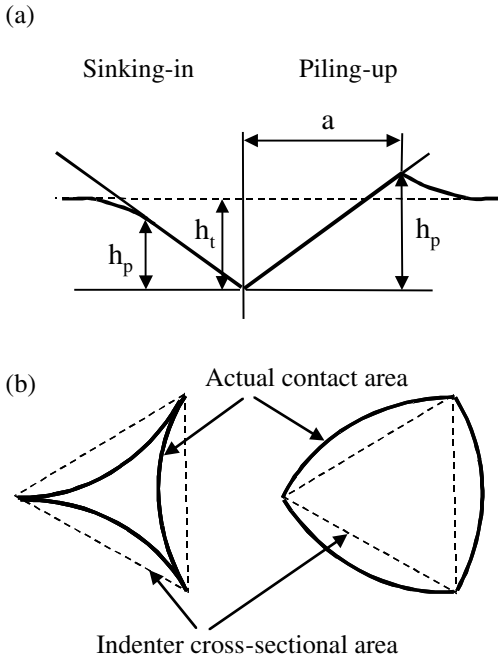


**Fig. 4.8** Effect of piling-up and sinking-in on the actual contact area for penetrations of the same depth  $h_t$ . (a) Cross-sectional view; (b) plan view. For a given penetration depth  $h_t$ , the actual contact area may be substantially different for different materials and to that of the cross-sectional area of the indenter and the expected plastic depth  $h_p$  if there were no piling-up or sinking-in. Hay, Oliver, Bolshakov, and Pharr<sup>6</sup> show that there is a unique relationship between the ratio of the slopes of the loading  $S_L$  and unloading  $S_U$  load-displacement responses with  $h_t/h_p$ .

Randall and Julia-Schmutz<sup>7</sup> compared the results for mechanical properties obtained from load-displacement curves on gold, titanium, and aluminum-coated silicon wafers with observed features of the residual impression obtained with an AFM. They found that for hard-coated specimens, the indenter load appears to be supported by a combination of elastic flexure and internal stresses of the coating resulting from plastic yielding of the substrate. For soft-coated systems, the indenter cuts through the softer surface layer causing it to be squeezed outwards. The effect on the computed mechanical properties was found to be dependent upon the mode of deformation observed using AFM imaging.

McElhane, Vlassak, and Nix<sup>8</sup> describe a procedure for accounting for the effects of piling-up and sinking-in based upon measurements of the contact stiffness and SEM pictures of the residual impressions from large indentations. This information provides a correction factor that quantifies the degree of piling-

up and or sinking-in and this can be applied to contact depths too small to be readily imaged thus providing a procedure for determination of the area correction function for the indenter.

Bolshakov and Pharr<sup>5</sup> found that the results of finite element analysis showed that ratio of the residual depth  $h_r$  to the total depth  $h_t$  is a useful parameter for predicting the constraint factor and the extent of pile-up during indentation in bulk materials for a given strain-hardening exponent. The disadvantage of using  $h_r/h_t$  for determining the extent of piling-up is that it assumes that the mechanical properties of the specimen are the same at the full penetration depth and the depth of the residual impression, that is, in bulk materials with uniform mechanical properties:

$$\frac{S_L}{S_U} = \frac{m_L}{m_U} \left( 1 - \frac{h_r}{h_t} \right) \quad (4.6c)$$

where  $S_L$  and  $S_U$  are the slopes of the loading and unloading curves. The quantity  $m$  is a power law exponent that describes the form of the loading and unloading curves.  $m_L = 2$  for a geometrically similar indenter (e.g., a cone) and finite element results indicate  $m_U$  to be approximately 1.35 for  $h_r/h_t > 0.4$ . Finite element results<sup>6</sup> indicate the dependence of the true contact area on the ratio  $S_L/S_U$  as a result of piling-up or sinking-in if the strain-hardening characteristics of the specimen are known.

## 4.7 Indentation Size Effect

In a homogeneous, isotropic material, one expects to measure only one value of hardness and modulus, yet, for a variety of reasons, experimental results often result in a variation of hardness and/or modulus with indentation depth. Some of the observed effects are indeed real reflections of material behavior and arise due to the presence of very thin oxide films of substantially different mechanical properties than the bulk material, or the presence of residual stresses and strain-hardening arising from the specimen preparation and polishing procedure. The presence of friction between the indenter and specimen has also been shown to lead to an indentation size effect.<sup>9</sup> The most common observed indentation size effect is probably the errors associated with the area function of the indenter, particularly at very small values of penetration depth. However, even if these effects are minimized, it is still generally observed that for some materials, e.g. crystalline solids, that are nominally isotropic, an indentation size effect is still observed.<sup>10,11</sup>

In materials exhibiting an indentation size effect, the conditions for plastic flow may depend not only on the strain, but also on the magnitude of any strain gradient that might be present in the material. Such gradients exist, for example, in the vicinity of a crack tip, where the stress fields are rapidly changing. Sub-

stantial strain gradients also exist in the indentation stress field. In general, the indentation hardness of these materials is observed to increase with decreasing size of indentation owing to the nucleation of dislocations within the plastic zone. Dislocations are created in two ways — those arising for statistical reasons and those arising from the geometry of the indenter. The latter are called geometrically necessary dislocations and take the form of circular dislocation loops as shown in Fig. 4.9.

The presence of dislocations serves to increase the effective yield strength of the material and this in turn means an increase in hardness. Nix and Gao<sup>12</sup> show that the number density of geometrically necessary dislocations created within the plastic zone bounded by the circle of contact for a conical indenter is given by:

$$\rho_g = \frac{3}{2bh} \tan^2 \theta \quad (4.7a)$$

In Eq. 4.7a,  $b$  is the Burgers vector and  $\theta$  is the angle of the cone made with the specimen free surface as shown in Fig. 4.9.

The significance of Eq. 4.7a is that the density of geometrically necessary dislocations  $\rho_g$  increases with decreasing indentation depth  $h$ . This leads to an expression for the hardness  $H$  in terms of the hardness  $H_o$ , which would be obtained without the presence of geometrically necessary dislocations:

$$\frac{H}{H_o} = \sqrt{1 + \frac{h^*}{h}} \quad (4.7b)$$

where  $h^*$  is a length which characterizes the depth dependence of the hardness and which itself depends upon  $H_o$  and also  $\rho_g$ .

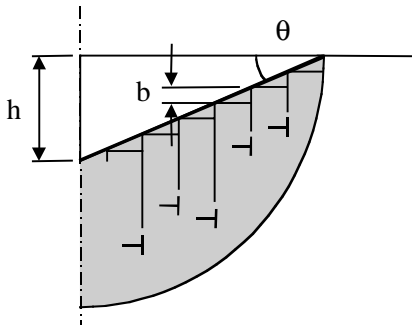


**Fig. 4.9** Geometrically necessary dislocations in the plastic zone created by a conical indenter. The plastic zone is contained within the circle of contact.

When  $H^2$  is plotted against  $h$ , the slope is a measure of  $h^*$  and the intercept gives a value for  $H_0$ . Nix and Gao present data for experiments on cold-worked polycrystalline copper and single crystal silver. Equation 4.7b shows that the indentation size effect is more pronounced in materials with a low value of intrinsic hardness  $H_0$ . For hard materials, we therefore expect little indentation size effect. For soft material, and especially crystalline materials, we do expect a significant indentation size effect.

The presence of geometrically necessary dislocations can be explained in terms of the existence of strain gradients in the vicinity of the indentation. The increase in yield strength due to these dislocations becomes more pronounced as the indentation depth becomes smaller, whereupon the strain *gradients* become larger.

## 4.8 Surface Roughness

Surface roughness is very important in nanoindentation. Since the contact area is measured indirectly from the depth of penetration, the natural roughness of real surfaces causes errors in the determination of the area of contact between the indenter and the specimen. There is a large literature on surface roughness since the field is intimately connected with the nature of friction between surfaces.<sup>13–15</sup> The analytical models proposed usually involve elastic or completely plastic contact and often take into consideration the statistical variation in asperity height in real surfaces. Our interest here is the effect of surface roughness on instrumented hardness measurements.

In general, surface roughness is characterized by the asperity height and the spatial distribution of them across the surface. Figure 4.10 shows an AFM scan of an aluminum film deposited onto a glass surface. Average asperity height in this example is in the order of 4 nm.

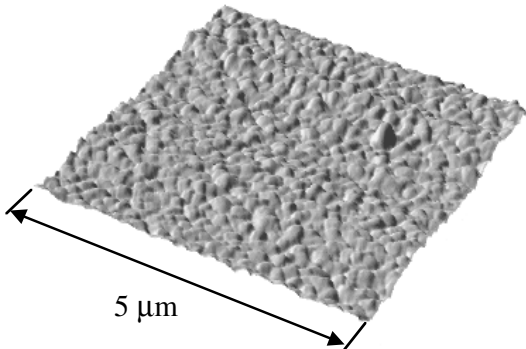


**Fig. 4.10** AFM scan of aluminum film on glass. The average “grain size” is estimated to be 300 nm and surface roughness of 4 nm (Courtesy CSIRO).

Surface roughness can be quantified by a roughness parameter  $\alpha$  where<sup>16</sup>:

$$\alpha = \frac{\sigma_s R}{a_0^2} \quad (4.8a)$$

In Eq. 4.8a,  $\sigma_s$  is, to a first approximation, equal to the maximum asperity height,  $R$  is the indenter radius, and  $a_0$  is the contact radius that would be obtained under the same load  $P$  for smooth surfaces. Note that  $\alpha$  depends indirectly upon the load applied to the indenter. A second parameter  $\mu$  is also used in combination with  $\alpha$  to characterize surface roughness. Johnson<sup>16</sup> finds that the effects of surface roughness on the validity of the elastic contact equations are of significance for  $\alpha > 0.05$ . The overall effect of surface roughness is to reduce the mean contact pressure by increasing the contact radius. Thus, for a given indenter load  $P$ , the depth of penetration is reduced and the computed combined modulus  $E^*$  is also reduced.

Equation 4.8a shows that the surface roughness parameter increases with increasing radius of indenter and increases with decreasing indenter load. Thus, for light loads with spherical indenters, surface roughness can be a significant effect. For sharper indenters, say, a Berkovich indenter with a tip radius of 100 nm, the effects of surface roughness are less severe. Joslin and Oliver<sup>17</sup> propose that a new parameter of materials performance, the ratio of  $H/E^2$ , is a measure of a material's resistance to plastic deformation, the measurement of which is accomplished by measuring the contact stiffness ( $dP/dh$ ) and is less sensitive to the effects of surface roughness.

## 4.9 Tip Rounding

The most commonly used indenter in nanoindentation experiments is the three-sided Berkovich diamond pyramid. In practice, such indenters are not perfectly sharp but have a tip radius in the order of 100 nm (see Fig. 4.11).

Tip rounding becomes important when one wishes to perform indentations on thin films more than about 500 nm thickness and when the maximum depth of penetration is on the order of 50 nm. A real indenter can therefore be modeled as a sphero-conical indenter as shown in Fig. 4.12, where for a cone of semi-angle  $\alpha$ , the depth  $h_s$  at which the spherical tip meets the flat face of the cone is given by:

$$h_s = R(1 - \sin \alpha) \quad (4.9a)$$

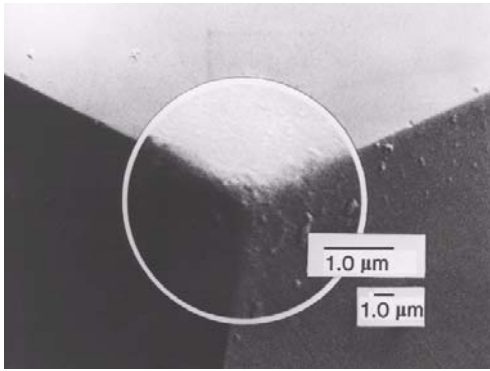


**Fig. 4.11** The tip of a Berkovich indenter. Tip radius is on the order of 100 nm. The correspondence in the edges from the center magnified view and the outer region is a fine example of the geometrical similarity associated with this indenter geometry (Courtesy CSIRO and after reference 18).

From Eq. 4.9a, the loading with a pyramidal indenter (of equivalent cone angle  $70.3^\circ$ ) with a rounded tip of radius  $R$  should be identical with that of a spherical indenter for  $h_t/R < 0.073$  and only approach that of a sharp indenter when  $h_t/R \gg 0.073$ . In the intermediate regime, we have an indentation with a sphero-cone and so the response is expected to be different to both the cases of spherical and ideally sharp conical indenters. In most cases, the effects of tip rounding are accommodated by the indenter area correction function (see Section 4.5).

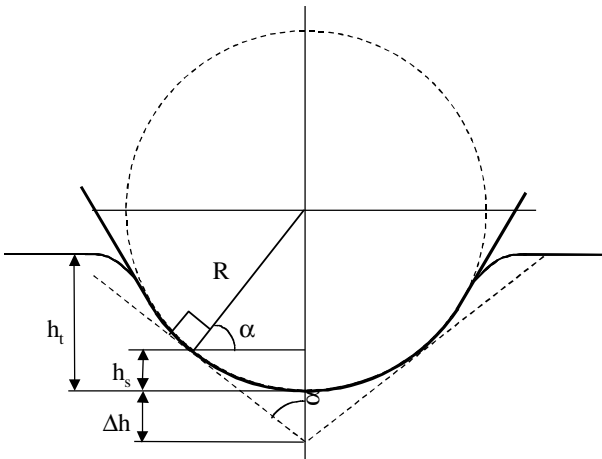


**Fig. 4.12** Geometry of a sphero-conical indenter. The conical sides meet the spherical tip at a depth  $h_s$ . For a cone angle of  $\alpha = 70.3^\circ$ , when  $h_t/R < 0.73$  the loading is by the spherical tip. For  $h_t/R \gg 0.73$ , the loading is dominated by the cone.

## 4.10 Residual Stresses

In the analysis procedures presented in Chapter 3, it was assumed that the specimen material was originally stress-free prior to indentation. In many materials, stresses, tensile or compressive, may be present within the specimen as a result of processing (temperature induced) or surface preparation (cold working from polishing). One way of determining the level of residual stress is to examine the shape of the pile-up occurring at the edge of the contact circle.<sup>19</sup> Deviations in shape give some information about the level and sign of residual stress within the specimen. Other workers have examined the critical load to initiate cone cracks in brittle materials to determine the magnitude and direction of surface residual stresses in brittle materials.<sup>20</sup> Yet another method uses the size of median cracks generated with sharp indenters in brittle solids as a means of determining the level of residual stresses arising from tempering. Chaudhri and Phillips,<sup>21</sup> and Chandrasekar and Chaudhri<sup>22</sup> report that the level of residual stress  $\sigma_R$  can be determined from:

$$\sigma_R = \frac{\chi(P^* - P)}{1.16c^2} \quad (4.10a)$$

where  $P^*$  and  $P$  are the loads that produce cracks of the same radius  $c$  in tempered glass with a residual stress and annealed glass, respectively, and, for a Vickers indenter, where:

$$\chi = \frac{1}{\pi^{3/2} \tan 68} \quad (4.10b)$$

Deviations in shape of the load-displacement response from the ideal shape could also be used an indication of residual stresses but experiments show that the effect is too small to be measured accurately.<sup>23,24</sup> More recently, Taljat and Pharr,<sup>25</sup> who compared the features of experimentally derived load-displacement responses obtained with a spherical indenter to those obtained by finite element calculation within which residual stresses could be incorporated to various degrees in a controlled manner. In this method, it is recognized that for an elastic contact, any residual stress in the specimen serves to alter the stress distribution from the Hertzian case and thus causes a change in the indentation strain ( $a/R$ ) at which yield might first occur. In Chapter 2, it was found that yield first occurs in the Hertzian stress field when the mean contact pressure is approximately equal to 1.1 times the material yield stress. If we then add a residual biaxial stress into this condition, we obtain:

$$p_m = 1.1(Y - \sigma_R) \quad (4.10c)$$

which, when combined with the Hertz equation, Eq. 1.2j, yields:

$$\sigma_R = Y - \left( \frac{4E^*}{3.3\pi} \right) \frac{a}{R} \quad (4.10d)$$

which allows  $\sigma_R$  to be determined if  $Y$  and  $E^*$  are known. Comparison with finite element results over a wide range of  $E$ ,  $Y$ , and residual stresses show that the parameter  $h_r/h_t$  has a unique correlation with residual stress for a particular value of the quantity  $E/Y \cdot 2h_t/a_t$ , where  $a_t$  is the radius of the indenter measured in line with the original specimen free surface.

## 4.11 Specimen Preparation

It is evident from Section 4.8 that surface roughness is an important issue for nanoindentation tests. In order to improve the quality of the specimen surface, it is common practice to polish the specimen. Specimen polishing is a specialized activity and requires considerable care and experience for an acceptable result.

Polishing is usually done either by holding the specimen in contact with a rotating polishing wheel upon which is placed a mat that has been impregnated with a polishing compound — usually a suspension of fine particles in a lubricant. Surfaces are usually polished with a compound containing a progressive decrease in grit size with thorough washing in between to minimize contamination of the polishing mat. A grit size of around 1  $\mu\text{m}$  usually results in what appears to be a very good mirror finish.

One important by-product of the polishing procedure, especially for metals, is the modification of the surface of the specimen due to strain-hardening or cold-working. The polishing procedure involves a substantial amount of deformation of the surface of the specimen material, and it is common to encounter an unwanted indentation size effect resulting from the polishing procedure. Langitan and Lawn<sup>26</sup> find that the resulting flaw size from polishing brittle materials is approximately half the nominal grit size. Allowing for the extended size of the plastic zone in ductile materials, it is reasonable to assume therefore that the polishing procedure affects the surface of the specimen to a depth of about the same size as the nominal grit size. For metal specimens that are likely to strain-harden, one could therefore expect to find a change in mechanical properties in the specimen over this depth range.

## References

1. N.M. Jennett and J. Meneve, "Depth sensing indentation of thin hard films: a study of modulus measurement sensitivity to indentation parameters," *Mat. Res. Soc. Symp. Proc.* 522, 1998, pp. 239–244.
2. K. Herrmann K, N.M. Jennett, W. Wegener, J. Meneve, K. Hasche, and R. Seemann, "Progress in determination of the area function of indenters used for nanoindentation," *Thin Solid Films*, 377, 2000, pp. 394–400.
3. S. Enders, P. Grau, and H.M. Hawthorne, "Determination of the real indenter shape for nanoindentation/nanotribology tests by surface metrological and analytical investigations," *Mat. Res. Soc. Symp. Proc.* 649, 2001, pp. Q3.6.1–Q3.6.6.
4. R.N. Bolster, unpublished work.
5. A. Bolshakov and G.M. Pharr, "Influences of pileup on the measurement of mechanical properties by load and depth sensing indentation techniques," *J. Mater. Res.* 13 4, 1998, pp. 1049–1058.
6. J.L. Hay, W.C. Oliver, A. Bolshakov, and G.M. Pharr "Using the ratio of loading slope and elastic stiffness to predict pile-up and constraint factor during indentation," *Mat. Res. Proc. Symp.* 522, 1998, pp. 101–106.
7. N. X. Randall and C. Julia-Schmutz, "Evolution of contact area and pile-up during the nanoindentation of soft coatings on hard substrates." *Mat. Res. Soc. Symp. Proc.* 522, 1998, pp. 21–26.
8. K.W. McElhane, J.J. Vlassak, and W.D. Nix, "Determination of indenter tip geometry and indentation contact area for depth-sensing indentation experiments," *J. Mater. Res.* 13 5, 1998, pp. 1300–1306.
9. H. Li, A. Ghosh, Y.H. Yan, and R.C. Bradt, "The frictional component of the indentation size effect in low load microhardness testing," *J. Mater. Res.* 8 5, 1993, pp. 1028–1032.
10. N. Gane, "The direct measurement of the strength of metals on a sub-micrometre scale," *Proc. R. Soc. Lond.* A317, 1970, pp. 367–391.
11. S.J. Bull, T.F. Page, and E.H. Yoffe, "An explanation of the indentation size effects in ceramics," *Phil. Mag. Lett.* 59 6, 1989, pp. 281–288.
12. W.D. Nix and H. Gao, "Indentation size effects in crystalline materials: a law for strain gradient plasticity," *J. Mech. Phys. Solids*, 46 3, 1998, pp. 411–425.
13. J.F. Archard, "Elastic deformations and the law of friction," *Proc. R. Soc. Lond.* A243, 1957, pp. 190–205.
14. J.A. Greenwood and J.B.P. Williamson, "Contact of nominally flat surfaces," *Proc. R. Soc. Lond.* A295, 1966, pp. 300–319.
15. J.A. Greenwood and J.H. Tripp, "The contact of two nominally rough surfaces," *Proc. Inst. Mech. Eng.* 185, 1971, pp. 625–633.
16. K.L. Johnson, *Contact Mechanics*, Cambridge University Press, Cambridge, 1985.
17. D.L. Joslin and W.C. Oliver, "A new method for analyzing data from continuous depth-sensing microindentation tests," *J. Mater. Res.* 5 1, 1990, pp. 123–126.
18. J.S. Field, "Understanding the penetration resistance of modified surface layers," *Surf. Coat. Tech.* 36, 1988, pp. 817–827.

19. J.H. Underwood, "Residual stress measurement using surface displacements around an indentation," *Experimental Mechanics*, 30, 1973, pp. 373–380.
20. S.G. Roberts, C.W. Lawrence, Y. Bisrat, and P.D. Warren, "Determination of surface residual stresses in brittle materials by Hertzian indentation: Theory and experiment," *J. Am. Ceram. Soc.* 82 7, 1999, pp. 1809–1816.
21. M.M. Chaudhri and M.A. Phillips, "Quasi-static cracking of thermally tempered soda-lime glass with spherical and Vickers indenters," *Phil. Mag.* A62 1, 1990, pp. 1–27.
22. S. Chandrasekar and M.M. Chaudhri, "Indentation cracking in soda-lime glass and Ni-Zn ferrite under Knoop and conical indenters and residual stress measurements," *Phil. Mag.* A67 6, 1993, pp. 1187–1218.
23. T.Y. Tsui, W.C. Oliver, and G.M. Pharr, "Influences of stress on the measurement of mechanical properties using nanoindentation. 1. Experimental studies in an aluminium alloy," *J. Mater. Res.* 11 3, 1996, pp. 752–759.
24. A. Bolshakov, W.C. Oliver, and G.M. Pharr, "Influences of stress on the measurement of mechanical properties using nanoindentation. 2. Finite element simulations," *J. Mater. Res.* 11 3, 1996, pp. 760–768.
25. B. Taljat and G.M. Pharr, "Measurement of residual stresses by load and depth sensing spherical indentation," *Mat. Res. Soc. Symp. Proc.* 594, 2000, pp. 519–524.
26. F.B. Langitan and B.R. Lawn, "Hertzian fracture experiments on abraded glass surfaces as definitive evidence for an energy balance explanation of Auerbach's law," *J. App. Phys.* 40 10, 1969, pp. 4009–4017.

# Chapter 5

## Simulation of Nanoindentation Test Data

### 5.1 Introduction

The methods of analysis described in Chapter 3 can be used to provide a useful computation of simulated load-depth curves, where the mechanical properties of both the specimen and indenter are given as input parameters. A simulated load-depth curve allows comparisons to be made with actual experimental data. For example, such comparisons may yield information about non-linear events such as cracking or phase changes that might occur with an actual specimen during an indentation test. In this chapter, the procedure for generating a simulated load-depth curve is described in detail and a comparison is made with experimental data from materials with a wide range of ratio of modulus to hardness.

### 5.2 Spherical Indenter

Upon the application of load during an indentation test with a spherical indenter, there is generally an initial elastic response followed by elastic plastic deformation. Following Field and Swain,<sup>1</sup> for the purposes of simulation, the transition between the two responses is assumed to occur at a mean contact pressure equal to the hardness  $H$ . That is, we are assuming that there is an abrupt transition from elastic deformation to a fully developed plastic zone and no intermediate region. The data to be calculated are the load and depth for both loading and unloading sequence. At low loads, the specimen response is elastic and the relationship between depth and load is given by Eqs. 3.2.3a and, in terms of the contact radius, 3.2.3.2a. When a critical load  $P_c$  is reached, full plasticity is assumed and  $p_m = H$ . Thus, with  $p_m = P/\pi a^2$ , it can be shown from Eq. 3.2.3.2a that the critical load is given by:

$$P_c = \left( \frac{3}{4E^*} \right)^2 (\pi H)^3 R_i^2 \quad (5.2a)$$

At the critical load  $P_c$ , there is a corresponding radius of circle of contact  $a_c$  which can be expressed in terms of the hardness  $H$ :

$$a_c = \sqrt{\frac{P_c}{\pi H}} \quad (5.2b)$$

Beyond the critical load, we will assume that no further increase in the mean contact pressure occurs with increasing depth ( $H$  is a constant). The contact is now considered “plastic.” In this plastic region, we wish to calculate the depth of penetration beneath the specimen free surface  $h_t$  as a function of indenter load given values of  $E^*$  and  $H$  for the material. The first step is to calculate the radius of the circle of contact from the hardness and the load in terms of the radius of the circle of contact at the critical load:

$$a = a_c \left( \frac{P_t}{P_c} \right)^{\frac{1}{2+n}} \quad (5.2c)$$

where  $n$  is the strain-hardening exponent. For a constant value of hardness, or a perfectly elastic–plastic material,  $n = 0$ . Upon unloading, we can assume that the response is elastic from the depth at full load,  $h_t$ , to the final residual depth  $h_r$  and the elastic displacement is  $h_e$  given by Eq. 3.2.3.2a. From Eq. 3.2.3.2b, we obtain:

$$h_t = h_p + \frac{h_e}{2} \quad (5.2d)$$

and thus:

$$h_t = \frac{1}{2} \left( 2h_p + \frac{3}{4E^*} \frac{P_t}{a} \right) \quad (5.2e)$$

where  $h_p$  and  $a$  are found from the hardness value  $H$  via Eqs. 3.2.3d and 3.2.3.1f to give:

$$h_t = \frac{1}{2} \left( \frac{P}{\pi R_i H} + \frac{3}{4} \frac{\sqrt{P\pi H}}{\beta E^*} \right) \quad (5.2f)$$

Equation 3.2.3.2a provides the loading curve up to a critical load  $P_c$  after which full plasticity is assumed and Eq. 5.2f is then appropriate.

The unloading curve is assumed to describe a fully elastic response from the total depth  $h_t$  to a residual depth  $h_r$  and, hence, the elastic displacement given by Eq. 3.2.3a is to be added to the residual depth  $h_r$  to give the total value of  $h_t$  upon unloading. However, the unloading involves that between the indenter and the residual impression of radius  $R_r$  and hence  $R$  in Eq. 3.2.3a is the combined radius of curvature  $R$  given by Eq. 3.2.3b. Now,  $R_r$  is unknown, but since the

radius of the circle of contact  $a$  at full load and the depth  $h_r$  are known  $R_r$  can be determined from Eq. 3.2.3.1f thus:

$$R_r \approx \frac{a^2}{2h_r} \quad (5.2g)$$

The penetration depth beneath the surface of the residual impression is thus given by Eq. 3.2.3a with  $R$ , the relative curvatures, given by Eq. 3.2.3b. The absolute value of the unloading penetration (from the original specimen free surface) is this value of  $h_e$  added to the depth of the residual impression  $h_r$ .

## 5.3 Berkovich Indenter

For the case of a Berkovich indenter, we can assume a completely plastic response throughout. The loading curve for a Berkovich indenter can be found from the addition of  $h_p$  and  $h_a$  as shown in Fig. 3.4 where, from Eq. 1.2m and Table 1, we have:

$$h_p = \left( \frac{P}{3\sqrt{3}H \tan^2 \theta} \right)^{\frac{1}{2}} \quad (5.3a)$$

The distance  $h_a$  is most easily determined from the intercept of the slope of the unloading curve at  $P_t$  as shown in Fig. 3.4.

$$h_a = \left[ \frac{2(\pi-2)}{\pi} \right] \frac{1}{2E^*} (P_t H \pi)^{1/2} \quad (5.3b)$$

The total depth  $h_t$  is thus:

$$h_t = \sqrt{P} \left[ \left( 3\sqrt{3}H \tan^2 \theta \right)^{-\frac{1}{2}} + \left[ \frac{2(\pi-2)}{\pi} \right] \frac{\sqrt{H\pi}}{2\beta E^*} \right] \quad (5.3c)$$

On unloading, the response is elastic from  $h_t$  to the depth of the partial un-load  $h_s$ . The depth associated with  $P_t$  can be calculated from Eq. 5.3c. All that is required is the corresponding depth  $h_s$ , where we are free to choose a value of  $P_s$ . Rearranging Eq. 3.2.4.2d, we obtain:

$$h_s = \left( \frac{P_s}{P_t} \right)^{1/2} \left[ h_r \left( \left( \frac{P_t}{P_s} \right)^{1/2} - 1 \right) + h_t \right] \quad (5.3d)$$

where  $h_r$  is found from a rearrangement of Eq. 3.2.4.2c.

It should be noted that for a general conical indenter of half-angle  $\alpha$ , Eq. 5.3c can be written:

$$P = E^* \left[ \frac{1}{\sqrt{3}\sqrt{3} \tan^2 \theta} \sqrt{\frac{E^*}{H}} + \left[ \frac{2(\pi - 2)}{\pi} \right] \sqrt{\frac{\pi}{4}} \sqrt{\frac{H}{E^*}} \right]^{-2} h_t^2 \quad (5.3e)$$

which illustrates the  $P \propto h^2$  relationship for elastic–plastic loading more clearly. Equation 1.2m shows a similar  $P \propto h^2$  relationship applicable to the elastic unloading portion of the test cycle.

## 5.4 Other Indenters

The analyses above may be readily applied to indenters of other geometries. Table 1.1 shows the relevant expressions for a range of common indenter geometries. Note that for the case of the Berkovich, Knoop, and cube corner indenters the intercept correction is given as 0.75 rather than 0.72 as found by Oliver and Pharr.<sup>2</sup> For axial-symmetric indenters, the geometry correction factor is 1.0 while for the others, it is that given by King.<sup>3</sup> It is of interest to note that the analyses given above for what are nominally conical indenters (i.e., Berkovich, Knoop, Vickers, cube corner, and cone) assume a condition of full plasticity from the moment of contact with the specimen. For indenters of ideal geometry, this is perfectly reasonable as the stress singularity at the indenter tip would ensure plastic deformation from the moment of contact. In practice, there is inevitable blunting of the indenter tip that would lead to some small initial elastic response.

There is an interesting issue with the use of the elastic equations that requires consideration. For elastic contact with a conical indenter, the mean contact pressure is given by:

$$p_m = \frac{E^*}{2} \cot \alpha \quad (5.4a)$$

which is independent of load. The significance of this is that, in the simulation analyses, it is assumed that the mean contact pressure is limited to the hardness value  $H$ . However, if the combination of  $E$  and the angle  $\alpha$  are such that the mean contact pressure given by Eq. 5.4a falls below the specified hardness value  $H$ , then the contact is entirely elastic. The elastic equations provide a value of mean contact pressure, even with the stress singularity at the indenter tip. The assumption in the simulation modeling is that a fully developed plastic zone occurs when the mean contact pressure becomes equal to the hardness  $H$ , and in the case of the sphere, this happens at a critical load  $P_c$  as given by Eq. 5.2a and the mean contact pressure increases with increasing load. In the case of a cone, the mean contact pressure is independent of load and, if it is less than the specified hardness value  $H$ , the load–depth response must be assumed to be entirely elastic with a zero residual depth for all values of load.

## 5.5 Comparison with Experimental Data

It is of interest to evaluate the applicability of the simulation equations by comparison with experimental data. Figure 5.1 shows the results from experiments on fused silica and hardened steel together with the load-depth curve predicted by the simulation methods described above.

In the simulation calculations, the values of modulus and hardness calculated from the experimental data, along with the maximum load in each experiment, were used as inputs for the simulation calculation. Any differences between the load-depth curves between the experimental and simulation data are thus due to characteristics of the indentation process not accounted for by the simulation equations. For the Berkovich indenter on fused silica (a material with a relatively low value of  $E/Y$ ), Fig. 5.1 shows a very good agreement between experimental and simulated data for the loading part of the response. There is also good agreement for the initial part of the unloading, but after about the first 30% of unload, the two responses begin to diverge until, at zero unload, there is evidently quite a difference between the actual depth of the residual impression and that predicted by the simulation.

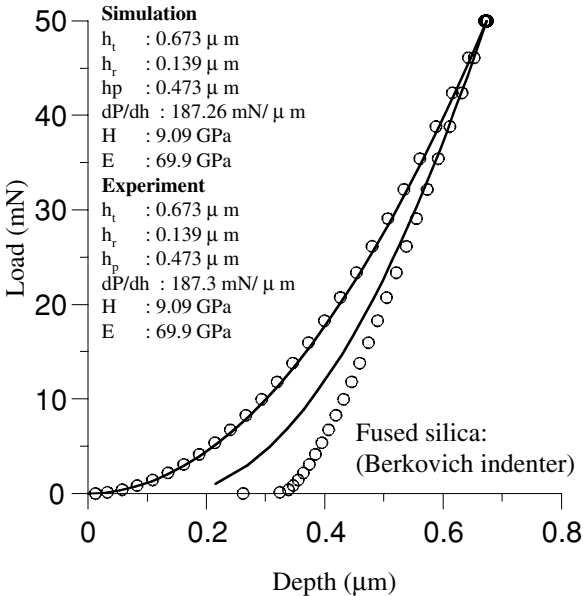


**Fig. 5.1** Load-depth curve for Berkovich indenter on fused silica. Data points indicate experimental results and solid lines represent simulation results. Table (inset) shows values of total penetration depth  $h_t$ , plastic depth  $h_p$ , and the residual depth  $h_r$ , along with the slope of the initial unloading, and the resulting computed value for hardness  $H$  and specimen modulus  $E$  (Courtesy CSIRO and after reference 4).

Since the experimentally determined values of  $E$  and  $H$  were used as the basis of the simulation, it is not surprising that there is good agreement for the values of  $dP/dh$ ,  $h_p$ ,  $h_r$ , and  $h_t$  as shown in the data in Fig. 5.1. However, it is of interest to compare the value of  $h_r$  from the calculation with that indicated by the experimental data. The unloading curve of the experimental data intercepts the depth axis at approximately  $0.325 \mu\text{m}$  as can be seen in Fig. 5.1. The analysis indicates a residual depth  $h_r$  of  $0.139 \mu\text{m}$ , a substantial difference. The reason is that the value of  $h_r$  determined by the analysis (of either experimental or simulated data) assumes a purely elastic unloading response from maximum to zero load. Evidently, this is true for approximately the first 30% of unloading, but not so for the remainder. There is substantially less elastic recovery observed in the experimental data than predicted by the theory and is possibly due to densification within the relatively open structure of the fused silica material. These observations indicate the importance of only treating the first 30% or so of unloading data for the purposes of analysis.

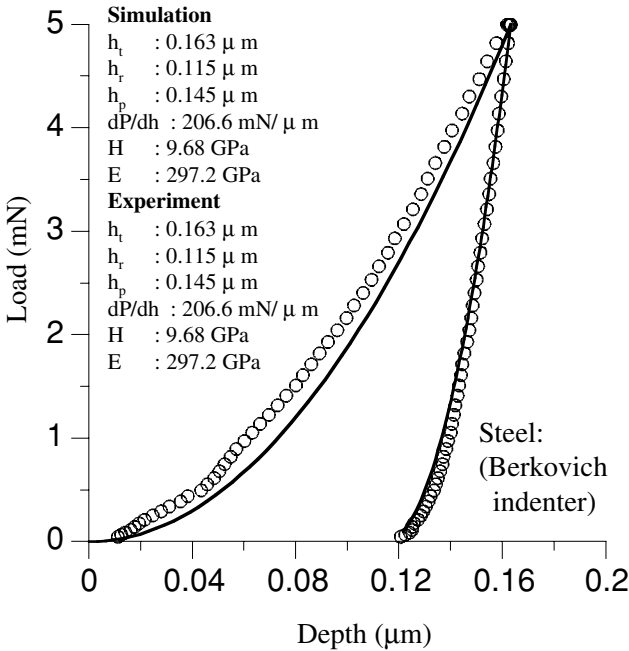


**Fig. 5.2** Load-depth curve for Berkovich indenter on hardened steel. Data points indicate experimental results and solid lines represent simulation results. Table (inset) shows values of total penetration depth  $h_t$ , plastic depth  $h_p$ , and the residual depth  $h_r$  along with the slope of the initial unloading, and the resulting computed value for hardness  $H$  and specimen modulus  $E$  (Courtesy CSIRO and after reference 4).

In a second experiment, a Berkovich indenter was used with a hardened steel specimen (a material with a relatively high value of  $E/Y$ ) and, as before, values of  $E$  and  $H$  determined from an analysis of the experimental data were used as the basis for a simulation calculation. Figure 5.2 shows a comparison between experimental and simulation results.

There is good agreement between the simulation and the experimental results at the point of maximum load and, unlike the case of fused silica, for the full range unloading. The calculated value of residual depth  $h_r$  compares well with that observed experimentally. Compared to fused silica, the amount of elastic recovery for the hardened steel specimen is considerably less and is consistent with the ratio  $E/Y$  for this material. The observations here show that for such a material, a greater range of unloading data may be used for analysis.

Overall, there is reasonably good agreement between the simulation load-depth curves and those obtained experimentally. It appears that the sudden transition from elastic to elastic-plastic behavior assumed in the simulated spherical data does detract from the usefulness of the calculation. The simulation data highlights the need for careful consideration of the choice of range of unloading data for analysis, particularly for materials with a low value of  $E/Y$ .

## References

1. J.S. Field and M.V. Swain, "A simple predictive model for spherical indentation," *J. Mater. Res.* 8 2, 1993, pp. 297–306.
2. W.C. Oliver and G.M. Pharr, "An improved technique for determining hardness and elastic modulus using load and displacement sensing indentation experiments," *J. Mater. Res.* 7 4, 1992, pp. 1564–1583.
3. R.B. King, "Elastic analysis of some punch problems for a layered medium," *Int. J. Solids Structures*, 23 12, 1987, pp. 1657–1664.
4. A.C. Fischer-Cripps, "Simulation of sub-micron indentation tests with spherical and Berkovich indenters," *J. Mater. Res.* 16 7, 2001, pp. 2149–2157.

# Chapter 6

## Scaling Relationships in Nanoindentation

### 6.1 Scaling Relationships in Nanoindentation

An interesting fundamental approach to the analysis of load-depth data is provided by dimensional analysis.<sup>1-9</sup> Consider the indentation of an elastic-plastic specimen with a rigid conical indenter. The mechanical properties of the specimen can be approximated by a uniaxial stress-strain response given by Eqs. 4.6a and 4.6b, here repeated for convenience:

$$\begin{aligned}\sigma &= E\varepsilon & \varepsilon &\leq Y/E \\ \sigma &= K\varepsilon^x & \varepsilon &\geq Y/E\end{aligned}\tag{6.1a}$$

where  $\sigma$  is the applied stress and  $\varepsilon$  is the resulting strain and  $K$  is equal to:

$$K = Y \left[ \frac{E}{Y} \right]^x\tag{6.1b}$$

In Eq. 6.1b,  $x$  is the strain-hardening exponent of the material. For  $x = 0$ , the solid is elastic perfectly-plastic.

During the loading portion of an indentation test, the quantities of interest are the radius of the circle of contact  $a$ , the depth of the contact  $h_p$ , and the load, from which the hardness can be calculated. Consider the two key experimental variables of interest, the indenter load  $P$  and total penetration  $h$ . For a given value of penetration depth, the required load must be a function of  $E$ ,  $\nu$ ,  $Y$ ,  $n$ , and  $h$  and, of course, the angle of the indenter  $\alpha$ . We may ask ourselves, of these variables, which are the governing parameters? That is, which of these parameters set the dimensions of the others? Obviously,  $\nu$  and  $n$  have no dimensions, and neither does  $\alpha$ . Evidently, the dimension of depth is important, and we are faced with a choice of selecting  $E$  or  $Y$ , since one sets the dimensions of the other. Let us therefore select  $E$  and  $h$  as the governing parameters for dimensional analysis. The dimensions of these set the dimensions of the others:

$$\begin{aligned} [Y] &= [E] \\ [P] &= [E][h]^2 \end{aligned} \quad (6.1c)$$

The contact depth  $h_p$ , which eventually provides the value of hardness, is desired to be expressed as a function  $g$  of these parameters. Similarly, the load  $P$  is to be expressed as a function  $f_L$  (for “loading”) of these same parameters:

$$\begin{aligned} h_c &= g(E, \nu, Y, n, h, \alpha) \\ P &= f_L(E, \nu, Y, n, h, \alpha) \end{aligned} \quad (6.1d)$$

The Buckingham Pi theorem in dimensional analysis yields:

$$\Pi_\alpha = \Pi_\alpha(\Pi_1, \nu, n, \alpha) \quad (6.1e)$$

which can be written:

$$P = Eh^2 \Pi_\alpha \left( \frac{Y}{E}, \nu, n, \alpha \right) \quad (6.1f)$$

where

$$\begin{aligned} \Pi_\alpha(\Pi_1, \nu, n, \alpha) &= \frac{P}{Eh^2} \\ \Pi_1 &= \frac{Y}{E} \end{aligned} \quad (6.1g)$$

Since  $\Pi_\alpha$ ,  $Y/E$ ,  $\nu$ ,  $n$ ,  $\alpha$  are all dimensionless, we can see that the force  $F$  is proportional to the square of the indentation depth  $h$ . A similar treatment provides information about the contact depth  $h_p$ :

$$h_p = h \Pi_\beta \left( \frac{Y}{E}, \nu, n, \alpha \right) \quad (6.1h)$$

where it is seen that the contact depth  $h_c$  is directly proportional to the total penetration depth  $h$ , the constant of proportionality being dependent on  $Y/E$  and  $n$  for a given indenter angle  $\alpha$ .

During unloading, the load  $P$  also depends, in addition to the above parameters, on the maximum depth of penetration:

$$P = f_L(E, \nu, Y, n, h, h_t, \alpha) \quad (6.1i)$$

Dimensional analysis yields:

$$P = Eh^2 \Pi_\gamma \left( \frac{Y}{E}, \frac{h}{h_t}, \nu, n, \alpha \right) \quad (6.1j)$$

Equation 6.1j shows that the load  $P$  now depends on  $h^2$  and the ratio  $h/h_t$ . Taking the derivative of Eq. 6.1j with respect to  $h$ , and evaluating this at  $h = h_t$ , the form of the slope of the initial unloading becomes:

$$\frac{dP}{dh} = Eh_t \Pi_\delta \left( \frac{Y}{E}, \nu, n, \alpha \right) \tag{6.1j}$$

where it is shown that the slope of the initial unloading is proportional to  $h_t$  (for a constant value of  $Y/E$ ,  $\nu$ ,  $n$  and  $\alpha$ ). The residual depth  $h_r$  at  $P = 0$  is found from Eq. 6.1j:

$$h_r = h_t \Pi_\phi \left( \frac{Y}{E}, \nu, n, \alpha \right) \tag{6.1k}$$

The total work done during the loading part of the indentation cycle is found from:

$$\begin{aligned} W_T &= \int_0^{h_t} Fdh \\ &= \frac{Eh_t^3}{3} \Pi_\alpha \left( \frac{Y}{E}, \nu, n, \alpha \right) \end{aligned} \tag{6.1l}$$

During unloading, the work done by the solid on the indenter is:

$$\begin{aligned} W_U &= \int_{h_r}^{h_t} Fdh \\ &= \frac{Eh_t^3}{3} \Pi_U \left( \frac{Y}{E}, \nu, n, \alpha \right) \end{aligned} \tag{6.1m}$$

The ratio of irreversible work, or energy dissipated within the solid, to the total work is independent of  $h_t$  and becomes:

$$\frac{W_T - W_U}{W_T} = \Pi_W \left( \frac{Y}{E}, \nu, n, \alpha \right) \tag{6.1n}$$

Finite element analysis can be used to test the relationships of Eqs. 6.1f and 6.1h and also the form of the dimensionless functions  $\Pi_{\alpha,\beta,\gamma,\phi}$ . These scaling relationships are important because they allow us to test the relationships between experimental variables within a theoretical framework. For example, comparison of finite element results shows that the quantities  $h_r/h_t$  (from Eq. 6.1k) and  $\Pi_W$  (from Eq. 6.1n) are linearly dependent.

As another example, consideration of the ratio  $h_p/h$  (see Eq. 6.1h) shows that it can be greater than or less than one, corresponding to piling-up and sinking-in,

respectively. For large values of  $Y/E$ , sinking-in occurs for  $n > 0$ . For small values of  $Y/E$ , both piling-up and sinking-in can occur depending on the value of  $n$ . When Eq. (3.2.3.1e) is combined with Eq. 3.2.3c, we obtain:

$$h_p = h_t - P\varepsilon \frac{dh}{dP} \quad (6.1o)$$

where in Eq. 6.1o,  $\varepsilon$  is the intercept factor in Table 1.1. Comparison with the results of finite element analysis shows that the multiple point unload method (the “Oliver and Pharr” method) is valid only for the case of sinking-in (large values of  $Y/E$ ).

Since the radius of the circle of contact for a conical indenter is given by Eq. 1.2o, we can write, using Eqs. 6.1h and 6.1j:

$$\frac{dP}{dh} = Ea \cot \alpha \left[ \frac{\Pi_\alpha(Y/E, \nu, n, \alpha)}{\Pi_\beta(Y/E, \nu, n, \alpha)} \right] \quad (6.1p)$$

Finite element analysis shows that the quantity  $dP/dh$  divided by the product  $Ea$  for particular values of  $\alpha$  is independent of  $Y/E$  and  $n$  and is approximately equal to 2 in accordance with Eq. 3.2.3.1h. This result confirms that the elastic modulus can be calculated from the initial unloading slope provided the contact radius  $a$  is known.

As another application of the scaling relationships, with  $H$  being given by Eq. 3.2.3d, the ratio  $H/Y$  becomes, by Eqs. 6.1f and 6.1h:

$$\frac{H}{Y} = \frac{\cot^2 \alpha}{\pi} \left[ \frac{\Pi_\alpha(Y/E, \nu, n, \alpha)}{Y/E \Pi_\beta^2(Y/E, \nu, n, \alpha)} \right] \quad (6.1q)$$

which implies that the hardness  $H$  is independent of depth  $h$  and that the constraint factor  $C$  depends upon the ratio  $Y/E$ . Finite element analysis shows that the constraint factor varies between 1.7 and 2.8 increasing with decreasing  $Y/E$ .

Given the mechanical properties of a material, the essential features of a nanoindentation loading and unloading response can be predicted by the scaling relationships given above. However, given a load-displacement curve, say from an experiment, there is not always a unique solution to the associated mechanical properties. While a value for modulus  $E$  can be found from the loading curves (Eq. 6.1f), values for  $Y$  and  $n$  cannot be uniquely extracted from the unloading curves.

Scaling relationships allow the estimation of material parameters even when the geometry of the indenter is not ideal. For example, from Eq. 4.9a, the loading with a pyramidal indenter (of equivalent cone angle  $70.3^\circ$ ) with a rounded tip of radius  $R$  should be identical with that of a spherical indenter for  $h_t/R < 0.073$  and only approach that of a sharp indenter when  $h_t/R \gg 0.073$ . By fitting a second-order polynomial to the load-displacement curve, the coefficients can

be used to determine the yield stress  $Y$  and the tip radius  $R$  if the elastic modulus  $E$  of the specimen is known.<sup>3</sup>

The method of dimensional analysis can be extended to cases involving non-linear solids, such as those that follow a power-law creep response.<sup>9,10</sup> In such a material, the mechanical response of the material depends upon the rate of application of strain:

$$\sigma = K\dot{\epsilon}^m \quad (6.1r)$$

where  $K$  and  $m$  are material constants. Introducing the dimension of time into the problem yields the following dimensional relationship for hardness  $H$ :

$$H = K \left( \frac{\dot{h}}{h} \right)^m \frac{\Pi_\alpha^c}{\Pi_\beta^c} \quad (6.1s)$$

where  $\Pi$  in Eq. 6.1s are dimensionless functions of both  $K$  and  $m$ . The importance of Eq. 6.1s is that it demonstrates the strain rate dependence on hardness observed in experimental work<sup>11</sup>. Equation 6.1s can be used to predict the load-displacement response of a power-law creeping solid under different conditions of application of load. For example, for a constant displacement rate, it is shown that the load is no longer proportional to  $h^2$  but proportional to  $h^{2-m}$  and the hardness decreases with increasing indentation depth. For a constant load rate, it is shown that the hardness increases with increasing load — the latter two conditions leading to an observed indentation size effect. The measured hardness in an indentation test is observed to reach a steady-state value when the load rate, divided by the load, is held constant during the test.

The generality of this method of dimensional analysis has the potential to yield new information about other mechanisms of deformation in indentation experiments.

## References

1. C.-M. Cheng and Y.-T. Cheng, "On the initial unloading slope in indentation of elastic-plastic solids by an indenter with an axisymmetric smooth profile," *Appl. Phys. Lett.* **71** 18, 1997, pp. 2623–2625.
2. Y.-T. Cheng and C.-M. Cheng, "Relationships between hardness, elastic modulus, and the work of indentation," *Appl. Phys. Lett.* **73** 5, 1997, pp. 614–616.
3. Y.-T. Cheng and C.-M. Cheng, "Further analysis of indentation loading curves: Effects of tip rounding on mechanical property measurements," *J. Mater. Res.* **13** 4, 1998, pp. 1059–1064.

4. Y.-T. Cheng and C.-M. Cheng, "Effects of 'sinking in' and 'piling up' on the estimating the contact area under load in indentation," *Phil. Mag. Lett.* 78 2, 1998, pp. 115–120.
5. Y.-T. Cheng and C.-M. Cheng, "Scaling approach to conical indentation in elastic-plastic solids with work-hardening," *J. App. Phys.* 84 3, 1998, pp. 1284–1291.
6. Y.-T. Cheng and C.-M. Cheng, "Analysis of indentation loading curves obtained using conical indenters," *Phil. Mag. Lett.* 77 1, 1998, pp. 39–47.
7. Y.-T. Cheng and C.-M. Cheng, "Scaling relationships in conical indentation of elastic-perfectly plastic solids," *Int. J. Solids Structures*, 36, 1999, pp. 1231–1243.
8. Y.-T. Cheng and C.-M. Cheng, "Can stress-strain relationships be obtained from indentation curves using conical and pyramidal indenters?," *J. Mater. Res.* 14 9, 1999, pp. 3493–3496.
9. Y.-T. Cheng and C.-M. Cheng, "What is indentation hardness?," *Surf. Coat. Tech.* 133-134, 2000, pp. 417–424.
10. R. Hill, "Similarity of creep indentation tests," *Proc. R. Soc. Lond.* A436, 1992, pp. 617–630.
11. M.J. Mayo and W.D. Nix, "Measuring and Understanding Strain Rate Sensitive Deformation with the Nanoindenter," *Proc. 8<sup>th</sup> int. Conf. On Strength of Metals and Alloys*, Tampere, Finland, P.O. Kettunen, T.K. Lepisto and M.E. Lehtonen, eds. Pergammon Press, Oxford, 1988, pp. 1415–1420.

# Chapter 7

## Methods of Nanoindentation Testing

### 7.1 Introduction

In the previous chapters, the indentation process has been implicitly assumed to be quasi static, and no time-dependent or rate effects were considered. In this chapter, the basic theory underlying various dynamic modes of testing is presented. Techniques such as oscillatory motion, impact, and scratch testing are covered in sufficient detail to provide an understanding for the interpretation of the results obtained.

### 7.2 Dynamic Indentation Testing

For many reasons, it is of interest to superimpose a small amplitude force oscillation at relatively high frequency onto the test force signal. In some nanoindentation instruments, this method is used primarily to measure the contact stiffness ( $dP/dh$ ) continuously while the load is applied up to maximum load and is referred to as the continuous stiffness mode of operation. When testing polymer or viscoelastic materials, the measurement of both load and depth in this manner allows any phase difference between them to be also measured. Furthermore, the method can also be used as a means for establishing initial contact with the specimen surface. In this section, some of the more fundamental underlying theory behind the technique is reviewed. Only with such an understanding can the results of such testing be correctly interpreted.

In a typical indentation test involving an oscillatory motion, a small AC modulated force  $p$  is applied with a frequency  $\omega$  and amplitude  $p_0$ :

$$p = p_0 e^{i\omega t} \quad (7.2a)$$

The resulting displacement  $h$  will have the same frequency of oscillation but may have a phase difference  $\phi$  leading to:

$$h = h_0 e^{i(\omega t + \phi)} \quad (7.2b)$$

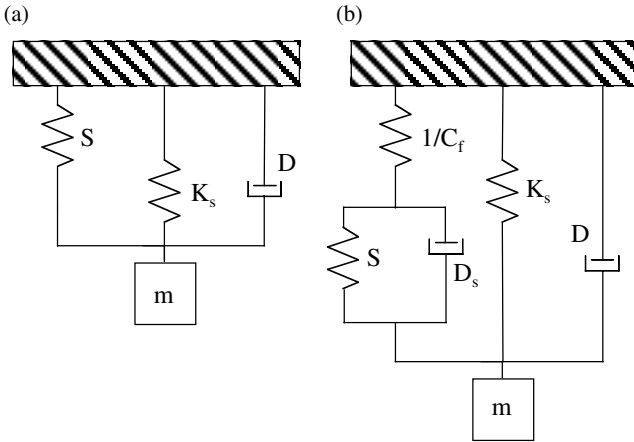


**Fig. 7.1** Dynamic mechanical model of a nanoindentation instrument. (a) Shows a simple model and (b) is a model that includes the compliance of the load frame and the tip/sample interaction.  $K_s$  is the stiffness of the indenter support springs,  $D$  is a damping coefficient,  $S$  is the stiffness of the contact,  $C_f$  is the compliance of the load frame,  $D_s$  is a damping coefficient at the contact, and  $m$  is the mass of the indenter and shaft.

An analysis of the model shown in Fig. 7.1 (a) leads to an expression that relates the applied oscillatory load to the resulting displacement thus:

$$\left| \frac{P_o}{h_o} \right| = \sqrt{(S + K_s - m\omega^2)^2 + \omega^2 D^2} \quad (7.2c)$$

with a phase difference  $\phi$  given by:

$$\tan \phi = \frac{\omega D}{S + K_s - m\omega^2} \quad (7.2d)$$

In Eqs. 7.2c and 7.2d,  $K_s$  is the stiffness of the indenter shaft support springs,  $p_o$  is the magnitude of the oscillatory load,  $D$  is the damping coefficient (similar to the inductance of an electrical circuit),  $h_o$  is the magnitude of the displacement oscillation,  $\omega$  is the frequency of the oscillation,  $m$  is the mass of the components, and  $S$  is the contact stiffness  $dP/dh$ .

A popular implementation of this technique<sup>1</sup> uses the measured stiffness  $S$  together with Eq. 3.2.3.1i to determine the area  $A$  of the contact continuously during the loading cycle of an indentation test:

$$A = \left[ \frac{dP}{dh} \right]^2 \frac{\pi}{4} \frac{1}{E^*} \quad (7.2e)$$

It should be noted that the determination of the area of contact in this manner does not depend upon the shape of the indenter, but does presume a prior knowledge of  $E^*$ .

The actual measured value of contact stiffness,  $S$ , in a static indentation test includes the stiffness or, compliance  $C_f$ , of the instrument, and the method by which this can be accounted for has been given in Chapter 4. In an oscillatory mode of operation, the dynamic characteristics of the instrument are also measured along with those of the sample and so the characteristics of the instrument must be taken into account in the interpretation of the results. For the mechanical model shown in Fig. 7.1 (b), we obtain:

$$\left| \frac{P_o}{h_o} \right| = \sqrt{\left[ \left( \frac{1}{S} + C_f \right)^{-1} + K_s - m\omega^2 \right]^2 + \omega^2 D^2} \tag{7.2f}$$

where  $C_f$  is the compliance of the load frame. The phase difference  $\phi$  between the load and displacement is given by:

$$\tan \phi = \frac{\omega D}{\left( \frac{1}{S} + C_f \right)^{-1} + K_s - m\omega^2} \tag{7.2g}$$

$K_s$  and  $D$  are determined from readings obtained with the indenter clear of the specimen surface ( $S = 0$ ) and sweeping over the frequency range of interest.

When the sample to be measured is viscoelastic, there is an additional damping term  $D_s$  associated with the tip-sample interaction. For tests done over a range of frequencies, a plot of stiffness  $S$  vs indenter displacement is proportional to the storage modulus of the material, and a plot of damping coefficient  $D_s\omega$  vs displacement is proportional to the loss modulus<sup>2</sup> of the material at the contact interaction.

In some respects, the oscillatory mode of operation is similar to that of an atomic force microscope, but there are several practical differences. In an AFM, the spring stiffness of the cantilever that supports the probe is made very compliant so as to enhance the force resolution of the instrument and to avoid unintentionally damaging the specimen surface. The AFM is primarily an imaging device. For a nanoindentation test instrument, the stiffness of the supporting springs for the indenter is high so as to provide enough load to enable the mechanical properties (rather than the surface topography) to be measured. Syed Asif, Colton, and Wahl<sup>3,4</sup> have coupled the piezo-controlled sample positioner of an AFM with a traditional nanoindentation instrument. The resulting dynamic mode of testing is referred to as “hybrid indentation” and offers the ability to measure surface forces, surface energies, interaction stiffness prior to contact, and a quantitative imaging technique for mechanical property mapping at the nano scale.

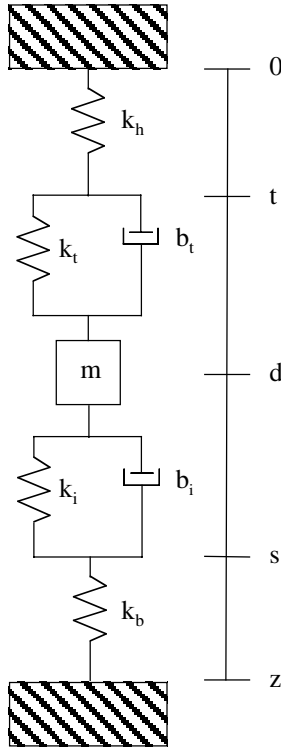


**Fig. 7.2** Improved dynamic mechanical model of a nanoindentation instrument,<sup>5</sup>  $k_t$  is the stiffness of the force actuator with damping  $b_t$ . The tip-sample interaction has a stiffness  $k_i$  ( $dP/dh$ ) and damping  $b_i$ .  $k_h$  and  $k_b$  are the stiffnesses of the head and base of the load frame, respectively.

Burnham, Baker, and Pollock<sup>5</sup> have recently prepared a universal mechanical model that accounts for the characteristics of these instruments and that of the tip-sample interaction. In this work, the elements of the mechanical model are placed in series as shown in Fig. 7.2. In the simplified model of Fig. 7.1, the velocity of one side of the dashpot associated with the tip-sample interaction is assumed to be fixed. In the improved model of Fig. 7.2, the velocities on all sides of the elements are accounted for in the expressions for amplitude and phase of the motion. The resulting expressions take the form:

$$\frac{d-t}{p} = \sqrt{\left[ \left( 1 + \frac{k_i}{k_b} \right)^2 + \left( \frac{\omega b_i}{k_b} \right)^2 \right] \left[ K^2 + (\omega B)^2 \right]^{-1}} \quad (7.2h)$$

where  $d$  and  $t$  are the points labeled on Fig. 7.2.

The phase difference is given by:

$$\tan \phi = \omega \left[ \frac{b_i}{k_b} K - \left( 1 + \frac{k_i}{k_b} \right) B \right] \left[ \left( 1 + \frac{k_i}{k_b} \right) K + \omega^2 \frac{b_i}{k_b} B \right]^{-1} \quad (7.2i)$$

where  $K$  and  $B$  are an effective stiffness and damping, respectively, for the system. In the limit of a very stiff machine, where  $k_i$ ,  $k_b$ ,  $b_i$ ,  $b_b$  are very much less than  $k_h$  and  $k_b$ , Eqs. 7.2h and 7.2i reduce to 7.2f and 7.2g<sup>5</sup>.

The significance of this is that the basic operation of a nanoindentation instrument can be described in the same way as that of similar surface mechanical probes, which together, can be referred to as a class called mechanical properties nanoprobess or MPNs.

### 7.3 Thin Films

One of the most popular applications of nanoindentation is the determination of the mechanical properties of thin films. In nanoindentation tests, the properties of the film may be measured without removing the film from the substrate as is done in other types of testing. The spatial distribution of properties, in both lateral and depth dimensions, may be measured, and a wide variety of films are amenable to the technique, from ion-implanted surfaces to optical coatings and polymer films. Apart from testing films in situ, nanoindentation techniques can also be used for films made as free-standing microbeams or membranes.<sup>6</sup> The chief difficulty encountered in nanoindentation of thin films is to avoid unintentional probing of the properties of the substrate. To avoid this, it is common to restrict the maximum depth of penetration in a test to no more than 10% of the film thickness, although research suggests that this rule has no physical basis<sup>7</sup>.

For indentations with a conical or pyramidal indenter, the indentation depth increases at the same rate as the radius of the circle of contact. Thus, for an indentation test on a thin film, the indentation scales with the ratio of the radius of the circle of contact divided by the film thickness  $a/t$ . The ratio of the penetration depth and the film thickness,  $h/t$ , can also be used as a scale parameter. The former is probably a more useful parameter for hard films on soft substrates since the contact radius is approximately equal to that of the hydrostatic core (see Section 1.4.2) beneath the indenter. For soft films,  $h/t$  is of more interest since it is a measure of how far the penetration depth has approached the substrate.

Both quantitative and qualitative information can be obtained from nanoindentation experiments on thin film systems. For example, comparison of load-displacement curves between coated and uncoated substrates often reveals changes in the elastic and plastic response of a system due to differences in surface treatment. The presence of discontinuities in the load-displacement response reveals information about cracking, delamination, and plasticity in the film and substrate.

### 7.3.1 Elastic modulus

When influence from the substrate is unavoidable, there are various treatments available to account for this.<sup>8,9</sup> King<sup>10</sup> evaluated the empirical treatment of Doerner and Nix<sup>11</sup> using the finite element method to arrive at a modified expression for Eq. 3.2.1c, which we can restate in terms of the contact stiffness,  $dP/dh$ :

$$\frac{dP}{dh} = \beta \frac{2}{\sqrt{\pi}} E_{\text{eff}} \sqrt{A} \left[ \frac{\frac{(1 - \nu_s^2)}{E_s} + \frac{(1 - \nu_i^2)}{E_i}}{\frac{(1 - \nu_f^2)}{E_f} \left(1 - e^{-\alpha \sqrt{A}}\right) + \frac{(1 - \nu_s^2)}{E_s} \left(e^{-\alpha \sqrt{A}}\right) + \frac{(1 - \nu_i^2)}{E_i}} \right] \quad (7.3.1a)$$

In Eq. 7.3.1a, the subscripts *s*, *I*, and *f* refer to the substrate, indenter, and film respectively.  $E_{\text{eff}}$  is the combined modulus of the indenter and the substrate. The constant  $\beta$  is that given in Table 1.1 and depends upon the shape of the indenter, while the constant  $\alpha$  is an empirical constant that is required to be evaluated from a series of experimental results. King provides some representative values of  $\alpha$ .

Gao, Chiu, and Lee<sup>12</sup> used a moduli-perturbation method in which a closed-form solution results in an expression for the combined elastic modulus  $E_{\text{eff}}$  of the film/substrate combination:

$$E_{\text{eff}} = E_s + (E_f - E_s)I_o \quad (7.3.1b)$$

where in Eq. 7.3.1b,  $I_o$  is a function of  $t/a$  (with *a* being the contact radius) given by:

$$I_o = \frac{2}{\pi} \tan^{-1} \frac{t}{a} + \left[ (1 - 2\nu) \frac{t}{a} \ln \left( 1 + \frac{(t/a)^2}{(t/a)^2} \right) - \frac{t/a}{1 + (t/a)^2} \right] \left[ 2\pi(1 - \nu) \right]^{-1} \quad (7.3.1c)$$

In Eq. 7.3.1c,  $I_o$  is a weighting function that equals zero as the film thickness approaches zero, and approaches unity for large values of film thickness. Swain and Weppelmann used Eq. 7.3.1c to evaluate  $I_o$  for a range of elastic indentations on a TiN film on a silicon substrate, to obtain the combined film/substrate modulus  $E_{\text{eff}}$ , and bulk silicon for  $E_s$ .  $E_f$  could be estimated from:

$$\frac{E_{\text{eff}}}{E_s} = (1 - I_o) + E_f I_o \quad (7.3.1d)$$

These equations are of considerable importance since the measurement of modulus for the film is inherently connected with that of the substrate. As a very rough approximation, the stiffness of the two (or more) elastic elements comprising the thin film and substrate are essentially in series as shown in Fig. 7.3 (a). No matter how low of a force is applied to the indenter, there will always be a contribution from the substrate. However, in the indentation stress field, the indenter load is supported not only by direct compression in the vertical direction, as shown in Fig. 7.3 (a), but also by compressive stresses acting inwards from the sides. This makes the contribution from the film somewhat more than that expected from simple compression in the vertical direction only. Since there is always some elastic displacement of the substrate during an indentation test, the traditional 10% rule (see Section 7.3.2) does not apply for nanoindentation measurements for modulus determination of thin film systems.

Despite the fundamental difficulties in extracting the film modulus from the load-penetration depth data from first principles, it is a relatively straight forward procedure to undertake a series of tests with a conical or pyramidal indenter at differing depths and to plot the measured combined modulus  $E_{\text{eff}}$  against the scaling parameter  $a/t$ . The film modulus  $E_f$  is found by extrapolating the curve of best fit to these data to zero  $a/t$  as shown in Fig. 7.3 (b).

The analytical computation of the stress distribution of a thin film system in indentation loading has traditionally been very difficult and so this information is usually obtained by finite element methods. Schwarzer and co-workers<sup>13,14</sup> have developed an analytical procedure using a method of image charges. This treatment provides an elastic solution for the complete stress distribution in the film and substrate. Values of tensile or shear stresses that might subsequently lead to fracture or plastic deformation can be readily identified.

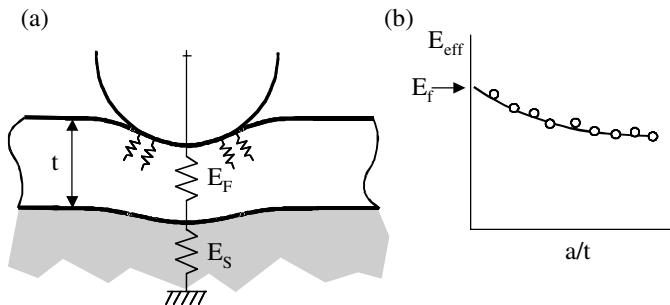


**Fig. 7.3** (a) A thin film system comprising two elastic elements in series. The measured stiffness of the film always has a contribution from the substrate. The contribution to  $E^*$  from the film includes that from the localized support from the indentation stress field. (b) For a geometrically similar indenter, the indentation scales with  $a/t$ . The modulus of the film  $E_f$  is found by extrapolating measured values of  $E^*$  to zero value of  $a/t$ .

### 7.3.2 Hardness

The hardness value measured for a film and substrate combination is more difficult to quantify than the combined elastic modulus due to the complex nature of the plastic zone as it interacts with the substrate material.

Bückle<sup>15</sup> proposed that the composite hardness of a thin film system  $H_{\text{eff}}$  could be expressed as:

$$H_{\text{eff}} = H_s + \alpha(H_f - H_s) \quad (7.3.2a)$$

where  $H_s$  is the hardness of the substrate and  $H_f$  is the hardness of the film with  $\alpha$  being an empirically derived parameter.

Jonsson and Hogmark<sup>16</sup> propose an area law of mixtures so that the hardness of the film can be extracted from the hardness of the film–substrate combination  $H_{\text{eff}}$  from:

$$H_{\text{eff}} = H_f \frac{A_f}{A} + H_s \frac{A_s}{A} \quad (7.3.2b)$$

where  $A_f$  and  $A_s$  are the relative parts of the contact carried by the film and the substrate, respectively, and  $A$  is the total contact area. A similar treatment, but based on a volume of deformation law of mixtures, was proposed by Burnett and Rickerby.<sup>17,18</sup>

For a soft film on a hard substrate, Bhattacharya and Nix<sup>19</sup> propose that the hardness of the film–substrate combination  $H_{\text{eff}}$  is determined by:

$$H_{\text{eff}} = H_s + (H_f - H_s) \exp\left(-\frac{Y_f}{Y_s} \frac{E_s}{E_f} \left(\frac{h}{t}\right)^2\right) \quad (7.3.2c)$$

where  $Y_f$  and  $Y_s$  are the material yield stresses for the film and substrate, respectively, and the exponential is a weighting function. For hard films on a soft substrate, the expression becomes:

$$H_{\text{eff}} = H_s + (H_f - H_s) \exp\left(-\frac{H_f}{H_s} \frac{Y_s}{Y_f} \sqrt{\frac{E_s}{E_f}} \frac{h}{t}\right) \quad (7.3.2d)$$

Stone, LaFontaine, Alexopolous, Wu, and Li<sup>20</sup> measured the hardness of aluminum films on silicon substrates as a function of depth of the indentation for different thicknesses of film and also altering the adhesion between the film and substrate by the prior deposition of a carbon layer. They found that the hardness increased as the indentation depth approached the interface.

Despite these analytical and sometimes empirical treatments, there is no one relationship as yet proposed which covers a wide range of materials behavior. In the absence of any rigorous relationship, the conventional 10% of the thickness rule appears to be that most generally used.

### 7.3.3 Film adhesion

The nanoindentation technique applied to thin film testing is not restricted to measuring mechanical properties of the film, but can also be applied to evaluate film adhesive strength. The strength of the bond between a film and substrate is intimately related to the residual stresses in the film and the stresses applied during service. Residual stresses are usually determined by a wafer technique using the Stoney<sup>21</sup> equation:

$$\sigma_f = \frac{E_s}{1-\nu_s} \frac{t_s^2}{6t_f} \left( \frac{1}{R} - \frac{1}{R_0} \right) \quad (7.3.3a)$$

where  $\sigma_f$  is the stress in the film,  $E_s$  and  $\nu_s$  refer to the properties of the substrate,  $t_s$  is the substrate thickness,  $t_f$  is the film thickness,  $R_0$  is the initial radius of curvature, and  $R$  is the final radius of curvature of the wafer. Stresses in the GPa regime are commonly encountered for thin hard films. The adhesion is controlled by the strain energy release rate that has been calculated by Marshall and Evans<sup>22</sup>:

$$G = \frac{h\sigma_I^2(1-\nu^2)}{2E_f} + (1-\alpha) \frac{h\sigma_R^2(1-\nu)}{E_f} - (1-\alpha) \frac{h(\sigma_I - \sigma_R)^2(1-\nu)}{E_f} \quad (7.3.3b)$$

where  $\sigma_I$  is the indentation stress,  $\sigma_R$  is the residual stress, and  $\alpha$  is a parameter between 0 and 1 depending on the degree of buckling in the film. If the film is not buckled,  $\alpha = 1$  and the residual stresses do not contribute to  $G$ .

In a nanoindentation test, load may be applied to the indenter in a controlled manner so that the film is tested to failure. Features on the load displacement curve can be linked to mechanical failure processes<sup>23,24</sup> and one such example is indicated in Fig. 7.4.

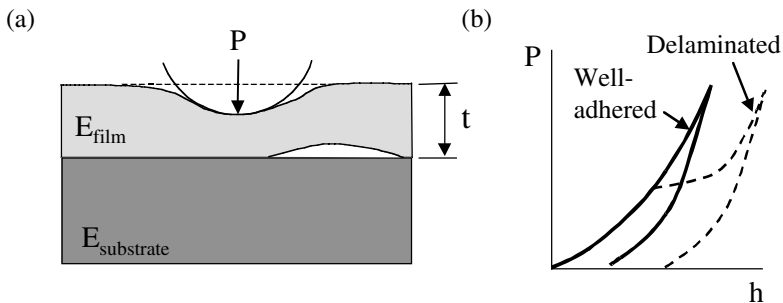


**Fig. 7.4** Mechanical failure of a thin film system can lead to observable and identifiable features on a load-displacement curve in a nanoindentation test.

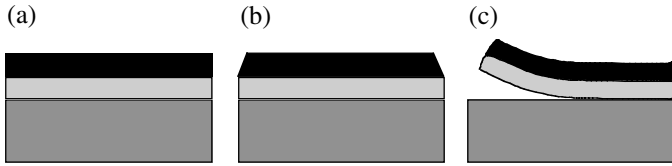


**Fig. 7.5** Superlayer film testing technique. (a) An epoxy “superlayer” is deposited onto the thin film system. (b) The epoxy is cured at approximately 180 °C and then cooled until (c) a tensile stress in the film is developed due to thermal expansion mismatch and delamination occurs.

In some cases, indentation stresses alone may not be sufficient to cause delamination or failure of the film. Conventional tests for adhesion involve depositing an epoxy “superlayer” on the thin film system. The epoxy is cured at 180 °C and when cooled to room temperature, a tensile stress in the film is developed due to thermal expansion mismatch as shown in Fig. 7.5. The system is then further cooled until spontaneous delamination is observed. The test seeks a critical temperature at which delamination occurs as a measure of adhesion.

For tests with ductile or well-adhered films, stresses generated using the superlayer technique may not be sufficient to generate delamination. Kriese, Moody, and Gerberich<sup>25</sup> have used the superlayer technique in addition to a nanoindentation test to generate the required failure stresses in such cases. As reported by Volinsky, Moody, and Gerberich,<sup>26</sup> the technique has been extended to examining the effect of residual tensile and compressive stresses in thin film systems.

## 7.4 Scratch Testing

The scratch resistance of thin films and protective coatings is usually expressed in terms of their ability to withstand abrasion without fracturing. Scratch testing on a large scale enables films and coatings to be ranked according to the results of a particular test method. A typical scratch test involves a ramped load and the measure of performance is the critical load at which the surface fails. However, various modes of failure can be generated at different loads with different shapes of indenter.

Many nanoindentation instruments can be configured to operate in a scratch testing mode. As shown in Fig. 7.6, in this mode of operation, a normal force  $F_N$  is applied to the indenter, while at the same time, the sample is moved sideways. In some instruments, an optional force transducer can be used to measure the friction, or tangential force  $F_T$ . In some cases, a lateral force  $F_L$ , normal to  $F_T$  can also be applied.<sup>27</sup>

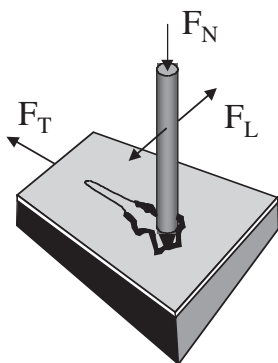


**Fig. 7.6** Configuration of an indentation scratch test. The normal force  $F_N$  can be held at a constant value or ramped up or down while the sample is moved sideways by a tangential force  $F_T$ . In addition, a lateral force  $F_L$  can sometimes also be applied.

Scratch tests on a micron scale were initially performed inside the chamber of an SEM.<sup>28</sup> The stylus or indenter in these tests was typically electro-polished tungsten tips with a radius of about 1  $\mu\text{m}$ . The “scratch hardness” was defined as the track width of the scratch divided by the diameter of the scratch tip.

The physical meaning of the results of such a scratch test are fairly open to interpretation. In modern methods, the applied normal force is ramped up in value while the sample is moved in a sideways direction and the minimum force  $F_C$  at which failure occurs is an indication of scratch resistance. The detection of this critical load can be determined using a variety of techniques such as optical microscopy, acoustic emission, and an analysis of the coefficient of friction, the latter method requiring a measurement of the tangential force  $F_T$  as well as the applied normal force  $F_N$ . The coefficient of friction  $\mu$  can be readily calculated from:

$$\mu = \frac{F_T}{F_N} \quad (7.4a)$$

A diamond sphero-conical indenter with a tip radius of 200  $\mu\text{m}$  is usually used as the stylus. The use of the critical load as a measure of scratch resistance is complicated by its dependence on scratching speed, loading rate, tip radius, substrate hardness, film thickness, film and substrate roughness, friction coefficient, and friction force.<sup>29</sup> Despite these difficulties, the method allows comparative tests to be performed with some degree of confidence to mechanical performance. Figures 7.7 and 7.8 show the results of a scratch test on multilayer Al/TiN/SiO film on a silicon substrate for a constant applied normal load of 30 mN using a 20  $\mu\text{m}$  scratch tip. The circled area in both figures is an indication of an area of poor adhesion of the film.

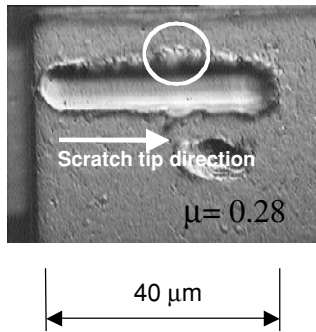


**Fig. 7.7** Scratch test on a multilayer Al/TiN/SiO film on a silicon substrates for three different processing conditions for an applied normal load of 30 mN using a 20  $\mu\text{m}$  scratch tip. The tip moved in a left to right direction as shown in the figure. The coefficient of friction is shown. The circled area indicates an area of poor adhesion of the film (Courtesy CSIRO).

In a ramping scratch test, there is usually observed a transition from elastic to plastic deformation in the surface, and if the surface is a thin film, delamination eventually occurs. For scratches made on very soft materials, the shape of the indenter often affects the visibility of the scratch owing to an increase in piling-up along the length of the scratch. Jardret and Oliver<sup>30</sup> demonstrate the differences in piling-up with a Berkovich indenter with the blunt face of the indenter facing forward, and the edge facing forward, on an automotive paint film.

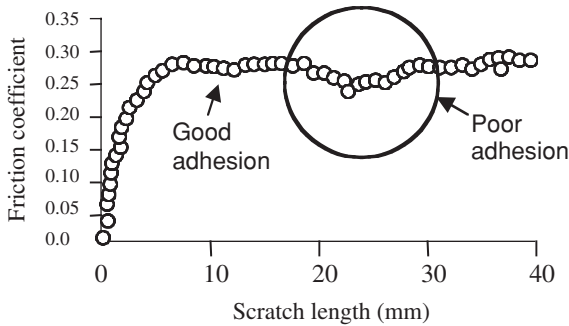


**Fig. 7.8** Plot of coefficient of friction vs scratch length for sample shown in Fig. 7.7. A marked decrease in the coefficient of friction is an indication of poor adhesion as shown in the circled area of Fig. 7.7 (Courtesy CSIRO).

Similar results obtained by Enders, Grau, and Berg<sup>31</sup> with sol-gel films on fused silica were interpreted in terms of an analytical model incorporating both

sliding and ploughing friction terms.<sup>32</sup> Interestingly, this latter work treated the contact at very low loads as a single asperity contact in which surface adhesive forces (see Appendix 2) were included. The sliding part of the friction coefficient is given as:

$$\mu_s = \pi \left( \frac{3}{4E^*} \right)^{2/3} TR^{2/3} F_N^{-1/3} \left[ 1 + \frac{F_A}{F_N} + \sqrt{\left( 1 + \frac{F_A}{F_N} \right)^2 - 1} \right]^{2/3} \quad (7.4b)$$

where  $T$  is the interfacial shear strength found from the tangential force  $F_T$  divided by the contact area,  $R$  is the radius of the indenter,  $F_A$  and  $F_N$  are the adhesive and normal forces respectively. The ploughing part as:

$$\mu_p = KP^* F_N^{(2-n)/n} \quad (7.4c)$$

where  $n$  and  $K$  are constants that depend upon the shape of the indenter. The total friction coefficient is the sum of these:

$$\mu = \mu_s + \mu_p \quad (7.4d)$$

Both the sliding and ploughing parts of the friction are functions of the normal force  $F_N$ . The sliding part of the friction coefficient dominates the process at low values of  $F_N$  and decreases with increasing load. The ploughing part of the friction is shown to dominate the process where, during the transition, the total friction coefficient passes through a minimum at a critical value of normal force  $F_N$ .

Scratch testing is of course closely related to the field of tribology. Tribological testing usually involves techniques such as pin-on-disk, ball-on-disk, and pins, rings, or disks on disks leading to measurements of friction force and friction coefficient, adhesion force of films, wear rate, contact resistance and acoustic emission of fracture events. While conventional nanoindentation instruments do not generally offer these capabilities, there is considerable overlap with some tribology instruments offering a nanoindentation mode of operation.

## 7.5 Acoustic Emission Testing

When nanoindentation techniques are used to investigate cracking and delamination of thin films, acoustic emission (AE) can sometime be used with some advantage. The object of the acoustic emission measurement is to record the amplitude and time at which specific events occur during the application of load to the indenter. Examples of such events are substrate cracking, delamination, film cracking, phase transformations, and slippage beneath the indenter.

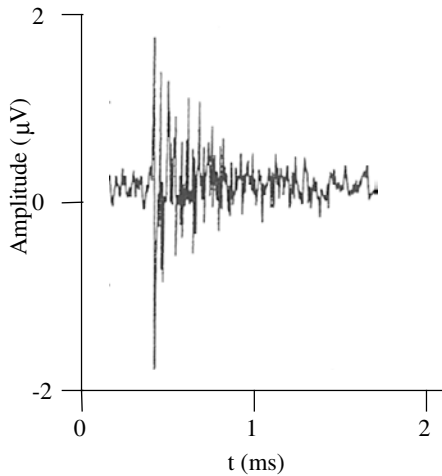


**Fig. 7.9** Acoustic emission signal burst from a nanoindentation test (Courtesy CSIRO).

The acoustic emission sensor is typically a high-resolution, low-noise device with a high resonant frequency ( $\approx 200 - 300$  kHz). This makes the sensor rather insensitive to mechanical vibrations from the environment. The sensor detects the elastic waves generated by the release of stored strain energy within the loaded system as some failure event occurs and is usually mounted either on the specimen or on the indenter shaft. The signal is amplified by a very high input impedance amplifier with a gain of approximately 100 db. The raw signal is typically filtered before presentation as either an rms voltage or an accumulation of “counts.”

The acoustic emission signal typically contains a burst-type signal as shown in Fig. 7.9. Each signal burst corresponds to a damage event. The amplitude of the burst signal is an indication of the magnitude of the damage event. Shiwa, Weppelmann, Munz, Swain, and Kishi<sup>33</sup> compared features on a load-displacement curve obtained with a spherical indenter on silicon with recorded acoustic emission signals during an indentation test and identified five distinct stages of behaviour during the complete cycle from loading to final unloading. Events such as pressure-induced phase transformations and cracking were identified.

A quantitative approach to this type of testing was undertaken by Sekler, Steimann, and Hintermann,<sup>27</sup> who integrated the acoustic emission signal obtained on scratch tests on a TiC-coated cemented carbide sample to produce an energy spectrum of events as a function of applied load. The critical load was determined by drawing a line through the average slope of the increasing energy data and reading off the intercept with the horizontal force axis. These authors found that despite the possibility of obtaining an objective measure of the criti-

cal load in a scratch test, it is frequently necessary for the output of the acoustic emission sensor to be adjusted by the operator so as to coincide with the damage event of interest before the technique can be used in an automated fashion.

## 7.6 Constant Strain Rate Testing

In earlier chapters, it was mentioned that the representative strain for testing with a Berkovich, Vickers, cube corner, or conical indenter was a constant owing to geometrical similarity of the contact. For a spherical indenter, Tabor<sup>34</sup> showed that the quantity  $0.2a/R$  is a measure of the representative strain and increases as the depth of penetration increases. This empirical result, proposed in 1951, was the subject of a rigorous theoretical treatment by Hill, Storåkers, and Zdunek<sup>35</sup> in 1989 and an experimental study by Chaudhri<sup>36</sup> in 1993. These treatments are concerned with solids that show no dependence on the rate of application of strain. In some non-linear solids, such as those that follow a power-law creep response, the mechanical response of the material depends upon the rate of application of strain:

$$\sigma = K\dot{\epsilon}^m \quad (7.6a)$$

where  $K$  and  $m$  are material constants. Several attempts have been made to extend the results of rate-independent materials to power-law creeping solids, the most rigorous perhaps being that of Bower, Fleck, Needleman and Ogbonna<sup>37</sup> and also Storåkers and Larsson.<sup>38</sup> The most popular treatment is that given by Mayo and Nix,<sup>39</sup> who define the strain rate for such tests as the indenter displacement velocity divided by the plastic depth:

$$\dot{\epsilon} = \frac{dh}{dt} \frac{1}{h} \quad (7.6b)$$

where  $h$  in Eq. 7.6b is, strictly speaking,  $h_p$ . However, in soft metals, the elastic displacement  $h_e$  is very small compared to  $h_p$  and so the plastic depth can be approximated by the total depth of penetration. Equation 7.6b shows that the stress, or the mean contact pressure, decreases as the depth of penetration increases according to the power law in Eq. 7.6a. Precautions should be taken in tests on strain-hardening materials to minimize the depth dependence on hardness arising from geometrically necessary dislocations (see Section 4.7). For this reason, comparative testing of material to determine their strain rate sensitivities should be carried out at a fixed chosen depth of penetration. The strain rate sensitivity  $m$  is defined as<sup>40</sup>:

$$m = \frac{\partial \ln H}{\partial \ln \dot{\epsilon}} \quad (7.6c)$$

and is a measure of the sensitivity of the hardness of a material to changes in strain rate. Cheng and Cheng<sup>41</sup> show that the hardness measured in an indentation test approaches a constant value when the strain rate is held constant and this can be obtained when the load rate divided by the load is held constant:

$$\frac{\dot{h}}{h} \propto \frac{\dot{P}}{P} \quad (7.6d)$$

In nanoindentation testing, it is sometimes desirable to undertake measurements on power-law creeping solids such that the conditions of Eq. 7.6d are satisfied during the application of load (and the unloading) so that meaningful value for hardness, independent of rate effects within the specimen, to be obtained. The issue of strain rate and its effect on the results of an indentation test are inextricably connected with the phenomenon of creep and this is the subject of Section 7.7.

## 7.7 Creep

Nanoindentation can be used to determine viscoelastic properties of the specimen material. In the analysis methods given in Chapter 3, it was assumed that the material behaved in an elastic–plastic manner and did not exhibit any time-dependent behavior. Creep within the specimen can occur under indentation loading and manifests itself as a change of the indentation depth with a constant test force applied. The relative change of the indentation depth is referred to as the creep of the specimen material. The precise mechanisms of creep depend upon the material being indented. Li and Warren<sup>42</sup> propose that the stress fields in the specimen material beneath the indenter create a chemical potential gradient that leads to a thermally activated diffusional flux of atoms flowing from the area beneath the indenter to the specimen surface, and along the interface between the indenter and specimen, even under what is nominally an elastic contact. The rate equation for a spherical indenter was found to be:

$$h = \frac{2(1+\nu)}{\pi} \frac{P}{\left[ h(2R-h)^{3/2} \right]} \frac{D_v \Omega}{kT} \left[ 1 + \frac{8\delta}{3 \left[ h(2R-h)^{1/2} \right]} \frac{D_i}{D_v} \right] \quad (7.7a)$$

and for a conical indenter:

$$h = \frac{2(1+\nu)}{\pi \tan^3 \alpha} \frac{P}{h^3} \frac{D_v \Omega}{kT} \left[ 1 + \frac{8\delta}{3h \tan \alpha} \frac{D_i}{D_v} \right] \quad (7.7b)$$

In Eqs. 7.7a and 7.7b,  $\nu$  is the Poisson's ratio of the specimen,  $D_v$  is the diffusion coefficient within the specimen,  $D_i$  is the diffusion coefficient along the interface between the specimen and the indenter,  $\Omega$  is the atomic volume of the

specimen material,  $k$  is Boltzmann's constant,  $T$  is the absolute temperature,  $\delta$  is the thickness of the interface along which diffusion occurs,  $\alpha$  is the cone semi-angle,  $h$  is the depth of penetration beneath the specimen surface measured at the circle of contact (i.e.,  $h$  in Eqs. 7.7a and 7.7b is the plastic depth  $h_p$ ), and  $R$  is the indenter radius.

This diffusion equation holds best when the indentation temperature is very much below the melting point of the specimen material. When the indentation temperature is more that one half of the specimen melting temperature, a simple steady-state power-law creep equation may be more appropriate<sup>43</sup> such as Eq. 7.6a.

A more empirical approach that yields information about the viscoelastic mechanical properties of the specimen is available through mechanical modeling. The simple Kelvin–Voigt three-element model shown in Fig. 7.10 is a suitable mechanical model for the system. In this model,  $K_1$ ,  $G_1$ ,  $K_2$ , and  $G_2$  represent the bulk and shear moduli of the two spring elements and  $\eta$  is the viscosity term that quantifies the time-dependent property of the material. For a rigid spherical indenter in contact with a viscoelastic specimen, Cheng, Scriven and Gerberich<sup>44</sup> used the functional equations method of Radok<sup>45</sup> and determined that the creep response (change in depth  $h$  over time) at constant load could be expressed as:

$$h(t)^{3/2} = \frac{3P_o(1-v^2)}{4\sqrt{RE_1}} \left( A_c e^{-\alpha t} + B_c e^{-\beta t} + C_c \right) \quad (7.7e)$$

In Eq. 7.7e,  $P_o$  is the fixed load,  $R$  is the radius of the indenter and  $A_c$ ,  $B_c$ ,  $C_c$ ,  $\alpha_c$  and  $\beta_c$  are given by:

$$A_c = \frac{\left(1 - \frac{t_c}{t_r}\right) \left(a - \frac{t_r}{t_c}\right)}{\left(b - \frac{t_r}{t_c}\right)}; B_c = \frac{(b-a)(b-1)}{b\left(b - \frac{t_r}{t_c}\right)}; C_c = \frac{a}{b} \frac{t_c}{t_r} \quad (7.7f)$$

$$\alpha_c = \frac{1}{t_c}; \beta_c = \frac{b}{t_r}$$

In Eqs. 7.7f,

$$a = \frac{3K_1P_1 + 2q_0P_1}{3K_1P_1 + 2q_1}; b = \frac{6K_1P_1 + q_0P_1}{6K_1P_1 + q_1}; t_r = P_1; t_c = \frac{q_1}{q_2} \quad (7.7g)$$

where

$$P_1 = \frac{\eta}{G_1 + G_2}; q_0 = \frac{2G_1G_2}{G_1 + G_2}; q_1 = \frac{2G_1\eta}{G_1 + G_2} \quad (7.7h)$$

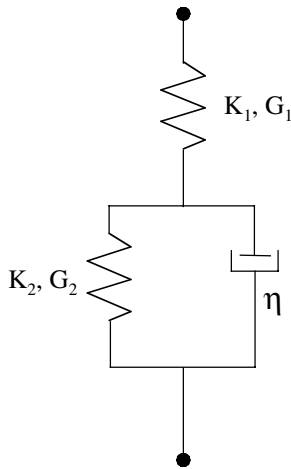


**Fig. 7.10** Three-element spring and dashpot representation of a viscoelastic solid.

The elastic modulus can be extracted from  $G$  and  $K$  by:

$$K = \frac{E}{3(1-2\nu)} \quad (7.7i)$$

$$G = \frac{E}{2(1+\nu)}$$

In practice, values for  $E_1$ ,  $G_2$ , and  $\eta$  can be used to compute the creep response  $h(t)$  and compared to experimentally derived creep data. Judicious adjustment of these three parameters can be used to fit the analytical prediction to the experimental data using a least squares method. The resulting values of  $E_1$ ,  $G_2$ , and  $\eta$  that provide a good fit are those selected as the measured material properties of the specimen. Strojny and Gerberich<sup>46</sup> used a least squares method to fit the three adjustable parameters to experimental results for polymeric thin films and found that the resulting elastic and shear moduli obtained for the films were comparable to those measured for the bulk materials.

## 7.8 Fracture Toughness

Nanoindentation can be used to evaluate the fracture toughness of materials and interfaces in a similar manner to that conventionally used in larger scale testing. During loading, tensile stresses are induced in the specimen material as the radius of the plastic zone increases. Upon unloading, additional stresses arise as the elastically strained material outside the plastic zone attempts to resume its original shape but is prevented from doing so by the permanent deformation

associated with the plastic zone. There exists a large body of literature on the subject of indentation cracking with Vickers and other sharp indenters. In this section, we briefly review the method by which fracture toughness is evaluated from measurements of the sizes of surface cracks.

Generally, there are three types of crack, and they are illustrated in Fig. 7.11. Radial cracks are “vertical” half-penny type cracks that occur on the surface of the specimen outside the plastic zone and at the corners of the residual impression at the indentation site. These radial cracks are formed by a hoop stress and extend downward into the specimen but are usually quite shallow. Lateral cracks are “horizontal” cracks that occur beneath the surface and are symmetric with the load axis. They are produced by a tensile stress and often extend to the surface, resulting in a surface ring that may lead to chipping of the surface of the specimen. Median cracks are “vertical” circular penny cracks that form beneath the surface along the axis of symmetry and have a direction aligned with the corners of the residual impression. Depending on the loading conditions, median cracks may extend upward and join with surface radial cracks, thus forming two half-penny cracks that intersect the surface as shown in Fig. 7.11 (d). They arise due to the action of an outward stress. The exact sequence of initiation of these three types of cracks is sensitive to experimental conditions. However, it is generally observed that in soda-lime glass loaded with a Vickers indenter, median cracks initiate first. When the load is removed, the elastically strained material surrounding the median cracks cannot resume its former shape owing to the presence of the permanently deformed plastic material and this leads to a residual impression in the surface of the specimen.

Residual tensile stresses in the normal direction then produce a “horizontal” lateral crack that may or may not curve upward and intersect the specimen surface. Upon reloading, the lateral cracks close and the median cracks reopen. For low values of indenter load, radial cracks also form during unloading (in other materials, radial cracks may form during loading). For larger loads, upon unloading, the median cracks extend outward and upward and may join with the radial cracks to form a system of half-penny cracks, which are then referred to as “median/radial” cracks. In glass, the observed cracks at the corners of the residual impression on the specimen surface are usually fully formed median/radial cracks.

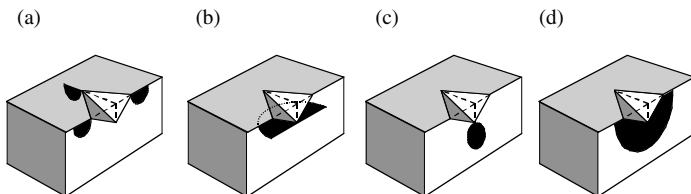


**Fig. 7.11** Crack systems for Vickers indenter: (a) radial cracks, (b) lateral cracks, (c) median cracks, (d) half-penny cracks (after reference 47).

It is the radial and lateral cracks that are of particular importance, since their proximity to the surface has a significant influence on the fracture strength of the specimen. Fracture mechanics treatments of these types of cracks seek to provide a measure of fracture toughness based on the length of the radial surface cracks. Attention is usually given to the length of the radial cracks as measured from the corner of the indentation and then radially outward along the specimen surface as shown in Fig. 7.12.

Palmqvist<sup>48</sup> noted that the crack length “*l*” varied as a linear function of the indentation load. Lawn, Evans, and Marshall<sup>49</sup> formulated a different relationship, where they treated the fully formed median/radial crack and found the ratio  $P/c^{3/2}$  (where *c* is measured from the centre of contact to the end of the corner radial crack) is a constant, the value of which depends on the specimen material.

Fracture toughness is found from:

$$K_c = k \left( \frac{E}{H} \right)^n \frac{P}{c^{3/2}} \quad (7.8a)$$

where *k* is an empirical calibration constant equal to 0.016 and  $n = \frac{1}{2}$  with  $c = l + a$ . Various other studies have since been performed, and Anstis, Chantikul, Lawn, and Marshall<sup>50</sup> determined  $n = 3/2$  and  $k = 0.0098$ . In 1987, Laugier<sup>51</sup> undertook an extensive review of previously reported experimental results and determined that:

$$K_c = x_v (a/l)^{1/2} \left( \frac{E}{H} \right)^{2/3} \frac{P}{c^{3/2}} \quad (7.8b)$$

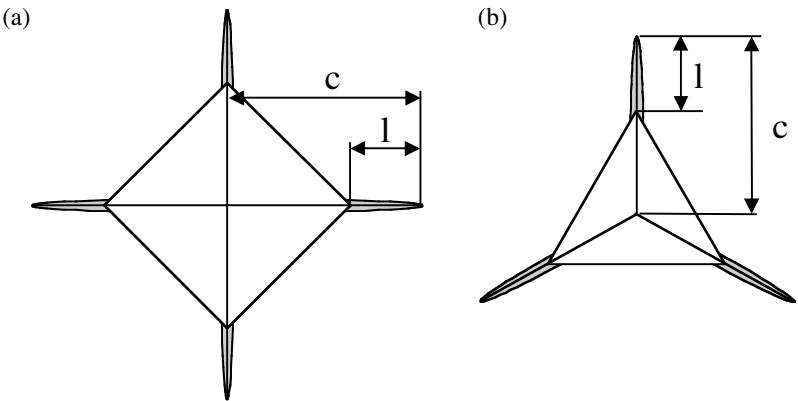


**Fig. 7.12** Crack parameters for Vickers and Berkovich indenters. Crack length *c* is measured from the center of contact to end of crack at the specimen surface (After reference 47).

With  $x_v = 0.015$ , Laugier showed that the radial and half-penny models make almost identical predictions of the dependence of crack length on load. Experiments show that the term  $(a/l)^{1/2}$  shows little variation between glasses (median/radial) and ceramics (radial).

Although the vast majority of toughness determinations using indentation techniques are performed with a Vickers diamond pyramid indenter, the Berkovich indenter has particular usefulness in nanoindentation work. However, the loss of symmetry presents some problems in determining specimen toughness because half-penny cracks can no longer join two corners of the indentation. Ouchterlony<sup>52</sup> investigated the nature of the radial cracking emanating from a centrally loaded expansion star crack and determined a modification factor for stress intensity factor to account for the number of radial cracks formed:

$$k_1 = \sqrt{\frac{n/2}{1 + \frac{n}{2\pi} \sin \frac{2\pi}{n}}} \quad (7.8c)$$

As proposed by Dukino and Swain,<sup>53</sup> this modification has relevance to the crack pattern observed from indentations with a Berkovich indenter. The ratio of  $k_1$  values for  $n = 4$  (Vickers) and  $n=3$  (Berkovich) is 1.073 and thus the length of a radial crack (as measured from the center of the indentation to the crack tip) from a Berkovich indenter should be  $1.073^{2/3} = 1.05$  that from a Vickers indenter for the same value of  $K_1$ . The Laugier expression can thus be written:

$$K_c = 1.073x_v (a/l)^{1/2} \left( \frac{E}{H} \right)^{2/3} \frac{P}{c^{3/2}}. \quad (7.8d)$$

## 7.9 High-Temperature Nanoindentation Testing

An understanding of the wear behaviour for many structural components can best be obtained from tests that are performed at a temperature corresponding to the in-service temperature of the sample. To this end, there have been a number of studies reported that are concerned with the development and use of hot hardness testers.<sup>54-58</sup> Experiments<sup>58</sup> show that, in general, the hardness of materials generally decreases with increasing temperature, especially at temperatures above 1000 °C. Hot hardness testing can also be used to evaluate creep properties of materials.<sup>59</sup>

Indentation testing at high temperatures brings with it several practical difficulties. Not only is the indenter material itself of some concern, but also the method of securely mounting it so as to withstand the indentation load. Figure 7.13 shows a Berkovich diamond indenter mounted by mechanical means only in a molybdenum chuck. This indenter is rated to approximately 750 °C in air.

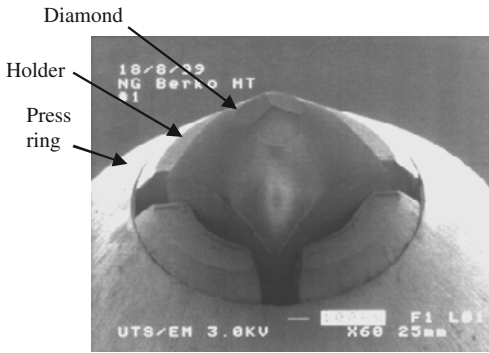


**Fig. 7.13** Berkovich diamond pyramid indenter mounted in a molybdenum chuck designed for high-temperature indentation testing. The diamond “log” is held in position by the “press ring” (Courtesy CSIRO and Synton Inc.).

High-temperature indentation on the nanometre scale is a less developed procedure than macroscopic hot hardness testing. Some nanoindentation instruments offer a hot stage accessory that raises the temperature of the sample to a high temperature (350 – 450 °C). In such instruments, special precautions must be taken to ensure that the indenter tip remains heated to the same temperature as the sample. As shown in Fig. 7.14, a “tip heater” may be employed that provides localized heating to the indenter during the indentation process. Force and displacement data is collected during an indentation test in the normal manner.

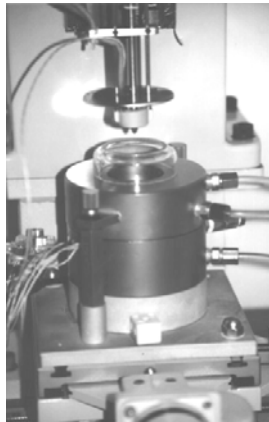


**Fig. 7.14** Hot stage accessory fitted to a nanoindentation test instrument. The indenter is enclosed in a special tip heater. A water-cooled jacket surrounds an insulated sample chamber that is heated using a temperature-controlled furnace coil (Courtesy CSIRO).

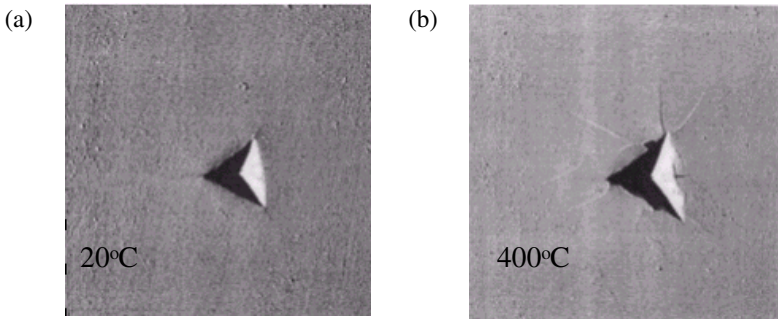


**Fig. 7.15** Residual impressions made in sapphire at (a) 20 °C and (b) 400 °C with a Berkovich indenter at a maximum load of 1 N. Note the presence of cracks in the specimen indented at high temperature (Courtesy CSIRO).

Figure 7.15 show AFM images of residual impressions made in sapphire at 20 °C and 400 °C with a Berkovich indenter at a maximum load of 1 N using the apparatus shown in Fig. 7.14. Note the presence of cracks in the specimen surface at 400 °C that are not in evidence in the sample tested at 20 °C.

In contrast to the apparatus illustrated in Fig. 7.14, Syed Asif and Pethica<sup>60</sup> have combined a Peltier device with a nanoindentation instrument to measure creep and strain-rate dependence of indium at a maximum temperature of 60 °C. This device has the capability of testing at temperatures below room temperature to a minimum of approximately  $-5$  °C.

A common difficulty encountered in hot hardness testing is deterioration of the indenter at high temperatures. The traditional diamond indenter graphitizes at temperatures above 1000 °C. Other indenter materials such as alumina, silicon nitride, silicon carbide, and cubic boron nitride offer possibilities but are often unsuitable because their hardness is comparable to that of the prospective test specimen. However, the technique of mutual indentation can be used in these circumstances.<sup>55</sup> In mutual indentation testing, two crossed cylinders or wedges are brought into contact and the depth of penetration between them measured.

While such nanoindentation testing at elevated temperatures is relatively rare, it is of considerable practical importance. For example, in the semiconductor industry the performance of structural materials on a micron scale are to be evaluated and optimized for in-service temperatures. Other applications include the properties and performance of thermal barrier coatings, the response of polymers at elevated temperatures and the surface properties of ceramic turbine blades.

## 7.10 Strain-hardening exponent

Traditional tensile tests are often used to generate a uniaxial stress strain curve for the specimen material from which elastic and plastic behaviour of the specimen material may be measured. For an ideal elastic–plastic material, the stress reaches a maximum value and thereafter remains constant with increasing strain. For many materials (e.g., annealed metals), the stress increases with increasing strain due to strain-hardening. Strain-hardening occurs due to the pile-up and interaction between dislocations in the material. These interactions serve to make the material “harder.”

As shown in Chapters 4 and 6, the strain-hardening exponent  $x$  is a measure of the strain-hardening properties of a particular material, and this is illustrated in Fig. 7.16. For  $x = 0$ , the solid is elastic perfectly-plastic. In many practical applications, uniaxial tensile tests are not available, or are unsuitable. A nanoindentation test, on the other hand, is a virtually non-destructive test method that yields values of hardness, modulus, and, in some circumstances, strain-hardening exponent.

There are a number of ways to determine the strain-hardening exponent. One of the most straight forward methods is to obtain an experimental load-displacement curve, using a spherical indenter, and then using the methods of Chapter 5 to create a simulated, or theoretical curve, adjusting  $E$ ,  $H$ , and  $x$  to obtain a best fit to the experimental data (see Eq. 5.2).

An alternative method is to make use of Meyer’s original work in which it was found that the slope of a plot of  $\log P$  vs  $\log d$ , where  $d$  is the diameter of the residual impression, gave a value for Meyer’s index, by which the strain-hardening exponent could be calculated from Eq. 2.3.1d

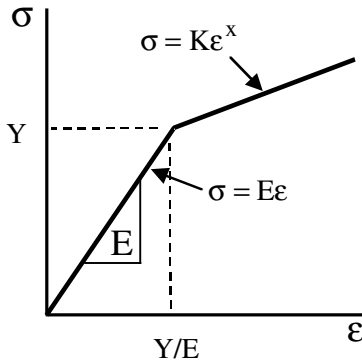


**Fig. 7.16** Uniaxial stress–strain curve for an ideal elastic–plastic specimen material with strain-hardening index  $x$ . When  $x = 0$ , the material is elastic perfectly-plastic.

Shinohara, Yasuda, Yamada, and Kinoshita<sup>61</sup> use an alternative approach specifically directed towards metals such as copper, aluminum, and nickel. It was found that in copper, the measured hardness  $H$  using a pyramidal indenter showed a dependence on the indenter load  $P$  and this load dependence systematically depended upon the value of the strain-hardening index  $x$ . These workers also showed that the slope of  $H$  vs  $\log P$  was linear and decreased with increasing  $n$ . However, such a procedure requires many measurements of  $H$  and  $P$  over a range of loads, and also requires tensile tests to be performed to establish the specific relationship between  $x$  and the slope for the material being tested. To overcome these limitations, a generalized relationship:

$$\frac{H(P)}{H_o(P)} = -0.83x + 0.95. \quad (7.10b)$$

was proposed where  $H_o(P)$  is the value of  $H$  obtained on the metal that shows no strain-hardening — i.e. fully hardened metals.

## 7.11 Impact

Results from conventional quasi-static indentation tests are sometimes not easily correlated with actual product performance where the actual surfaces are subjected to erosive wear, multiple impacts, or stress-strain cycling. A typical example is a tool bit coating which experience an aggressive vibration contact with the workpiece during machining.

Impact testing on a nanometre scale is a fairly novel testing technique. In one commercially available device, a repetitive contact at a single point is obtained by oscillating the sample against the indenter that is mounted on a freely swinging pendulum. When a change in the contact energy occurs (after fracture of the surface or partial debonding of a coating), a change in indenter recoil takes place. Changes in indentation depth are a measure of surface damage. With scanning impact testing, the sample is moved sideways at either constant or steadily increasing normal load and this causes the indenter to continuously impact along a wear track, simulating many in-service film failure situations, e.g., erosive wear and coating adhesion failure. The impact energy is determined by the oscillation amplitude, frequency, and the applied load.

For quantitative impact testing, the pendulum is moved away from the specimen by a known distance and then released to produce a single impact. The impact energy is known. Successive impacts can be produced at a single point until failure occurs. In most cases, an initial period of fatigue damage generation occurs, in which small cracks develop and expand, but in which no appreciable increase in penetration depth is observed. Eventually, the cracks coalesce, material is removed, and a sudden depth increase is recorded.

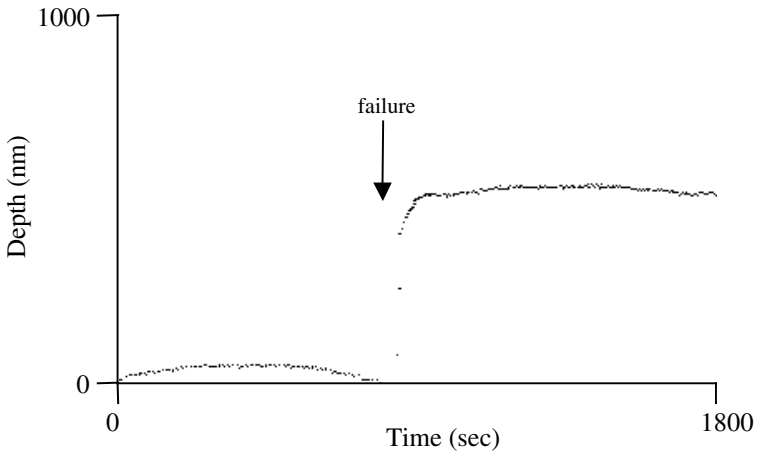


**Fig. 7.17** Impact result for 567 nm thick diamond-like carbon (DLC) film on a silicon substrate with 25  $\mu\text{m}$  radius indenter. One impact every four seconds. Failure of the film occurred after 14 minutes (Courtesy Micro Materials Ltd.).

Figure 7.17 shows an impact test result for a 567 nm thick diamond-like carbon (DLC) film on a silicon substrate using the successive single impact method. In this test, there was one impact every 4 seconds, each with an energy of 27 nJ. The indenter was a 25  $\mu\text{m}$  radius diamond sphere. The result illustrates fatigue crack growth (the diamond begins to move away from the surface due to increasing crack volume as evidenced by an decrease in indentation depth) followed by an abrupt film delamination. The silicon substrate itself showed no sign of failure under the same test conditions.

One quantitative result from impact testing is the “dynamic hardness,” which is defined as the energy consumed during the indentation divided by the volume of the indentation. The energy of the indentation can be determined from the ratio of the impact and rebound velocities. An example of the technique is given in Chapter 10.

## References

1. B.N. Lucas, W.C. Oliver, and J.E. Swindeman, "The dynamics of frequency specific, depth sensing indentation testing," *Mat. Res. Soc. Symp. Proc.* 522, 1998, pp. 3–14.
2. J.-L. Loubet, B.N. Lucas, and W.C. Oliver, in *NIST Special Publication 896, Conference Proceedings: International Workshop on Instrumented Indentation*, eds. D.T. Smith (NIST) 1995, pp. 31–34.
3. S.A. Syed Asif, R.J. Colton, and K.J. Wahl, "Nanoscale surface mechanical property measurements: Force modulation techniques applied to nanoindentation," in *Interfacial properties on the submicron scale*, J. Frommer and R. Overney, eds. ACS Books, Washington, DC, 2001, pp. 189–215.
4. S.A. Syed Asif, K.J. Wahl, and R.J. Colton, "The influence of oxide and adsorbates on the nanomechanical response of silicon surfaces," *J. Mater. Res.* 15 2, 2000, pp. 546–553.
5. N.A. Burnham, S.P. Baker, and H.M. Pollock, "A model for mechanical properties of nanoprobcs," *J. Mater. Res.* 15 9, 2000, pp. 2006–2014.
6. T.P. Weihs, S. Hong, J.C. Bravman, and W.D. Nix, "Mechanical deflection of cantilever microbeams: A new technique for testing the mechanical properties of thin films," *J. Mater. Res.* 3 5, 1988, 931–942.
7. J.L. Hay, M.E. O'Hern, and W.C. Oliver, "The importance of contact radius for substrate-independent property measurement of thin films," *Mat. Res. Soc. Symp. Proc.* 522, 1998, pp. 27–32.
8. M.G.D. El-Sherbiny and J. Halling, "The Hertzian contact of surfaces covered with metallic films," *Wear*, 40, 1976, pp. 325–337.
9. J.A. Ogilvy, "A parametric elastic model for indentation testing of thin films," *J. Phys. D: Appl. Phys.* 26, 1993, pp. 2123–2131.
10. R.B. King, "Elastic analysis of some punch problems for a layered medium," *Int. J. Solids Structures*, 23 12, 1987, pp. 1657–1664.
11. M.F. Doerner and W.D. Nix, "A method of interpreting the data from depth-sensing indentation instruments," *J. Mater. Res.* 1 4, 1986, pp. 601–609.
12. H. Gao, C-H Chiu, and J. Lee, "Elastic contact versus indentation modeling of multi-layered materials," *Int. J. Solids Structures*, 29 20, 1992, pp. 2471–2492.
13. N. Schwarzer, M. Whittling, M. Swain, and F. Richter, "The analytical solution of the contact problem of spherical indenters on layered materials: Application for the investigation of TiN films on silicon," *Thin Solid Films*, 270 1-2, 1995, pp. 371–375.
14. N. Schwarzer, "Coating design due to analytical modelling of mechanical contact problems on multilayer systems," *Surf. Coat. Technol.* 133, 2000, pp. 397–402.
15. H. Bückle, in J.W. Westbrook and H. Conrad, eds. *The Science of Hardness Testing and its Applications*, American Society for Metals, Metals Park, OH, 1973, pp. 453–491.
16. B. Jonsson and S. Hogmark, "Hardness measurements of thin films," *Thin Solid Films*, 114, 1984, pp. 257–269.

17. P.J. Burnett and D.S. Rickerby, "The mechanical properties of wear-resistance coatings I: Modelling of hardness behaviour," *Thin Solid Films*, 148, 1987, pp. 41–50.
18. P.J. Burnett and D.S. Rickerby, "The mechanical properties of wear-resistance coatings II: Experimental studies and interpretation of hardness," *Thin Solid Films*, 148, 1987, pp. 51–65.
19. A.K. Bhattacharya and W.D. Nix, "Finite element simulation of indentation experiments," *Int. J. Solids Structures*, 24 12, 1988, pp. 1287–1298.
20. D. Stone, W.R. LaFontaine, P. Alexopolous, T.-W. Wu, and Che-Yu Li, "An investigation of hardness and adhesion of sputter-deposited aluminium on silicon by utilizing a continuous indentation test," *J. Mater. Res.* 3 1, 1988, pp. 141–147.
21. G.G. Stoney, "The tension of metallic films deposited by electrolysis," *Proc. R. Soc. A* 9, 1909, pp. 172–175.
22. D.B. Marshall and A.G. Evans, "Measurement of adherence of residually stressed thin films by indentation mechanics of interface delamination," *J. Appl. Phys.* 56 10, 1984, pp. 2632–2638.
23. M.V. Swain and J. Menčík, "Mechanical property characterization of thin films using spherical tipped indenters," *Thin Solid Films*, 253, 1994, pp. 204–211.
24. A.J. Whitehead and T.F. Page, "Nanoindentation studies of thin film coated systems," *Thin Solid Films*, 220, 1992, pp. 277–283.
25. M.D. Kriese, N.R. Moody, and W.W. Gerberich, "Effects of annealing and interlayers on the adhesion energy of copper thin films to SiO<sub>2</sub>/Si substrates," *Acta Mater.* 46, 1998, pp. 6623–6630.
26. A. A. Volinsky, N.R. Moody, and W.W. Gerberich, "Superlayer residual stress effect on the indentation adhesion measurements," *Mat. Res. Soc. Symp. Proc.* 594, 2000, pp. 383–388.
27. J. Sekler, P.A. Steinmann, and H.E. Hintermann, "The scratch test: Different critical load determination techniques," *Surface and Coatings Technology*, 36, 1988, pp. 519–529.
28. N. Gane and J. Skinner, "The friction and scratch deformation of metals on a micro scale," *Wear*, 24, 1973, pp. 207–217.
29. P.A. Steinmann, Y. Tardy, and H.E. Hintermann, "Adhesion testing by the scratch test method: The influence of intrinsic and extrinsic parameters on the critical load," *Thin Solid Films*, 154, 1987, pp. 333–349.
30. V.D. Jardret and W.C. Oliver, "Viscoelastic behaviour of polymer films during scratch test: A quantitative analysis," *Mat. Res. Soc. Symp. Proc.* 594, 2000, pp. 251–256.
31. S. Enders, P. Grau, and G. Berg, "Mechanical characterization of surfaces by nanotribological measurements of sliding and abrasive terms," *Mat. Res. Soc. Symp. Proc.* 594, 2000, pp. 531–536.
32. F.P. Bowden and D. Tabor, *The Friction and Lubrication of Solids*, Oxford University Press, Oxford, 1950.
33. M. Shiwa, E.R. Weppelmann, D. Munz, M.V. Swain, and T. Kishi, "Acoustic emission and precision force-displacement observations on pointed and spherical indentation of silicon and TiN film on silicon," *J. Mat. Sci.* 31, 1996, 5985–5991.
34. D. Tabor, *Hardness of Metals*, Clarendon Press, Oxford, 1951.

35. R. Hill, B. Storåkers, and A.B. Zdunek, "A theoretical study of the Brinell hardness test," *Proc. R. Soc. Lond.* A423, 1989, pp. 301–330.
36. M.M. Chaudhri, "Subsurface deformation patterns around indentation in work-hardened mild steel," *Phil. Mag. Lett.* 67 2, 1993, pp. 107–115.
37. A.F. Bower, N.A. Fleck, A. Needleman, and N. Ogbonna, "Indentation of a power-law creeping solid," *Proc. R. Soc. Lond.* A441, 1993, pp. 97–124.
38. B. Storåkers and P.-L. Larsson, "On Brinell and Boussinesq indentation of creeping solids," *J. Mech. Phys. Solids*, 42 2, 1994, pp. 307–332.
39. M.J. Mayo and W.D. Nix, "A microindentation study of superplasticity in Pb, Sn, and Sn-38wt%Pb," *Acta Metall.* 36 8, 1988, pp. 2183–2192.
40. N.R. Moody, A. Strojny, D. Medlin, S. Guthrie, and W.W. Gerberich, "Test rate effects on the mechanical behaviour of thin aluminium films," *Mat. Res. Soc. Symp. Proc.* 522, 1998, pp. 281–286.
41. Y.-T. Cheng and C.-M. Cheng, "What is indentation hardness?," *Surf. Coat. Tech.* 133-134, 2000, pp. 417–424.
42. W.B. Li and R. Warren, "A model for nano-indentation creep," *Acta Metall. Mater.* 41 10, 1993, pp. 3065–3069.
43. P.M. Sargent and M.F. Ashby, "Indentation creep," *Mat. Sci. and Tech.* 8, 1992, pp. 594–601.
44. L. Cheng, L.E. Scriven, and W.W. Gerberich, "Viscoelastic analysis of micro- and nanoindentation," *Mat. Res. Symp. Proc.* 522, 1998, pp. 193–198.
45. J.R.M. Radok, "Viscoelastic stress analysis," *Q. Appl. Math.* 15, 1957, pp. 198–202.
46. A. Strojny and W.W. Gerberich, "Experimental analysis of viscoelastic behaviour in nanoindentation," *Mat. Res. Soc. Symp. Proc.* 522, 1998, pp. 159–164.
47. A.C. Fischer-Cripps, *Introduction to Contact Mechanics*, Springer-Verlag, New York, 2000.
48. S. Palmqvist, "A method to determine the toughness of brittle materials, especially hard materials," *Jernkontorets Ann.* 141, 1957, pp. 303–307.
49. B.R. Lawn, A.G. Evans, and D.B. Marshall, "Elastic/plastic indentation damage in ceramics: the median/radial crack system," *J. Am. Ceram. Soc.* 63, 1980, pp. 574–581.
50. G.R. Anstis, P. Chantikul, B.R. Lawn, and D.B. Marshall, "A critical evaluation of indentation techniques for measuring fracture toughness: I Direct crack measurements," *J. Am. Ceram. Soc.* 64 9, 1981, pp. 533–538.
51. M.T. Laugier, "Palmqvist indentation toughness in WC-Co composites," *J. Mater. Sci. Lett.* 6, 1987, pp. 897–900.
52. F. Ouchterlony, "Stress intensity factors for the expansion loaded star crack," *Eng. Frac. Mech.* 8, 1976, pp. 447–448.
53. R. Dukino and M.V. Swain, "Comparative measurement of indentation fracture toughness with Berkovich and Vickers indenters," *J. Am. Ceram. Soc.* 75 12, 1992, pp. 3299–3304.
54. E.R. Petty and H. O'Neill, "Hot hardness values in relation to the physical properties of metals," *Metallurgica*, 63, 1961, pp. 25–30.
55. A.G. Atkins and D. Tabor, "Mutual indentation hardness apparatus for use at very high temperatures," *Brit. J. Appl. Phys.* 16, 1965, pp. 1015–1021.

56. A.G. Atkins and D. Tabor, "Hardness and deformation properties of solids at very high temperatures," *Proc. R. Soc. Lond.* A292, 1966, pp. 441–459.
57. A.G. Atkins and D. Tabor, "The plastic deformation of crossed cylinders and wedges," *J. Inst. Metals*, 94, 1966, pp. 107–115.
58. E.A. Payzant, H.W. King, S. Das Gupta, and J.K. Jacobs, "Hot hardness of ceramic cutting tools using depth of penetration measurements," in *Development and Applications of Ceramics and New Metal Alloys*, H. Mostaghaci and R.A.L. Drew, eds. Canadian Institute of Mining and Metallurgy, Montreal, 1993.
59. T.R.G. Kutty, C. Ganguly, and D.H. Sastry, "Development of creep curves from hot indentation hardness data," *Scripta Materialia*, 34 12, 1996, pp. 1833–1838.
60. S.A. Syed Asif and J.B. Pethica, "Nano-scale indentation creep testing at non-ambient temperatures," *J. Adhesion*, 67, 1998, pp. 153–165.
61. K. Shinohara, K. Yasuda, M. Yamada, and C. Kinoshita, "Universal method for evaluating work-hardening exponent of metals using ultra-microhardness tests," *Acta. Metall. Mater.* 42 11, 1994, pp. 3909–3915.

# Chapter 8

## Nanoindentation Test Standards

### 8.1 Nanoindentation Test Standards

The ISO (the International Organization for Standardization) has recently issued a draft international standard ISO 14577 entitled “Metallic materials — Instrumented indentation test for hardness and materials parameters.”<sup>1</sup> The standard covers depth-sensing indentation testing for indentations in the macro, micro and nano depth ranges.

The ISO is a worldwide federation of national standards bodies. Preparation of international standards is normally carried out through ISO technical committees. Member bodies interested in a subject for which a technical committee has been established have the right to be represented on that committee.

International Standards are prepared in accordance with ISO/IEC Directives, Part 3. Draft international standards are circulated to the member bodies for voting. Publication as an International Standard requires approval by at least 75 % of the member bodies. Draft International Standard ISO 14577 was prepared by Technical Committee ISO/TC 164, Mechanical testing of metals, Subcommittee SC 3. In this chapter, the basic features of the draft standard are summarized.

### 8.2 ISO 14577

ISO 14577 is a proposed international standard that deals with instrumented indentation tests for determining hardness and materials parameters. It is generally agreed that hardness is a measure of a material’s resistance to permanent penetration by another harder material. Conventional hardness tests typically use the results of measurements of the size of residual impression made by an indenter loaded onto the specimen surface after the test force has been removed. These types of test ignore any elastic recovery of the specimen material that might occur upon removal of the test load. For large-scale testing, the effects of this are not too severe since experience has shown that the lateral dimensions of most indenters (with the exception perhaps of those made with a Knoop indenter) are not significantly different from full load to full unload.

ISO 14577 allows the evaluation of indentation hardness using instrumented indentation (or depth-sensing indentation) where both the force and displacement during plastic and elastic deformation are measured. Traditional hardness values can be determined as well as indentation hardness and modulus of the test material. With the instrumented indentation technique, it is not necessary to measure the dimensions of the residual impression optically. ISO 14577 consists of three parts together with various annexes.

Part 1 of the Standard contains a description of the method and principles of the indentation test and also contains an Annex that provides definitions and methods of calculation of the material parameters to be measured.

Part 2 of the Standard specifies the method of verification and calibration of the test instruments. A direct method is given for verification of the main functions of the instrument and an indirect method for determining the repeatability of the instrument is also given. The annexes to Part 2 give recommendations for the design of the instrument and methods to be used for calibration and verification of the instruments on a periodic basis.

Part 3 of ISO 12577 specifies the method of calibration of reference blocks that are to be used for verification of indentation testing instruments.

The notation in the Standard is different to that presented elsewhere in this book and in the literature. Figure 8.1 shows the notation used for the relevant features of the indentation test in the Standard.

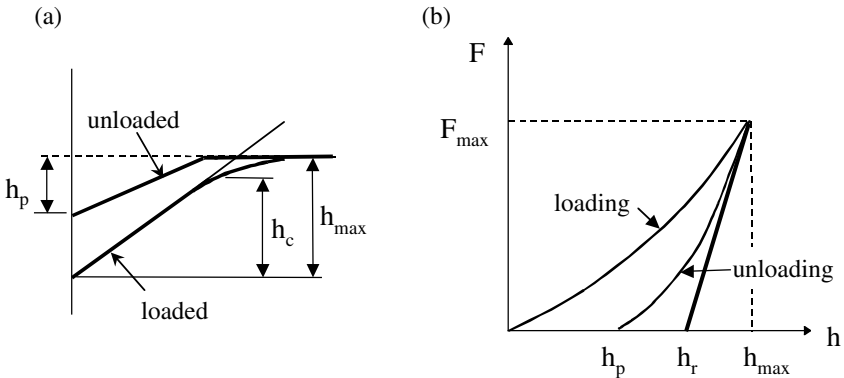


**Fig. 8.1** Indentation test procedure. A loading sequence is followed by an unloading sequence.  $h_p$  is the depth of the residual impression,  $h_r$  is the intercept of the tangent to the initial unloading curve,  $h_{max}$  is the maximum penetration beneath the specimen surface, and  $F_{max}$  is the maximum load applied to the indenter.

## 8.2.1 ISO 14577 Part 1: Test method

Part 1 of the Standard contains a description of the method and principles of the indentation test and also contains an Annex that provides definitions and methods of calculation of the material parameters to be measured.

### 8.2.1.1 Test method and requirements

Part 1 of ISO 14577 specifies the method of instrumented indentation test for determination of hardness and other material parameters for three defined ranges of hardness as shown in Table 8.1, where  $h$  is the total indentation depth and  $F$  is the test force:

**Table 8.1** Ranges of hardness testing as defined in ISO 14577 Part 1.

Macro Range	Micro Range	Nano Range
$2 \text{ N} \leq F \leq 30\,000 \text{ N}$	$2 \text{ N} > F; h > 0.02 \mu\text{m}$	$h \leq 0.02 \mu\text{m}$

For testing under this standard, an indenter that is harder than the specimen is required. The indenter may take the form of a four-sided Vickers diamond indenter, a Berkovich triangular diamond pyramid indenter,<sup>††</sup> a hardmetal ball of a specified composition (see Section 8.2.2), or a diamond spherical indenter. The Standard allows for the use of indenters with other geometries and manufacture.

The indentation test procedure can either be load or displacement controlled. The test force  $F$ , indentation depth  $h$ , and time are recorded during the test procedure. The resulting load-displacement data set is used to calculate the relevant properties of the specimen material. The zero point, or initial penetration depth, for the displacement measurements are required to be determined for each individual test. For time-dependent effects such as creep and/or thermal drift, the force is to be kept constant and the change of indentation depth is to be recorded (for load-controlled testing) or the depth is to be kept constant by varying the load for depth-controlled testing.

The indentation testing instrument is required to have the capability of applying the test forces within the limits set down in Part 2 of the Standard. The instrument shall have the capability for continuous measuring of applied load, displacement, and time and is required to be able to compensate for the compliance of the instrument and non-ideal indenter geometry by the use of an area function.

The Standard specifies that the indentation test shall be carried out on a specimen surface that is smooth and free from lubricants and contaminants and

<sup>††</sup> There are two kinds of Berkovich indenters. The Berkovich indenter was originally designed with a face angle of  $65.03^\circ$  that gives the same actual surface area to depth ratio as a Vickers indenter. The modified Berkovich indenter is constructed with a face angle of  $65.27^\circ$  that gives the same projected area to depth ratio as a Vickers indenter.

is of an acceptable surface roughness. The surface of the specimen should be prepared so that its surface properties are not unintentionally modified by cold working or strain-hardening. The specimen thickness shall be such that the results are not influenced by the method of support of the specimen. As a rule of thumb, the specimen thickness should be at least 10 times the indentation depth or 3 times the indentation diameter. The specimen shall be firmly supported on a rigid support and, if required, fixed in place with a suitable specimen holder.

Each individual test should be carried out at stable temperature conditions after both the specimen and instrument have reached an equilibrium temperature and within which the instrument has been shown to be in calibration. The temperature of the system shall be maintained to an appropriate level during the test so as to minimize errors in displacement readings due to thermal drift.

During the test, a sufficient number of data points should be recorded so that initial penetration depth may be calculated with the required accuracy. The initial penetration depth can be calculated using a polynomial regression to the first 10% of the load-displacement data or from the first increase in load during the indenter approach phase. During the initial approach, the approach speed of the indenter should be less than 0.010  $\mu\text{m}/\text{sec}$  for the micro range and less than 0.0020  $\mu\text{m}/\text{sec}$  for the nano range. The load (or displacement) can be controlled either continuously or stepwise. Both force and depth are to be recorded at specified time intervals. The applied force should be applied at a constant rate (N/sec) for load controlled testing or to provide a constant displacement rate (mm/sec) for depth controlled testing. The load removal rate is not specified by the Standard.

Hold periods where the load is held constant and the depth measured continuously or for a specified interval for load controlled testing (or constant depth and the load monitored in depth control) may be inserted at convenient points in the test cycle. The data taken within the hold periods may be used to determine the thermal drift rate during the test.

The Standard recommends that sufficient care be taken so that the results are not affected by the presence of an edge or any previous residual impression in the specimen surface. Indentations shall be spaced at approximately three to five times their diameter of residual impression from such features.

The Standard requires an estimation of the uncertainty of the measurement to be made. These arise from uncertainties resulting from the calibration of the instrument, and uncertainties arising from standard deviations from a series of measurements. The Standard also specifies the format of the test report.

### *8.2.1.2 Analysis procedures*

Part 1 of the Standard deals with the procedure and the principle of the instrumented indentation test. Annex A of the Standard specifies the definitions of the material properties to be calculated and their method of calculation.

### 8.2.1.2.1 Martens (Universal) hardness (HM)

The Martens hardness is defined as the test force  $F$  divided by the actual surface contact area of the indentation and is measured under applied test force — not from the dimensions of the residual impression. The Martens hardness value  $HM$  is defined for Vickers and Berkovich indenters. It is not defined for spherical or Knoop indenters. The Martens hardness was previously designated “Universal hardness”  $HU$ . For a Vickers indenter, Martens hardness is given by:

$$\begin{aligned} HM &= \frac{F}{A_s(h)} \\ &= \frac{F}{26.43 h^2} \end{aligned} \quad (8.2.1.2.1a)$$

where

$$A_s(h) = \frac{4 \sin(\alpha)}{\cos^2(\alpha)} h^2 \quad (8.2.1.2.1b)$$

For an unmodified Berkovich indenter, the Martens hardness is found from:

$$\begin{aligned} HM &= \frac{F}{A_s(h)} \\ &= \frac{F}{26.44 h^2} \end{aligned} \quad (8.2.1.2.1c)$$

where

$$A_s(h) = \frac{3\sqrt{3} \tan \alpha}{\cos \alpha} h^2 \quad (8.2.1.2.1d)$$

In Eqs. 8.2.1.2.1b and 8.2.1.2.1d  $\alpha$  is the face angle of the indenter ( $68^\circ$  for a Vickers indenter and  $65.03^\circ$  for a Berkovich indenter) and  $h$  is the penetration depth measured from the initial penetration depth. The quantity  $A_p$  is the surface area of the indenter that penetrates beyond the initial contact point.

Martens hardness values are determined from load and depth readings during the application of the test force. An indentation depth of greater than  $0.2 \mu\text{m}$  is required.

The Martens hardness value is denoted by the symbol  $HM$ , followed by the test conditions:

1. indenter, if not Vickers
2. test force in N
3. time for the application of the test force in s
4. number of steps until the maximum test force is reached if the test force is not applied continuously

For example, “HM (Berkovich) 0.5/20/30 = 6500 N/mm<sup>2</sup>” represents a Martens hardness value of 6500 N/mm<sup>2</sup>, determined with a test force of 0.5 N, applied during 20 seconds in 30 steps. If the hardness is determined with a Vickers indenter, then the bracketed description of the indenter type is not required.

### 8.2.1.2.2 Martens hardness $HM_S$

The Martens hardness can be computed from the slope of the increasing load-displacement curve and, when measured in this way, is designated  $HM_S$ . It is found that for many materials, the load and depth are related according to:

$$h = m \sqrt{F} \quad (8.2.1.2.2a)$$

where  $m$  is a constant that depends upon the shape of the indenter which is found by linear regression of data plotted in accordance with Eq. 8.2.1.2.2a. The Martens hardness is then found from:

$$HM_S = \frac{1}{m^2 A_s(h)/h^2} \quad (8.2.1.2.2b)$$

where  $A_s(h)/h^2$  is 26.43 for a Vickers indenter and 26.44 for a Berkovich indenter. This method does not rely on the determination of the initial penetration depth nor is it influenced by surface roughness. However, for specimens which show a variation in hardness as a function of depth, the value determined using this method will be different from that given in Section 8.2.1.2.1.

### 8.2.1.2.3 Indentation hardness ( $H_{IT}$ )

Indentation hardness  $H_{IT}$  is defined as the mean contact pressure, that is, the indentation load divided by the projected area of contact, and as such is physically equivalent to the Meyer hardness (see Section 2.3.1). Using the notation specified in the Standard, the indentation hardness is found from:

$$H_{IT} = \frac{F_{\max}}{A_p} \quad (8.2.1.2.3a)$$

where  $F_{\max}$  is the maximum load and  $A_p$  is the projected (or cross-sectional) area of contact at that load.  $A_p$  is determined from the load-displacement curve using what is essentially the multiple-point unload method described in Chapter 3. In the Standard,  $A_p$  is referred to as the “area function” of the indenter and relates the projected area to the distance from the tip of the indenter. For non-ideal indenters, cubic or polynomial fitting, look-up table or calibration graph, or a spline fit may be used to define the area function. For ideal indenters, the area function can be determined from the expressions shown in Table 8.2 that are equivalent to those given in Table 1.1 in Chapter 1.

**Table 8.2** Projected areas, intercept corrections, and geometry correction factors for various types of indenters used in the determination of Indentation hardness.

Indenter type	Projected area	Geometry correction factor $\epsilon$
Berkovich	$A_p = 23.97h_c^2$	0.75
Berkovich (modified)	$A_p = 24.5h_c^2$	0.75
Vickers	$A_p = 24.5h_c^2$	0.75

In the Standard,  $h_c$  is the depth of contact of the indenter (equivalent to  $h_p$  elsewhere in this book) with the specimen given by:

$$h_c = h_{\max} - \epsilon(h_{\max} - h_r) \quad (8.2.1.2.3b)$$

where  $\epsilon$  is a geometry correction factor given in Table 8.2,  $h_r$  is the depth found from extrapolating the slope of the tangent of the initial unloading to the depth axis, and  $h_{\max}$  is the maximum penetration depth as shown in Fig. 8.1.<sup>‡‡</sup> Different methods for the determination of  $h_r$  are allowed: Linear fit to the initial unloading data or a power-law fit in accordance with Doerner and Nix<sup>2</sup> and Oliver and Pharr<sup>3</sup> respectively.

The Standard specifies that the upper 80 % of the unloading curve is to be taken for the least squares fitting procedure. If only 50 % or less of the unloading data are used, the indentation test shall be interpreted with some care. The slope of the tangent is found by differentiating the least squares fitted line, or curve, and evaluating this at  $F_{\max}$ . The intercept of this tangent with the displacement axis gives a value for  $h_r$ .

The indentation hardness  $H_{IT}$  value is expressed together with the test conditions in a manner similar to that for the Martens hardness.

#### 8.2.1.2.4 Indentation modulus ( $E_{IT}$ )

The indentation modulus  $E_{IT}$  is calculated from the slope of the tangent for the calculation of indentation hardness following the method given by Oliver and Pharr.<sup>3</sup> The indentation modulus typically provides values that are similar to Young's modulus for the specimen material. The indentation modulus is found from:

<sup>‡‡</sup> Note, the terminology used in the draft standard is slightly different from that used elsewhere in this book. In particular, the geometry correction factor  $\epsilon$  given above should not be confused with the geometry correction factor  $\beta$  described in Chapter 3.

$$E_{IT} = \frac{1 - (\nu_s)^2}{\frac{1}{E_r} - \frac{1 - (\nu_i)^2}{E_i}} \quad (8.2.1.2.4a)$$

where the subscripts i and r refer to properties of the specimen and the indenter, respectively. For the specimen,  $E_r$  is the reduced modulus, which is found from the indentation test data and is given by:

$$E_r = \frac{\sqrt{\pi}}{2 C \sqrt{A_p}} \quad (8.2.1.2.4b)$$

where  $C$  is the compliance of the contact,  $dh/dF$ ,  $\nu_s$  is Poisson's ratio of the specimen, and  $A_p$  is the projected contact area given by:

$$\sqrt{A_p} = 4.950h_c \quad (8.2.1.2.4c)$$

for a Vickers and modified Berkovich indenter and

$$\sqrt{A_p} = 4.896h_c \quad (8.2.1.2.4d)$$

for a Berkovich indenter.

The indentation modulus is expressed together with the test conditions in the following manner:  $E_{IT} 0.5/10 = 210000 \text{ N/mm}^2$ . In this example, the indentation modulus is  $210000 \text{ N/mm}^2$ , determined using a maximum applied test force of  $0.5 \text{ N}$ , which was removed continuously over a period of 10 seconds. Interestingly, according to the Standard, no correction is applied to account for the non-axial-symmetric nature of the indenter ( $\beta$  in Eq. 3.2.4.1d); however, the Standard does refer to the existence of such a correction, but does not require it to be applied.

### 8.2.1.2.5 Creep

Creep within the specimen can occur under indentation loading and manifests itself as a change of the indentation depth with a constant test force applied. The relative change of the indentation depth is referred to as the creep of the specimen material. Naturally, creep is indistinguishable from thermal drift so that care must be taken to interpret the results. Figure 8.2 shows the type of data obtained from a creep test.

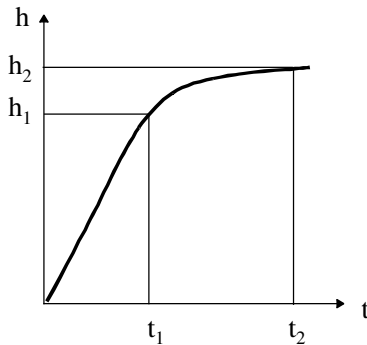


**Fig. 8.2** The test force is applied over a time period 0 to  $t_1$ . The test force is held constant during time  $t_1$  to  $t_2$  and the change in penetration depth  $h_1$  to  $h_2$  is measured.

The creep value  $C_{IT}$  is expressed as a percentage and is calculated from:

$$C_{IT} = \frac{h_2 - h_1}{h_1} 100 \quad (8.2.1.2.5a)$$

where  $h_1$  is the indentation depth (in mm) at the test force and which is kept constant,  $t_1$  is the time at which the test force is reached,  $h_2$  is the indentation depth at a later time  $t_2$ . The creep value is reported as the relative change of the indentation depth  $C_{IT}$  (as a %) together with the test conditions. For example,  $C_{IT} 0.5/10/50 = 2.5\%$  means a creep of 2.5% determined with a test force of 0.5 N, which was applied in 10 seconds and kept constant for 50 seconds. Note that  $C_{IT}$  is *not* expressed as a displacement vs time (mm/sec).

### 8.2.1.2.6 Relaxation

The relaxation  $R_{IT}$  is the relative change of the test force and is the “depth control” equivalent to creep. For measuring relaxation, the indentation depth is held constant and the relative change in test force is calculated. The relaxation value is given by:

$$R_{IT} = \frac{F_1 - F_2}{F_1} 100 \quad (8.2.1.2.6a)$$

and is expressed as a percentage. In Eq. 8.2.1.2.6a,  $F_1$  is the force at the indentation depth.  $F_2$  is the force after the time during which the indentation depth was kept constant. The relaxation value is expressed as the percentage change in force along with the test conditions. For example,  $R_{IT} 3/10/50 = 0.01\%$  indicates a relaxation of 0.01% determined at a maximum indentation depth of 0.003 mm, which was reached within 10 seconds and was kept constant over a 50 second period.

### 8.2.1.2.7 Indentation work

Application of the load to the indenter and the resulting displacement represents work done on the system. During unloading, work is returned from the system as the material elastically recovers. The total work done by the system during unloading is usually less than that applied to the system during loading owing to plastic deformation within the specimen. The amount of work done on or by the system is given by the area underneath the load-penetration response. The ratio of the elastic work recovered during unloading to the total work characterizes the elastic portion of the total work done during an indentation test. This ratio,  $\eta_{IT}$ , is expressed as a percentage and is given by:

$$\eta_{IT} = \frac{W_{Elastic}}{W_{Total}} 100 \quad (8.2.1.2.7a)$$

where  $W_{total} = W_{elastic} + W_{plastic}$ . The elastic part of the indentation work is reported as a percentage along with the test conditions. For example,  $\eta_{IT} 0.5/10 = 36.5\%$  indicates 36.5% elastic work for a 0.5 N force applied over a time of 10 seconds.

### 8.2.1.3 Load and Depth Control

Annex B of the Standard provides schematic representations of load and depth control for the different phases in an indentation test: load, creep, and unload.

### 8.2.1.4 Diamond Indenters

Annex C of the Standard provides information about the use of diamond indenters used in indentation testing. Experience shows that indenters can become defective after a period of use owing to the growth of flaws or cracks. The Standard recommends regrinding indenters that show such deformities upon optical inspection and then recalibrating the indenter.

Indenters may also become contaminated by the adherence of foreign matter from the test specimens. Diamond indenters can be effectively cleaned by forcing them gently into a block of high-density polystyrene foam followed by a rinse with acetone. Optical inspection using a high-quality microscope with a magnification of at least 400 times is sufficient to determine if any foreign matter remains on the indenter.

### 8.2.1.5 Specimen Roughness

The results of round-robin tests<sup>4</sup> have shown that surface roughness of the specimen can have an influence on the test results. At shallow depths of penetration, asperity contact with the indenter results in relatively large uncertainties in the determination of the contact area. At larger indentation depths, this uncertainty is reduced. In order to obtain an uncertainty of the indentation depth

less than 5 % of the indentation depth, the indentation depth should be made at least 20 times the arithmetic roughness  $R_a$  of the specimen surface.

For example, for a sample of aluminum, the Standard shows that for a Martens hardness of  $600 \text{ N/mm}^2$ , the allowed arithmetic roughness for a 0.1 N load is  $0.13 \mu\text{m}$ . For tests in the nano range, it may not be possible to meet the condition of surface roughness for specimens of high hardness. In this case, the number of tests should be increased and this stated in the test report.

### *8.2.1.6 Instrument Compliance and Indenter Area Function*

Annex E of the Standard refers to procedures for correcting the results of the indentation test for the compliance of the load frame of the testing instrument and the non-ideal shape of the indenter.

#### **8.2.1.6.1 Instrument compliance**

As load is applied to the indenter and specimen, reaction forces cause the load frame to be elastically deflected and, in most indentation test instruments, this results in an error in the reported penetration depths. The elastic deformation of the load frame is usually directly proportional to the applied load. Annex E of the Standard recommends that the recorded penetration depths be corrected for this deflection using a method specified in Part 2 of the Standard. The Standard places the burden providing a means of establishing the instrument compliance with the manufacturer prior to delivery of the instrument.

#### **8.2.1.6.2 Indenter area function**

The calculations given in Annex A of the Standard are based on the contact area (or projected contact area) of the indenter with the specimen. However, non-ideal geometry of the indenter, such as blunting of the tip, can cause errors in the estimation of the contact area, especially at small penetration depths. For a Vickers indenter, the line of junction at the tip may also cause errors.

The Standard specifies that the actual area function of the indenter be established for use in calculations. The area function is that function which provides the true contact area as a function of the contact depth  $h_c$ . There are three recommended methods of determining the area function:

1. A direct measurement method using an atomic force microscope.
2. Indirectly by performing indentations into a material of known Young's modulus and using the known modulus to determine the true contact area by applying the analysis procedures in reverse.
3. Indirectly by measuring the difference in hardness calculated with the test force and depth to the constant value of hardness for a special reference material that shows no depth-dependent hardness value.

For the indirect measurements, it is necessary to determine and account for load frame compliance before determining the area function of the indenter.

The area function is normally expressed as a mathematical function relating the contact area to the distance from the tip of the indenter. Where a cubic or polynomial function is not suitable, an estimate may be made either by using a graph or by using a look-up table. A procedure for the verification of the indenter area function is given in Part 2 of the Standard.

#### 8.2.1.7 Correlation of $H_{IT}$ with Other Scales

The indentation hardness  $H_{IT}$  may be correlated to other hardness scales in certain circumstances. For example, a common request is to express indentation hardness as equivalent Vickers hardness value. The indentation hardness uses the projected area of contact, while the Vickers hardness uses the actual surface area of contact. Since for a Vickers indenter, the projected and actual surface areas of contact differ by about 7%, it is to be expected that the Vickers hardness value will be some 7% less than the equivalent indentation hardness  $H_{IT}$ . Note that such a conversion assumes perfect indenter geometry which is generally not the case for very small penetration depths.

Annex F of the Standard provides information about the relationship between indentation hardness and Vickers and Berkovich indenters.

### 8.2.2 ISO 12577 Part 2: Verification and calibration of machines

Part 2 of the Standard specifies the method of verification and calibration of the test instruments. A direct method is given for verification of the main functions of the instrument and an indirect method for determining the repeatability of the instrument is also given.

Before verification and calibration, the requirements and guidelines of the manufacturer shall be taken into account when installing the instrument. Also, the instrument shall be isolated from vibrations, air currents, and temperature fluctuations and the indenter holder shall be firmly mounted into the instrument. Furthermore, the indenter holder should be designed in such a way so as to minimize its contribution to the overall compliance of the system. The test force shall be applied and removed without shock or vibration, and the process of increasing, holding, and removal of the test force be verified.

The direct verification shall be carried out at a temperature of  $23 \pm 5$  °C. Direct verification involves verification of the indenter, calibration of the test force, calibration of the displacement measuring device, verification of the machine compliance, verification of the indenter area function, and verification of the testing cycle.

#### 8.2.2.1 Indenters

The indenter used for the indentation test shall be calibrated independently of the indentation instrument by a direct optical method, and the calibration certificate should include the relevant geometrical measurements. If the measured an-

gle of the indenter deviates from its nominal value, then the average of the measured angles should be used in all calculations.

### 8.2.2.1.1 Vickers indenter

Vickers indenters shall have four faces with the angle between the opposite faces of the vertex of the pyramid to be  $136 \pm 0.3^\circ$ . The angle between the axis of the diamond pyramid and the axis of the indenter holder shall not exceed  $0.5^\circ$ . The line of conjunction at the tip of the indenter shall be no greater than 0.001 mm for an indentation depth range  $> 0.03$  mm, 0.0005 mm for an indentation depth range of 0.03 to 0.006 mm, and less than 0.0005 mm for an indentation depth range less than 0.006 mm. The radius of the tip of the indenter shall not exceed 0.0005 mm for the micro range. The verification of the shape of the indenter should be made by a microscope or other suitable device. For indenters to be used in testing in the micro and nano ranges, an AFM type of microscope is recommended.

### 8.2.2.1.2 Berkovich and cube corner indenters

There are two types of Berkovich pyramidal indenters in common use. The original Berkovich indenter is designed to have the same ratio of actual surface area to indentation depth as a Vickers indenter. The modified Berkovich indenter is designed to have the same ratio of projected area to indentation depth as the Vickers indenter.

The radius of the tip of the indenter shall not exceed  $0.5 \mu\text{m}$  for the micro range and  $0.2 \mu\text{m}$  for the nano range. The angle between the three faces of the diamond pyramid at the base shall be  $60^\circ \pm 0.3^\circ$ . The included face angle for the different types of indenter are to be as shown in Table 8.3:

**Table 8.3** Face angles for triangular pyramid indenters

Berkovich indenter	$65.03^\circ \pm 0.3^\circ$
Modified Berkovich indenter	$65.27^\circ \pm 0.3^\circ$
Cube corner indenter	$35.26^\circ \pm 0.3^\circ$

### 8.2.2.1.3 Spherical indenters

The Standard describes the requirements for metal spherical indenters and diamond sphero-conical indenters. For spherical indenters the hardness shall be not less than 1500 HV 10, when determined in accordance with ISO 3878 and shall have a density of  $14.8 \text{ g/cm}^3 \pm 0.2 \text{ g/cm}^3$ . The indenters are typically made from tungsten carbide with 5 – 7% cobalt and up to 2% other carbides.

The calibration certificate for the indenter shall show the diameter of the average value of at least three measured points of different positions and, if any of these measurements falls outside a specified tolerance, the indenter shall be rejected for use. The tolerances are  $\pm 5 \mu\text{m}$  for a 10 mm diameter indenter,  $\pm 4 \mu\text{m}$  for a 5 mm indenter, and  $\pm 3 \mu\text{m}$  for smaller indenters.

For sphero-conical indenters, with a cone of semi-angle  $\alpha$ , the depth at which the spherical tip is defined is given by Eq. 4.9a. In practice, owing to the gradual transition between the sphere and the cone, and allowed tolerances in the dimensions of  $\alpha$  and  $R$ , the penetration depth should be no greater than  $0.5 h_s$ .

### 8.2.2.2 Calibration of force and depth

The Standard requires that each range of load offered by the instrument be calibrated using at least 16 evenly spaced points and that the procedure be repeated three times. The test force shall be measured by a traceable method using, for example: an elastic proving ring, a calibrated mass, or an electronic balance with an accuracy of 0.1 % of maximum test force. The smallest indentation depth to be measured for the micro range is  $0.2 \mu\text{m}$  and for the macro range  $2 \mu\text{m}$ . The displacement measuring device shall be calibrated for every range offered by the instrument using a minimum of 16 evenly distributed points in each direction.

### 8.2.2.3 Verification of compliance and area function

Verification of instrument compliance shall be made after calibration of the load and depth measurement systems. Instrument compliance is determined by the measurement of hardness or modulus at a minimum of five different test forces on a reference specimen with certified hardness value or modulus.

Procedures for determination of indenter area function are given in Annex D Part 2 of the Standard. This part of the Standard is concerned with verification of the area function only. The verification procedure of the indenter area function consists of a comparison of the measured indenter area function with that determined for the newly certified and calibrated indenter. If the difference of these values at the same test forces exceeds 30 % of the initial value, the indenter should be discarded.

### 8.2.2.4 Verification of the instrument

Indirect verification should be carried out at least weekly for instruments in the micro and nano ranges using reference blocks calibrated in accordance with Part 3 of the Standard. Two different reference blocks shall be chosen that span the range of normal application of the instrument as widely as possible. The Standard specifies the method of calculating the mean values of results on each reference block and also the standard deviation of these readings.

The Standard specifies that direct verification shall be carried out when the instrument is installed, after its dismantling and reassembly or relocation, or when the result of an indirect verification is unsatisfactory.

A test shall be performed at two different test forces on a specimen of known properties on a daily basis. The results should be recorded on a time chart and, if the results are outside the normal range, an indirect verification should be performed.

The Standard specifies the format of the Verification Report and Calibration Certificate. In general, the following information is to be reported: reference to the Standard, method of verification (direct and/or indirect), identification of the testing machine, means of verification (reference blocks, elastic proving devices, etc.), test forces, temperature, results, date of verification, and reference to the verification institution.

### 8.2.2.5 Annexes to Part 2

Annex A of this part of the Standard describes a recommended design for the construction of the indenter holder. The design is intended to minimize the compliance of the holder and to provide a firm mounting for the indenter material.

Annex B of Part 2 of the Standard is similar to that of Annex C of Part 1 and provides information about methods of cleaning of contaminated indenters. The Standard recommends that the condition of indenters should be monitored by visually checking the aspect of the indentation on a reference block, each day the testing machine is used.

Annex C of this part of the Standard gives examples for direct verification of the displacement measuring system using either a laser interferometer, an Inductive method, a capacitive method, or a piezotranslator method.

Annex D of Part 2 of the Standard describes procedures for verification of indenter area function. A series of at least 10 different forces shall be chosen to span the range of interest and, for each load, at least 10 indentations shall be made into the reference material and the mean value used to determine  $A_p$ . The area function takes the form of a plot of  $A_p$  versus indentation contact depth  $h_c$ .

Annex E of Part 2 of the Standard shows examples for the documentation of the results of indirect verification in the form of charts by which the performance of a test instrument can be monitored over time.

### 8.2.3 ISO 12577 Part 3: Calibration of reference blocks

Part 3 of ISO 12577 specifies the method of calibration of reference blocks that are to be used for verification and calibration of indentation testing instruments.

The Standard specifies that the reference block shall be specially prepared with a suitable level of homogeneity, stability of structure, and uniformity. The Standard specifies the minimum thickness of reference block for each hardness range. The reference block shall be demagnetized, the test surface and free of scratches and flat to within 0.005 mm over a length of 50 mm.

Reference blocks are calibrated using a depth-sensing indentation test using a calibration test instrument. The calibration instrument is required to be calibrated to a traceable standard in terms of its test force, indenter shape, displacement measurement system, and the testing cycle.

The indenter shape is to be measured directly. The displacement measuring device shall be capable of measuring to within 0.01  $\mu\text{m}$  with an error of  $\pm 0.5\%$

for the macro range, to within 0.2 nm with an error of  $\pm 1\%$  for the micro and nano ranges. The testing cycle shall be such that the time for application of the test force is 20 seconds, the time for duration of the test force is 10 seconds, and the time for removal of the test force is 20 seconds, with an approach velocity of 0.02 to 0.005 mm/sec for the macro range, 0.001 mm/sec for the micro range, and 0.10  $\mu\text{m}/\text{sec}$  for the nano range.

The average and standard deviation for hardness measured on the reference block is to be reported. The maximum value of standard deviation is to be less than 2%. Each reference block shall be marked with the arithmetic mean of the measured values of hardness and modulus; the name of the manufacturer of the block; a serial number; the name or mark of calibrating agency; the thickness of the block or an identifying mark on the test surface and the year of calibration. The Standard recommends that calibration validity should be limited to 5 years.

## References

1. ISO Central Secretariat, 1 rue de Varembe, 1211 Geneva 20 Switzerland.
2. M.F. Doerner and W.D. Nix, "A method for interpreting the data from depth-sensing indentation instruments," *J. Mater. Res.* 1 4, 1986, pp. 601–609.
3. W.C. Oliver and G.M. Pharr, "An improved technique for determining hardness and elastic modulus using load and displacement sensing indentation experiments," *J. Mater. Res.* 7 4, 1992, pp. 1564–1583.
4. H.-H. Behncke, "Bestimmung der Universalhärte und anderer Kennwertr an dünnen Schichten, insbesondere Hartstoffsichten," *Härterei-Technische Mitteilung HTM*, 48 5, 1993, pp. 3–10.

# Chapter 9

## Nanoindentation Test Instruments

### 9.1 Specifications of Nanoindentation Test Instruments

Interest in nanoindentation has spawned a number of nanoindentation instruments that compete on a world market. Purchasers of such instruments are universities, private and government research organisations, and quality control laboratories. There is particular interest within the semiconductor industry that is concerned with the mechanical properties of a wide range of thin films. All of the products described in this chapter are depth-sensing devices. The instruments typically measure depth of penetration using either a changing inductance or capacitance displacement sensor. A typical nanoindentation test instrument has a depth resolution of less than a tenth of a nanometre and a force resolution of less than a nanonewton. The load can be applied by the expansion of the piezoelectric element, the movement of a coil in a magnetic field, or electrostatically. Maximum loads are usually limited to the millinewton range. The minimum load is usually less than a micronewton.

Nanoindentation instruments are typically load-controlled machines. A common question asked by the novice is the specification of the minimum thickness of film or sample that can be measured. This is difficult to answer since it is the minimum load that is the important parameter. When operated at the minimum load, the resulting depth depends upon the mechanical properties of the specimen. The minimum load quoted in manufacturer's specifications is very important and gives an indication of the minimum load range for testing on actual samples. Force and displacement resolutions are not so important, since they are limited in practice by the noise floor of the instrument and the environment in which it is placed.

Table 9.1 provides a description of the most commonly quoted specifications for nanoindentation instruments. The description of the instruments given in this chapter represents no specific order in terms of market share, price, or number of features nor does it include all the instruments presently available. Details of the specifications and features were obtained from publicly available advertising material and scientific literature or directly from the manufacturer. The prospective purchaser should consult the most up-to-date material provided by the manufacturer, since specifications and features are continually being modified and improved.

**Table 9.1** Useful definitions for specifications of nanoindentation instruments.

Minimum Contact Force	The minimum contact force is typically limited by the noise floor of the instrument and the test environment. The value should be as low as possible so as to minimize the error associated with the initial penetration.
Force Resolution	The force resolution determines the minimum change in force that can be detected by the instrument. Most manufacturers would either employ a 16 bit, or 20 bit analogue to digital converter (ADC) in their systems and the theoretical resolution for each instrument can be determined by dividing the range (whether force or depth) by 2 raised to the power of the width of the ADC. For example, for a range of 50 mN and a 16 bit ADC, the theoretical resolution would be 50 mN divided by $2^{16} = 750$ nN. Some manufacturers then further divide this value by a factor equal to the square root of the number of readings taken for averaging. The very low values of resolution presented by some manufacturers is thus a combination of the smoothing effect of taking many readings and averaging the results and the width of the ADC and the range. The theoretical resolution is often not the most appropriate measure of performance of an instrument.
Force Noise Floor	The noise floor of the specifications is the most important factor that determines the minimum contact force attainable by the system. Any increase in resolution beyond the noise floor will only mean that the noise is being measured more precisely. The noise floor is generally limited by electronic noise or the environment in which the instrument is located. Typically, the noise floor quoted by manufacturers represents the best possible results obtained under ideal laboratory conditions.
Displacement Resolution	The displacement resolution is typically found by dividing the maximum displacement voltage reading by the number of bits in the data acquisition system.
Displacement Noise Floor	The noise floor in the displacement measurement system will determine what the minimum useable indentation depth. The displacement noise floor is one of the most important measures of performance of an instrument.
Maximum Number of Data Points	This is the maximum number of data points that can be collected for a single test. More data points allow for better resolution of “pop-in” events and other features in the force-displacement curves. However, the data acquisition rate will also be important for large data sets, since

	data should be collected as quickly as possible so as to minimize errors due to thermal drift.
Data Acquisition Rate	This is how fast the machine will collect force and displacement data. The data acquisition rate should be as high as possible so as to allow the time for a test to be shorter, thus minimising errors due to thermal drift.
Variable Loading Rate	The mechanical properties of some specimen materials depend upon the rate of application of load. This ability of vary the loading rate allows such studies to be performed. Slow loading may be desirable for some materials followed by a fast unloading.
Unattended Operation	This is the ability of the instrument to be programmed to collect data on a single site, or an array of sites, while not requiring any operator intervention during the tests.
Specimen Positioning	This is how accurately the instrument can position the indenter. Most instruments allow $\pm 0.5 \mu\text{m}$ positioning resolution with optical rotary encoders with some allowing $\pm 0.1 \mu\text{m}$ with linear track encoders.
Field of Testing	This is the dimension of the testing area accessible by the indenter based upon maximum movement of the positioning stages. This can be important for allowing tests to be performed on large specimens such as silicon wafers.
Resonant Frequency	This is the natural resonant frequency of the instrument. It depends upon the mass of the instrument and the characteristics of the mounting springs and dampers. A high resonant frequency makes the instrument less susceptible to mechanical environmental interference. Also, a higher resonance allows higher-frequency dynamic measurements to be made. High frequency dynamic measurements can be made with a low resonant frequency system if the sample, rather than the indenter, is oscillated.
Thermal Drift	Thermal drift is almost unavoidable if the temperature of the environment surrounding the instrument is not kept within very tightly controlled limits. Most instruments are supplied with an enclosure with very high thermal insulating properties.
Machine Stabilization Time	This is the time needed by the instrument to stabilize after initial power up. The time is usually dependent on the thermal characteristics of the measurement system. A short time allows more efficient use of the test facility.
Indentation Time	This is the average time of a typical indentation cycle from load to full unload. A nanoindentation instrument should be able to perform a single indentation within one or two minutes.

Tip Exchange Time	This is the time needed for the operator to change the indenter. This time should be no more than a minute or so for maximum convenience of operation of the instrument where different indenters are used for different types of testing.
Loading Step	Load can be applied in a variety of ways in typical nanoindentation instruments. A square root spacing of load increments gives an approximate even spacing of depth measurements. A linear spacing of load increments may provide a constant loading rate. The instrument should offer one or two options in this regard.
Constant Strain Rate	Constant strain rate testing involves the application of load so that the depth measurements follow a pre-defined relationship. Some nanoindentation instruments offer the ability of set the loading rate so as to give a constant rate of strain within the specimen material. This may be important for viscoelastic materials or those that exhibit creep.
Topographical Imaging	In situ topographical imaging provides scans of a surface before it is indented for accurate tip placement and also provides immediate imaging after the indent is completed to measure the size of the residual impression. Such imaging can be done with an atomic force microscope accessory mounted as either another testing station on the instrument assembly or as an in situ device.
Dynamic Properties	This is the ability to measure the response of surfaces under a sinusoidal or other oscillating load. This technique is important for measuring the viscoelastic properties of materials. The method usually involves the application of an oscillatory motion to the indenter or the sample. A lock-in amplifier measures phase and amplitude of force and displacement signals.
High Temperature Testing	It is sometimes of considerable interest to measure the mechanical properties of materials at their operating temperature. Some nanoindentation instruments allow testing of smaller sized samples at temperatures ranging from $-5$ to $+500$ °C.
Acoustic Emission Testing	This allows the fitting of an acoustic microphone to the indenter or specimen for recording of non-linear events such as cracking or delamination of thin films.

## 9.2 “Nano Indenter<sup>®</sup>,” MTS Systems Corporation<sup>1</sup>

The Nano Indenter<sup>®</sup> indentation instrument is widely used in the field and has a development history dating back to about 1981.<sup>2</sup> The instrument applies load via a calibrated electromagnetic coil and displacement of the indenter is measured using a capacitive plate transducer.

The load and displacement resolutions are reported to be 50 nN and 0.04 nm respectively.<sup>3</sup> The patented<sup>4</sup> Continuous Stiffness Measurement, “CSM,” option is of particular interest in this instrument. The analysis methods given in Chapter 3 show how a measurement of the stiffness of the contact ( $dP/dh$ ) between the indenter and the materials being tested can be used in the multiple-point unload technique to determine the elastic modulus and hardness of the specimen material. This can be done by partially unloading the indenter at each load increment or by superimposing a small sinusoidal load signal onto the normal load signal. With the CSM technique, the latter method is used. The CSM method has an added benefit in that if the specimen material has a viscoelastic behaviour, then the phase difference between the force and depth signals provides information about the storage and loss moduli of the sample.

The Nano Indenter<sup>®</sup> can operate in a scratch testing mode that is also suitable for surface profile measurements. The optional lateral force measurement system provides a friction force measurement capability.

The Dynamic Contact Module (DCM) is a low-load accessory for the Nano Indenter<sup>®</sup>.<sup>3</sup> Its operation is similar in principle to the standard Nano Indenter<sup>®</sup> system but offers a high resonant frequency, an increased dynamic frequency range, and a low damping coefficient. This makes the unit less sensitive to environmental noise than conventional instruments, and with a theoretical displacement resolution of 0.0002 nm and a load resolution of 1 nN, the DCM is suitable for detecting surface forces on an atomic scale.

The Nano Indenter<sup>®</sup> is operated by the MTS TestWorks<sup>®</sup> instrument control environment, which is common to all MTS test equipment and allows the user infinite flexibility in the specification of test procedure and data analysis. The TestWorks<sup>®</sup> software is available in the Professional or more advanced Explorer level. Included with the installation is the TestWorks<sup>®</sup> Analyst package. The Analyst package offers calculations of hardness and modulus (Oliver and Pharr method), calculation of hardness and modulus as a function of depth and the storage and loss moduli (if the CSM option is included). The software also provides flexibility for the user to specify their own calculation methods.

Additionally, the optional NanoSP1<sup>®</sup> software acts as a user-friendly interface to the finite element-analysis engine, COSMOS<sup>®</sup>.<sup>5</sup> NanoSP1<sup>®</sup> software dramatically simplifies the setup and interpretation of simulations of indentation experiments, including those of thin films on substrates. Mesh generation is automated and optimized to produce accurate results with minimal run times on the order of 20 minutes.

### 9.3 “NanoTest<sup>®</sup>,” Micro Materials Ltd.<sup>6</sup>

The Micro Materials NanoTest<sup>®</sup> platform has been designed to support three modules: (i) nanoindentation, (ii) scanning for scratch testing, and (iii) impact (for thin film adhesion failure, erosive wear, and contact fatigue).

In the indentation module, a very small, calibrated diamond probe is brought into contact with the specimen surface and load is applied by means of a coil and magnet located at the top of the pendulum. The pendulum is supported by on a frictionless spring flexure. The resultant displacement of the probe into the surface is monitored with a sensitive capacitive transducer and displayed in real time as a function of load.

In the NanoTest<sup>®</sup> scanning module, the specimen is moved perpendicularly to the axis of the indenter movement allowing either single or repetitive scratch tests. It is important to note that the pendulum spring support is extremely stiff in the scanning direction, thus minimising errors due to tilt of the loading head as the scratch load is increased. Accurate repositioning combined with optional software enables complex multi-pass scratch tests to be scheduled.

For quantitative impact testing using the impact module, a static load is applied to the pendulum, which is then pushed away from the specimen by a known amount and released, causing the test probe to impact the surface. The impact energy is determined for individual or repetitive impacts.

Figure 9.1 shows a schematic of the relevant features of the instrument including dynamic oscillation for dynamic measurements.

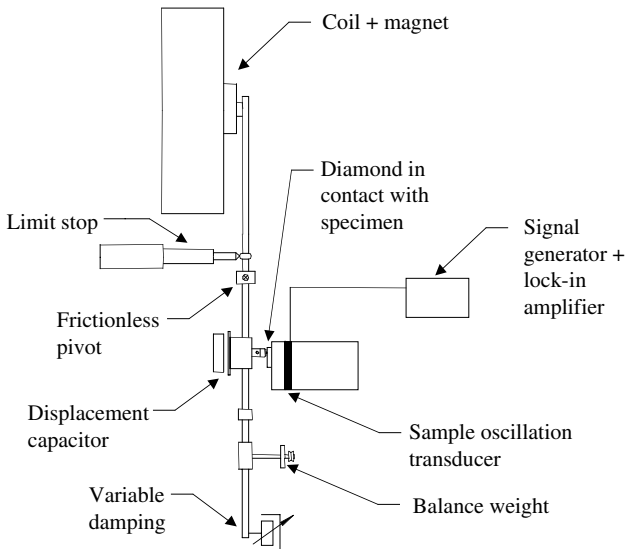


**Fig. 9.1** Schematic of the method of construction for the NanoTest<sup>®</sup> instrument (Courtesy Micro Materials Ltd.).

Significant features and options of the NanoTest<sup>®</sup> instrument are:

- Unique and versatile pendulum design.
- Precise repositioning technique allows investigation of small particles, fibres, wires, and complex inhomogeneous samples such as integrated circuits.
- NanoTest<sup>®</sup> head with load ranges 0 – 50 mN and 0 – 500 mN. Maximum load resolution better than 100 nN. Maximum depth resolution better than 0.1 nm.
- High load capability for load ranges 0 – 2 N and 0 – 20 N. The high load option can be fitted alongside the NanoTest<sup>®</sup> head.
- Dynamic contact compliance calculation using a lock-in amplifier and specimen oscillation system. The oscillation frequency range is adjustable up to 250 Hz.
- High temperature option offers room temperature to over 500 °C specimen heating stage, probe heater, thermal barrier, and high-temperature capacitor assembly.
- Spherical indenter and analysis software to calculate plastic depth, hardness vs. penetration depth, creep, and stress–strain.
- Automatic 2D specimen leveling stage for hardness/modulus and roughness/topography measurements on curved or uneven samples.
- High resolution and zoom microscopes with video capture offers high resolution (x1000) with accurate repositioning and specimen translation capabilities. Video zoom 30X – 160X or 60X – 320X. Video capture capability can be added to the system for image storage.
- Pin-Disk with rotations of  $\ll 1$  rpm – 3600 rpm with high-torque motor and gearbox, software for control of speed, acceleration, time, load, depth and track location
- Humidity control system comprising a constant temperature, 15 – 90 % RH control unit, designed to operate with a thermally insulated environmental chamber.
- Acoustic emission system with shielded detector, for use with indentation or scanning modules.
- Powder adhesion software to load–unload specimen and measure pull-off forces repeatedly at the same position.
- Integration with an atomic force microscope.
- Fully automated scheduling system — allows overnight operation to ensure maximum productivity — up to 100 nanoindentation experiments each containing up to 100 nanoindentations to be performed at a convenient time at specified locations on one or more specimens.
- Environmental control for excellent data reproducibility even at ultra-low load.



**Fig. 9.2** The “NanoTest<sup>®</sup>” instrument (Courtesy Micro Materials Ltd.).

As shown in Fig. 9.2, there are two load heads side-by-side in the NanoTest<sup>®</sup> unit. The load head on the left of the instrument can apply a load of up to 20 N, while the one on the right has a maximum load of 500 mN. In both cases, the maximum depth is 100  $\mu\text{m}$ . Depth resolution is less than 0.1 nm and force resolution is better than 100 nN. The specimen is moved to the front of the microscope for test set-up and then moved to one of the loading heads for actual testing. With the two-head design, it is possible, for example, to perform a wear test with the high-load head and then probe around the wear track with the low-load head.

A particularly unique feature of the NanoTest<sup>®</sup> instrument is the facility for impact testing. This modular add-on option to the NanoTest<sup>®</sup> allows the impact technique to be used with or without transverse specimen movement during testing. In one type of test, an oscillating piezoelectric transducer is placed behind the specimen holder. This causes the probe to “bounce” on the specimen surface. The impact frequency, static load, and duration of the experiment are pre-programmed and the impact angle is variable. The initial and final static probe positions are determined in order to calculate the resulting depth increase, and the instantaneous probe position is monitored and plotted throughout the procedure.

With scanning impact testing, transverse specimen movement during scanning at either constant or steadily increasing load causes the test probe to continuously impact along the wear track, simulating many film failure situations, e.g., erosive wear and coating adhesion failure. The impact energy is determined by the oscillation amplitude and frequency and the applied load. Film failure is detected through changes in probe displacement during scanning. The NanoTest<sup>®</sup> impact testing operates from 0 to 500 Hz and up to 7  $\mu\text{m}$  specimen displacement amplitude.

Another unusual feature offered by the NanoTest<sup>®</sup> instrument is the optional high-temperature attachment. In this configuration of the instrument, the displacement measurement capacitor is moved from its original position on the indenter holder to the bottom of the pendulum and a thermal shield is placed between the pendulum and the stage. A very small heater element capable of maintaining a maximum temperature of 500 °C together with a miniature thermocouple have been added to the diamond indenter stub, close to the tip itself. With both the diamond and specimen at the same temperature, heat flow between them does not occur upon contact, thus preventing instantaneous dimensional changes due to thermal expansion. The hot stage itself consists of a thermally insulating ceramic block that is attached to the NanoTest<sup>®</sup> specimen holder. With the heater at 500 °C, the increase in temperature behind the ceramic block is typically less than 1 °C. Temperature controllers with automatic tuning are used for both the main hot stage and the diamond heater.

The overall distinguishing feature of the NanoTest<sup>®</sup> system is its versatility, offering conventional nanoindentation (including oscillatory motion), impact, scratch, surface forces, and high-temperature testing.

#### 9.4 “TriboIndenter<sup>®</sup>,” Hysitron Inc.<sup>7</sup>

The Hysitron TriboIndenter<sup>®</sup> is a low-load indentation test system designed for measuring the hardness and elastic modulus of thin films, coatings, and bulk materials. The TriboIndenter<sup>®</sup> provides quantitative testing capabilities with both normal and lateral force (nanoscratch) loading configurations. It can operate in static or dynamic loading modes. The main unit, with the environmental cover removed, is shown in Fig. 9.3.

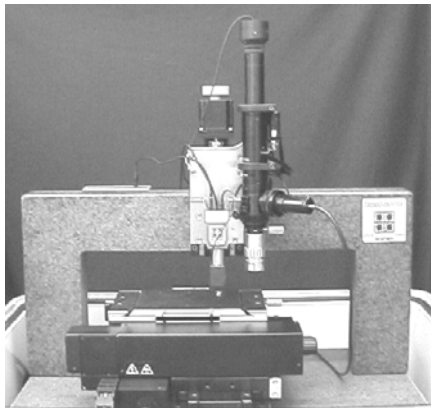


**Fig. 9.3** The “TriboIndenter<sup>®</sup>” (Courtesy Hysitron Inc.).

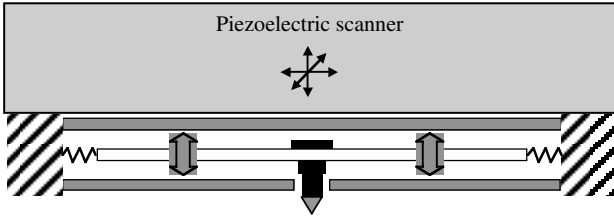


**Fig. 9.4** The unique combined actuator transducer of the Hysitron TriboIndenter<sup>®</sup> is capable of raster scanning over the specimen surface.

The patented transducer technology<sup>8-12</sup> used within the instrument uses a capacitive displacement measurement technique combined with electrostatic force generation (see Fig. 9.4). Because of the compact size of the sensor/actuator, it can be connected to a piezoelectric scanner that provides very precise X, Y, and Z controlled indenter tip positioning. The impressive low-drift characteristics are also a result of Hysitron's transducer design. The revolutionary three-plate capacitor transducer technology provides simultaneous actuation and measurement of force and displacement with a dynamic range of 1 nN to 30 mN.

The TriboIndenter<sup>®</sup>, when operated in a dynamic mode, can detect forces as small as 1 nN, and respond to phenomena such as surface pull-on and pull-off forces typically associated with an AFM force-depth curve. In quasi-static mode, the TriboIndenter<sup>®</sup> has a noise floor better than 100 nN. When operated in a dynamic mode, it approaches the force resolution of 1 nN. The displacement noise floor for the TriboIndenter<sup>®</sup> is less than 0.2 nm. This allows the user to make repeatable indentations below 10 nm maximum depth. The noise floor is much less when run in dynamic mode.

Because the transducer and the indenter tip are both fixed to a piezoelectric scanner (see Fig. 9.4), the TriboIndenter<sup>®</sup> is capable of in situ SPM (scanning probe microscopy) imaging. The piezoelectric scanner is able to raster the tip over a specimen, while a feedback loop controls the Z axis height of the scanner to maintain a constant force between the indenter tip and specimen. The Z axis movement of the scanner is then calibrated to a height to get a three-dimensional topographical image. Using in situ imaging, it is possible to place indentations on a surface with a precision of 10 nm.

The TriboIndenter<sup>®</sup> is inherently a load-controlled instrument. This means that the user chooses the type and amount of force that will be applied with the indenter. The system measures the corresponding displacement of the indenter into the material. Usually, the load is increased and decreased in a linear fashion, which implies a constant loading rate. Special software is available to allow constant strain rate testing. Using the Load Function Generator in the TriboIndenter<sup>®</sup> software, the user can define any type of loading profile. The dynamic stiffness measurement software provided by Hysitron is completely automated

for setup, execution, and analysis of dynamic tests and allows measurement of the viscoelastic properties of materials. The lock-in amplifier that measures phase and amplitude of signals is software controlled. The high resonance frequency allows higher-frequency testing to be done as well. The low noise floor allows users to experiment at much lower forces and test real surface properties of specimens. The specifications and features of the Hysitron TriboIndenter<sup>®</sup> are given in Table 9.2.

**Table 9.2** Specifications and features of the Hysitron TriboIndenter<sup>®</sup>.

<b>Force</b>	
Maximum	30 mN, 500 mN
Minimum Contact Force	1 nN
Resolution	<1 nN
Noise Floor	<100 nN
<b>Displacement</b>	
Maximum	50 $\mu\text{m}$
Resolution	0.0002 nm
Noise Floor	0.2 nm
<b>Positioning</b>	
Placement of Indents	$\pm 10$ nm
Field of Testing	120 mm x 100 mm
<b>Instrument Features</b>	
Resonance Frequency	150 Hz
Load Frame Stiffness	$5 \times 10^5$ N/m
User Interface	Windows 95/98/NT/2000
<b>Testing Capabilities</b>	
Constant Loading Rate	50 mN/sec max
Constant Strain Rate Loading	yes
Step Loading	yes
In Situ Topographical Imaging	yes
Dynamic Properties	yes
Acoustic Emission Detection	yes
<b>Temperature Control</b>	-5 $^{\circ}\text{C}$ to +150 $^{\circ}\text{C}$

The overall distinguishing feature of the TriboIndenter<sup>®</sup> system is its extremely low noise floor allowing very shallow penetration depths of less than 10 nm and the piezo-electric scanning system allowing in situ imaging of pre and post indentation features on the specimen surface.

## 9.5 “Nano-Hardness Tester<sup>®</sup>,” CSEM Instruments<sup>13</sup>

In the Nano-Hardness Tester<sup>®</sup> an indenter tip with a known geometry is driven into a specific site of the material to be tested by applying an increased normal load. Indenter displacement is measured using a capacitive transducer.<sup>14</sup> Using the partial-unload technique, the contact stiffness and hardness of the specimen material can be calculated as a function of depth of penetration into the specimen. The indenter load is measured using a load cell attached to the indenter shaft. A photograph of the instrument is shown in Fig. 9.5.

A particular feature of this instrument is the use of a sapphire reference ring that remains in contact with the specimen surface during the indentation. The reference ring provides a differential measurement of penetration depth and thus the load frame compliance and thermal drift are automatically compensated for. The sapphire ring also acts as a local environmental enclosure protecting the measurement spot from air currents, sound waves, and changes in humidity and temperature, thus obviating the need for special environmental conditions in order to obtain perfect measurements. The ring also allows the working distance to be set very rapidly as the ring contacts the surface before the indenter and so the final approach, to be made very slowly, takes place only over a few microns displacement.

One of the main advantages of this instrument is the ability to quickly and easily make an AFM image of a residual imprint. As shown in Fig. 9.6, an optional AFM objective fits to the microscope in place of a standard optical objective.



**Fig. 9.5** The “Nano-Hardness Tester<sup>®</sup>” (Courtesy CSEM Instruments).

The Nano-Hardness Tester<sup>®</sup> specimen holder will accommodate specimens up to 100 mm thick, on a 105 x 135 mm work table. Special specimen holders are available to accommodate other specimen sizes such as 12 inch silicon wafers. The precise positioning (0.5  $\mu\text{m}$ ) capability of the X-Y motorized table combined with the large X-Y ranges (20x20  $\mu\text{m}$  or 40x40  $\mu\text{m}$ ) of the objective ensures that the indent will always be in the centre of the field of view in both optical and AFM modes.

#### Specifications of the Nano-Hardness Tester<sup>®</sup>

Depth resolution	0.03 nm
Maximum indentation depth	>20 $\mu\text{m}$
Maximum load	300 mN
Load resolution	$\pm 1 \mu\text{N}$
Work table dimension	105 x 135 mm
X-Y range	30x21 mm (45mm optional)
Spatial Resolution	$\pm 0.25 \mu\text{m}$
Magnification	50 X and 1000 X (200X, 500X, and AFM Objectives Optional )
AFM Resolution x, y, z	< 1 nm
AFM Scan range	20x20 microns, (40x40 microns optional)
AFM Vertical range	2 $\mu\text{m}$ (4 $\mu\text{m}$ optional)

The Dynamic Mechanical Analysis mode of operation uses sine wave loading curves to obtain a more complete analysis of the mechanical properties of viscoelastic materials. Measurements of phase angle and amplitude between the force sine wave and the penetration depth signal, produces the storage and loss modulus of the material.

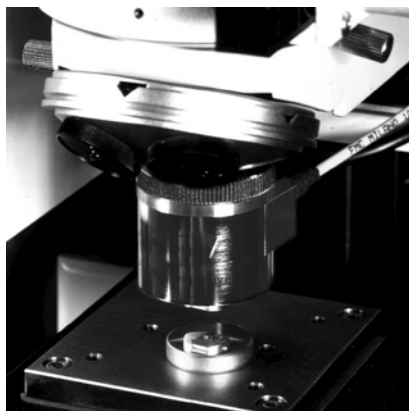


**Fig. 9.6** AFM objective on the Nano-Hardness Tester<sup>®</sup> fits onto the mounting of the standard optical objectives (Courtesy CSEM Instruments).

The Nano-Hardness Tester<sup>®</sup> is related to the Nano-Scratch Tester<sup>®</sup> also available from CSEM Instruments. The Nano-Scratch Tester<sup>®</sup> operates with a normal force in the range 10  $\mu\text{N}$  – 1 N. Different load ranges are selected by interchangeable cantilevers of varying stiffness. The scratch tip is mounted on the cantilever and the deflection is measured by a linear voltage differential transformer (LVDT). An optional AFM attachment allows imaging of the resulting very small scratch profile. The scratch length can be up to 20 mm with a lateral force specification to 1 N with resolution of 30  $\mu\text{N}$ .

## 9.6 “UMIS<sup>®</sup>,” CSIRO<sup>15</sup>

The UMIS<sup>®</sup> is a load-controlled nanoindentation instrument. A particular feature of the UMIS<sup>®</sup> is the patented<sup>16</sup> load feedback system that ensures that the applied load is held equal to the set force. This separation of the load measurement and actuation ensures that the actual load applied to the indenter shaft is recorded. A photograph of the unit with the isolation stand and environmental enclosure removed is shown in Fig. 9.7.

The heavy construction of the UMIS<sup>®</sup> acts as a seismic mass for the damped support springs that isolate the instrument from mechanical vibration and minimize compliance of the load frame. The environmental enclosure is insulated with glass wool and an electromagnetic screen to minimize thermal and electrical interference. Illumination within the enclosure is provided by super-bright, low infra-red light-emitting diode arrays.

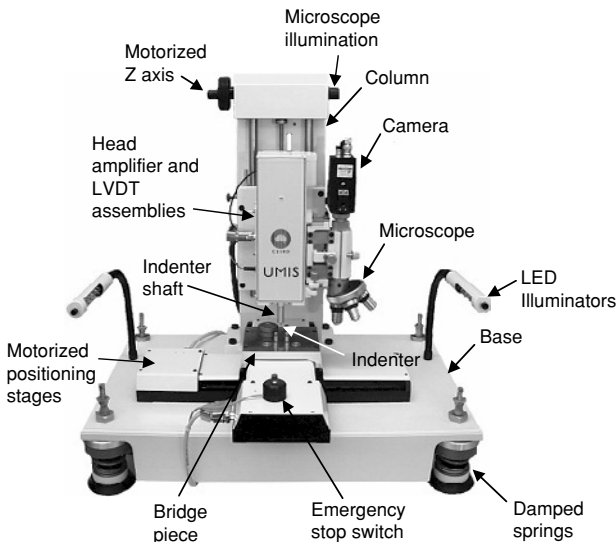


**Fig. 9.7** The “UMIS<sup>®</sup>” (Courtesy CSIRO).

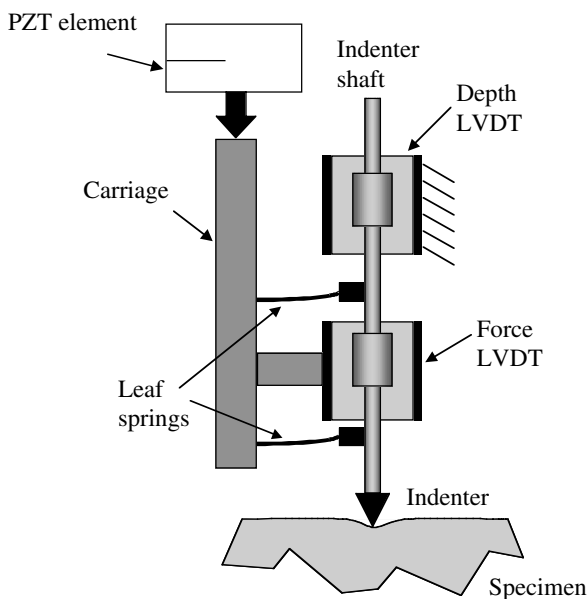


**Fig. 9.8** Schematic of the operating principle of the UMIS<sup>®</sup>. An electronic feedback system measures the force from the force LVDT and adjusts the expansion of the PZT until the requested or commanded force is actually achieved at the indenter shaft.

The UMIS<sup>®</sup> applies load via the expansion of a piezoelectric element connected to the indenter shaft by a series of carefully machined leaf springs. The deflection of the springs is a measure of the load applied to the indenter and this deflection, along with the displacement of the shaft relative to the loading frame, is done using very high-quality linear variable differential transformers (LVDTs). Figure 9.8 shows a schematic of the operating principle used in the UMIS<sup>®</sup>.

As with other instruments of this type, an optical microscope is fitted to allow for precise sample positioning and post-indentation crack length measurement. The instrument is software controlled and can be run in an automated, unattended mode for multiple indentations on multiple specimens. Sample positioning is by means of servo-controlled dc motor driven positioning stages. The same stage allows the specimen to be translated from the indenter position to the optical microscope and alternately to the optional AFM attachment. Alternately, an AFM probe head can be inserted in place of one of the optical microscope objectives.

The UMIS<sup>®</sup> control software uses the partial-unload technique for measuring the contact stiffness at each load increment that provides both elastic modulus and hardness of the specimen as a function of depth of penetration. Provision is

made for thermal drift correction, initial penetration, compliance determination, and indenter area function calibration. The software also provides a simulation mode of operation whereby mechanical properties of the specimen and indenter are used as inputs to calculate a theoretical load-displacement response that may be compared with experimental results. The control software allows any combination of loading and unloading to take place through the use of “script” files that can be assembled automatically for standard tests or created by the user as desired. The UMIS<sup>®</sup> is a dual range instrument with x1 and x10 on load and force ranges selectable by the user.

The specifications of the instrument are as follows:

Maximum load	50 mN (Range A), 500 mN (Range B)
Minimum contact force	2 $\mu$ N
Force resolution	500 nN
Force noise floor	750 nN
Maximum depth	2 $\mu$ m (Range A), 20 $\mu$ m (Range B)
Depth resolution	0.03 nm
Depth noise floor	0.05 nm
Sample positioning	$\pm 0.5 \mu$ m ( $\pm 0.1 \mu$ m optional)
Field of testing	100 mm x 100 mm
Load frame compliance	0.1 nm/mN
User interface	Windows 95/98/NT/2000

The UMIS<sup>®</sup> can be configured for additional ranges from 1 mN to a maximum of 5 N.

The UMIS<sup>®</sup> is offered with optional components such as a scratch tester and a hot stage. The scratch tester has a unique “tone arm” design that decouples the transverse or lateral force from the main indenter shaft thus shielding the sensitive depth and force sensors from mechanical interference. The lateral force is measured with another separate LVDT displacement transducer via a series of calibrated leaf springs. The hot stage accessory incorporates a special tip heater to ensure that both specimen and indenter are at the same temperature when they come into contact, thus minimizing errors due to thermal expansion and contraction at this sensitive area. The main specimen heater has a water-cooled exterior to maximize temperature stability of the system.

The unique features of the UMIS<sup>®</sup> that distinguish it from its competitors are the exceptional repeatability, stability, and robustness of the complete system. This makes the unit extremely easy to use, even by inexperienced operators. The robustness of the design makes the UMIS<sup>®</sup> suitable for use in industrial, research, and teaching laboratories.

## References

1. "MTS," "Nano," and "Nano Indenter" are registered trademarks of MTS Systems Corporation, Nano Instruments Innovation Center, 1001 Larson Drive, Oak Ridge, TN 37830 USA.
2. J.B. Pethica, "Microhardness tests with penetration depths less than ion implanted layer thickness in ion implantation into metals," Third International Conference on Modification of Surface Properties of Metals by Ion-Implantation, Manchester, England, 23-26, 1981, V. Ashworth et al. eds. Pergamon Press, Oxford, 1982, pp. 147-157.
3. B.N. Lucas, W.C. Oliver, and J.E. Swindeman, "The dynamics of frequency-specific, depth sensing indentation testing," *Mat. Res. Soc. Symp. Proc.* 522, 1998, pp. 3-14.
4. W.C. Oliver and J.B. Pethica, "Method for continuous determination of the elastic stiffness of contact between two bodies," United States Patent, 4848141, 1989.
5. COMOS is a registered trademark of Structural Research and Analysis Corporation.
6. Micro Materials Ltd., Unit 3, The Byre, Wrexham Technology Park, Wrexham LL13 7YP, United Kingdom.
7. Hysitron Inc., 5251 West 73rd Street, Minneapolis, MN, 55439 USA.
8. W.A. Bonin and Hysitron Inc., "Apparatus for microindentation hardness testing and surface imaging incorporating a multi-plate capacitor system," United States Patent, 5553486, 1996.
9. W.A. Bonin and Hysitron Inc., "Capacitive transducer with electrostatic actuation," United States Patent, 5576483, 1996.
10. W.A. Bonin and Hysitron Inc., "Multi-dimensional capacitive transducer," United States Patent, 5661235, 1997.
11. W.A. Bonin and Hysitron Inc., "Multi-dimensional capacitive transducer," United States Patent, 5869751, 1999.
12. W.A. Bonin and Hysitron Inc., "Apparatus for microindentation hardness testing and surface imaging incorporating a multi-plate capacitor system," United States Patent, 6026677, 2000.
13. CSEM Instruments, Jaquet-Droz 1, P.O Box 41, CH-2007 Neuchâtel Switzerland.
14. N. X. Randall, C. Julia-Schmutz, J. M. Soro, J. von Stebut, and G. Zacharie, "Novel nanoindentation method for characterising multiphase materials," *Thin Solid Films*, 308-309, 1997, pp. 297-303.
15. CSIRO, Bradfield Rd, West Lindfield, NSW 2070 Australia.
16. J.S. Field, "Penetrating measuring instrument," United States Patent, 5067346, 1991.

# Chapter 10

## Examples of Nanoindentation Testing

### 10.1 Introduction

Nanoindentation finds a wide application. The test results provide information on the elastic modulus, hardness, strain-hardening, cracking, phase transformations, creep, fracture toughness, and energy absorption. Since the scale of deformation is very small, the technique is applicable to thin surface films and surface modified layers. In many cases, the microstructural features of a thin film or coating differs markedly from that of the bulk material due to the presence of residual stresses, preferred orientations of crystallographic planes, and the morphology of the microstructure. The proceedings of annual symposiums are a rich source of information about the applications of nanoindentation. In this chapter, we present some rather straight forward examples of analysis of nanoindentation test data using the methods described in the previous chapters.

The two most commonly measured properties during an nanoindentation test are elastic modulus and hardness. Both may be measured as a function of depth of penetration into the specimen surface, thus providing a depth profile of these properties. Hardness is important since it is related in many cases to the strength or fracture toughness of the specimen. A high hardness generally corresponds to a high abrasive wear resistance. Hardness and modulus values can also be used to monitor surface or material consistency. Elastic modulus provides a measure of stiffness or compliance of the specimen. Hard materials are usually also very brittle and a hard protective coating may often be deposited on a relatively soft material with a high elastic modulus to provide a rigid support that will help prevent brittle fracture. Measurements of modulus of both film and substrate allow such thin film systems to be optimized for a particular application. The ratio of modulus and hardness ( $E/H$ ) also provides valuable information about a material since it is this ratio that determines the spatial extent of the elastic deformation that might occur under loading before permanent yielding occurs.

## 10.2 Fused Silica

Perhaps one of the most common and easiest samples to test using nanoindentation is fused silica (or fused quartz as it is sometimes called). The specimen is typically polished flat and mounted in accordance with the recommendations given in earlier chapters. A maximum load of 50 mN with 25 load increments will result in a depth of penetration of about 650 nm for a Berkovich indenter, well within the capability of any good instrument.

Figure 10.1 shows the load-displacement curve obtained with a Berkovich indenter on a fused silica specimen. For a load of 50 mN, the uncorrected depth of penetration was found to be 637.5 nm. After correction for thermal drift (calculated to be  $6.20 \times 10^{-5} \mu\text{m}/\text{sec}$ ), the depth of penetration was estimated to be 631.8 nm. After correction for instrument compliance, the penetration was 626.8 nm. An initial penetration depth of  $h_i = 0.2 \text{ nm}$  was determined using the logarithmic fitting method (see Chapter 4) for an initial contact force of  $P_i = 2.13 \mu\text{N}$  leading to a maximum depth of penetration for this test of  $h_t = 627.0 \text{ nm}$ .

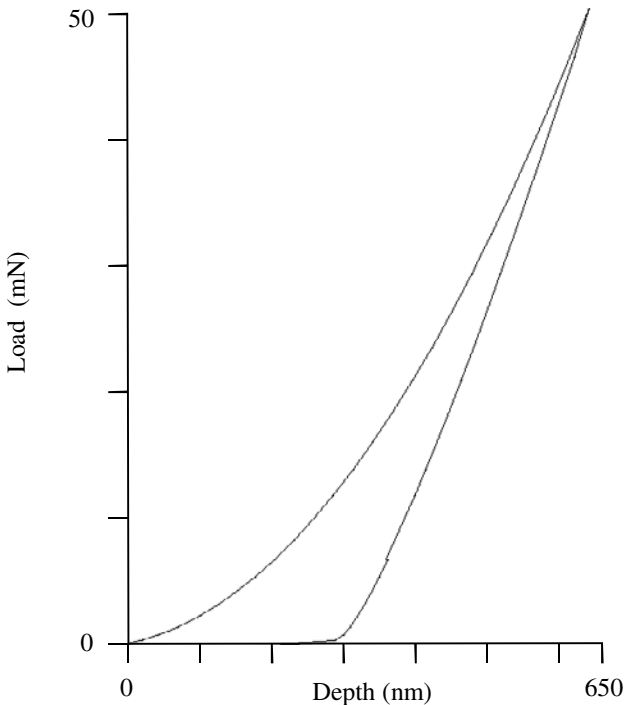


**Fig. 10.1** Load-displacement curves for a nanoindentation experiment on fused silica for Berkovich indenter at 50 mN maximum load. Data have been corrected for thermal drift, load frame compliance, and initial penetration. Maximum depth of penetration is 627 nm (Courtesy CSIRO).

It is important to apply the area correction function appropriate to the indenter being used in any analysis. Without the area correction function being applied, and using the first eight unloading points for the fitting of the data for the initial unloading slope, we find a value for  $dP/dh$  of 177.9 mN/ $\mu\text{m}$  with an estimated residual depth,  $h_r$ , of 65.2 nm and a plastic depth  $h_p$  equal to 416.3 nm. Using the multiple point unload method, this leads to a value for the combined modulus of the system  $E^*$  of 73.91 GPa from which follows an estimation of the specimen modulus of 76.59 GPa (using a modulus of 1000 GPa and a Poisson's ratio of 0.07 for the diamond indenter). The hardness is computed to be 11.74 GPa. With the area correction function applied, we obtain a specimen modulus of 70.0 GPa and a hardness of 9.93 GPa, in reasonable agreement with the literature values<sup>1</sup> of 70 GPa and 7.6 GPa, respectively.<sup>§§</sup> It should be appreciated that this test, trivial as it may seem, provides a very good example of induced plasticity in what is nominally a brittle material.<sup>2</sup> The existence of a residual impression is proof of plastic deformation within the material.

### 10.3 Titanium Dioxide Thin Film

A common application of nanoindentation testing is the measurement of properties of thin film specimens. This is not often an easy task, since the films of interest are often on the order of 500 nm thickness or less. Using the 10% rule, the maximum depth of penetration is usually limited to about 50 nm or less for hardness determinations. Quantitative information about mechanical properties of thin films is of particular practical interest. In the work reported here, 500 nm films of  $\text{TiO}_2$  were deposited on silicon substrates using a filtered arc deposition process in which the process parameters were changed in order to study the resulting change in mechanical and optical properties. Using a gradually increasing bias voltage, Bendavid, Martin, and Takikawa<sup>3</sup> found that an observed change in hardness and modulus of the films corresponded to a change in phase of the film material from anatase to rutile forms. By increasing the bias voltage, the energy of the bombarding ions in the arc deposition process is increased, and this causes structural modifications to the microstructure that increase its hardness.

Figure 10.2 shows how the measured film hardness (for nanoindentation tests done at 2 mN maximum load) resulted in a change of hardness from 11.6 GPa to 17.6 GPa over a range of bias voltages from zero to  $-400$  V. Testing of this kind enables the mechanical properties of such films to be tailored to particular applications.

<sup>§§</sup> It should be noted that a close agreement between hardness values in comparison tests with published literature values is not so easily obtained, since hardness is not an intrinsic material property — depending as it does on the method of testing. Nanoindentation tests on fused silica nearly always give a result greater than published values of macro scale test results.

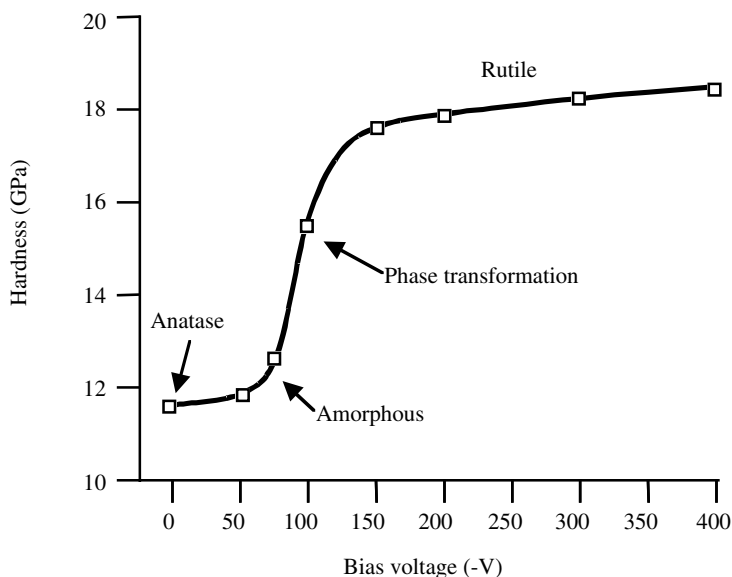


**Fig. 10.2** Hardness of  $\text{TiO}_2$  films on a Si substrate as a function of substrate bias voltage. A rapid increase in hardness is observed at about  $-100$  V bias which coincides with a phase transformation from anatase to rutile (Courtesy CSIRO and after reference 3).

## 10.4 Superhard Thin Film

An emerging application of nanoindentation with respect to thin films is the hardness testing of very hard coatings. The hardness of hardened steel is in the order of 10 GPa, and of ceramics is on the order of 20 – 30 GPa. Recent developments in thin film technology have resulted in measured indentation hardness values of greater than 40 GPa. Such materials are called “superhard.” The hardness of nanostructured materials have been measured at greater than 50 GPa and Vepřek<sup>4</sup> reports a measured hardness of a nc-TiN/SiN material of 105 GPa, harder than that of diamond (usually taken to be 100 GPa).

Figure 10.3 shows the load displacement curves for two thin film systems, the first, a conventional TiN film, and the second, a nanocomposite film. In the nanocomposite material, the amorphous silicon phase serves to restrict the growth of TiN structures, and this has the effect of increasing the hardness of the composite material. The measured hardness in this case for the nanocomposite film is approximately 60 GPa. Note that for a maximum load of about 4 mN, the penetration depth for these types of coatings is about 80 nm.

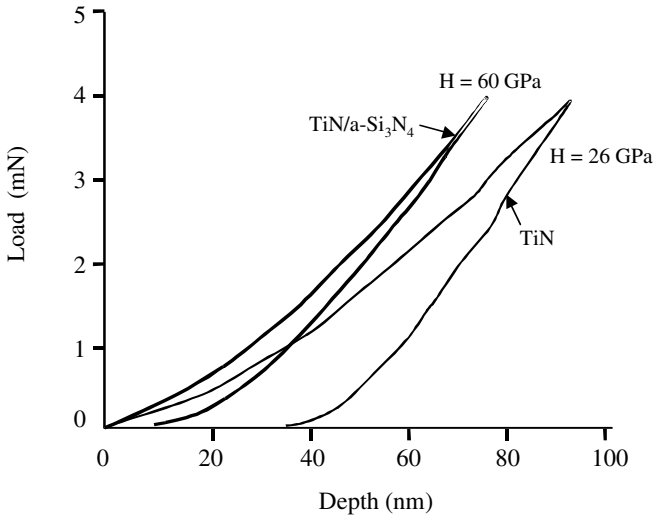
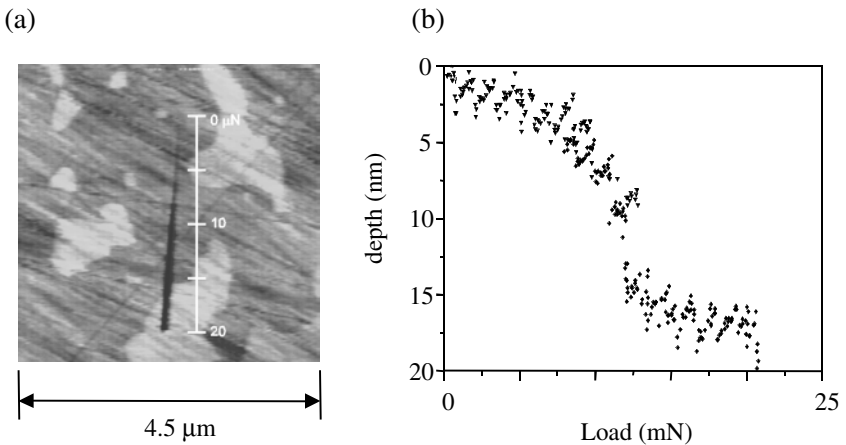


**Fig. 10.3** Load-displacement response of TiN thin films, one doped with an amorphous silicon phase that serves to restrict the growth of the TiN grains during the deposition process and this provides an effective increase in hardness (Courtesy CSIRO).

The use of nanoindentation for the measurement of superhard materials is a particularly difficult challenge. The depths of penetration are on the order of the radius of the tip of a typical Berkovich indenter and are also comparable to the surface roughness of the specimen surface. Such thin films are often prepared with a considerable level of residual stress that also affects the indentation hardness value. Attention to the methods of correction and factors affecting nanoindentation test results described in Chapters 3 and 4 have to be taken seriously indeed if values of hardness in excess of 40 GPa are to be considered meaningful rather than just comparative. An interesting theoretical and practical challenge is how to measure the hardness of materials that may well be harder than diamond – traditionally considered the hardest known substance.

## 10.5 Diamond-like Carbon (DLC) Thin Film

Diamond-like carbon is a very important material in anti-wear films in the semiconductor and computer industry. Film thicknesses are typically on the order of 10 nm. In these cases, substrate effects are almost impossible to avoid during indentation testing. Scratch testing of DLC films is a useful alternative to evaluate adhesion and mechanical properties.



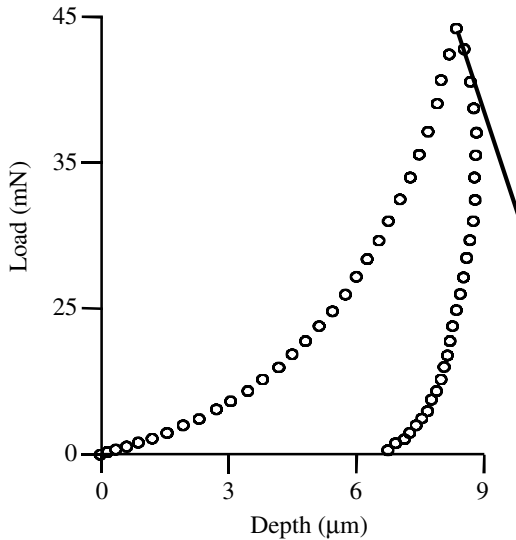
**Fig. 10.4** (a) Residual impression from a scratch test in a 7.5 nm DLC film using a ramped force up to 20  $\mu\text{N}$ . (b) Penetration depths for multiple scratch tests plotted against normal load  $F_N$ . Failure of film is evidenced by sudden increase in depth at a load of about 12  $\mu\text{N}$  (Courtesy Hysitron Inc.).

Figure 10.4 (a) shows a ramped load scratch from 0 up to 20  $\mu\text{N}$  on a 7.5 nm DLC film on a computer hard disk head slider. Figure 10.4 (b) shows the normal displacement as a function of the normal force. At a critical load of about 12  $\mu\text{N}$ , the film fails and a sudden increase in penetration depth is recorded.

## 10.6 Creep in Polymer Film

One of the less well-known applications of nanoindentation is the estimation of the viscoelastic properties of biomaterials and polymers. Figure 10.5 shows a conventional load-displacement curve obtained with a spherical indenter on a polymer film. In this case, creep within the specimen material leads to a negative slope for the unloading, and this invalidates the conventional methods of analysis given in Chapter 3.

In Chapter 7, it was shown how a simple three-element model could be used to extract viscoelastic properties of the specimen from the creep curve of a nanoindentation test. The creep curve is obtained by holding the load constant (usually at maximum load) and monitoring the change in depth. Figure 10.6 shows creep curves obtained on samples of a polyethylene and a cross-linked resin using a 20  $\mu\text{m}$  sphero-conical indenter with an applied load of 5 mN held for 60 seconds. The theoretical creep curves shown in Fig. 10.6 were generated from Eq. 7.7e and the parameters  $E_1$ ,  $G_2$ , and  $\eta$  systematically adjusted for a good fit.



**Fig. 10.5** Conventional load-displacement curve resulting from indentation of a polymer film with a 20  $\mu\text{m}$  radius spherical indenter. Creep within the specimen material during the test results in a negative slope of the unloading curve.

The results in Table 10.1 indicate that the cross-linked resin is stiffer and more solid-like than the polyethylene, but both materials exhibit creep behavior during an indentation test. The conventional method of analysis using the slope of the unloading curve would not provide meaningful information about the mechanical properties of these materials.

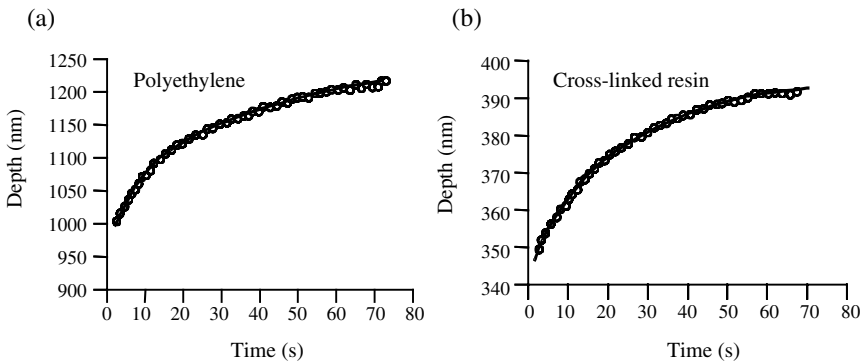


**Fig. 10.6** Creep curves for (a) polyethylene and (b) cross-linked resin using a 20  $\mu\text{m}$  sphero-conical indenter with an applied load of 5 mN over 60 seconds. Data points indicate experimental results, solid lines indicate best fit to Eq. 7.7e (Courtesy CSIRO).

**Table 10.1** Results of creep analysis for polyethylene and cross-linked resin. Parameters  $E_1$ ,  $G_2$ , and  $\eta$  were systematically adjusted for the best fit between experimental data and Eq. 7.7e.  $E_2$  is calculated from Eq. 7.7i.

	$E_1$ GPa	$E_2$ GPa	$\eta$ Gpas
Polyethylene	0.7	1.6	13.0
Cross-linked resin	3.3	12.4	99.6

## 10.7 Fracture and Delamination of Silicon Oxide Film

Nanoindentation testing can be used not only to measure hardness and modulus of thin films, but also to induce a controlled amount of damage within the film and/or the substrate. As mentioned in Section 2.4, an experienced person can relate features on the load-displacement curve to particular modes of damage in the specimen.

In the example shown in Fig. 10.7, a  $1\ \mu\text{m}$  sphero-conical indenter has been used to intentionally fracture a  $1\ \mu\text{m}$  thick  $\text{SiO}_2$  film on silicon. Delamination is evidence by the light area surrounding the indentation, and radial cracks are evident. These events manifest themselves as discontinuities on the load-displacement curve.

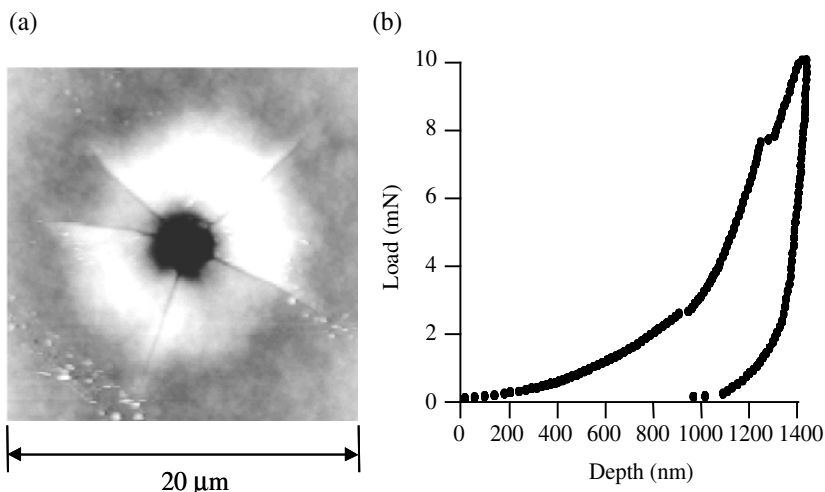


**Fig. 10.7** (a) The result of an indentation with a  $1\ \mu\text{m}$  sphero-conical tip into  $1\ \mu\text{m}$   $\text{SiO}_2$  film on silicon. (b) Pop-in events on a load-displacement curve can be used to quantify the conditions for the initiation of cracks and delamination (Courtesy Hysitron Inc.).

## 10.8 High-Temperature Testing on Fused Silica

In most materials, the elastic modulus decreases with increasing temperature. One unusual property of fused silica is that its elastic modulus increases with increasing temperature. Figure 10.8 (a) shows a load-displacement response of a fused silica specimen at room temperature and at 200 °C. Figure 10.8 (b) shows the variation in modulus with temperature for the same material where the temperature ranged from room temperature to 400 °C. Henley, Mao, Bell, and Mysen<sup>5</sup> showed that under hydrostatic pressures of up to 8 GPa a reversible structural change occurred corresponding to a change in the Si-O-Si bond angle. Above 8 GPa, the structural change was irreversible. Galeener<sup>6</sup> showed that a change in the bond angle also occurred at temperatures above 900 °C. Thus, in an indentation test on fused silica, both hydrostatic pressure and temperature play a role in this behaviour.

There are many other examples which justify high temperature measurements, including the investigation of microelectronic thin films normally processed at temperatures up to 500 °C, indentation creep studies, scratch testing of polymer coatings and other thin films, and the investigation of temperature-sensitive fibre-matrix bonding forces. In addition, dislocation mobility (and therefore hardness) is temperature sensitive.

From a practical standpoint, the wear performance of a film-substrate combination will ideally require optimisation of the relative properties of the film and substrate materials at the service temperature rather than inferring their properties from room temperature results.

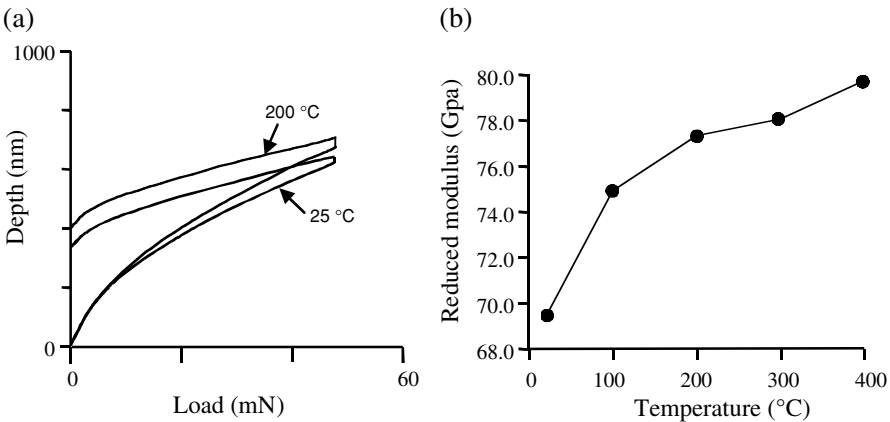


**Fig. 10.8.** (a) Load-displacement curve for fused silica at 400 °C. (b) Variation in elastic modulus computed from nanoindentation test results as a function of temperature (Courtesy Micro Materials Ltd.).

## 10.9 Adhesion Measurement

A particularly novel application of nanoindentation testing is the measurement of adhesion for powder particles. This application is of particular relevance in the pharmaceutical industry. Powder-coated samples in the form of cylinders (e.g., wires coated with the powder) are attached to the sample stage and indenter mounting. The cylinders are then brought into contact with a very low force. The force is then slowly reduced through zero to negative (pulling) values until the surfaces separate. The force at separation is identified and is a measure of the adhesion of the particles due to van der Waals attractions (see Appendix 3). The use of coated surfaces together ensures a statistically more meaningful result than a measurement with single particles.

A typical adhesion result using the NanoTest<sup>®</sup> instrument is shown in Fig. 10.9. Here, the depth and load were monitored continuously as the load was increased, held, and then decreased through zero to negative values until eventually the pendulum moved away from the specimen surface. The maximum applied load was 250  $\mu\text{N}$  prior to load reversal for specimen separation. The adhesion force was found to range from 0.14 mN to 0.19 mN for tests on different parts of the specimen.

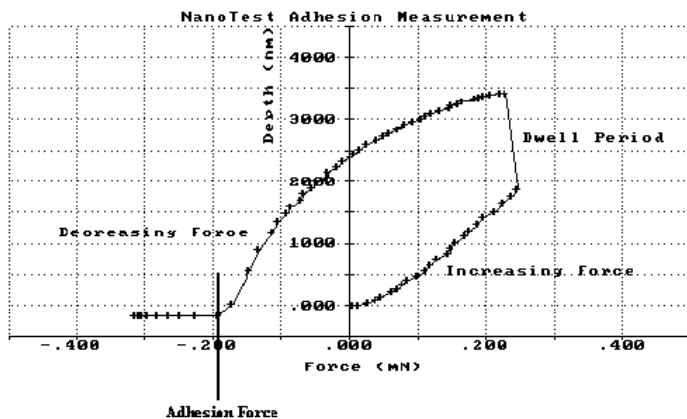


**Fig. 10.9** Adhesive force result using the NanoTest<sup>®</sup> pendulum arrangement. The load was increased, held, and then decreased through zero to negative values until the surfaces separated (Courtesy Micro Materials Ltd.).

## 10.10 Dynamic Hardness

The “dynamic hardness” is defined as the energy consumed during a rapid indentation divided by the volume of the indentation. The energy of the indentation can be determined from the ratio of the impact and rebound velocities as the indenter bounces on the specimen surface. The volume of indentation is found from the penetration depth and the known geometry of the indenter.

Figure 10.10 shows the results for an aluminium sample with a Berkovich indenter. The impact and rebound velocities are obtained from the slopes of the responses just before, and just after, impact. For the sample tested, the quasi-static hardness was measured to be 0.27 GPa while the dynamic hardness was measured to be 0.54 GPa. This type of result is relevant for dynamic processes such as impact wire bonding.

Successful dynamic hardness testing requires a relatively low system resonant frequency.

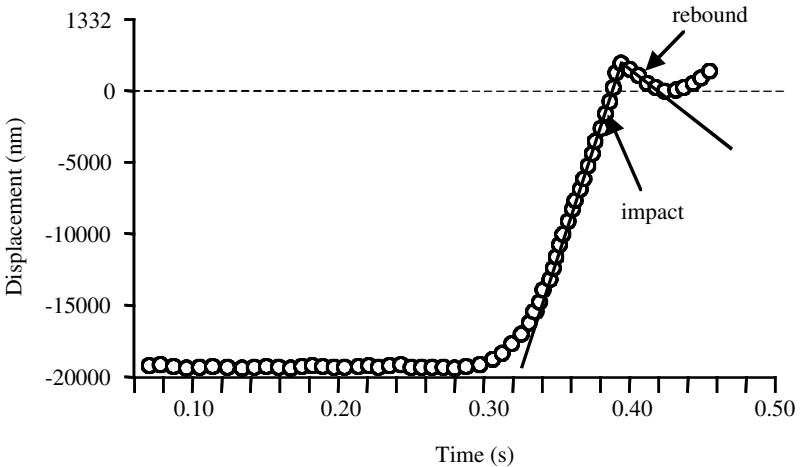


**Fig. 10.10** Displacement vs time measurements during impact and rebound for an aluminium sample with a Berkovich indenter (Courtesy Micro Materials Ltd.).

## 10.11 Repeatability Testing

It is of interest to purchasers of nanoindentation instruments to be able to evaluate their relative features and performance. A very good test of repeatability of an instrument is the comparison of load-displacement curves for different maximum loads. Figure 10.11 shows such a comparison. An overlay of the load-displacement curves for a wide range of loads should all fall within acceptable limits on the loading curve, and show a smooth response for both the loading and unloading portions. The inset in Fig. 10.11 shows the residual impressions in the specimen surface for the load-displacement curves shown.

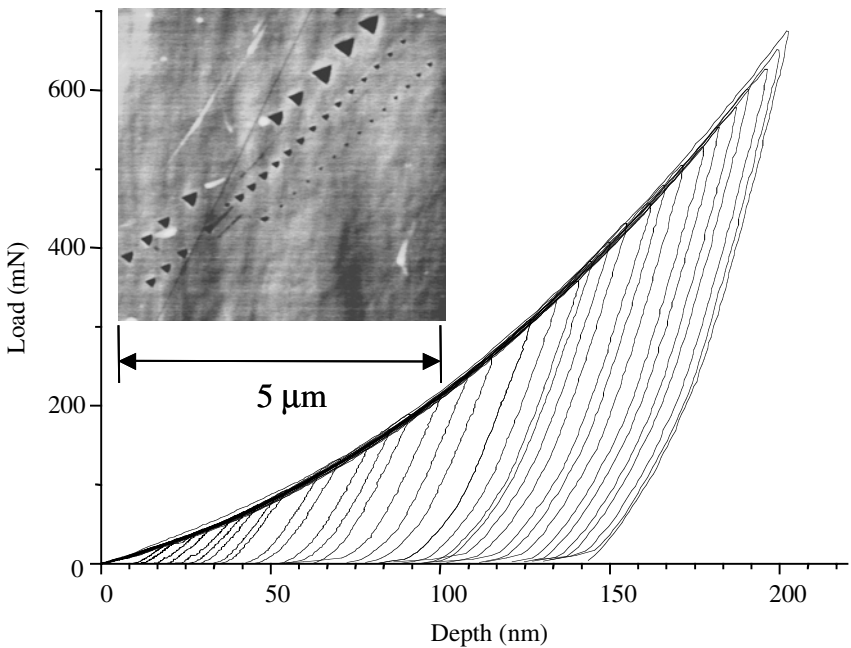


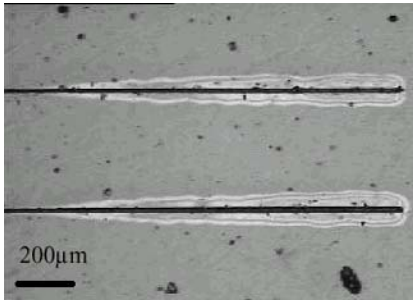
**Fig. 10.11** Load-displacement curves for varying maximum loads on fused silica. The curves should all fall on top of one another for the loading half of the cycle and show a smooth and regular spacing for the unloading portion of the response. The inset shows the residual impressions made in the surface for the load-displacement curves shown (Courtesy Hysitron Inc.).

## 10.12 Assessment of Thin Film Adhesion by Scratch Testing

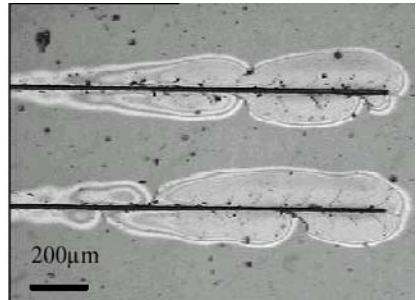
The need for quantitative assessment of the adhesion of thin films and coatings is a pressing one as manufacturers of such structures are called upon to increase the film performance while decreasing their thickness. Conventional scratch tests involve the measurement of the critical load for failure under an increasing load. The critical load can be determined by inspection or, in some cases, by a sudden change in the friction coefficient. Conventional large-scale scratch testers are limited by the magnitude of the forces at the low end of the range, while AFM-based instruments are often limited by their short range of scratch length. Purpose-built nanoindentation scratch testers overcome these limitations by offering a suitable range of normal and lateral forces as well as reasonably large scratch lengths.

Figure 10.12 shows the results of scratch tests involving a ramped, increasing force applied to a 10  $\mu\text{m}$  spherical indenter on two titanium oxide thin films. The scratch length is about 2.5 mm while the normal force varied from zero to 50 mN.

(a)



(b)



**Fig. 10.12** A comparison of two  $\text{TiO}_2$  coated glass substrates subjected to a progressive normal load scratch of 0-50 mN with a 10  $\mu\text{m}$  diamond indenter. The scratch speed is 2.5 mm/minute at a length of 2.5 mm. (a) High roughness sample; (b) low roughness sample (Courtesy CSEM Instruments).

## 10.13 Other Applications

Nanoindentation testing finds a wide application and the examples given above represent only a very small cross-section of those. Figure 10.13 shows some further examples of the technique.

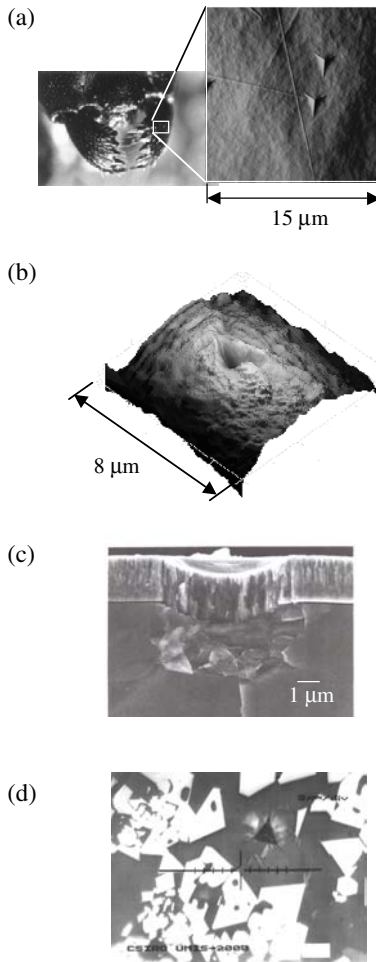


**Fig. 10.13** Examples of nanoindentation testing. (a) Ant mandible (Courtesy Hysitron Inc.) (b) Optical fiber (Courtesy Hysitron Inc.), (c) Cross-section of controlled damage in  $2.7\ \mu\text{m}$  TiN film on silicon using  $5\ \mu\text{m}$  spherical indenter at  $350\ \text{mN}$  load. Note the up-lifting of the film from the substrate (Courtesy CSIRO and after reference 7). (d) Precise positioning of indentations on a multiphase iron ore sinter (Courtesy CSIRO).

## References

1. L.J. McColm, *Ceramic Hardness*, Plenum Press, New York, 1990.
2. D.M. Marsh, "Plastic flow in glass," *Proc. R. Soc. London*, A279, 1964, pp. 420–435.
3. A. Bendavid, P.J. Martin, and H. Takikawa, "Deposition and modification of titanium dioxide thin films by filtered arc deposition," *Thin Solid Films*, 360, 2000, pp. 241–249.
4. S. Vepřek "The search for novel, superhard materials," *J. Vac. Sci. Technol.* A17 5, 1999, pp. 2401–2420.
5. R.J. Hemley, H.K. Mao, P.M. Bell, and B.O. Mysen, "Raman-Spectroscopy of SiO<sub>2</sub> glass at high pressure," *Phys. Rev. Lett.* 57 6, 1986, pp. 747–750.
6. F.L. Galeener, "Raman and ESR studies of the thermal history of amorphous SiO<sub>2</sub>," *J. Non-Cryst. Solids*, 71, 1985, pp. 373–386.
7. E. Weppelmann, M. Whittling, M.V. Swain, and D. Munz, "Indentation cracking of brittle thin films on brittle substrates," in *Fracture Mechanics of Ceramics*, Vol. 12, R.C. Bradt et al. eds., Plenum Press, N.Y., 1996.

# Appendix 1

## Elastic Indentation Stress Fields

The methods of analysis of nanoindentation test data rely heavily on the elastic unloading response of the system. It is of interest therefore to have some appreciation of the equations for elastic contact and the associated indentation stress fields. The following assumptions are an essential component of the analytical equations:

- The radii of curvature of the contacting bodies are large compared with the radius of the circle of contact.
- The dimensions of each body are large compared with the radius of the circle of contact. This allows indentation stresses and strains to be considered independently of those arising from the geometry, method of attachment, and boundaries of each solid.
- The contacting bodies are in frictionless contact. That is, only a normal pressure is transmitted between the indenter and the specimen.

### A1.1 Contact Pressure Distributions

The indentation stress fields arise from the pressure distributions shown in Table A.1, which are applied over a contact radius on the surface of a linearly elastic semi-infinite half-space.

**Table A.1** Equations for surface pressure distributions beneath the indenter for different types of indenters.

Indenter type	Equation for normal pressure distribution $r < a$
Sphere	$\frac{\sigma_z}{p_m} = -\frac{3}{2} \left( 1 - \frac{r^2}{a^2} \right)^{1/2}$
Cylindrical flat punch	$\frac{\sigma_z}{p_m} = -\frac{1}{2} \left( 1 - \frac{r^2}{a^2} \right)^{-1/2}$
Cone	$\frac{\sigma_z}{p_m} = -\frac{a}{r} \cosh^{-1} \frac{a}{r}$

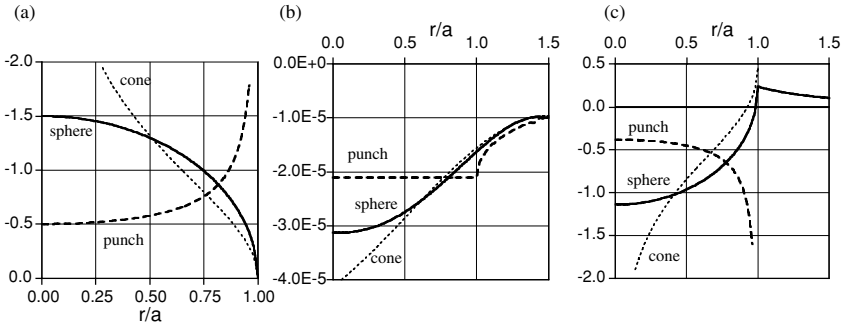


**Fig. A1.1** (a) Normalized contact pressure distribution  $\sigma_z/p_m$  for spherical indenter, cylindrical punch, and conical indenters. (b) Deflection of the surface spherical, cylindrical, and conical indenters. Deflections in mm calculated for  $p_m = 1$  MPa and radius of circle of contact = 1 mm and for  $E = 70$  GPa. (c) Magnitude of normalized surface radial stress  $\sigma_r/p_m$  for spherical, cylindrical, and conical indenters. Calculated for  $\nu = 0.26$  (after reference 1).

The pressure distributions, normal displacements and the magnitude of the radial stresses associated with an elastic contact with these indenters are shown in Fig. A1.1.

## A1.2 Indentation Stress Fields

### A1.2.1 Spherical indenter

An equation for the normal pressure distribution directly beneath a spherical indenter was given by Hertz and is shown in Table A.1. As shown in Fig. A1.1a, the normal pressure  $\sigma_z = 1.5p_m$  is a maximum at the center of contact and is zero at the edge of the contact circle. Outside the contact circle, the normal stress  $\sigma_z$  is zero, it being a free surface. The displacement of points on the surface of the specimen within the contact circle, measured with respect to the original specimen free surface, is given by:

$$u_z = \frac{1 - \nu^2}{E} \frac{3}{2} p_m \frac{\pi}{4a} (2a^2 - r^2) \quad r \leq a \quad (\text{A1.2.1a})$$

Note that for all values of  $r < a$ , the displacement of points on the surface is inward toward the center of contact. Within the interior of the specimen, the stresses have a distribution depicted in Fig. A1.2. The contours shown in Figs. A.2 (a) to (e) give no information about the direction or line of action of these

stresses. Such information is only available by examining stress trajectories. Stress trajectories are curves whose tangents show the direction of one of the principal stresses at the point of tangency and are particularly useful in visualizing the directions in which the principal stresses act. The stress trajectories of  $\sigma_2$ , being a hoop stress, are circles around the  $z$  axis. Stress trajectories for  $\sigma_1$  and  $\sigma_3$  are shown in Figs. A1.2 (f).

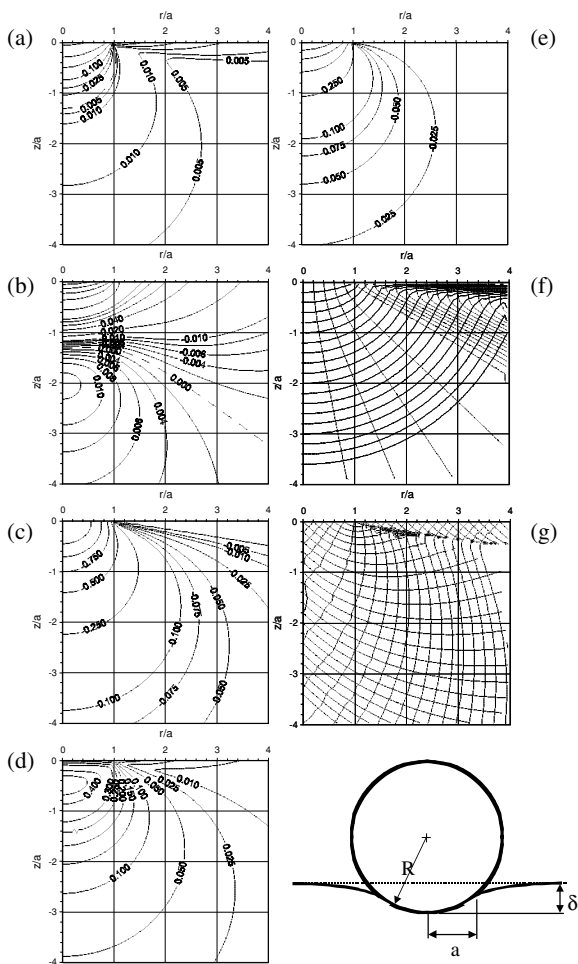


**Fig. A1.2** Stress trajectories and contours of equal stress for spherical indenter calculated for Poisson's ratio  $\nu = 0.26$ . Distances  $r$  and  $z$  normalized to the contact radius  $a$  and stresses expressed in terms of the mean contact pressure  $p_m$ . (a)  $\sigma_1$ , (b)  $\sigma_2$ , (c)  $\sigma_3$ , (d)  $\tau_{\max}$ , (e)  $\sigma_H$ , (f)  $\sigma_1$  and  $\sigma_3$  trajectories, (g)  $\tau_{\max}$  trajectories (after reference 1).

### A1.2.2 Conical indenter

The mean contact pressure for a conical indenter depends only on the cone angle. The displacement beneath the original specimen surface is given by:

$$u_z = \left( \frac{\pi}{2} - \frac{r}{a} \right) a \cot \alpha \quad r \leq a \quad (\text{A1.2.2a})$$

Contours of equal stress and stress trajectories for a conical indenter are shown in Fig. A1.3.

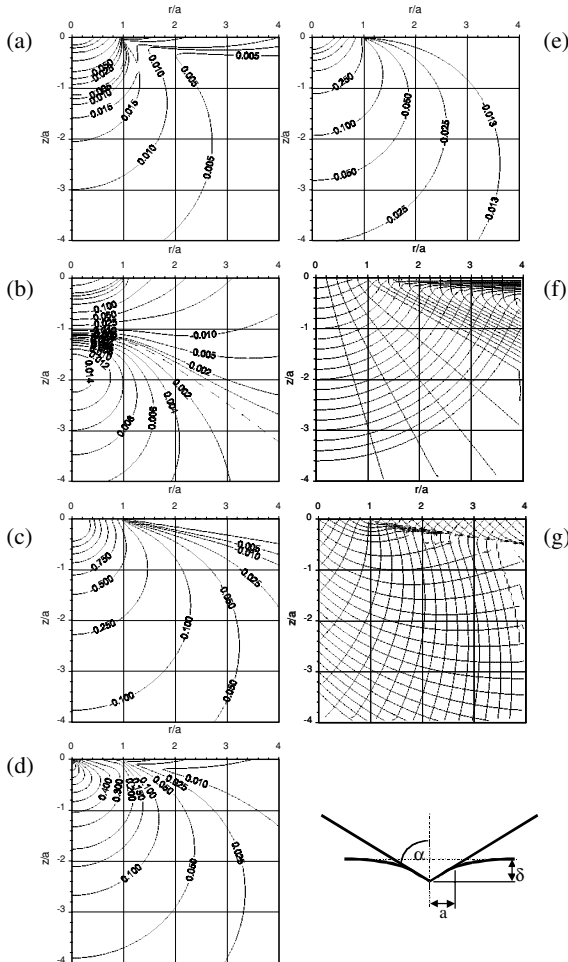


**Fig. A1.3** Stress trajectories and contours of equal stress for conical indenter calculated for Poisson's ratio  $\nu = 0.26$ . Distances  $r$  and  $z$  normalized to the contact radius  $a$  and stresses expressed in terms of the mean contact pressure  $p_m$ . (a)  $\sigma_1$ , (b)  $\sigma_2$ , (c)  $\sigma_3$ , (d)  $\tau_{\max}$ , (e)  $\sigma_H$ , (f)  $\sigma_1$  and  $\sigma_3$  trajectories, (g)  $\tau_{\max}$  trajectories (after reference 1).

## References

1. A.C. Fischer-Cripps, *Introduction to Contact Mechanics*, Springer-Verlag, New York, 2000.

# Appendix 2

## Surface Forces, Adhesion, and Friction

### A2.1 Adhesion Forces in Nanoindentation

With the increasing popularity of nanoscale technology, and the increasing sensitivity of nanoindentation instruments, it is appropriate to consider the effect of surface forces and adhesion in nanoindentation testing. The treatments of analysis presented in this book assume that there are no adhesive forces involved in the contact. That is, when the load is reduced to zero, the radius or dimension of the contact area also goes to zero. For contacts between very smooth surfaces, this is not the case owing to surface adhesion forces. In this appendix, the basic principles and significance of these types of forces in nanoindentation testing is introduced.

### A2.2 Forces in Nature

It is generally agreed that there are four fundamental forces in nature. The so-called “strong” and “weak” nuclear forces are those found to exist over a very short range between neutrons, electrons, and protons and do not concern us here. The other two forces are the gravitational force and the electromagnetic force. It is the electromagnetic force that determines the nature of the physical interactions between molecules and is of most interest to us in this book. The electromagnetic force and the gravitational force often act together to provide physical phenomena that we are familiar with on a macroscopic scale.

Interactions (attractive and repulsive forces) between molecules take place over a relatively short distance scale of usually no more than 100 nm or so. However, the sum total effect of these short range interactions often lead to long-range macroscopic effects, e.g., the capillary rise of liquid in a narrow tube. It is important to note that the actual macroscopic physical properties of a liquid or a solid are determined by these relatively short-range interactions and do not generally depend on the size and shape of the solid or the container in the case of a liquid.

## A2.3 Interaction Potentials

Intermolecular forces can generally not be fully described by a simple force law, such as the Universal Law of Gravitation. The forces between molecules are influenced by the chemical nature of the elements involved, and also the proximity of neighboring molecules, whether they be of the same type or not. The combination of intermolecular forces from a variety of causes may result in a net attraction or repulsion between two molecules. It is sometimes convenient to talk of the molecular interactions in terms of their potential energy. Two widely separated molecules are said to have a high potential energy if there is an attractive force between them. If two such molecules are allowed to approach each other, the attractive force between them will cause them to accelerate and their initial potential energy is converted into kinetic energy. When these two molecules come together at an equilibrium position, this kinetic energy may be dissipated as heat and the potential energy of the interaction is at a minimum — a chemical bond has formed.

It is convenient to assign a potential energy of zero to widely spaced molecules so that when they approach and settle at their equilibrium position, the potential energy is a negative quantity. Since we generally assign a positive number to work done on a system (energy entering a system) and a negative number to work done by a system (energy leaving the system), work has to be done on the molecules to separate them.

Now, because of this assignment of signs to energy, we must be careful to assign the correct sign to intermolecular forces. It is common to define a positive force representing an attraction between two molecules. However, it turns out to be more convenient to assign negative forces as being attractive and positive forces as being repulsive. When multiplied by an appropriate distance, the energy change, positive or negative, will be then correctly assigned.

A very common interaction potential is the Lennard-Jones potential<sup>1</sup> between two atoms. It takes the form:

$$w(r) = -\frac{A}{r^6} + \frac{B}{r^{12}} \quad (\text{A2.3.1})$$

where  $r$  is the distance between the atoms and the negative term represents the energy associated with attractive forces and the positive term represents that associated with the repulsive forces. The energies and forces associated with the Lennard-Jones potential are shown in Fig. A2.1.

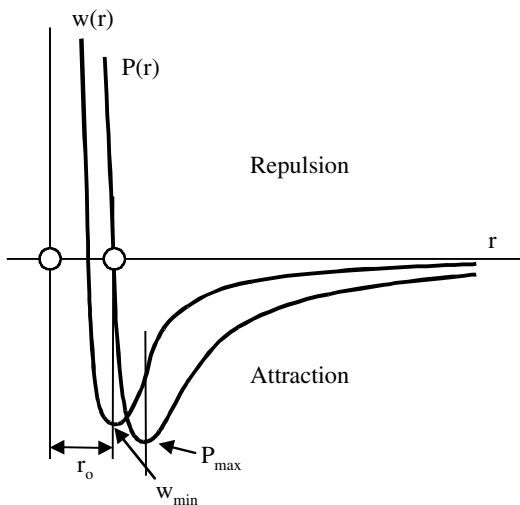


**Fig. A2.1** The Lennard-Jones potential and interatomic forces between two atoms. The interaction force  $P(r)$  is zero where the energy  $w(r)$  is at a minimum, and the interaction force is a maximum when the rate of change of energy with respect to the distance between the two atoms is a maximum.

Note that in Fig. A2.1, the interaction force  $P(r)$  is zero where the energy  $w(r)$  is at a minimum, and the interaction force is a maximum (attractive in this case) when the rate of change, of energy with respect to the distance between the two atoms, is a maximum. Since we are mainly concerned with the significance of surface forces on adhesion and friction between solids in contact, we will find that we are dealing with the relatively long-range attractive forces.

## A2.4 Van der Waals Forces

The attractive forces between atoms and molecules are known as the van der Waals forces after the scientist who studied them in 1873. van der Waals forces encompass electrostatic interactions that might arise from attractions between polar molecules, attractions between polarized molecules, and what are known as dispersion, or “London,” forces. The dispersion forces, unlike the others mentioned, act between all molecules and are thus the most important component of the total van der Waals interactions between molecules. They may be attractive or repulsive and arise due to quantum mechanical effects. Very simply, they arise due to the instantaneous fluctuation in dipole moment, or distribution of charge, within an atom. Such instantaneous dipoles may polarize a nearby atom, thus causing a mutual attraction or repulsion. Dispersion forces

can be quite substantial and can account for a large part of the intermolecular interactions of interest to us in this chapter.

Thus far we have considered interaction potentials, which invariably depend on distance. The associated forces  $P(r)$  between atoms and molecules can readily be found by differentiation, thus, for the case of the Lennard-Jones potential, we have:

$$\begin{aligned} P(r) &= -\frac{dw}{dr} \\ &= 6\frac{A}{7} - 12\frac{B}{13} \end{aligned} \tag{A2.4.1}$$

van der Waals forces bind atoms or molecules together to form solids and liquids in many materials and are called “physical” bonds to distinguish them from chemical bonds — covalent and ionic bonds that act over very short distances.

## A2.5 Surface Interactions

Intermolecular forces can be classified as being short range — operating over distance of less than a nanometre, and long range — operating up to distances of about 100 nm after which they are of negligible practical importance. The physical properties of gases are chiefly governed by interactive forces from neighboring atoms or molecules operating over relatively large distances. By contrast, the physical properties of solids are determined by intermolecular binding forces operating over relatively small distances. It should be remembered that all these interactions are electrostatic in origin, but their nature, on a molecular scale, is dictated by the cumulative effect of the proximity of neighboring atoms and the distance scale over which they operate. For example, a very important consequence of the effect of nearby ions of opposite sign in an ionic substance causes a screening effect that reduces the inverse square dependence of the Coulomb force so that the fall off with distance is more rapid.

For surfaces of bodies in contact, the situation is different again. It is found that the interaction potential between two bodies depends upon their absolute size and falls off much more slowly with increasing distance of separation compared to the interaction between two single molecules. The nature of the interaction potential may be quite complex, containing energy that prevents two molecules from attaining a minimum potential energy.

It is of interest to determine the surface interactions between two parallel plane surfaces since this offers a baseline for comparison with other surface interactions. It can be shown by calculating the interaction potential of one molecule on one surface with all the molecules on the other surface and then summing for all the molecules on the first surface, the total interaction potential for the case of van der Waals forces becomes<sup>2</sup>:

$$w(r)_{\text{planes}} = -\frac{\pi C \rho^2}{12r^2} \quad (\text{A2.5.1})$$

where  $\rho$  is the number density of molecules within the two surfaces and  $C$  is a constant. For a large rigid sphere of radius  $R$  in close proximity to a flat rigid surface, the interaction potential can be derived in a similar way and is<sup>2</sup>:

$$w(r)_{\text{sphere-plane}} = -\frac{\pi^2 C \rho^2 R}{6r} \quad (\text{A2.5.2})$$

Comparison with Eq. A2.3.1 shows that the interaction potentials for aggregated bodies decay at a substantially lower rate than that normally associated with van der Waals forces between two isolated atoms or molecules.

The associated expressions for the forces for the above two cases can be readily determined by differentiation. For the case of two plane surfaces, we obtain from Eq. A2.5.1:

$$P(r)_{\text{planes}} = \frac{dw}{dr} = -2 \frac{\pi C \rho^2}{12r^3} \quad (\text{A2.5.1})$$

And for the case of a sphere and a flat surface, differentiation of Eq. A2.5.2 gives:

$$\begin{aligned} P(r)_{\text{sphere-plane}} &= \frac{dw}{dr} = -\frac{\pi^2 C \rho^2 R}{6r^2} \\ &= -[2\pi R] \frac{\pi C \rho^2}{12r^2} \\ &= [2\pi R] w(r)_{\text{planes}} \end{aligned} \quad (\text{A2.5.2})$$

Equation A2.5.2 expresses the surface forces between a sphere and a plane surface in terms of the interaction potential of two plane surfaces for the case of small separations (i.e.,  $r \ll R$ ).

For the case of two rigid spheres of radii  $R_1$  and  $R_2$ , it can be shown that the surface force between them is<sup>3</sup>:

$$P(r)_{\text{sphere-sphere}} = [2\pi R] w(r)_{\text{planes}} \quad r \ll R_1, R_2 \quad (\text{A2.5.3})$$

where  $R$  is the relative radii of curvature of the two spheres (see Eq. 1.2c). Equation A2.5.3 is known as the Derjaguin approximation.<sup>4</sup> The advantage of expressing surface forces in this way is that it is easy to determine interaction potentials between two planar surfaces and this potential can be then be used to determine the forces associated with more complicated geometrical surfaces.

An important practical result arising from the Derjaguin approximation is the force law associated with two crossed cylinders of radii  $R_1$  and  $R_2$ . The resulting expression is:

$$P(r)_{\text{cylinder-cylinder}} = \left[ 2\pi\sqrt{R_1 R_2} \right] w(r)_{\text{planes}} \quad r \ll R_1, R_2 \quad (\text{A2.5.4})$$

When  $R_1 = R_2$ , we very conveniently obtain Eq. A2.5.2 — an important consequence for users of surface force apparatus (SFA) consisting of two crossed cylinders of equal radii. That is, contact between two crossed cylinders of equal radii is equivalent to that between a sphere of the same radius and a plane.

## A2.6 Adhesion

We are now in a position to discuss the change in potential energy of a system when two surfaces of the same material brought together into contact in a vacuum. When the two surfaces come together, there is a negative potential energy  $\Delta W$  associated with the contact. This energy is called the work of cohesion of the interface. (If the two surfaces are of the different materials, the energy is called the work of “adhesion.”) If the material is then cleaved and the two halves separated, then work, equal to the work of cohesion, is done on the system and appears as “surface energy” of the two new surfaces, thus:

$$-\Delta W = 2\gamma \quad (\text{A2.6.1})$$

If two surfaces of a material 1 are initially in a medium 2 and then brought into contact, then it can be shown that the energy associated with the interface is given by:

$$\gamma = \gamma_1 + \lambda_2 - 2\sqrt{\gamma_1 \gamma_2} \quad (\text{A2.6.2})$$

In Eq. A2.6.2,  $\gamma$  is half of the total energy required to separate two surfaces of material 1 immersed in a medium 2.\*\*\*

For the case of two rigid spheres in contact, the adhesion force  $P_A$  is given by the Derjaguin approximation, where we can now express the force in terms of the unit surface energy of the contact of two planar surfaces (See Eq. A2.5.3). Expressing the adhesion force as that required to separate the two spheres of relative radii  $R$ , we have<sup>3</sup>:

$$P_A = -4\pi R \Delta\gamma \quad (\text{A2.6.3})$$

Equation A2.6.3 applies to the case of rigid spheres in contact — i.e., the contact radius is zero. In practice, the spheres deform when placed in contact due to their finite value of elastic modulus. Under zero applied external load, two non-rigid spheres placed in contact will deform locally because of adhesion

\*\*\* It should be noted that many texts define  $\gamma$  as the “interfacial surface energy” equal to the total energy required to separate two surfaces. Here, we define  $\gamma$  as the surface energy associated with each of the two new surfaces that is half of the interfacial surface energy. We have left the  $2\gamma$  terms in these equations to remind ourselves of the distinction.

forces that produce a finite radius of circle of contact. Derjaguin, Muller, and Topov<sup>5</sup> accounted for the case of deformable bodies by adding the force given by Eq. A2.6.3 to the Hertz contact equations and the resulting contact is referred to as the “DMT” theory. The contact deformation remains Hertzian and the adhesion force  $P_A$  acts in addition to the externally applied force:

$$P = \frac{4E^*}{3} \frac{a^3}{R} - 4\pi R\Delta\gamma \quad (\text{A2.6.4})$$

Following Johnson, Kendal, and Roberts,<sup>6</sup> one could take that view that the finite size of the contact area is equivalent to a subsequent loss of surface energy  $U_S = -2\gamma\pi a^2$  as the spheres come into contact. The contact radius grows in size until a balance is reached between the loss of surface energy and the increase in stored elastic energy at the deformed material in the vicinity of the contact:

$$\frac{dU_E}{da} = \frac{dU_S}{da} = -4\gamma\pi a \quad (\text{A2.6.5})$$

Now, the Hertz pressure distribution  $p(r)$  can be rewritten as:

$$p(r) = -\frac{3}{2} \frac{P}{\pi a^2} \left(1 - \frac{r^2}{a^2}\right)^{1/2} \quad r \leq a \quad (\text{A2.6.6})$$

where the minus sign indicates compression.

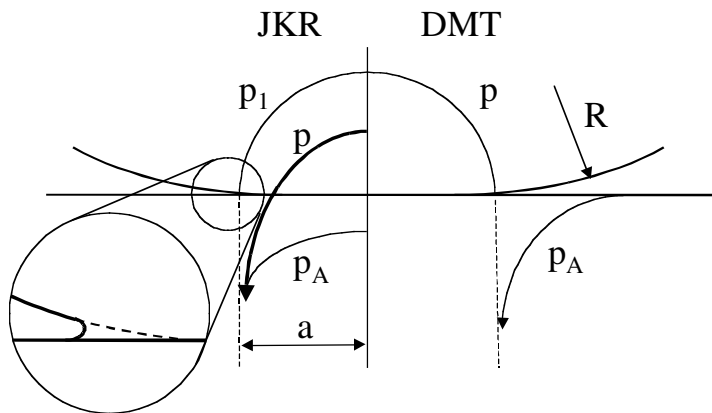


**Fig. A2.2** Contact conditions for a deformable sphere under external load  $P$  on a rigid flat surface. In the JKR case,  $p$  is the Hertz contact pressure distribution,  $p_A$  is the tensile stress due to adhesion, and  $p_1$  is the actual contact pressure distribution, which is the sum of  $p$  and  $p_A$ . The contact radius  $a$  is larger than that predicted by the Hertz equations alone. The corresponding features of the DMT theory are also shown where the stresses due to adhesion forces act outside the radius of the circle of contact.

The pressure distribution (tension) due to adhesion forces is shown by Johnson<sup>7</sup> to be:

$$p_A(r) = \frac{P}{2\pi a^2} \left(1 - \frac{r^2}{a^2}\right)^{-1/2} \quad (\text{A2.6.7})$$

These two pressure distributions and their sum are shown in Fig. A2.2 as the “JKR” theory along with the corresponding features of the DMT theory. The net pressure distribution results in a stored elastic strain energy given by:

$$p_A(r) = \frac{P}{2\pi a^2} \left(1 - \frac{r^2}{a^2}\right)^{-1/2} \quad (\text{A2.6.8})$$

and taking the derivative with respect to  $a$ , and equating with the energy balance in Eq. A2.6.3, we find that the force due to adhesion for an external load that produces a total contact of radius  $a$  is<sup>8</sup>:

$$P_A = \sqrt{8\pi a^3 2\gamma E^*} \quad (\text{A2.6.9})$$

Adhesion forces increase the contact radius for a particular applied load  $P$  over that predicted by the Hertz equations. The apparent load  $P_1$  acting between two surfaces in which adhesion is acting is thus  $P_1 = P + P_A$ , or:

$$\begin{aligned} P &= P_1 - P_A \\ &= \frac{4}{3} \frac{E^* a^3}{R} - \sqrt{8\pi a^3 2\gamma E^*} \end{aligned} \quad (\text{A2.6.10})$$

where  $a$  is the actual radius of the circle of contact, greater than that predicted by the Hertz equations. For a given applied load  $P$ , the actual radius of the circle of contact is given:

$$a^3 = \frac{3}{4} \frac{R}{E^*} \left[ P + 3\pi R 2\gamma + \sqrt{6\pi R 2\gamma P + (3\pi R 2\gamma)^2} \right] \quad (\text{A2.6.11})$$

When  $P = 0$ , the contact radius is  $a_0$  and from Eq. A2.6.11 is found to be:

$$a_0^3 = \frac{3}{4} \frac{6\pi R^2 2\gamma}{E^*} \quad (\text{A2.6.12})$$

and the adhesion force  $P_0$  acting to keep the spheres in contact at this condition is:

$$P_0 = 6\pi R 2\gamma \quad (\text{A2.6.13})$$

For the case of  $\gamma = 0$ , Eq. A2.6.11 reduces to the Hertz equation. It should be noted that  $P_0$  is not the force required to separate the two spheres. If a negative load  $P$  is applied, then as long as the term inside the square root in Eq. A2.6.11

remains positive, the spheres remain in contact with an ever decreasing contact radius until a critical negative load  $P_C$  is reached, at which time the spheres abruptly separate.

$$\begin{aligned} P_C &= -\frac{3}{2}\pi R 2\gamma \\ &= -3\pi R \gamma \end{aligned} \quad (\text{A2.6.14})$$

It should be noted that the pull-off force  $P_C$  is independent of the elastic modulus but only depends on the relative radii of curvature and the surface energy. The significance is that Eq. A2.6.14 should apply equally well to rigid spheres, but this would be contradictory to Eq. A2.6.3. The apparent conflict was resolved by Tabor who proposed that the two theories represented the opposite extremes of a dimensionless parameter  $\mu$  given by:

$$\mu = \left( \frac{4R\gamma^2}{E^* z_o^3} \right)^{1/3} \quad (\text{A2.6.15})$$

In Eq. A2.6.15,  $z_o$  is the equilibrium spacing in the Lennard-Jones potential. The significance of Eq. A2.6.15 is that it represents the ratio of the elastic deformation due to adhesion to their range of action. The JKR theory (Eq. A2.6.10) is applicable to large radius compliant solids ( $\mu > 5$ ) and the DMT theory applies to small rigid solids ( $\mu < 0.1$ ). Physically, the JKR theory accounts for adhesion forces only within the expanded area of contact, whereas the DMT theory accounts for adhesion forces only just outside the contact circle. The intermediate regime has been extensively studied<sup>9-12</sup> but for most practical applications, the JKR theory applies.

Taking the ratio of  $P_1$  and  $P_A$  in Eq. A2.6.9, we find:

$$\frac{P_1}{P_A} = \frac{1}{3} \frac{a}{R} \frac{\sqrt{E^* a}}{\sqrt{\pi\gamma}} \quad (\text{A2.6.16})$$

Now, the quantity  $a/R$  is the indentation strain and sets the scale of the contact. For a particular contact, then, the value of  $E^* a$  determines whether or not the adhesion force is significant. As  $E^* a$  becomes smaller, the adhesion force  $P_A$  becomes larger. Thus, the adhesive force is significant for very compliant surfaces even when the contacts are large. For the case of large  $E^*$ , the adhesion force becomes significant at very small contacts.

The load-point displacement when accounting for adhesive contact is also greater than that predicted by the Hertz equations and is found to be:

$$\delta = \frac{a^2}{R} \left( 1 - \frac{2}{3} \left( \frac{a_o}{a} \right)^{3/2} \right) \quad (\text{A2.6.17})$$

The influence of surface roughness upon the adhesive forces acting between two solids has been studied by Fuller and Tabor<sup>13</sup> and also by Maugis<sup>14</sup>. In practice, surfaces consist of a range of asperity heights that may deform elastically or plastically when pressed together. As these surfaces separate, the junctions between the lower asperities are progressively broken by the relaxation of the compressive stresses in the higher ones until only a few junctions remain. The pull-off force drops rapidly with increasing surface roughness.<sup>15</sup>

## A2.7 Friction

Amontons' laws of (dry) friction, in which it is stated that the resistance to motion between two bodies in contact is proportional to the load and the nature of the contacting surfaces and is independent on the area of contact, was formulated a little over 300 years ago. These famous laws are of considerable practical importance in engineering applications and are most usually expressed in terms of a coefficient of friction,  $\mu$ , such that:

$$F = \mu N \quad (\text{A2.7.1})$$

where  $N$  is the applied normal load and  $F$  is the sideways force required to initiate tangential sliding between the two bodies. Once the two bodies in question are sliding past one another, it is found that the coefficient of friction is usually reduced. It should be recognized that the real area of contact between two bodies is usually less than the apparent area of contact due to the inherent roughness of real surfaces. Contact thus only takes place at asperities on each surface and friction arises from elastic deformation, shearing, welding, ploughing, or plastic deformation of the asperities as they move, or attempt to move, past one another. Amontons' law implies that the real area of contact is directly proportional to the applied normal load, since it is the shear strength (or stress) of the interface which remains constant. The Bowden and Tabor plastic junction theory<sup>16</sup> proposes that the real area of contact between two surfaces is very small, and, subsequently, the contact pressure at those asperities in contact is very high. This results in plastic deformation of the asperities during contact with load  $P$  and so the real area of contact  $A$  can be calculated from the material's indentation hardness value  $H$ :

$$A = \frac{P}{H} \quad (\text{A2.7.2})$$

Archard<sup>17</sup> subsequently proposed that, although the deformation of the asperities may be initially plastic, there is a steady-state condition in which the contact becomes elastic. That is, for rough contacting surfaces, the deformation of the asperities may be plastic, but for smooth contacting surfaces, the contact may well be elastic. Archard<sup>17</sup> showed that if, for elastic contact, the average size of the contacts remains constant, and an increase in load produces an in-

crease in the total number of asperities coming into contact, then the proportionality between load and real area of contact is maintained. It is now generally agreed that Amontons' law, the proportionality between friction force and load, is independent of the nature of the contact at the asperities and is a consequence of the random roughness of real surfaces.<sup>18</sup>

A more fundamental knowledge of the phenomenon of friction and its relationship to adhesion is obtained through contacts in which the real and apparent area coincide, thus removing the problems associated with surface roughness. Recent developments in this field have been made possible by the use of new instrumentation such as the surface force apparatus (SFA) and the atomic force microscope (AFM). In the SFA, contact is usually made between two crossed cylinders that have been lined with a thin sheet of cleaved mica. In the AFM, a very fine needle with a radius of approximately 10 nm or so is brought into close proximity to the surface to be measured and the resulting deflection of the cantilever, to which the needle or tip is attached, is used to measure the topography of the surface. In the Atomic Friction Microscope, contact is made with the specimen surface and a tangential force is applied. The resulting twist of the cantilever is a measure of the friction force. Johnson<sup>18</sup> proposes that the observed variations in frictional stress (or shear strength) when measured with different types of instruments such as the AFM and the SFA is due to the different physical mechanism associated with the scale of the contact. In the AFM, the scale or diameter of the contact is measured in nanometres. In the SFA, the scale of the contact is measured in micrometres. With these two instruments, a different value of frictional stress is measured for dry mica. In the AFM, the frictional shear stress is reported at about 1 GPa, whereas with the SFA, a frictional shear stress of about 20 MPa is found. We would expect the frictional shear strength of an interface to be a constant, independent of the area of contact, in accordance with Amontons' law.

According to Johnson,<sup>18</sup> the physical mechanism of friction is due to the nucleation and propagation of dislocation-like defects through the interface under the influence of the applied shear force. For small contacts (<20 nm), dislocation-like defects cannot be nucleated and atoms move relative to one another collaboratively with a shear strength equal to the theoretical strength of the material. For large contacts (>50 nm), the rate of nucleation of dislocation-like continuities at the leading edge of the contact becomes equal to the rate at which they disappear at the trailing edge and the frictional stress reaches a steady-state value. In the intermediate range, the shear stress required to nucleate dislocation-like defects at the leading edge of the contact depends upon  $a^{-1/2}$  in a manner similar to that of a Mode II crack.

The significance of this is that frictional effects within the microstructure of many materials may be influenced by the scale of their microstructural features which, in turn, dictate the mechanical strength of the solid in practical applications, especially in indentation loading.<sup>19</sup>

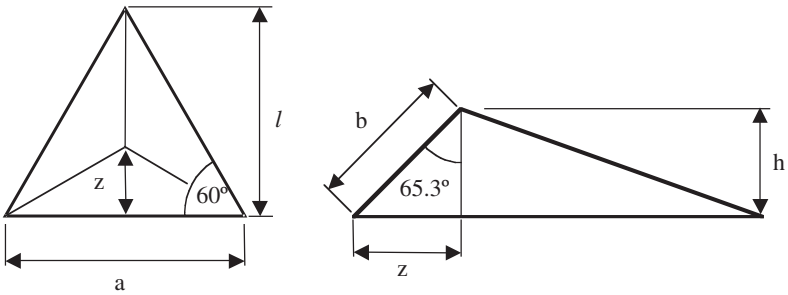
## References

1. J.E. Lennard-Jones and B.M. Dent, "Cohesion at a Crystal Surface," *Trans. Faraday Soc.* 24, 1928, pp. 92–108.
2. J.N. Israelachvili, *Intermolecular and Surface Forces*, 2<sup>nd</sup> Ed. 1992, Academic Press, London.
3. R.S. Bradley, "The cohesive force between solid surfaces and the surface energy of solids," *Phil. Mag.* 13, 1932, pp. 853–862.
4. B.V. Derjaguin, "Theorie des Anhaftens kleiner Teilchen," *Koll. Z.* 69, 1934, pp. 155–164.
5. B.V. Derjaguin, V.M. Muller, and Y.P. Toporov, "Effect of contact deformations on the adhesion of particles," *J. Coll. Interf. Sci.* 53, 1975, pp. 314–326.
6. K.L. Johnson, K. Kendall, and A.D. Roberts, "Surface energy and the contact of elastic solids," *Proc. R. Soc.* A324, 1971, pp. 303–313.
7. K.L. Johnson, "Adhesion and Friction between a smooth elastic spherical asperity and a plane surface," *Proc. R. Soc.* A453, 1997, pp. 163–179.
8. K.L. Johnson, *Contact Mechanics*, Cambridge University Press, Cambridge, 1985.
9. J.A. Greenwood, "Contact of elastic spheres," *Proc. R. Soc. Lond.* A453, 1997, pp. 1277–1297.
10. V.M. Muller, V.S. Yushenko, and B.V. Derjaguin, "On the influence of molecular forces on the deformation of an elastic sphere and its sticking to a rigid plane," *J. Coll. Interf. Sci.* 77, 1980, pp. 91–101.
11. D. Maugis, "Adhesion of spheres: the JKR-DMT transition using a Dugdale model," *J. Coll. Interf. Sci.* 150, 1992, pp. 243–269.
12. N.A. Burnham and R.J. Colton, "Force Microscopy," in *Scanning Tunneling Microscopy and Spectroscopy: Theory, Techniques and Applications*, 1993, D.A. Bonnell, ed., VCH Publishers, New York.
13. K.N.G. Fuller and D. Tabor, "The effect of surface roughness on the adhesion of elastic solids," *Proc. R. Soc. Lond.* A324, 1975, pp. 327–342.
14. D. Maugis, "On the contact and adhesion of rough surfaces," *J. Adhesion Sci. and Tech.* 10, 1996, pp.161–175.
15. K.L. Johnson, "Mechanics of adhesion," *Tribology International*, 31 8, 1998, pp. 413–418.
16. F.P. Bowden and D. Tabor, *Friction and Lubrication of Solids*, Clarendon Press, Oxford, 1950.
17. J.F. Archard, "Elastic deformation and the laws of friction," *Proc. R. Soc.* A243, 1957, pp. 190–205.
18. K.L. Johnson, "The contribution of micro/nano-tribology to the interpretation of dry friction," *Proc. Instn. Mech. Engrs.*, 214 C, 2000, pp. 11–22.
19. A.C. Fischer-Cripps, "The role of internal friction in indentation damage in a mica-containing glass-ceramic," *J. Am. Ceram. Soc.*, 84 11, 2001, pp.2603–2606.

# Appendix 3

## Common Indenter Geometries

### A3.1 Berkovich Indenter



Projected area

$$\tan 60 = \frac{l}{a/2}$$

$$l = \frac{\sqrt{3}}{2}a$$

$$A_{\text{proj}} = \frac{al}{2}$$

$$= \frac{\sqrt{3}}{4}a^2 \quad 0.433a^2$$

$$\cos 65.27 = \frac{h}{b}$$

$$h = \frac{a \cos 65.3}{2\sqrt{3} \sin 65.3}$$

$$= \frac{a}{2\sqrt{3} \tan 65.3}$$

$$a = 2\sqrt{3}h \tan 65.3$$

$$A_{\text{proj}} = 3\sqrt{3}h^2 \tan^2 65.3$$

$$24.56h^2$$

Surface area

$$A_{\text{surf}} = 3 \frac{ab}{2}$$

$$\sin 65.3 = \frac{z}{b}$$

$$z = \frac{a}{2} \tan 30$$

$$= \frac{a}{2\sqrt{3}}$$

$$b = \frac{a}{2\sqrt{3} \sin 65.3}$$

$$A_{\text{surf}} = 3 \frac{a^2}{4\sqrt{3} \sin 65.3}$$

$$0.477a^2$$

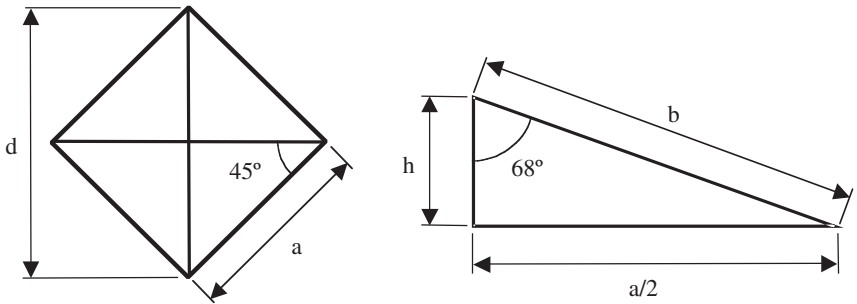
$$a = 2\sqrt{3}h \tan 65.3$$

$$A_{\text{surf}} = 27.05h^2$$

Equivalent  
cone angle:  
70.32°

**Fig. A3.1** Berkovich indenter.

### A3.2 Vickers Indenter



#### Projected area

$$\sin 45 = \frac{d}{2a}$$

$$a = \frac{d}{\sqrt{2}}$$

$$A_{\text{proj}} = a^2 = \frac{d^2}{2}$$

$$\tan 68 = \frac{a}{2h} \implies a = 2h \tan 68$$

$$A_{\text{proj}} = a^2 = 4h^2 \tan^2 68 = 24.504h^2$$

#### Surface area

$$A_{\text{surf}} = 4 \frac{ab}{2}$$

$$\sin 68 = \frac{a}{2b}$$

$$b = \frac{a}{2 \sin 68}$$

$$A_{\text{surf}} = \frac{a^2}{\sin 68} = \frac{4h^2 \tan^2 68}{\sin 68} = 26.429h^2$$

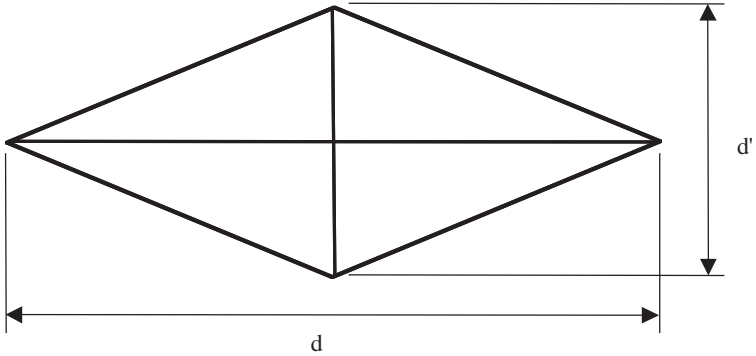
#### Equivalent cone angle:

70.3°

For cube corner, replace 68° with 35.264°  
Equivalent cone angle: 42.28°

**Fig. A3.2** Vickers indenter.

## A3.3 Knoop Indenter



Projected area

$$A_{\text{proj}} = 2 \frac{d}{2} \frac{d'}{2}$$

$$d = 2h \tan \alpha_1$$

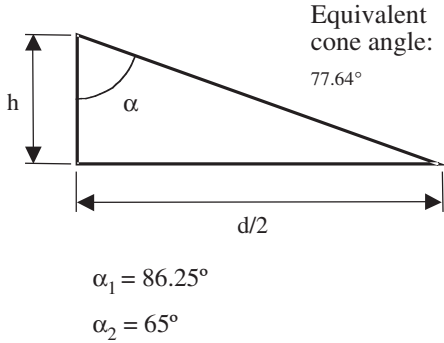
$$d' = 2h \tan \alpha_2$$

$$d' = d \frac{\tan \alpha_2}{\tan \alpha_1}$$

$$A_{\text{proj}} = \frac{d^2}{2} \cot \alpha_1 \tan \alpha_2$$

$$0.070275d^2$$

$$A_{\text{proj}} = 2h^2 \tan \alpha_1 \tan \alpha_2$$



$$\alpha_1 = 86.25^\circ$$

$$\alpha_2 = 65^\circ$$

**Fig. A3.3** Knoop indenter.

### A3.4 Sphero-Conical Indenter

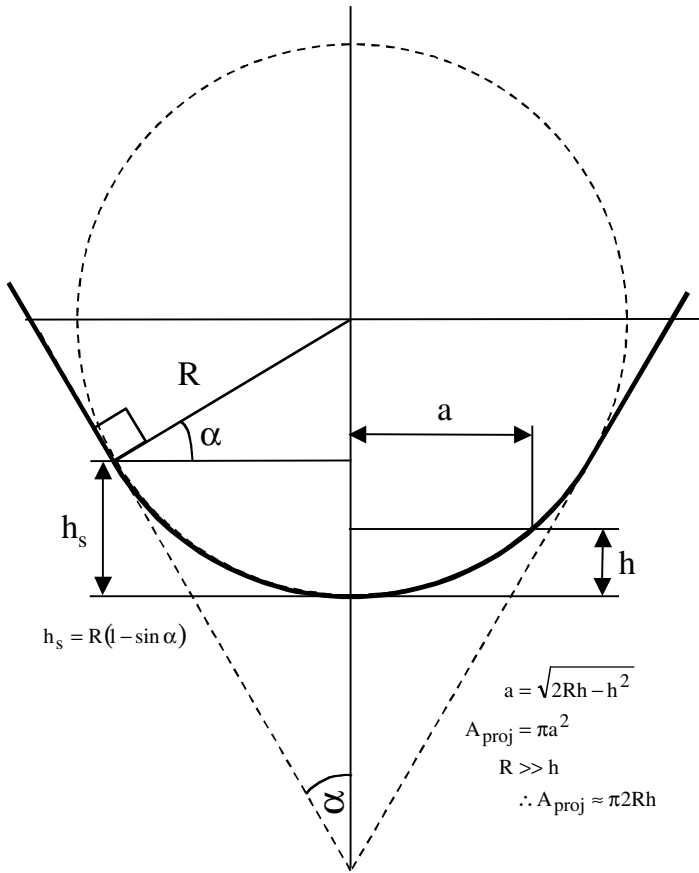


Fig. A3.4 Sphero-conical indenter.

# Index

- acoustic emission, 106, 108, 109
- adhesion, 104
- adhesive forces, 108, 179, 188
- approach speed, 129
- area function, 52, 66, 69, 70, 72, 74, 128, 131, 136, 137, 139, 140
- Auerbach, 8
  
- Berkovich indenter, 5, 8, 21, 22, 25, 28, 32, 44, 48, 66, 69, 85, 107, 115, 116, 128, 130, 138, 191
- Brinell hardness, 7, 20, 23, 24
- Buckingham Pi theorem, 91
- Burgers vector, 75
  
- calibration, 69, 115, 127, 129, 131, 137, 139, 140, 141
- center of curvature, 2, 41
- chemical bond, 180, 182
- coefficient of friction, 106, 107, 188
- combined modulus, 2, 43, 47, 77, 101, 161
- compliance, 28, 31, 32, 65, 66, 67, 69, 98, 128, 133, 136, 137, 139, 140, 153, 155, 160
- compression, 4, 8, 9, 11, 50, 185
- conical indenter, 4, 5, 6, 7, 8, 11, 12, 21, 50, 68, 75, 78, 86, 90, 93, 100, 110, 175, 177
- constraint factor, 8, 9, 11, 13, 14, 74, 93
  
- contact stiffness, 56, 58, 73, 77, 96, 98, 101, 153, 156
- continuous stiffness, 96, 146
- crack tip, 74, 116
- creep, 15, 35, 61, 62, 94, 110, 111, 112, 113, 128, 133, 134, 135, 159, 164
- critical load, 106
- CSM, 146
- cube corner indenter, 21, 26
- cylindrical punch indenter, 36, 37, 38
  
- damping coefficient, 97, 98, 146
- DCM, 146
- delamination, 30, 101, 105, 107, 108
- depth-sensing indentation, xviii, 14
- Derjaguin approximation, 183, 184
- diamond, 162
- dimensional analysis, 90, 91, 94
- dislocations, 14, 75, 76, 110
- distance of mutual approach, 3, 4
- DMT theory, 187
- dynamic hardness, 121, 169
  
- elastic constraint, 11, 23
- elastic recovery, 15, 23, 26, 27, 28, 49, 50, 51, 61, 88, 89, 126
- expanding cavity model, 11, 12, 23, 26
  
- face angle, 6, 21, 44, 128, 130, 138

- Field and Swain method, 43  
 flow stress, 8  
 fracture toughness, 8, 26, 113, 115, 159  
 friction, 11, 74, 76, 105, 106, 107, 108, 181, 188, 189  
 geometrical similarity, 6, 7, 39, 110  
 geometry correction factor, 6, 56, 86, 132  
 Hertz, 2, 5, 8, 10, 41, 42, 43, 63, 79, 175, 185, 186, 187  
 high temperature, xix, 116, 117, 145, 148  
 hydrostatic core, 12, 100  
 hydrostatic pressure, 9  
 impact, 120, 121, 147, 169  
 indentation hardness, 8, 20, 23, 24, 27, 75, 126, 131, 132, 137, 188  
 indentation modulus, 23, 132, 133  
 indentation size effect, 61, 74  
 indentation strain, 4, 7, 9, 10, 11, 20, 24, 79, 187  
 indentation stress, 4, 9, 75, 104, 105, 174  
 initial contact force, 14, 34, 62, 64, 160  
 initial penetration depth, 62, 63, 128, 129, 130, 131, 160  
 instrument compliance, 66, 67, 136, 139, 160  
 intermolecular forces, 180  
 internal pressure, 11  
 ISO 14577, 126, 128  
 JKR theory, 187  
 Knoop indenter, 8, 21, 26, 27, 48, 49, 50, 51, 126, 193  
 lateral cracks, 114, 115  
 law of mixtures, 103  
 Lennard-Jones potential, 180, 181, 182, 187  
 linear elasticity, 9  
 Martens hardness, 130, 131, 132, 136  
 mean contact pressure, 1, 3, 4, 7, 8, 9, 11, 13, 23, 24, 25, 27, 42, 45, 77, 79, 83, 84, 86, 110, 131, 176, 177  
 mechanical properties nanoprobe, 100  
 median cracks, 26, 114  
 Meyer, 8  
 Meyer hardness, 24, 131  
 Meyer's index, 119  
 Meyer's law, 24  
 Moh's hardness scale, xviii  
 multiple-point unload method, 42, 43, 46, 47, 131  
 Nano Indenter<sup>®</sup>, 146  
 nanocomposite film, 162  
 Nano-Hardness Tester<sup>®</sup>, 153  
 NanoTest<sup>®</sup>, 147  
 Oliver and Pharr method, 16, 42  
 oscillatory motion, 30, 34, 55, 96  
 picroindenter, 16  
 pile-up parameter, 72  
 piling-up, 61, 71, 72, 73, 74, 79, 92, 107  
 plastic zone, 7, 9, 10, 11, 12, 13, 23, 24, 32, 72, 75, 83, 86, 103, 113, 114  
 plasticity, 8, 11, 30, 32, 40, 83, 84, 86, 101, 161  
 pressure distribution, 8, 10, 11, 174, 175, 185, 186  
 principal stresses, 8, 176  
 projected area of contact, 21, 25, 26, 45, 47, 48, 61, 131, 137  
 radial cracks, 114, 115, 116

- reaction forces, 31, 65, 136
- reduced modulus, 2, 133
- reference blocks, 127, 139, 140
- relative radius, 2, 41, 43
- relaxation, 27, 49, 50, 134, 188
- representative strain, 7, 25, 32, 110
- residual stresses, 8, 15, 74, 79, 80, 104, 159
  
- scanning electron microscope, 16
- scratch hardness, 106
- simulated data, 87, 88, 89
- simulation, 83, 86, 87, 88, 89
- single-point unload method, 41, 43, 47, 48
- sinking-in, 61, 71, 72, 73, 74, 92, 93
- slip lines, 11, 13
- slip-line theory, 23
- spherical indenter, 20, 22, 23, 24, 28, 42, 45, 67, 70, 78, 128, 175
- spherical indenters, 5
- stiffness, 20, 34, 56, 58, 65, 73, 77, 96, 97, 98, 100, 101, 146, 153, 156
- strain gauge, 16
- strain gradient, 74, 76
- strain rate, 94, 110, 111
- strain rate sensitivity, 110
- strain-hardening, 11, 15, 32, 71, 72, 74, 90, 110, 129, 159
- strain-hardening exponent, 119
- stress intensity factor, 116
- stress trajectories, 176, 177
- stress-strain relationship, 4, 71
  
- superhard materials, 163
- surface roughness, 56, 76, 77, 129, 131, 135, 136, 188, 189
  
- tangential force, 105
- tension, 4, 186
- thermal drift, 30, 35, 61, 62, 128, 129, 133, 143, 144, 153, 160
- thin films, 30, 32, 77, 100, 105, 108, 113, 150
- three-element model, 112, 164
- tip rounding, 32, 77, 78
- Tresca, 9, 13, 14
- TriboIndenter<sup>®</sup>, 150
  
- UMIS<sup>®</sup>, 155, 156
- Universal hardness, 130
  
- van der Waals forces, 181, 182, 183
- Vickers hardness, 25, 45
- Vickers indenter, 5, 7, 8, 20, 21, 24, 25, 26, 32, 44, 116, 128, 131, 136, 137, 138, 192
- visco-elastic properties, 30, 164
- von Mises, 9, 13, 14
  
- wear, 120, 149
- work, 57, 92, 135, 180
- work hardening, 9
- work of adhesion, 184
- work of cohesion, 184
- work of indentation, 54
  
- yield stress, 9, 79, 94, 103